ABSTRACT

FACETED NANOMATERIAL SYNTHESIS, CHARACTERIZATIONS AND APPLICATIONS IN REACTIVE ELECTROCHEMICAL MEMBRANE FILTRATION

by
Qingquan Ma

Facet engineering of nanomaterials, especially metals and metal oxides has become an important strategy for tuning catalytic properties and functions from heterogeneous catalysis to electrochemical catalysis, photocatalysis, biomedicine, fuel cells, and gas sensors. The catalytic properties are highly related to the surface electronic structures, surface electron transport characteristics, and active center structures of catalysts, which can be tailored by surface facet control. The aim of this doctoral dissertation research is to study the facet-dependent properties of metal or metal oxide nanoparticles using multiple advanced characterization techniques. Specifically, the novel atomic force microscope-scanning electrochemical microscope (AFM-SECM) and density functional theory (DFT) calculations were both applied to both experimentally and theoretically investigate facet dependent electrochemical properties, molecular adsorption, and dissolution properties of cuprous oxide and silver nanoparticles.

To promote the facet engineered nanomaterials for environmental engineering apparitions, our research has evaluated the performances of electrochemically reactive membranes that were prepared with novel 2D nanomaterials with surface functioal modifications to enable electrochemical advanced oxidation processes (EAOPs) in membrane filtration process. Our results demonstrated many advantages such as tunable reactivity, tailored surface reactions, antifouling features, and feasibility of large-scale

continuous operations. Specifically, this dissertation will introduce our electrochemical membrane synthesis, reactivity, aging, byproducts formation and electrochemical adsorption and desorption, oxidation of pollutants such as two typical per-and poly-fluoroalkyl substances (PFAS), perfluorooctanoic Acid (PFOA) and perfluorobutanoic acid (PFBA).

FACETED NANOMATERIAL SYNTHESIS, CHARACTERIZATIONS AND APPLICATIONS IN REACTIVE ELECTROCHEMICAL MEMBRANE FILTRATION

by
Qingquan Ma

A Dissertation
Submitted to the Faculty of
New Jersey Institute of Technology
in Partial Fulfilment of the Requirements for the Degree of
Doctor of Philosophy in Environmental Engineering

John A. Reif, Jr. Department of Civil and Environmental Engineering

December 2022

APPROVAL PAGE

FACETED NANOMATERIAL SYNTHESIS, CHARACTERIZATIONS AND APPLICATIONS IN REACTIVE ELECTROCHEMICAL MEMBRANE FILTRATION

Qingquan Ma

Wen Zhang, Dissertation Advisor — Date
Associate Professor of Civil and Environmental Engineering, NJIT
Affiliated faculty of Chemical and Materials Engineering, NJIT

Joshua A Young, Co-Advisor — Date
Assistant Professor, Chemical and Materials Engineering, NJIT

Taha Marhaba, Committee Member — Date
Professor and Chair of Civil and Environmental Engineering, NJIT

Sagnik Basuray, Committee Member — Date
Associate Professor, Chemical and Materials Engineering, NJIT

Jaehong Kim, Committee Member — Date
Professor and Chair of Chemical and Environmental Engineering
Yale University, New Haven, Connecticut

Lucía Rodríguez Freire, Committee Member — Date
Assistant Professor, School of Engineering, Newcastle University
Newcastle upon Tyne, Tyne and Wear, United Kingdom

BIOGRAPHICAL SKETCH

Author: Qingquan Ma

Degree: Doctor of Philosophy

Date: December 2022

Undergraduate and Graduate Education:

- Doctor of Philosophy in Environmental Engineering,
  New Jersey Institute of Technology, Newark, NJ, 2022

- Master of Science in Environmental Engineering,
  Beihang University, Beijing, P. R. China, 2019

- Bachelor of Science in Environmental Engineering,
  Beihang University, Beijing, P. R. China, 2016

Major: Environmental Engineering

Presentations and Publications:

Qingquan Ma, Joshua Young, Sagnik Basuray, Guangming Cheng, Jianan Gao, Nan Yao, Wen Zhang. "Elucidating Facet Dependent Electronic and Electrochemical Properties of Cu_2O Nanocrystals Using AFM/SCEM and DFT." ***Nano Today***, 45 (2022): 101538.

Qingquan Ma, Jianan Gao, Courtney Potts, Xiao Tong, Wen Zhang. "Electrochemical Aging and Halogen Oxides Formation on Carbon Nanotube (CNT) and Fe_3O_4/g-C_3N_4 coated Conductive Membranes." ***Industrial and Engineering Chemistry Research*** (2022).

Qingquan Ma, Wen Zhang, and Joshua Young. "Effect of Single Atom Platinum (Pt) Doping and Facet Dependent on The Electronic Structure and Light Absorption of Lanthanum Titanium Oxide ($La_2Ti_2O_7$): A Density Functional Theory study." ***Surface Science***,715 (2022): 121949.

Weihua Qing, Zhifeng Hu, **Qingquan Ma,** and Wen Zhang. "Conductive Fe_3O_4/PANI@ PTFE Membrane for High Thermal Efficiency in Interfacial Induction Heating Membrane Distillation." ***Nano Energy*** (2021): 106339.

Chen Chen, **Qingquan Ma,** Fangzhou Liu, Jianan Gao, Xinyang Li, Shaobin Sun, Hong Yao, Changqing Liu, Joshua Young, and Wen Zhang. "Photocatalytically Reductive Defluorination of Perfluorooctanoic Acid (PFOA) Using Pt/$La_2Ti_2O_7$ Nanoplates: Experimental and DFT Assessment." ***Journal of Hazardous Materials*** (2021): 126452.

Xiaonan Shi, **Qingquan Ma,** Taha Marhaba, Wen Zhang. "Probing Surface Electrochemical Activity of Nanomaterials using Hybrid Atomic Force Microscope-Scanning Electrochemical Microscope (AFM-SECM). " ***Journal of Visualized Experiments***.2021.

Likun Hua, Han Cao, **Qingquan Ma**, Xiaonan Shi, Xuezhi Zhang and Wen Zhang. "Microalgae Filtration using Electrochemically Reactive Ceramic Membrane: Filtration Performances, Fouling Kinetics and Foulant Layer Characteristics." ***Environmental Science and Technology***. 2020.

Xiaomin Li, **Qingquan Ma**, Tong Liu, Zhaomin Dong, Wenhong Fan. "Effect of TiO_2-Nanoparticles on Copper Toxicity to Bacteria: Role of Bacterial Surface." ***Royal Society of Chemistry Advances*** 10(9), 2020: 5058-5065.

Xiangrui Wang, Dingyuan Liang, Ying Wang, **Qingquan Ma**, Baoshan Xing, and Wenhong Fan. "Effects of Organic Matter on Uptake and Intracellular Trafficking of Nanoparticles in Tetrahymena thermophila." ***Environmental Science: Nano*** 6(7), 2019: 2116-2128.

Jinqian Ren, Wenhong Fan, Xiangrui Wang, **Qingquan Ma**, Xiaoming Li, Zhizhen Xu. "Influences of Size-fractionated Humic Acids on Arsenite and Arsenate Complexation and Toxicity to Daphnia Magna." ***Water Research*** 108 (2017), 68-77.

Qingquan Ma, Wen Zhang. Photocatalytic Degradation of PFOA using Pt/$La_2Ti_2O_7$ Nanosheets: Roles of Electron Donors in Reductive Defluorination. Qingquan Ma. **The 10th Sustainable Nanotechnology Conference,** Online oral presentation, Nov. 3th, 2021.

Qingquan Ma, Wen Zhang, Joshua Young. Single atom Pt Doping and Facet Dependent Photocatalytic Activity of $La_2Ti_2O_7$: A DFT study. **The Virtual Dana Knox Student Research Showcase, NJIT** Online oral presentation, April, 21th,2021.

Qingquan Ma, Wen Zhang. Shape-Controlled Dissolution of Silver Nanoparticles: a Case Study by Atomic Force Microscope-Scanning Electrochemical Microscope (AFM-SECM). **Eastern Analytical Symposium 58th Annual Meeting**, Plainsboro, NJ (Oral presentation), Nov. 20th, 2019.

Qingquan Ma, Joshua Young, Mengqiang Zhao, Wen Zhang. Electro-sorption, Desorption and Oxidation of Perfluoroalkyl Carboxylic Acids (PFCAs, C4&C8) via High performance MXene/PANI Membrane. **The 11th Sustainable Nanotechnology Conference,** Austin, TX, Nov. 10-14th, 2022.

Qingquan Ma, Joshua Young, Wen Zhang. Facet-Dependent Photocatalytic Degradation of PFOS: Theoretical Prediction. **FLUOROS Global**, Online, October 3, 2021.

Qingquan Ma, Jianan Gao, Courtney Potts, Wen Zhang. Electrochemical Membrane Aging and Oxides of Halogen Formation. **North American Membrane Society**, Larimer County, CO, August 28– 31,2021.

Qingquan Ma, Wen Zhang, Joshua Young. Facet-Dependent Electrochemical Behavior of Cu_2O Microcrystals for Methyl Orange: Theoretical Prediction and Experimental Validation. **American Chemical Society Annual Conference**, Atlanta, GA, Aug 22 – 26, 2021.

Qingquan Ma, Courtney Potts, Wen Zhang. Electrochemical Membrane Aging and Oxides of Halogen Formation. **American Chemical Society Annual Conference**, Atlanta, GA, Aug 22 – 26, 2021.

Qingquan Ma, Wen Zhang, Joshua Young. Single atom Pt Doping and Facet Dependent Photocatalytic Activity of $La_2Ti_2O_7$: A DFT study. **The First Chinese-American Professors in Environmental Engineering and Science Student E-Poster Competition**, Online, Jul. 17th, 2021.

Chen Chen, Qingquan Ma, Wen Zhang. Photocatalytic Degradation of PFOA using Pt/$La_2Ti_2O_7$ Catalyst: Roles of Electron Donors in Reductive Defluorination. **The American Geophysical Union Fall meeting.** Online, Dec. 16th, 2020.

Qingquan Ma, Wen Zhang. Facet-dependent Adsorption Properties of Polyhedral Nanocrystals of Cu_2O Studied by Atomic Force Microscope Coupled with IR and Scanning Probe Electrochemistry. **Eastern Analytical Symposium 59th Annual Meeting**, Online, Nov. 18th, 2020.

Qingquan, Wen Zhang. Carbon-Metal Nanohybrids (CMNHs)-Impregnated Electrochemical Reactive Membrane (ERM) Filtration for PFAS Removal. **North American Membrane Society**, Online, May 18th, 2020.

Qingquan Ma, Xiaonan Shi, Wen Zhang. Shape-Controlled Dissolution of Faceted Nanomaterials by Hybrid Scanning Electrochemical Microscope-Atomic Force Microscope (SECM-AFM). **American Chemical Society Spring National Meeting & Exposition**, Philadelphia, PA, 03/2020.

Qingquan Ma, Wen Zhang. Shape-Controlled Dissolution of Silver Nanoparticles: a Case Study by SECM/AFM. **Graduate Student Association Events**, NJIT Newark, NJ, Nov. 25th, 2019

Qingquan Ma, Likun Hua, Wen Zhang. Reactive Electrochemical Membrane (REM) Filtration for PFOA/PFOS Removal, **U.S. Environmental Protection Agency's National Student Design Competition**, Boston, MA, Jun. 18th, 2019.

Likun Hua, Qingquan Ma, Wen Zhang. Multifunctional Reactive Electrochemical Membranes (REM) for Emerging Contaminant Removal, **U.S. Environmental Protection Agency's National Student Design Competition**, Boston, MA, Jun. 18th, 2019.

Likun Hua, Qingquan Ma, Wen Zhang. Evaluation of Ti_4O_7 Ceramic Membrane Filtration and Fouling Mitigation in Algal Biomass Harvesting, **U.S. Environmental Protection Agency's National Student Design Competition**, Boston, MA, Jun. 18th, 2019.

To my parents, relatives, girlfriend, and everyone accompanied me through this journey.
Thank you for making my life confident and colorful.

ACKNOWLEDGEMENTS

Pursuing a PhD degree is not only arduous, but also joyful journey. I could not have made through mine so successfully without supports and encourages from many people. Here, I would like to mention those people who made this journey a paramount experience for my PhD life.

Words will never be enough to express my gratitude to my advisor, Dr. Wen Zhang, for his constant and precious guidance all the time and providing me the opportunities to expand my knowledge and experience. I am always grateful for his trust, his encouragement, believing in my potential and letting me explore the field of nanotechnologies. I believe that he is one of the most reliable and helpful mentor and advisor that cares about students the most. He always keeps in mind my career goal as faculty and helps me build up critical skills for this profession. I have also been very fortunate to have had the opportunity to get involved in multiple research projects, attend numerous international and regional conferences, get involved in proposal writing and mentor students. What he taught me is not limited to the research study but also how to be an independent researcher and mentor. It has been an honor and a pleasure to study under the supervision of such an individual of exceptional professional, teaching and personal qualities.

Special thanks go to my co-advisor, Prof. Joshua Young, for continuously providing me guidance, insightful suggestions, and support throughout the density function theory and Ab initio molecular dynamics (AIMD) simulations of my PhD research. Moreover, Dr. Young has always been supportive of the ideas I created, and most of which have proven to be of great importance for the success of my research. His insight and

suggestions have pushed me toward a better and deeper understanding of computational simulation.

I would like to thank my committee, Dr. Taha Marhaba, Dr. Sagnik Basuray, Dr. Jaehong Kim and Dr. Lucía Rodríguez Freire, for their valuable contributions to this dissertation. Their insightful suggestions and encouragement are deeply appreciated. I would also like to express my special thanks to Dr. Jaehong Kim for encouraging and advising me after my proposal defense, his guidance allowed me to be more confident to finish my PhD degree. Moreover, I would also like to express Dr. Sagnik Basuray's helping on electrochemical theory and related equipment. His helpful ideas and valuable work contribute a lot to my projects related to this dissertation.

For the most important, I want to give my endless gratitude to financial support from National Science Foundation (Grant No.1756444), NSF INTERN (Grant No.1836036 and 2016472), the United States Environmental Protection Agency (Grant No.83945201), New Jersey Water Resources Research Institute (Grant No.2020NJ025B), NJIT York Center and Undergraduate Research and Innovation program (URI) Phase-1 & Phase-2 program. And also, my DFT simulation supercomputer performed on the Kong and Lochness clusters at the New Jersey Institute of Technology, the Extreme Science and Engineering Discovery Environment (XSEDE, supported by NSF Grant No. ACI-1053575) under allocation TG-DMR180009, and the CARBON cluster at the Center for Nanoscale Materials (Argonne National Laboratory, supported by the U.S. DOE, Office of Basic Energy Sciences (BES), DE-AC02-06CH11357) under allocations CNM72868, CNM77374, CNM 79443.

In addition, I received lots of help from the professors and students in NJIT. I want to thank Professor Sagnik Basuray and his PhD student Dr. Zhenglong Li for solving lots of question on electrochemical test and supporting me to run my own electrochemical system. And many thanks to Prof. Lucia Rodriguez-Freire for helping on qualify examination and experimental text of water samples. Moreover, I'd like to thank Dr. Larisa Krishtopa, Dr. Xueyan Zhang Dr. Linfeng Rao and Dr. Jeong Shim for their training, help and advice on GC-MS, LC-QQQ, Raman, AFM, FTIR, XRD, Raman and SEM measurement and operation. In particular, I want to thank Dr. Taha Marhaba, our department chair, for providing a comfortable place for me to work and study. Also, Nasser and Steve are truly appreciated for their kind help on my research.

Moreover, the collaborators and professors from other universities and institutes helped me a lot during my doctoral study. I appreciate the opportunity to learn the SEM operation and measurement technique in Dr. Laying Wu's Center for Environmental and Life Sciences. I really appreciate the opportunity to learn the AFM-IR operation and measurement technique under Dr. Samuel Tenney's helping in Center for Functional Nanomaterials of Brookhaven National Laboratory. I also really appreciate the opportunity to learn the TEM operation and measurement technique under Dr. Sooyeon Hwang's helping in Center for Functional Nanomaterials of Brookhaven National Laboratory. I also want to give my specific thanks to Dr. Xiao Tong from Brookhaven National Laboratory and Dr. Sylvie Rangan from Rutgers University for providing the opportunity to learn the XPS operation and measurement technique and also relevant manuscript writhing. Furthermore, I really appreciate the opportunity to learn the SEM and TEM operation and measurement technique under Dr. Guangming Cheng's and Director Nan Yao helping in

Princeton's Imaging and Analysis Center of Princeton University. I would like to express my appreciation to my collaborators Dr. Boris Khusid, Albert Wu and Uwe Beuscher for their helpful suggestions to my MAST projects who provided supportive ideas and efforts. Besides, I want to thank Thomas Mueller, Director of Business Manager from Bruker Nano, for providing great help before and during my short-term internship at Bruker. Thomas helps us a lot on finalize the support letter, the agreement file and other paperwork. The internship enables me to learn more in depth knowledge of AFM characterization techniques from Bruker experts and operations of industrial laboratories, which will empower my career development.

I also thank my current and previous group members, Wanyi Fu, Xiaonan Shi, Chunzhao Chen, Shan Xue, Xiaoyu Wang, Fangzhou Liu, Jianan Gao, Yihan Zhang, Likun Hua, Weihua Qing and all the students who worked in our lab. And they are: Kaiqin Dong, Xinyuan Wang, Ran Yan, Mark Lee, Mason Kung. I really appreciate their valuable help and support during the period of my research. I feel grateful to my current and former office mates: Mandeep Pokhrel, Anuruddha Jayasuriya, and Jin Fan for providing a fun filled environment.

Most importantly, I would not succeed in this endeavor without my families' long-lasting support, understanding, encouragement, and patience, which accompany me through all the hardship during the research adventure.

TABLE OF CONTENTS

TABLE OF CONTENTS
(Continued)

TABLE OF CONTENTS
(Continued)

TABLE OF CONTENTS
(Continued)

TABLE OF CONTENTS
(Continued)

LIST OF TABLES

LIST OF TABLES
(Continued)

LIST OF FIGURES

LIST OF FIGURES
(Continued)

LIST OF FIGURES
(Continued)

LIST OF FIGURES
(Continued)

LIST OF FIGURES
(Continued)

LIST OF FIGURES
(Continued)

LIST OF FIGURES
(Continued)

Figure **Page**

LIST OF FIGURES
(Continued)

CHAPTER 1

LITERATURE REVIEW

Because of the rapid growth of global population, explosive development of industrialization and greater demand of energy in the past century, water scarcity has already become a serious global emerging challenge that is predicted to be worse in the future. Hence, a much better clean, safe and drinkable water treatment technology with higher efficiency and more sustainability is urgently required. Membrane technology are favored over other technologies for water/wastewater treatment, such as distillation, photodegradation, electrolysis or adsorption method, because, in theory, they take lower energy consumption, need no regeneration of spend media, achieve higher separation selectivity, and operate in a continuous mode. Although membrane technologies have already played a significant role in water purification with efficient, selective, and reliable separation performances, membrane processes often suffer from membrane fouling, physical diverting, ineffective to micropollutants and organic compounds (especially, highly recalcitrant contaminants). Reactive Electrochemical Membranes (REM) combined membrane technologies coupled with electrochemical advanced oxidation processes (EAOPs) has shown the significant improvement in the removal efficiency of organic contaminants from wastewater and antifouling ability of membranes compared to conventional EAOPs and membrane processes. Nanomaterial and nanotechnology are the key as the best possible methods to overcome the limitations of REM, such as mass transfer limitations, membrane materials' performance, stability and cost, life span of membranes. Firstly, a comprehensive understanding of shape-controlled syntheses factor and typical

mechanisms is in need for delineating and predicting the influences of morphology on nanomaterials properties. Secondly, proper characterization is the key to accurately evaluate shape dependent physical, chemical and electrochemical properties of nanomaterials on exploring the novel, highly efficient, cost-effective membrane materials. There still remains a challenge to perform rapid, *in situ*, and possibly real-time characterization and quantification of nanomaterials, which is crucial for unravel new information about nanomaterial properties. Thirdly, the potential for nanotechnology to enable reactive electrochemical membranes filtration may substantially improve the energy efficiency of water treatment and expand access to safe water. However, enabling the real application of nanotechnology to REM will require strategies for resolving operational risks: such as, electrode stability (membrane aging or fouling), trade-offs between electrodes material performance (novel electrode material and nanoarchitectures and transition towards earth-abundant metals), byproducts formation (realistic aquatic application), increasing pollutant selectivity (crystal facets, DFT enabling bottom-up electrode design), life cycle analyses for nano-REM.

Nanomaterials often show enhanced activities or characteristics compared with their bulk counterpart materials owing to their unique morphological, electronic and chemical surface properties. These properties can be carefully tuned to modify the activity and selectivity of electrocatalytic reactions or other particular functionalities. In many cases, catalytic performance of a catalyst highly depends on size or shape of this catalyst. Size modulates the fraction of atoms of the topmost surface layer among all atoms of a nanoparticle, the fractions of atoms at corner and edge among all atoms of the topmost surface layer of the nanoparticle, and the specific surface area of a catalyst in unit of mm^2

per gram. Other than these size-dependent fractions of under-coordinated sites, electronic state of a metal nanoparticle could vary or even transit from a metallic state to molecular along with the decrease of size. Catalyst nanoparticles with different shapes could have different crystallographic shapes, packing, density and even electronic state of atoms of different surfaces.

These shape-dependent factors are closely related to surface chemistry and structure of a catalyst, which essentially determines catalytic performance. This is because a catalytic event at a solid–gas or solid–liquid interface is performed on a catalytic site of the catalyst surface through necessary elemental steps called surface adsorption. From surface science point of view, typically reactant molecules, dissociated species and intermediates must interact with atoms of a catalytic site if a catalytic reaction follows the Langmuir–Hinshelwood mechanism. For example, the binding configuration of reactant molecules, dissociated species, and intermediates, and even products, and the binding strengths could all influence the selection of a specific reaction pathway. Surface of a catalyst nanoparticle with a different facet could yield a different binding configuration and strength; thus, they provide different sites of surface terraces, steps and corners. Thus, the influences of shape of a catalyst nanoparticle on its catalytic performance are essentially reflected by variation of chemical and structural factors of surface of catalyst nanoparticles. The measured catalytic performance of an industrial catalyst is in fact a sum of contributions of individual nanoparticles with different structural and chemical variations. Due to the interplay between the structural and chemical factors, it is quite challenging to achieve fundamental insights into how each of these factors influences the catalytic

performance. Yet, such fundamental insights are crucial for rational design of a catalyst with high activity, selectivity and durability.

Among different tools for probing nanomaterial properties, atomic force microscope (AFM) is one of the most attractive and unparalleled means that could characterize in situ surface properties at a nanometer resolution. AFM utilizes a cantilever with a sharp tip (radius of curvature: 5-10 nm) that oscillates over the surface of samples while scanning. The subtle changes in heterogeneity of local material surfaces will induce sensitive changes of the cantilever tip's vibration amplitude and frequency. For example, AFM can measure hardness and elasticity, surface adhesiveness, surface energy and surface electrical properties. Particularly, Kelvin probe force microscopy (KPFM) operated in the electric mode of AFM generates mapping of the local surface work functions (or Fermi energy levels). Local work function can reveal surface defects, grain boundaries and surface charges on single crystal planes. Furthermore, scanning electrochemical microscopy–atomic force microscopy (SECM–AFM) can characterize electrochemical reactions or processes (*e.g.,* corrosion) in real time, simultaneously collect nanomaterials' topography and electrochemical properties at local material surfaces with high spatial resolution. Such local-scale characterizations are crucial for understanding nanomaterials' structure-activity relationships.

1.1 Shape Control of Metal and Metal-Oxide Nanomaterials

Nanotechnology is design, fabrication and application of nanostructures or nanomaterials, and the fundamental understanding of the relationships between physical properties or phenomenon and material dimensions. Nanotechnology deals with materials or structures in nanometer scales, typically ranging from sub-nanometers to several hundred nanometers.

Advances in nanotechnology have significantly contributed to many science and engineering fields such as material science, biotechnology, environmental engineering, among other disciplines. Unique properties at the nanoscale have led to a large number of material applications in a wide range of commercial and industrial products such as catalysts, construction materials, electronic devices, and cosmetics, among others . It is estimated that by the year 2020, nanotechnology industries will reach to a market value of approximately $3 trillion. Among engineered nanomaterials, metal- and metal-oxide nanoparticles currently comprise a significant fraction of all produced and applied engineered nanoparticles. For example, nanoscale silver and nanoscale titanium are widely used in treated paints for car, outdoor, and indoor facilities. As a color additives, food industries have widely used titanium dioxide nanoparticles. Nano sized titanium dioxide and zinc oxide currently are also routinely used in skin cosmetics and sunscreens as ultraviolet (UV) filters.

Along with unique material properties, the impacts of nanomaterials on environment and human health must also be evaluated for technology safety and sustainability. In 2007, Science Policy Council of U.S. Environmental Protection Agency published a "Nanotechnology White Paper" to address potential risks from environmental exposure to nanomaterials. The White Paper provided information regarding the potential risk of nanomaterials including human health (toxicity), fate, and transport research. Since, concerns regarding the possible unwanted release of nanoparticles into the environment during their production, usage, or disposal have been topics of considerable attention.

1.1.1 Metal and Metal-Oxide Nanomaterials

Metal and metal-oxide nanomaterials exhibit different physiochemical properties and are different than their native bulk compounds in several respects which includes its surface, optical, thermal, magnetic, mechanical, biological and electrical properties. The properties that make the nanophase structures indispensable tools in modern nanotechnology are their various nonlinear optical properties, higher ductility at elevated temperatures than the coarse-grained ceramics, cold welding properties, superparamagnetic behavior, unique catalytic, sensitivity, and selective activity. For example, the melting point of the nanosized material is lower than that of a bulk material with the same composition. At the same time, NPs exhibit unusual adsorptive properties and fast diffusivities and they are not stable in critical conditions.

Metal and metal-oxide nanomaterials with fundamental properties have been found to hold great potential and promise for use in biomedical, biosensor, pharmaceutical, catalytic, fuel cells, drug delivery, healthcare, cosmetics, household, agricultural, optical, chemical, magnetic data storage and antimicrobial applications. Owing to their interesting properties, which are affected by their structural morphology, nanoparticles have been studied extensively, and many studies have synthesized nanoparticles via chemical and physical methods.

Among above applications, electrocatalysis has broadly been employed in chemical reactions, separation, energy conversion and storage. For most electrocatalytic systems, the reasonable construction of active sites is important for catalytic activity and reaction mechanisms. For example, **Figure 1.1a−e** shows faceted CeO_2 nanocrystals that are oriented along [110], with [111], [110], and [002] lattice planes imaged edge-on. **Figure 1.1f** shows that the truncated octahedral CeO_2 could be enclosed by [111] and [100] planes

that have different surface density of atoms [111] > [100]] and different surface energy [γ[111] < γ[100]] (**Figure 1.1h–j**). The exposed crystal facets greatly dictate the surface redox chemistry and catalytic activities of ceria nanomaterials. Rod-shaped nanostructures of CeO_2 preferentially expose the reactive [110] and [100] planes, providing higher catalytic activity for CO oxidation. Adsorption mechanisms and reaction kinetics of acetaldehyde on [111] and [100] of CeO_2 differ significantly. Similarly, a greater proportion of exposed polar surfaces of ZnO crystals has been found to have greater photocatalytic activity. Catalytic activities of high-index facets of Au NPs exhibit dramatically enhanced catalytic activities toward a variety of chemical and electrochemical reactions because high-index facets are open surface structures with high densities of coordinatively unsaturated atoms at the surface steps and kinks in comparison to the close-packed low-index facets.

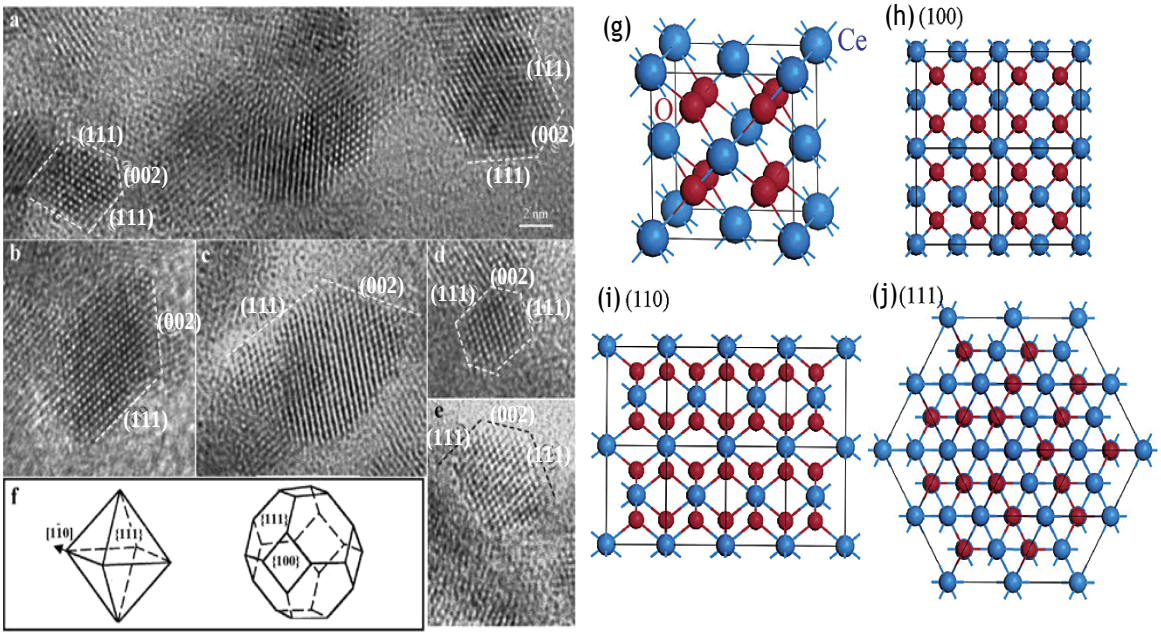

Figure 1.1 (a–e) Typical high-resolution TEM images of CeO_2 oriented along [110], showing the facet structures as defined by the [002] and [111] facets. (f) Structural models of the octahedral and truncated octahedral shapes. (g) Unit cell of the CeO_2 structure. (h–j) The [100], [110], and [111] planes of the CeO_2 structure.

1.1.2 Syntheses of Metal and Metal-Oxide Nanomaterials

There has been great progress in the fabrication of various metal and metal-oxide nanostructures as well as the investigation of their field uses over the last two or three decades. The study and production of novel materials at the nanoscale are included in nanotechnology. In nanotechnology, a number of synthetic methods and techniques were employed. The "top-down" technique and the "bottom-up" approach are two main categories of synthetic strategies that can be used to produce and fabricate metal and metal-oxide nanostructures, as shown in **Figure 1.2**.

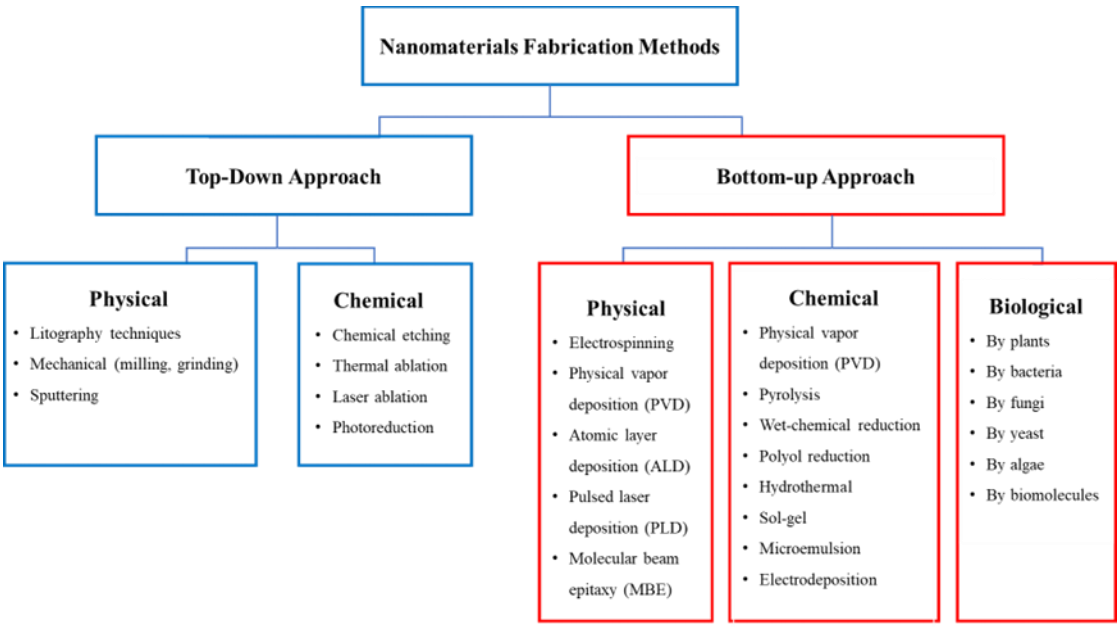

Figure 1.2 Two approaches to nanoparticle syntheses.

In the top-down approach, nanoparticles are synthesized by size reduction, degenerating from the bulk material into fine particles. This process could be achieved through physical and chemical methods by lithographic, mechanical(e.g., milling, grinding), sputtering, chemical etching, thermal evaporation, pulsed laser ablation and photo reduction techniques. However, the top-down approach is based on the physical and lithographic principle of micro- and nanotechnology and starts from a large material entity.

The produced metal and metal-oxide nanoparticles (NPs) have sizes in the medium to lower nanometer range but with a relatively broad size distribution and uncontrollable shape. In the bottom-up approach, nanoparticle synthesis relies on chemical methods (e.g., chemical reduction/oxidation of metal ions), sol-gel chemistry, chemical vapour deposition(CVD), co-precipitation, microemulsion, pyrolysis, hydrothermal, solvothermal, radiation induced, and electrodeposition methods. In the bottom-up synthesis, also known as the self-assembly approach, the nanoparticles with high structural purity and diverse shapes, sizes, compositions and surface properties are assembled from smaller units, for example, by ionic, atomic, molecular and smaller particles. Recently, a strong focus is placed on biological synthesis, where metal and metal-oxide NPs are extracted from fungi, algae, bacteria, and plants (usually terrestrial) in which a variety of metabolites act as reducing agents in NPs synthesis. Biosynthesis is a green synthetic approach that can be categorized as a bottom-up approach where the metal atoms assemble to form clusters and eventually nanoparticles. The biosynthetic process is similar to the chemical reduction process, but with the expensive and noxious reagents substituted by plant extracts to synthesize the nanoparticles. Amooaghaie et al and Kummara et al differentiated between the chemical reduction of AgNPs using green synthesis with plant extracts and a conventional wet-chemistry method via monitoring of the toxic response by a comparison study. The resulting AgNPs from green synthesis showed significantly lower cytotoxicity and phytotoxicity than that of the AgNPs synthesized by chemistry approach, which confirmed that green approach Ag NPs are safer and can be extensively used in biomedical fields, particularly in cancer fields. Therefore, due to these reasons and the increased recognition regarding the importance of fundamental green chemistry techniques, biological synthesis

is a promising eco-friendly alternative that appears to offer the green approach and beneficial results. Despite the many advantages of plant extracts, there are several other obstacles that should be considered before they can be applied practically, such as the well-defined control of the size, shape, structure, crystallinity and monodispersity of the plant-synthesized nanoparticles. From the fundamental and functional viewpoints, the bottom-up approach is far more popular in the synthesis of metal and metal-oxide NPs and is considered as a promising route to control the composition, growth, morphology and properties of metal and metal-oxide NPs.

Metal and metal-oxide NPs obtained from the bottom-up approach have tunable novel properties due to the possibility of significantly affecting their dimensional shape. In terms of the dimensions of metal and metal-oxide NPs, shapes can be classified as zero dimensional (0D) (isotropic structure), one dimensional (1D), two dimensional (2D), and three dimensional (3D) (anisotropic structure). Zero dimensional are nanosized particles that have their length and width within the nanometer range, they are simply nanoparticles. One dimensional are shaped like filaments. If a filament with a nanometric diameter and having a length that is much bigger, then you have a 1D material. Two dimensional are thin films. The thickness is very small, but they extend in a 2D plane. Three dimensional materials are the old classical shaped objects. They have a length, a width and a thickness that are relatively beyond a few nanometers. The typical solid and hollow shapes of metal and metal-oxide NPs based on dimensionality are shown in **Figure 1.3**. In the case of 0D metal and metal-oxide NPs, typical shapes include spherical, pseudo-spherical, dodecahedral, tetrahedral, octahedral, cubic, and the corresponding hollow structure morphologies. One dimensional morphologies of metal and metal-oxide NPs are nanotubes,

nanoneedles, nanorods or nanowires, nanoshuttles, nanocapsules and hollow structures. Round disks, hexagonal/ triangular/ quadrangular plates or sheets, belts, mesoporous-hollow nanospheres, hollow rings, etc. belong to the 2D shape class of metal and metal-oxide NPs. Three dimensional morphologies of metal and metal-oxide NPs are complex, and include nanourchins, nanoflowers, nanostars, polygonal nanoframes, multiple hollow shelled NPs, hollow bunches.

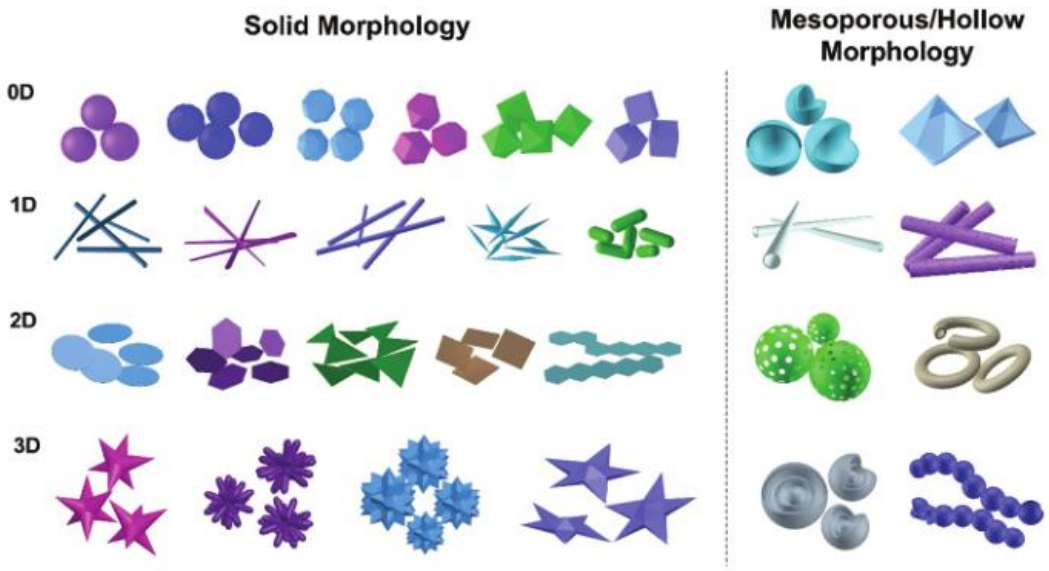

Figure 1.3 Typical morphologies of solid and mesoporous/hollow metal and metal-oxide nanoparticles with 0D, 1D, and 2D shapes and other 3D complex structures.

Compared with the simple isotropic morphologies of metal and metal-oxide NPs, novel anisotropic morphologies of metal and metal-oxide NPs give rise to new features and unique physicochemical properties due to the number of step edges and kink sites on the surface and the high surface area-to-volume ratios in the nanoscale regime. For instance, polyhedral Au NPs with high-index facets exhibit excellent optical and catalytic properties, Au rods with different ratios of length and width display different transverse and longitudinal plasmon bands for surface enhanced Raman scattering and biomedicine, and branched Au NPs with multiple tips (such as stars and flowers) have been attracting

increasing interest in catalysis, surface-enhanced Raman scattering, and sensing. A great deal of effort has been devoted to the control over the shape of metal and metal-oxide NPs, and much progress in the synthesis of shape-controlled metal and metal-oxide NPs and their corresponding shape-dependent properties have been made over the past decades. Generally, the shape formation of metal and metal-oxide NPs can be controlled or varied by thermodynamic or kinetic control in the solution. Normally, the thermodynamically controlled morphology of metal and metal-oxide NPs was produced when the reaction was driven by the chemical potential of the reaction solution, which is directly related to the temperature and supersaturation of the solution. Kinetically controlled morphologies of different dimensions can be obtained by altering the reaction conditions and happens when freshly produced atoms are in rapid collision with a smaller number of embryos in local regions of high supersaturation for the formation of nucleus, according to nucleation theory. And then the growth of nucleus in kinetically controlled processes contributes to the formation of nanoparticles with anisotropic shapes. Thus, the synergistic effects of thermodynamic and kinetic aspects are considered as critical roles in determining the final shape of metal and metal-oxide NPs.

Recently, most efforts in the literature have been placed on the effect of adjusting reaction parameters on the shape evolution in capping molecule-assisted synthesis and other innovative synthesis approaches. To design and delicately control the shape of nanocrystals is one of the most important issues in nanoscience, chemistry and physics owing to the close correlations of the surface morphologies with the electronic structure, bonding, surface energy, and chemical reactivity. The facets with different crystallographic characters have distinctive surface atomic structures, reconstructions, and atomic

termination features corresponding to sharp differences that have been demonstrated in light-sensing, gas and chemical reactivity, field emission properties etc. The ability to understand, predict and control the exposed surfaces and the corresponding volume fractions of nanocrystals is of critical importance to elucidate and explore shape-dependent chemical and physical properties. However, it is worth noting that there are no simple rules to determine the final shape of metal and metal-oxide nanomaterials. A comprehensive understanding of the basic principle of nucleation and growth that typically occurs in the bulk solution throughout all the reactions, and the corresponding influential reaction parameters including precursor concentration or supersaturation, reaction temperature/aging time and additives are indispensably important for the shape control of metal and metal-oxide NPs.

1.1.3 Nucleation and Growth Theory of Metal and Metal-Oxide Nanomaterials

1.1.3.1 Classical Nucleation. The definition and classification of nucleation have been described by Mullin since 1961, where nucleation is a process whereby a second phase is generated from one phase. In solution state, solid particles are considered as the second phase that generated from the precursor solution phase by the nucleation process. Here, if the solid nucleus are generated from a homogenous supersaturated bulk solution this is referred to as “primary nucleation”. Conversely, if the fresh nucleus are generated in a supersaturated bulk solution in the presence of other particles or materials with the same or different components (such as container surfaces, impurities, grain boundaries, dislocations), this is named “secondary nucleation” or “heterogeneous nucleation”, respectively. Additionally, heterogeneous nucleation and secondary nucleation are much easier than primary nucleation due to the low energy barrier, since stable nucleating sites

are already present in the system. As presented by Mullin and other researchers, the formation of homogeneous nucleus is considered as a thermodynamic process driven by the supersaturation of the bulk solution and decided by the total free energy (ΔG) of a NP, defined as the sum of the surface free energy and bulk free energy ΔG_v , as shown in Equation (1.1)

$$\Delta G = 4\pi r^2\gamma - \frac{4}{3}\pi r^3 \Delta G_v \tag{1.1}$$

where r and γ are the radius of the particle and the surface energy, respectively. With regards to the free energy of the bulk crystal ΔG_v is defined as the free energy change for the transformation to a unit volume of particles, dependent upon temperature T, Boltzmann's constant k_B , its molar volume v, and the supersaturation ratio of the bulk solution S. That is, $\Delta G_v = \frac{-2\gamma}{r} = \frac{-2k_B T \ ln\, S}{v}$. Particularly, S is defined as the ratio of the monomer concentration in solution C to the equilibrium monomer concentration C^* in the crystals ($S = C/C^*$).

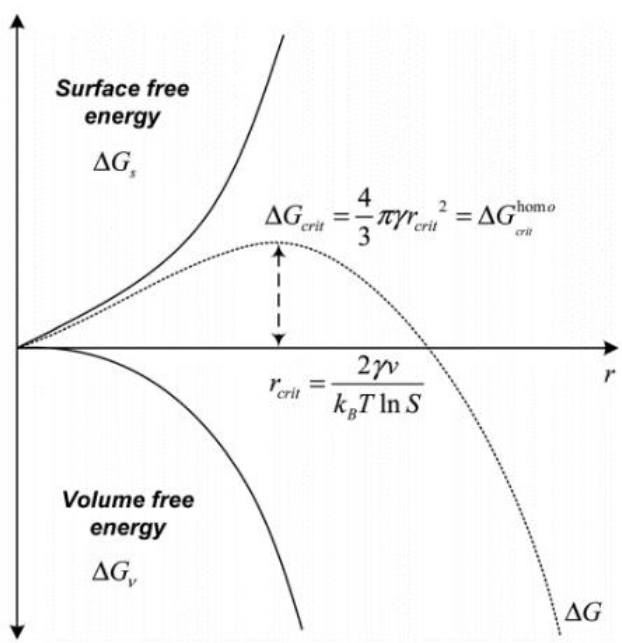

Figure 1.4 Schematic illustration of the free energy diagram for nucleation.

In homogeneous solution, the nucleation process is accomplished by assessing the increase in free energy to form an interface between the bulk solution and the surface solid nucleus. The radius of the formed nucleus are highly dependent on the supersaturation level, and the rapid increase and narrow distribution of supersaturation results in small particles in terms of the definition of the bulk free energy ΔG_v . The critical value of ΔG and the critical radius of the nucleus that exist in the bulk solution are calculated by differentiating ΔG with respect to radius r and setting to zero, $d(\Delta G_{crit})/dr = 0$, giving the critical free energy in Equation (1.2)

$$\Delta G_{crit} = \frac{4}{3}\pi\gamma {r_{crut}}^2 = \Delta G_{crit}^{hom\,e} \tag{1.2}$$

Apparently, ΔG_{critis}^{homo} required lowest energy barrier to obtain stable nucleus within homogenous solution (**Figure 1.4**). Then, the critical radius corresponds to the minimum size of nucleus surviving in solution without being redissolved, as defined in Equation (1.3)

$$r_{crit} = \frac{-2\gamma}{\Delta G_v} = \frac{2\gamma v}{k_B T\ \ln S} \tag{1.3}$$

A nucleation rate of nucleus *N* formed per unit time per unit volume, was written in the form of the Arrhenius reaction velocity equation, which is commonly used for the rate of a thermally activated process:

$$\frac{dN}{dt} = A\,exp(-\Delta G_{crit}/k_B T) = A\,exp(\frac{-16\pi\gamma^3 v^2}{3k_B^3 T^3 (\ln S)^2}) \tag{1.4}$$

where *A* is a pre-exponential factor. According to Equation (1.4), the nucleation rate can be varied by the experimental parameters involving supersaturation, temperature and surface free energy, and the detailed influence will be introduced in the following part. The higher concentration of monomer, high temperature and lower critical energy barrier favor a rapid nucleation rate, resulting in a high population of nucleus with small size, as

demonstrated by a large number of synthetic processes. Additionally, some non-classical nucleation theories, such as two-step nucleation for protein crystallization, and cluster aggregation for agglomeration of particles, were also explored to address the nucleation process.

1.1.3.2 Classical Growth and Dissolution. After nucleation, the subsequent growth of nucleus strongly determines the shape of the nanomaterials, which is thermodynamically driven by the decreasing surface free energy of the generated particles. The growth process involves deposition of elementary units (including atoms, molecules, assemblies or particles) onto the preformed NPs in a growth medium (plasma, melt, solution, gel, etc.). And this attachment occurs at the sites of the nucleus surface. The density of existing sites on the preformed nucleus surface together with the kinetics of incorporation into these sites are crucial factors to determine the growth rate of NPs. In classical growth theory, there are two growth mechanisms including surface reactions and monomer diffusion to the particle surface.

As described by Fick's first law of diffusion, the diffusion rate of monomers through a surface of spherical NPs with radius *x* can be written as

$$\frac{dm}{dt} = JA = -4\pi x^2 D \frac{dC}{dx} \tag{1.5}$$

where *J* is the monomer flux and *D* is the diffusion constant. For the diffusion rate of the monomers at the surface of spherical NPs with radius *r* at steady state, the above equation can be written as

$$\frac{dm}{dt} = 4\pi r D(C_b - C_i) \tag{1.6}$$

where C_b is the concentration of monomers in the bulk solution, and C_i is the concentration of monomers at the interface of the solid/liquid. Similarly, equations can be written for the rate of the surface reaction,

$$\frac{dm}{dt} = 4\pi r k(C_i - C_r) \tag{1.7}$$

where k is the mass transfer coefficient, and C_r is the equilibrium concentration of solid NPs. If the diffusion is the limiting factor and the particle size changes with time, the diffusion of monomers onto the surface of NPs is given by Equation (1.8). Similarly, if the surface reaction is the limiting factor, Equation (1.7)can be described in Equation (1.9)

$$\frac{dr}{dt} = \frac{Dv}{r}(C_b - C_r) \tag{1.8}$$

$$\frac{dr}{dt} = kv(C_b - C_r) \tag{1.9}$$

where C_r is the solubility of the NPs, and v is molar volume of bulk NPs. If the limiting factor of the growth of nanoparticles is controlled neither by diffusion nor surface reaction, then the increase in particle size with time follows Equation (1.10)

$$\frac{dr}{dt} = \frac{Dv}{r + D/k}(C_b - C_r) \tag{1.10}$$

A scheme of crystal growth under limitation of diffusion or reaction with concentration changes is given in **Figure 1.5**. Diffusion-limited or reaction-limited processes with a different concentration of precursor monomer determine the shape of NPs by growth rate. Within a solution with a high concentration of precursor monomer solution, the growth rate is controlled by the diffusion-limited process. That is, diffusion of the precursor monomer is the rate-determining step. Then, the precursor monomers are precipitated immediately onto the surface of NPs through the bulk reaction medium and

solvent. In the case of the reaction-limited growth process, when the concentration of precursor monomer is low and growth is greatly limited by the surface reaction of monomers, the total growth rate is determined by the relative nucleation and growth rates of the monomers on the surface of the NPs.

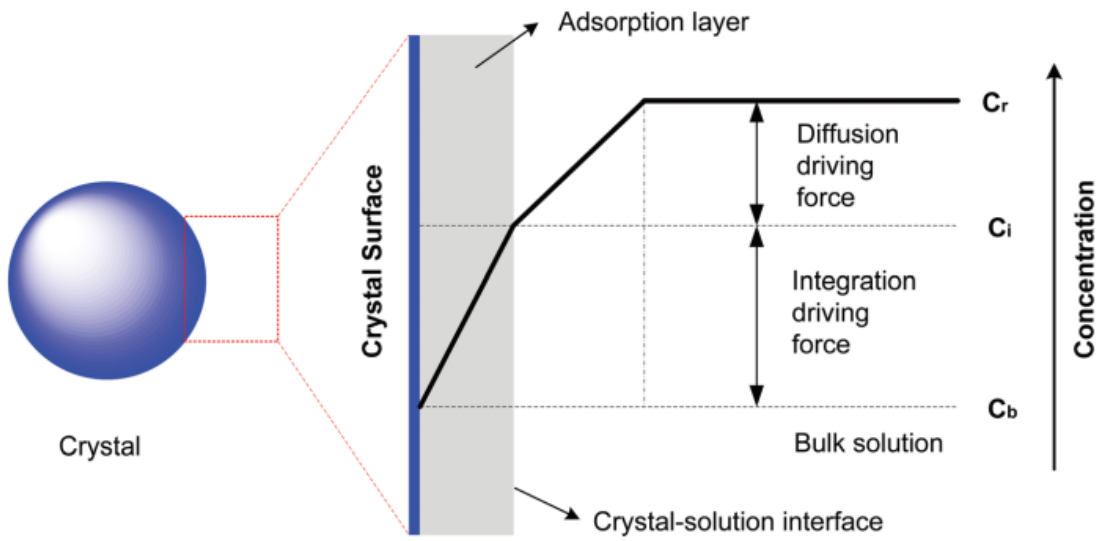

Figure 1.5 Diffusion-reaction model for crystal growth with concentration in the solution state.

From Equation (1.8) and (1.9), both diffusion-limited and reaction-limited growth are driven by the precursor monomer concentration. Then, the diffusion-limited growth or reaction-limited growth is the decisive factor for the shape and size control of NPs. Normally, diffusion-limited growth is the desirable process for the production of NPs with monodispersity, but reaction-limited growth determines the final shape of the NPs. During the diffusion-limited growth process, organic ligands or surfactants adsorbed on the surface of the preformed NPs introducing a diffusion barrier is a flexible and effective approach to get controlled shape with monodisperse sizes.

Here, it worth noting that the occurrence of growth is on condition of a positive concentration gradient between a higher bulk concentration of solution and the particle

equilibrium concentration. Whereas, dissolution of particles occurs in the case of a negative concentration gradient between the bulk concentration of the solution and the higher particle equilibrium concentration as the driving force. Generally, the dissolution of NPs is induced by temperature, pH, polymorphic form, and size. However, the thermodynamic parameter temperature has a negative effect on the dissolution of metal and metal-oxide NPs. Thus, the common parameters for the dissolution of metal and metal-oxide NPs are the polymorphic form, and the pH change of solution. Practically, varying the pH of the solution is the most direct and effective route to get dissolution of metal and metal-oxide NPs (such as adding H^+, OH^-, NH_3), and this principle is based on the combination ability of metal ions and hydroxyl ions, resulting in the increased concentration of the solution by dissolving the solid particles. Recently, intensive studies have been carried out to address novel shape control through a growth–dissolution–recrystallization process with the pH adjustment of bulk solution. Furthermore, the dissolution–recrystallization process has also been developed for the phase transformation of polymorphism of metal and metal-oxide NPs with different shapes, and for producing hollow structures. For instance, 3D rhombohedral α-Fe_2O_3 has been synthesized by the phase transformation of initial intermediate β-FeOOH nanowires through such a dissolution–recrystallization process, as reported by Lin and co-workers. The polynucleus but unstable β-FeOOH nanowires were hydrolyzed to form two-line ferrihydrite (α-Fe_2O_3) nucleus through dissolution–recrystallization, then the small α-Fe_2O_3 nucleus formed went through the mechanisms of aggregation, orientation attachment and recrystallization of Ostwald ripening to form 3D rhombohedral α-Fe_2O_3 NPs. 2D or 3D hollow α-Fe_2O_3 nanostructures with tunable shapes (nanotubes, nanobeads, and nanorings) were formed with dissolution–recrystallization

control after 48 h via a hydrothermal route. The formation of α-Fe_2O_3 NPs with hollow structures obeyed the mechanisms of nucleation, aggregation, dissolution and re-crystallization successively. Further, the dissolution process occurred on the (001) planes perpendicular to the c-axis due to the weak adsorption of the phosphate ion, resulting in the coordination effect between Fe^{3+} and phosphate ions to accelerate the dissolution process.44 Additionally, Wu and co-workers also found that the sulfate ions favored the dissolution of α-Fe_2O_3 owing to the coordinated effect with ferric ions during the synthetic process of 1D magnetic iron oxide short nanotubes.

1.1.3.3 Conventional Factors for Shape Control. (a) Supersaturation. Supersaturation is generally expressed as a concentration difference, $\Delta C = C_b - C_r$. In a typical synthetic process for metal and metal-oxide NPs, however, the reaction solution contains precursor, reductant agents, solvent, and stabilizers and other additives. Supersaturation refers to the precursor concentration or precursor ratio in a single or multiple precursor chemicals system, respectively. From classical nucleation and growth theory, supersaturation plays a major and direct role in determining the nucleation and growth rate. For the synthesis of metal and metal-oxide NPs in the solution, LaMer theory is a widespread accepted theory for the nucleation and growth of NPs, in which the nucleation and growth theory can be divided into two stages, as shown in **Figure 1.6**.

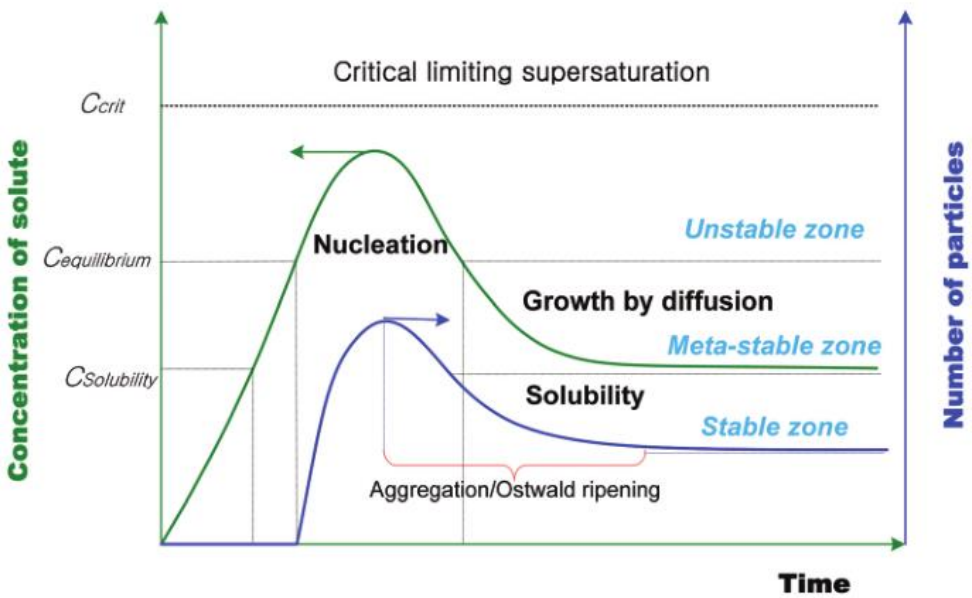

Figure 1.6 Scheme for the LaMer theory for nucleation and growth and the variation of particle numbers during the nucleation and growth process.

In the initial stage, the concentration of free precursor monomers in the bulk solution increases rapidly and crosses into the metastable zone until the "burst nucleation" point is reached, consuming the concentration of free precursor monomers significantly in the solution and increasing the number of solid particles rapidly. During this process, the number of nucleus and the concentration consuming rate are mainly dependent on the nucleation rate. That is, a fast nucleation rate is able to decrease monomer concentration sharply and generates a huge number of nucleus rapidly. The nucleus formed under the control of the diffusion of monomers also consumes monomer concentration during the growth period, causing the monomer concentration in the solution to decrease continuously. Furthermore, aggregation/ agglomeration, or Ostwald Ripening and other mechanisms may occur among the preformed nucleus, reducing the number of solid particles until the equilibrium state of the bulk solution is reached. During the growth process, if the generated nucleus have a tendency to form low-energy NPs by supplying sufficient energy

to the bulk solution or by having a low concentration of precursor monomer under thermodynamic control, 0D spherical, pseudo-spherical, or other isotropic NPs are usually formed. Otherwise, the growth of nucleus driven by kinetic control forms anisotropic shapes at high precursor monomer concentrations. In other words, the producing rate and consuming rate of precursor monomer concentration have a strong influence on the nucleation and growth, which can be altered by the concentration of the precursor monomer directly, the coordination of the solvent, and the chelation effect of pH.

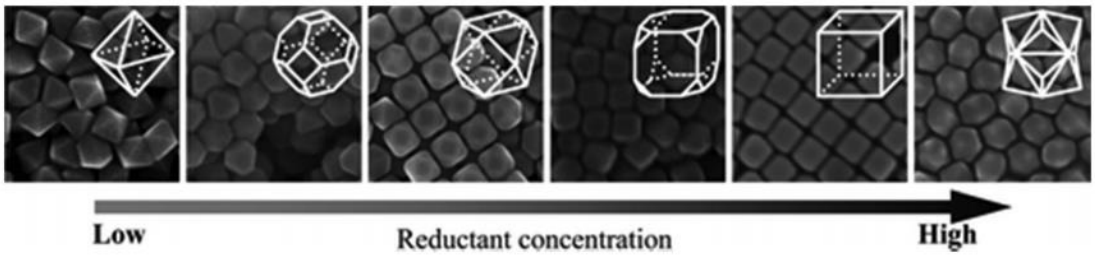

Figure 1.7 Schematic illustration of many-faceted polyhedral Au nanoparticles changing with the concentration of the reductant using SEM images.

(i) The concentration of the precursor and additives. Supersaturation is directly and significantly altered by the addition of precursor (injection or dumping), the reductant concentration or reductant ratio, coordination with other ions or agents in a one-pot synthesis or seed-mediated route. Particularly, for reducing agents, the ratio between the precursor and the reductant is also a significant parameter to control the depletion rate of the precursor monomer for the formation of metal and metal-oxide NPs. For example, Teranishi and co-workers have reported that by progressively increasing the concentration of the reducing agent (ascorbic acid) in the growth solution, polyhedral morphologies of Au NPs evolved from octahedral to truncated octahedral, cuboctahedral, truncated cubic, cubic, and finally trisoctahedral structures as facilitated in a facile seed-mediated route (**Figure 1.7**). The shape control of the Au NPs by the reductant (ascorbic acid) was

explained in terms of the effect of the exposed surface planes of the Au seeds in different concentrations of ascorbic acid. That is, with higher concentrations of ascorbic acid in the growth solution, the Au seeds were surrounded by higher lattice planes for a face-centered-cubic structure due to the rapid growth of seeds, producing a thermodynamically unstable structure. Conversely, with the addition of a low concentration of ascorbic acid, the formation of a thermodynamically stable structure was favored by precipitating a small amount of atoms onto the Au seeds. Additionally, the amount of seed NPs also has a tremendous impact on the final shape of metal and metal-oxide NPs in the seed-mediated process due to the surface area for growth.

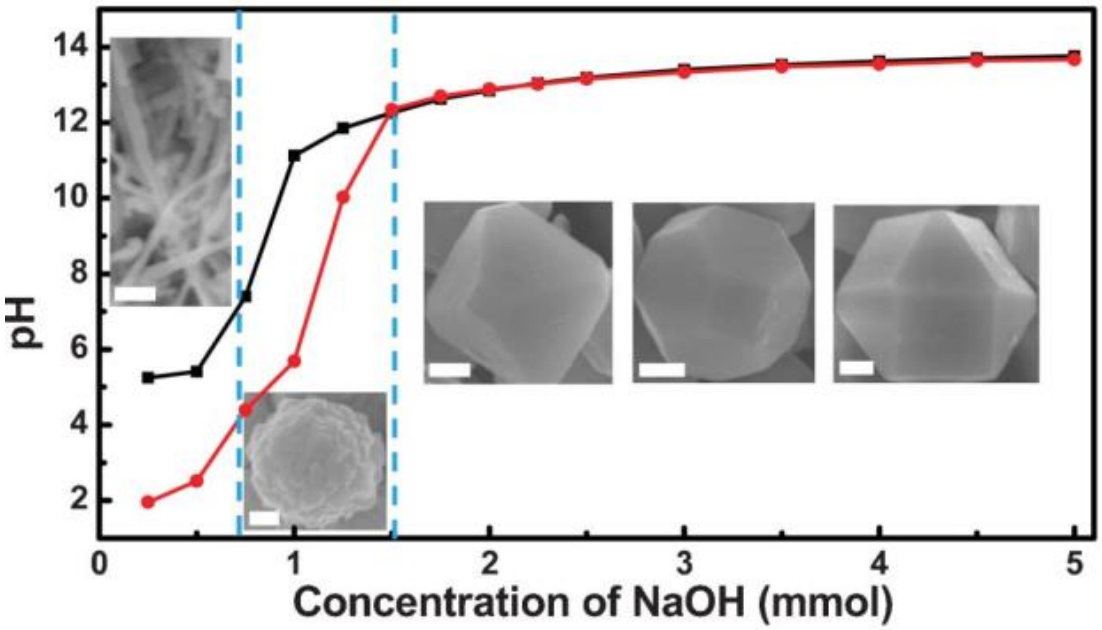

Figure 1.8 Mother solution pH versus the concentrations of NaOH before (black squares) and after (red circles) hydrothermal reaction. The insets show the shape evolution of Cu2O nanocrystals from nanowires, through nanoparticle-aggregated spheres, and finally to truncated octahedra. Scale bars are 200 nm.

(2) pH effect. Altering the pH through the addition of acid oralkali (H^+ , OH^- or NH_3) results in the modulation of the state of a chemical species in solution and coordination bonding with ions in the precursor monomer solution to form a complex.

Eventually, promoting or postponing the release rate of ions from the coordination bonding for supersaturation enables the adjustment of the initial nucleation rate for shape control. This general trend is obviously observed in the synthesis of metal oxides or metal materials. Xue and coworkers have used pH-dependent precursor species $Cu(OH)_2$, $Cu_2(OH)_3NO_3$, and $Cu(OH)_4^{2-}$ in a starch reduction solution to achieve Cu_2O NPs with shapes evolving from 1D nanowires to 3D polyhedra. During this process, pH-dependent precursors were available to manipulate the reaction kinetics of the reduction and complexation reactions for exquisite control over the shape and composition of Cu_2O NPs (**Figure 1.8**). Furthermore, high pH is of benefit to promote the reduction power of starch and the complexation ability of OH^- facilitated the shape evolution of Cu_2O NPs. Additionally, pH also adjusts the surface properties of the preformed NPs and the chemical or physical state of the surfactants or additives, leading to different adsorption modes or adsorption amounts on the surface of the preformed NPs. As a result, selective growth or aggregation/agglomeration, and self-assembly favor the shape evolution of metal and metal-oxide NPs. For instance, as presented by Wang and co-workers, α-Fe_2O_3 hierarchical nanostructures including 3D houseleek-like and 2D snowflake-like dendrites were produced by changing the pH via different formation mechanisms, as shown in **Figure 1.9**. The change in pH significantly affected the growth rate of α-Fe_2O_3 by adjusting the supply of Fe^{3+}. When the pH≥6, 2D snowflake-like α-Fe_2O_3 dendrites were formed by the self-assembly of primary α-Fe_2O_3 NPs preferentially along six crystallographically equivalent (1100) planes. Whereas, in the case of pH≤5, 3D houseleek-like α-Fe_2O_3 NPs were generated by the successive aggregation of round flakes with their top and bottom surfaces parallel to the (0001) plane, and continuous growth along [0001] for single crystalline

spindle-like α-Fe_2O_3, which continuously aggregated at each tip to form 3D houseleek-like α-Fe_2O_3 NPs. Furthermore, for some metal and metal-oxide nanomaterials with polymorphism, the adjustment of pH also promotes dissolution for phase transformation.

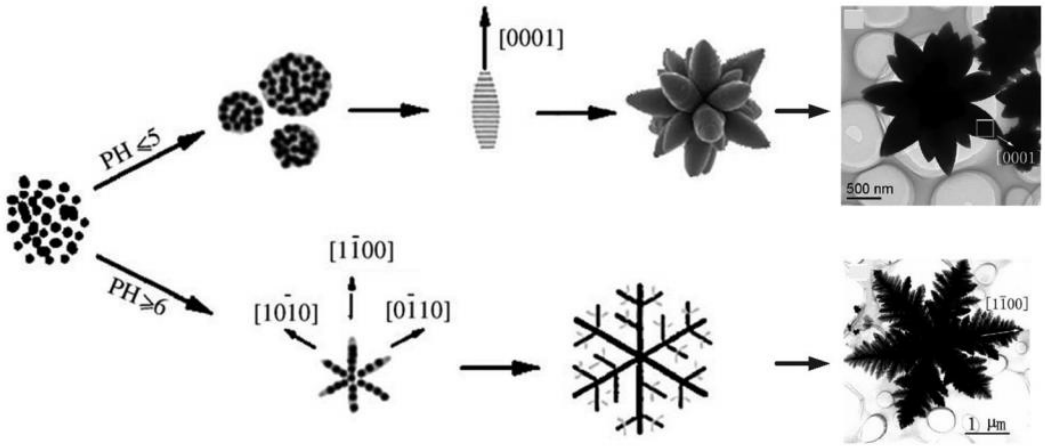

Figure 1.9 Schematic illustration for the self-assembly of two kinds of α-Fe_2O_3 dendrites by altering the pH of the bulk solution and their corresponding TEM images.

(3) Solvent. Solvents with different functional groups (such as ionic liquids) provide special coordination with the precursor monomer, which is advantageous for the formation process of metal and metal-oxide NPs under thermodynamic or kinetic control due to the adjustment of the supersaturation increase or depletion rate. In addition, the mixture of different solvents or solvents with different components enables the shape control of metal and metal-oxide NPs. For example, Zhang and co-workers have selectively prepared magnetic greigite nanosheets and NPs by altering the mixed ratio of ethylene glycol and water. That is, magnetic greigite nanosheets were generated in pure ethylene glycol, and irregular NPs were obtained in mixed solvents (EG+H_2O). Surface-coordinating ligands or selective adsorption from solvents on the surface of the NPs also help to define the monodispersity and shape of the NPs and have been frequently explored in the polyol process. For instance, Schaak and co-workers added different precursors

including rhodium(II) trifluoroacetate dimer [$Rh_2(TFA)_4$], rhodium bromide ($RhBr_3$), and rhodium chloride ($RhCl_3$) into the polyol solvents ethylene glycol (EG), diethylene glycol (DEG), triethylene glycol (TREG), and tetraethylene glycol (TEG) individually to yield different shapes of Rh NPs, as shown in **Figure 1.10**. When using precursor $RhBr_3$, a Rh truncated cube was produced in EG, a Rh cube with the highest quality was formed in DEG, but a concave cube, and mixed concave and branched morphology appeared in TEG. The reasonable explanation for the shape evolution of Rh NPs using different solvents is the surface-adsorbing species, based on each polyol solvent with only the anion changed.

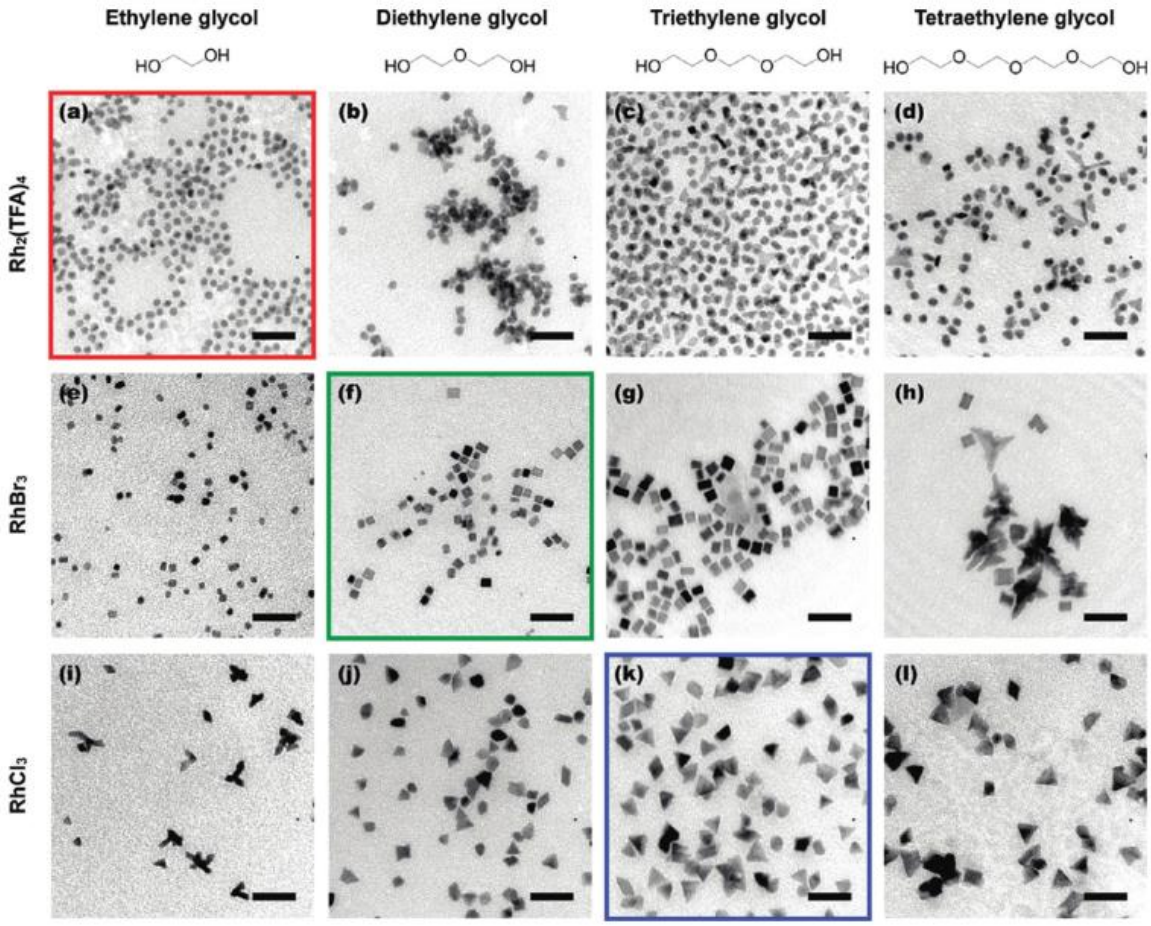

Figure 1.10 Representative TEM images of Rh nanoparticles synthesized using ethylene glycol, diethylene glycol, triethylene glycol, and tetraethylene glycol solvents with the reagents (a–d) $Rh_2(TFA)_4$, (e–h) $RhBr_3$, and (i–l) $RhCl_3$ (TFA = trifluoroacetate). Outlined images indicate the set of reaction conditions which results in the most monodisperse yield of Rh icosahedra (red), cubes (green), and triangular plates (blue). Scale bars are 20 nm.

(b)Temperature. From classical nucleation and growth theory, temperature is a thermodynamic parameter of the reaction solution. High temperature indicates the energetic movement of molecules and ions, causing instability of the reaction solution due to a high Gibbs free energy. In the reaction solution for the synthesis of metal and metal-oxide NPs, such an increase in the temperature of the reaction causes the supersaturation increase rate or the reduction rate of the precursor monomer in the solution to increase rapidly. Subsequently, the nucleation and growth process will be shortened by accelerating the nucleation and growth rate due to thermodynamic control of metal and metal-oxide NPs. Eventually, metal and metal-oxide NPs with pseudo-spherical or spherical morphologies are the preferential products. Thus, it is reasonable to control nucleation and growth processes at proper temperatures to modulate the nucleation and growth processes under kinetic control for the formation of anisotropic metal and metal-oxide NPs. Additionally, temperature also affects the growth kinetics of metal and metal-oxide NPs by shifting the equilibrium established between the metal and metal-oxide NPs and the participating species in the solution state through varying the activity of the stabilizers or additives and the chemical state of the metal and metal-oxide NPs. Hence, varying the temperature of the nucleation and growth process can be a useful route for the control of the shape of metal and metal-oxide NPs in the solution state. For instance, as observed by Zhu and co-workers, Au plates with a unique and well-defined morphology have been synthesized using an alternative temperature in the presence of PVP surfactants through a modified polyol process. When altering the formation and precipitation temperature of the Au NPs, the morphology of the final shape evolved from hexagonal, triangular and truncated triangular plates to novel star-like and shield-like Au plates, as shown in **Figure**

1.11. Additionally, controlling the heating rate to reach the desired reaction temperature is also another route for controlling the nucleation and growth rate.

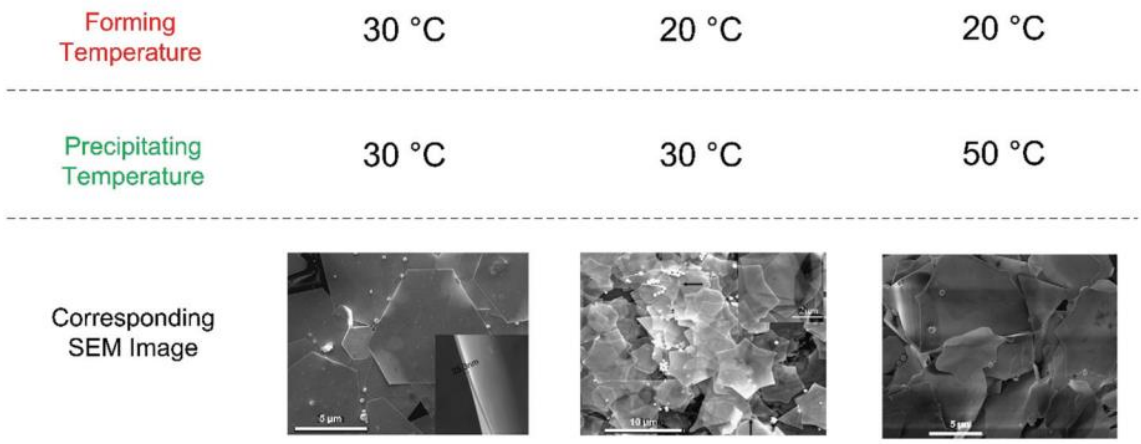

Figure 1.11 Schematic illustration of the temperature variation process for the evolution of Au plates and the corresponding SEM images.

Generally, the proper reaction temperature is a critical factor to yield anisotropic shapes by managing the reaction procedure under kinetic control. However, it should be noted that high and low temperatures are a relative concept, for example, for the polyol method, the temperature should be varying over 120 °C. Under high temperature conditions, aggregation, orientated attachment, component diffusion (such as metal alloys) and phase transitions are common phenomena occurring among the existing particles due to the minimization of the free energy of the reaction system and the NPs.

(c) Seeds and templates. Seeds or templates serve as common and effective mediators for the shape control of metal and metal-oxide NPs because the existing surface provides sites for further growth by depleting the precursor monomer in bulk solution. Here, it is worth noting that the seeds or templates component can be the same as or different to the final particles, eventually generating final NPs with homogenous or heterogeneous structures. The effective facilitated route of using seeds or templates for the shape control

of metal and metal-oxide NPs is referred to as the seed-mediated or template method. The seed-mediated or template growth procedure offers advantages for the shape control of metal and metal-oxide NPs, in which the activation energy barrier for the addition of precursor monomers onto preformed seeds or templates is much lower, compared with the formation of new nucleus from homogenous bulk solution. However, the shapes of the final metal and metal-oxide NPs from the seed-mediated and template routes have differences in that various shapes of metal and metal-oxide NPs can be obtained using the seed-mediated method, but the final shape of metal and metal-oxide NPs generated using the template method is highly dependent on the initial shape of the template.

The size of seeds should be extremely small when the seed-mediated method is carried out because the final shape of metal and metal-oxide NPs is barely affected by the already formed shape of seeds if the size of the initial seed crystals is over the critical size. Furthermore, the seed amount, concentration of the precursor monomers, surfactants, temperatures, and pH are significant factors for the final shape of the metal and metal-oxide NPs. 84 Particularly, the presence of surfactants generally including CTAB/CTAC, PVP, SDS, etc. is also a necessary factor for generating metal and metal-oxide NPs with anisotropic shapes through such seed-mediated processes. For instance, Liz-Marzán and co-workers have synthesized Au@Ag NPs with diverse well-defined morphologies and crystalline structures through the kinetic control of slow reduction and stabilization of (100) facets, when employing benzyldimethylhexadecylammonium chloride as a stabilizer in the seed-mediated method. The adsorption of halide ions Cl^- from the stabilizer caused a significant change in the surface energies of different facets, as confirmed by density functional theory calculations of the surface energies. Eventually, single crystalline core–

shell Au@Ag cubes enclosed by six (100) facets evolved from initial single crystalline Au cores with octahedral and nanorod shapes due to the adsorption of Cl^- on the (100) facet, while core–shell Au@Ag nanorods with an increased aspect ratio were produced from the originated pentatwinned Au nanorods by adsorption of AgCl on the (100) and (110) facets.

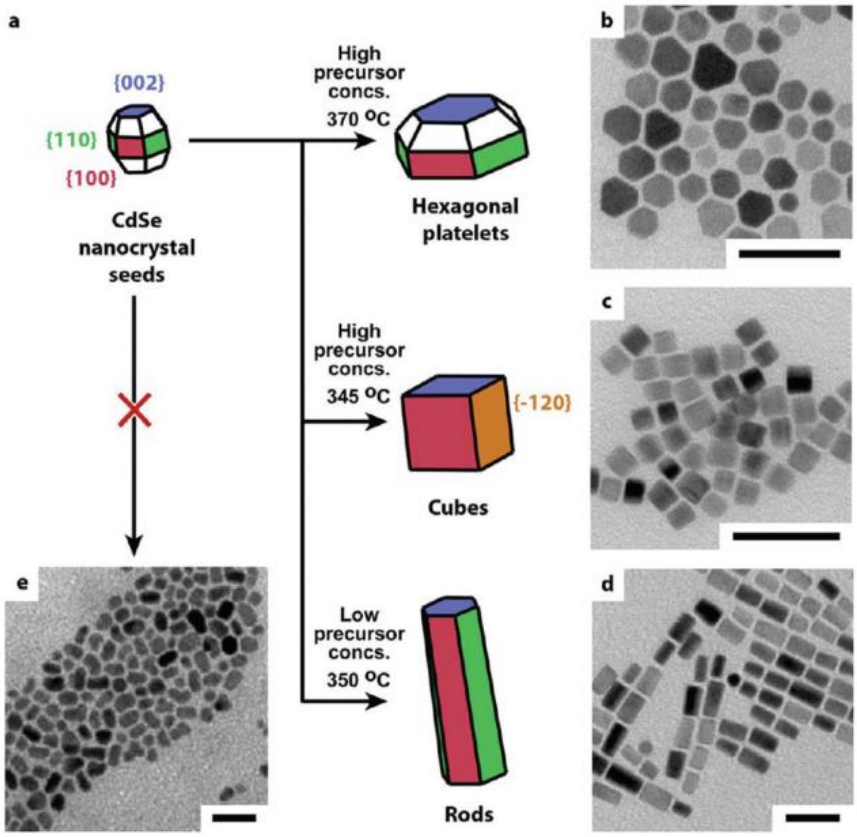

Figure 1.12 (a) Schematic illustrating the relationship between the geometry and the bounding crystal facets (colored) of the wurtzite CdSe nanocrystal seeds and the nanocrystals produced in the seed-mediated synthesis. Typical TEM images of the wz-CdSe nanocrystals with shapes of (b) hexagonal platelets, (c) cubes, and (d) rods. (e) TEM image from a similar synthesis conducted without using the CdSe nanocrystal seeds, resulting in elongated and misshapen particles. The scale bars each correspond to 50 nm.

Additionally, the seed-mediated method is also easily achieved for metal and metal-oxide NPs with high-index facets, core–shell structures, branches or alloys. For instance, colloidal wurtzite crystal structures (wz-CdSe) including nanocubes, hexagonal nanoplatelets, nanorods and bullet-shaped particles were yielded through a seed-mediated

method using small (2–3 nm) wz-CdSe nanocrystals as seeds, as shown in **Figure 1.12**. Selective growth of different facets on the seed nanocrystals drive the initial shape of wz-CdSe to a different one. Radial growth from the (002) facet at high concentrations of precursor and a higher reaction temperature of 370 °C leads to wz-CdSe hexagonal platelets, while preferentially adding precursor monomers onto the (002) and (002) facets of the seeds at a low precursor concentration and a lower reaction temperature of 350 °C forms wz-CdSe nanorods. Additionally, a multi-step seed mediated technique can also be applied for the control of the shape of metal and metal-oxide NPs.However, the concentration of seeds and precursors, reaction temperature, pH and growth time are also significant parameters to control the anisotropic shape of metal and metal-oxide NPs during seed-mediated processes.

(d) Surfactants or additives. Most metal and metal-oxide NPs have a strong tendency to aggregate into bigger particles with irregular and undesirable morphologies during the growth procedure in bulk solution due to their high surface free energy of nanoscale size. To address this shortcoming, surfactants and additives are considered as excellent candidates as shape modulators in bulk solution, with the expectation that surfactants or additives can adsorb onto some facets of the growing Ps dynamically to reduce their surface energy and render a controllable growth rate of specific facets for desirable morphologies of metal and metal-oxide NPs. Furthermore, stabilized layers formed by surfactants or additives on the surface of NPs also protect particles against aggregation in the solution state. Generally, surfactants or additives are composed of functional or coordinating groups, which are key as capping agents to adsorb onto the surface of the growing NPs. Thus, the adsorption ability and stability of the functional or

coordinating groups should be well considered for the selection of capping agents. As such, the capping agents commonly used for the synthesis of metal and metal-oxide NPs with tunable shapes are small molecules and polymers. The functional or coordinating groups from small molecules and polymers such as hydroxyl groups, amine groups (primary, secondary and tertiary amine groups), thiol groups, and long alkyl chains are considered as selectively adsorbed groups onto special facets of NPs. Common polymers are poly(vinylpyrollidone) (PVP), poly(acrylic acid) (PAA) and poly(allylamine hydrochloride) (PAH), polyetherimide (PEI), poly(vinyl alcohol) (PVA), poly(ethylene glycol) (PEG) and complexes of PEGylated polymers. Typical small molecules include cetyltrimethylammonium bromide (CTAB), cetyltrimethylammonium chloride (CTAC), oleic acid and/or oleylamine, trioctylphosphine oxide (TOPO), octadecylamine (ODA), trioctylphosphine (TOP), and sodium dodecyl sulfate (SDS). Additionally, strong interactions between halides (Cl^-, Br^-, I^-) from small molecules and the surface of the NPs is another common control factor for the modulation of the shape of NPs by selective growth, particularly for novel metals. Adsorption of functional or coordinating groups onto different crystal planes of NPs is not limited to small molecules and long-chain polymers, and some solvents with functional or coordinating groups also provide similar adsorption abilities as the small molecules and polymers, such as N,N-dimethylformamide (DMF), and EG. Here, the relationships between the small molecules, polymers and solvents for the shape modulation of NPs and the typical shapes of different materials by the adsorption of functional or coordinating groups are clearly summarized in **Figure 1.13.**

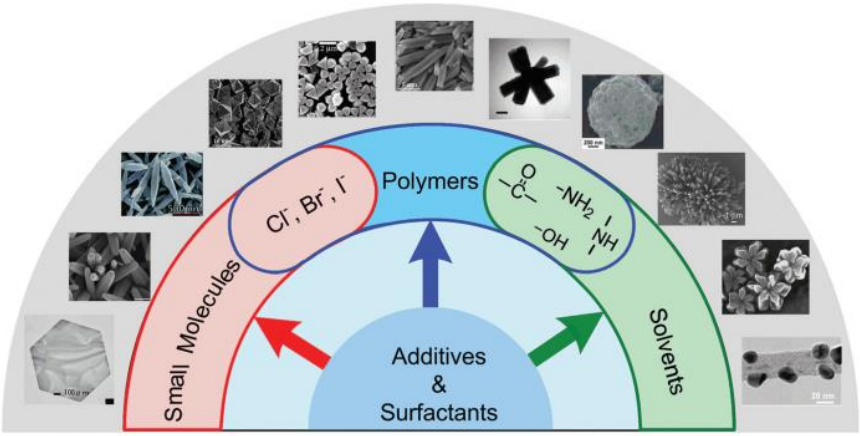

Figure 1.13 Schematic of the additives/surfactants for the shape control of metal and metal-oxide nanoparticles with selective adsorption.

1.2 Current Research on Reactive Electrochemical Membrane

1.2.1 Background and Challenges

Nearly 70.8% of the Earth's surface is covered by water, accounting for about 361 million square kilometres. Only 2.5% of the water on Earth is fresh water; most of the available water should be purified before it is safe to drink or use for other purposes. **Water is essential for maintaining an adequate** food supply and a productive environment for the human population and for other animals, plants, and microbes worldwide. Importantly, due to population growth and industry development, there is ever increasing amounts of uncontrolled wastewater discharge; this not only reduces the clean water resources, but also causes serious environmental problems and even threatens the health and safety of human beings and other living organisms. Emerging water contaminants in natural waters such as rivers and groundwater aquifers is a widespread problem. These emerging contaminants could be persistent in the environment and pose adverse effects on ecosystems and human health. Environmentally persistent organic micropollutants may

include polyromantic hydrocarbons (PAHs), organophosphate flame retardants, endocrine disrupting compounds (EDCs), pesticides, herbicides, pharmaceuticals and personal care products (PPCPs). The wastewater containing various synthetic organic contaminants as associated with petrochemicals, pharmaceuticals, pesticides, and dyestuffs, has become a concern globally due to their toxicity, carcinogenicity and persistence. Over the past few decades, various technologies have been explored for the treatment of organic wastewater. In this case, such conventional processes as biological treatment, adsorption, sedimentation, and coagulation are not very effective for complete removal of organic pollutants. These technologies usually need complicated equipment, with a high energy consumption and high operating costs, and some of them also require large amounts of chemicals, resulting in by-products wastes and sludge.

Membrane technology has been considered as one of the most promising methods for water decontamination owing to its advantages of high separation selectivity, low energy consumption, no requirements for additional chemicals, easy scale up and continuous operation. In recent years, membrane-based processes have been developed and applied for different applications, including particle filtration (PF), microfiltration (MF), ultrafiltration (UF), nanofiltration (NF), reverse osmosis (RO), forward osmosis (FO), membrane distillation (MD) and membrane bioreactor (MBR). However, these membrane processes often suffer from their own “Achilles heel”. During the course of filtration, the retention and accumulation of pollutants on the membrane surface or/and inside the membrane pores as a result of the membrane rejection will lead to membrane fouling, which inevitably deteriorates the membrane performance. Moreover, membrane separation is a physical process, while it can concentrate the contaminants, the wastewater is actually

not “decontaminated”. And membrane filtration is not effective to remove small molecular weight compounds such as nitrate or nitrite, phosphate, metal ions and trace-level micropollutants. This is especially the case for wastewater with complex compositions where a complete retention of the contaminants is difficult or impractical.

Advanced oxidation processes (AOPs) are widely studied to effectively treat biorefractory organic substances or resistant microbes. Three categories of AOPs exist: (1) UV/O_3; (2) Photocatalysis (TiO_2 or other semiconductor particles under UV-vis illumination); (3) Fenton process (Fe^{2+} / H_2O_2), Photo Fenton process (Fe^{2+} / H_2O_2 / UV) and Photo-Fenton-like processes of homogeneous nature (Fe^{3+}/ H_2O_2 / UV, Fe^{3+}/ APS / UV and Fe^{2+}/ APS / UV) and heterogeneous nature (Fe^0 / oxidants) (where APS is $(NH_4)_2S_2O_8$). AOPs such as photocatalytic oxidation, photochemical oxidation, electrochemical oxidation, photochemical reduction, persulfate radical treatment, thermally induced reduction, and sonochemical pyrolysis involves the production of hydroxyl radicals (•OH) as potent, nonselective oxidants to degrade recalcitrant pollutants. However, continuous UV irradiation and consumption of chemical reagents (e.g., H_2O_2, O_3, and ferrous iron) cause potentially high operation and maintenance costs.

Coupling AOP with physical membrane filtration has been extensively studied to enable the destruction of organic pollutants by free radicals (mainly hydroxyl radicals or •OH) and antifouling capabilities. For instance, photocatalytic ceramic membranes (PCMs) utilize semiconducting inorganic materials, such as TiO_2 and ZnO, as photocatalysts to enable surface reactions on water-permeable porous membranes. Along with the physical separation of contaminants in water through the porous structure of PCMs, the contaminants are chemically decomposed by reactive radical species generated on the

PCMs under UV radiation. However, there are still some practical challenges when implementing the PCMs technology, including: (1) difficulty in providing effective UV illumination; (2) the reduced light penetration in tabular and spiral membrane surfaces; (3) the reduced active surface on catalyst and membranes accessible to chemicals and photons. Therefore, other than photo irradiation, an alternative irradiation source that can evenly pass-through membrane modules and distribute energy to water, catalysts and membrane surface is highly needed.

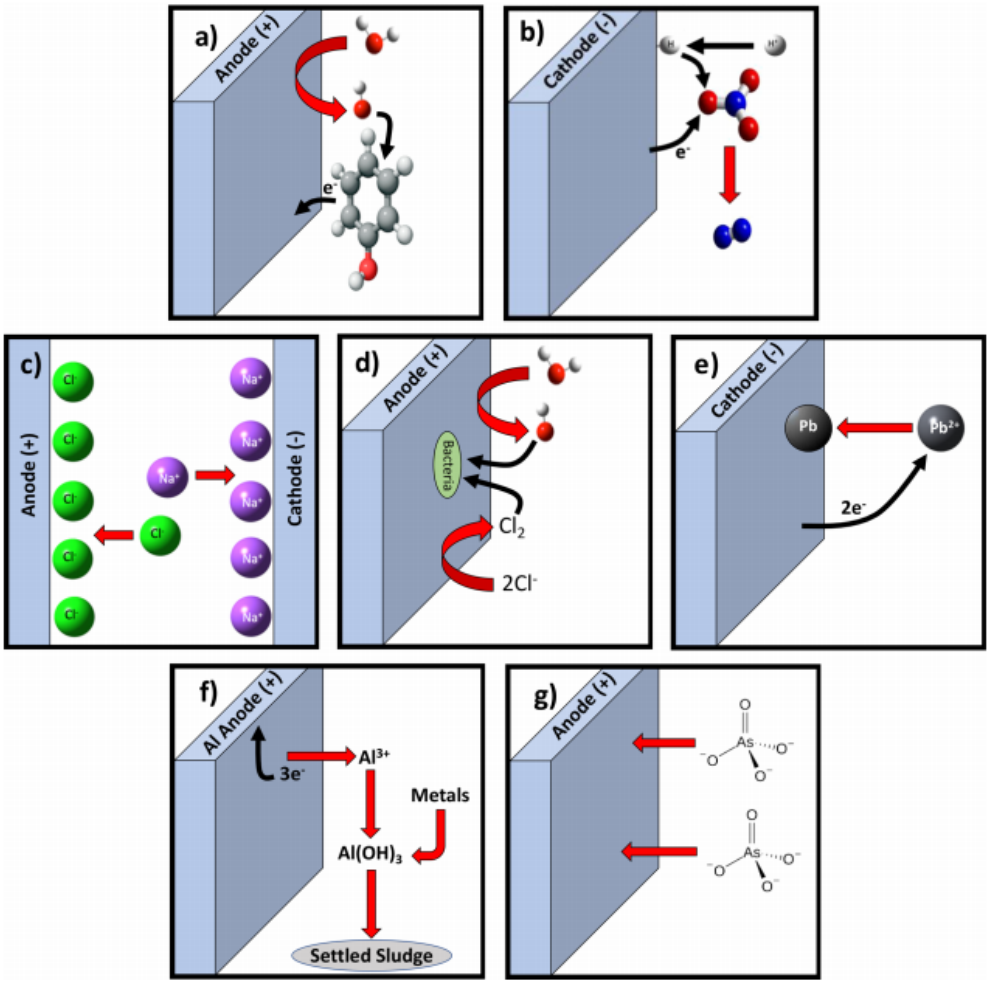

Figure 1.14 Treatment capabilities of electrochemical technologies. Examples include (a) electrochemical oxidation of phenol (C_6H_5OH); (b) electrochemical reduction of nitrate (NO_3^-) to N_2; (c) electro-deionization of NaCl; (d) microorganism inactivation by electrochemically produced Cl_2 and OH•; (e) electrodeposition of lead; (f) electro-coagulation of metals; and (g) electrosorption of arsenate.

On the other hand, electrochemical advanced oxidation processes (EAOPs) are also known as electrolytic treatment have emerged as promising technologies for the destruction of recalcitrant and complex waste. EAOPs are a group of emerging technologies which can decompose the organic compounds to fewer refractory products, and even mineralize them to CO_2, H_2O, and other inorganic species. In recent years, EAOPs have gained increasing attentions due to their favourable characteristics (i.e., no chemical reagents needed, easy process control, stabile performance, and environmental friendliness). However, there are some limitations for each individual EAOP to scale up for large-scale industrial applications. The efficiencies of conventional EAOP reactors are often limited by the weak mass transfer of the pollutant molecules in the reactor, and the energy consumption is still at a relative high level for commercial uses. Moreover, the EAOPs are not particularly feasible to treat large-volumes of wastewater at low contaminant concentrations. However, it is encouraging that the combination of membrane technology with EAOPs can effectively mitigate the membrane fouling problems, thereby improving the overall separation performance. As expected, a synergistic design of such coupling processes can further improve the process performance and reduce the energy consumption.

In the past decade, many studies on the coupling process of membrane technology and EAOPs (membrane-EAOPs) for wastewater decontamination have been reported. Reactive Electrochemical Membranes (REM) or electrochemically reactive membranes combined electrochemistry with ceramic membranes may provide a solution by *in situ* and real-time production of chemical oxidants, higher flux, and less maintenance. This combination may help overcome some of limitations of traditional EAOP such as the intrinsic mass transport limitations associated with organic pollutants required to interact

with the electrode surface, high cost of electrodes, and low current densities without high concentrations of electrolyte. Because the radicals can be generated *in-situ* via electrochemistry, which means the oxidation process can be driven by electricity rather than by chemicals to produce radicals. The reduced chemical consumption potentially leads to a more environment-friendly approach.

1.2.2 The Design of Membrane Technology Coupled with EAOPs

The combination of membrane filtration with EAOPs can be achieved in two modes: two-stage coupling process and one-pot coupling process.

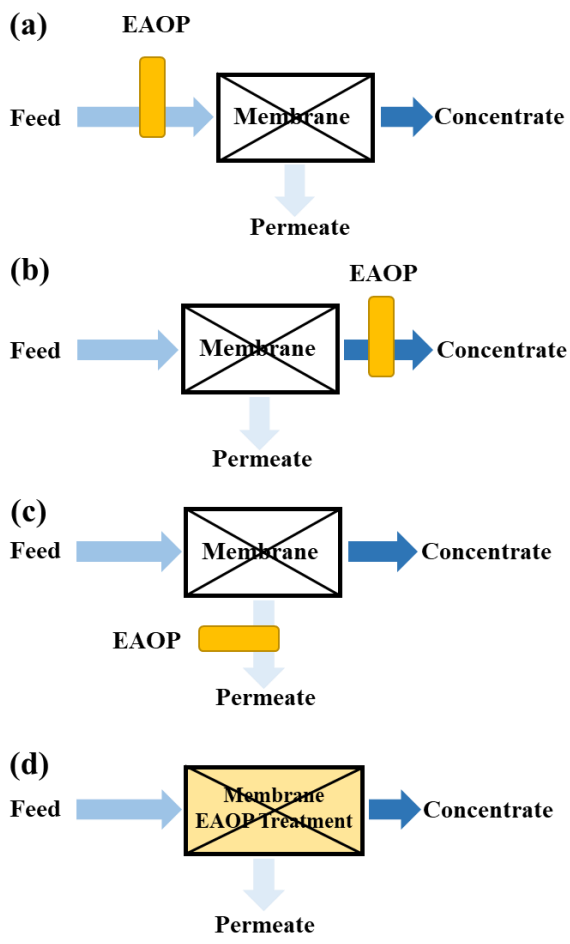

Figure 1.15 Coupling of membrane processes with EAOPs (the two-stage processes). (a) Pre-treatment of feed; (b) Post-treatment of concentrate; (c) Advance treatment of permeate; (d) The one-pot process coupling membrane with EAOP.

In the two-stage coupling process, the membrane technology and EAOP are set as two stand-alone units. Depending on the location and function of the EAOP unit in the coupled processes, the following three process integrations are proposed. (a): The EAOP acts as a pre-treatment stage for the membrane process (**Figure 1.15a**). This process mode is usually used for decontamination of wastewater that imposes serious problems of membrane fouling. Pretreating the wastewater with an EAOPs will decrease the pollutant concentration and thus reduce or eliminate membrane fouling. (b): The EAOP acts as a post-treatment of the membrane concentrate (**Figure 1.15b**). The membrane process (*e.g.*, NF, RO) will concentrate the organic compounds and salts, and "clean water" is generated on the permeate side of the membrane. The membrane concentrate is enriched with pollutants and must be further degraded so as to reduce its impact on the environment. In view of the electrical conductivity of the membrane concentrate due to increased salinity, the EAOPs are expected to be promising methods for post-treatment of membrane concentrate stream. (c): The EAOPs are used for further treatment of the membrane permeate (**Figure 1.15c**). This is, however, not particularly advantageous due to the relative low pollutant concentration and thus the low electric-conductivity in the permeate stream from membrane unit. In the one-pot coupling process, the removal of pollutants by membrane separation and EAOPs is accomplished simultaneously in a single unit (**Figure 1.15d**).

Compared with the two-stage coupling processes, the one-pot coupling process provides additional advantages in waste-water treatment: (a) The membrane process is enhanced under the assistance of electrical field due to such electro kinetic effects as electroosmosis, electrophoresis, and electrostatic interaction, thereby achieving a high

permeation flux and treatment efficiency. (b) The concentration polarization and membrane fouling are reduced by the in-situ electrochemical oxidation of the pollutants and the microflow disturbance near the electrode surface, which helps maintain the high permeation flux and extend the life span of the membrane. (c) The membrane and electrodes are set in one single reactor, yielding a small footprint because of its compact design.

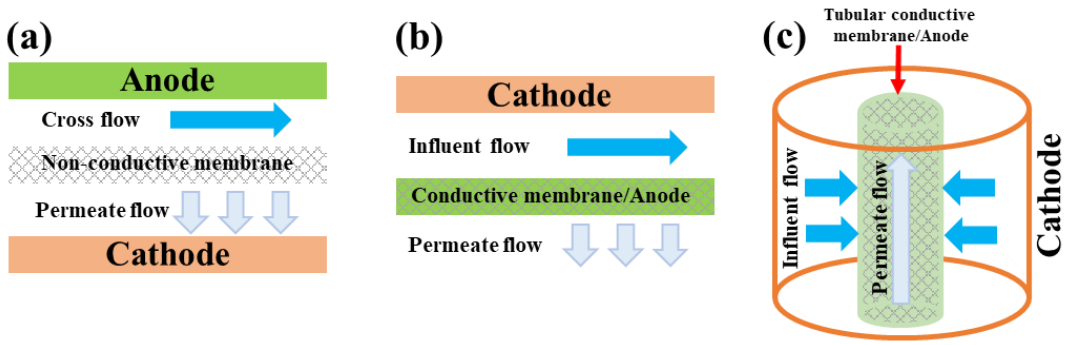

Figure 1.16 (a) A schematic of one-pot membrane-EAOP design using non-conductive membranes and A schematic of the one-pot membrane-EAOP design using conductive membranes (b) flat membrane; (c) tubular membrane.

Moreover, in the one-pot coupling mode, two types of integration patterns are reported depending on the conductivity of membrane materials. Different from the system that integrate non-conductive membranes and electrodes for physical filtration and electrochemical degradation respectively (**Figure 1.16a**), the one-pot mode, which adopts a conductive membrane as the electrode, has several advantages. On the one hand, this makes the coupling system more compact, allowing it to achieve higher removal efficiency at the same voltage, thus reducing energy consumption (**Figure 1.6b-c**). On the other hand, the flow of the feed solution will drag the organic pollutants toward the surface of the membrane/electrode, which enhance the mass transfer coefficient in the liquid phase effectively.

1.2.3 Membrane Materials

A large number of membrane materials with different unique properties have been synthesized and reported. Depending on the nature of the membrane materials, current membranes can be divided into organic membranes, inorganic membranes and inorganic-organic hybrid membranes (**Figure 1.17**). They can also be categorized as isotropic and anisotropic membranes. Isotropic membranes are uniform in composition and structure, while anisotropic membranes include phase-separation membranes and composite membranes that are often asymmetric in structure. Furthermore, based on membrane geometry, the membranes may also be classified into flat sheet, tubular, capillary and hollow fiber membranes, which are aimed to suit for different engineering applications.

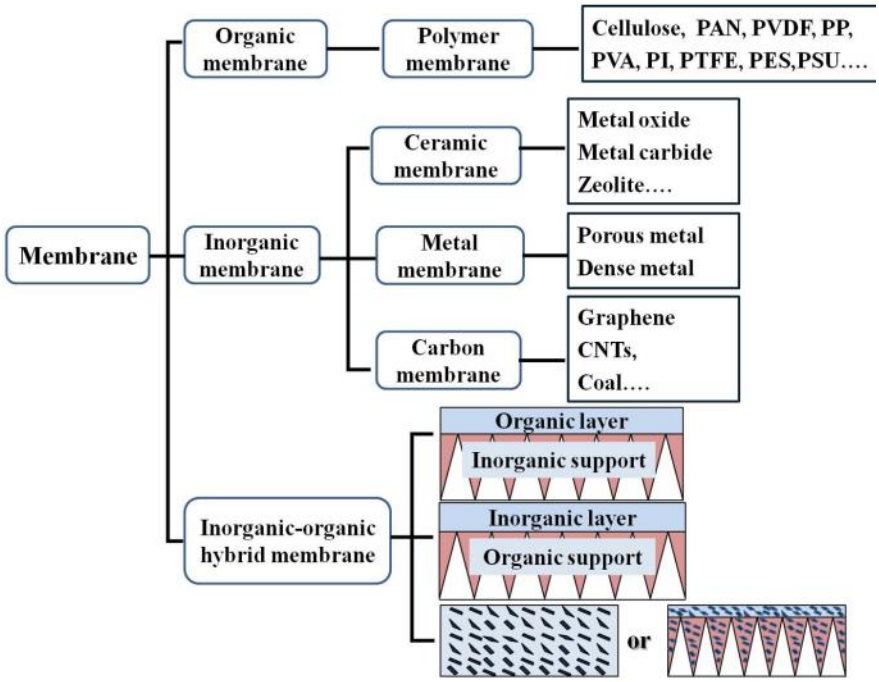

Figure 1.17 The classification of membranes according to the nature of membrane materials.

The electrical conductivity of the membrane materials has a significant effect on the structure, design and manner of coupling of a membrane-EAOP system and is also

relevant for treatment performance and energy consumption. Here, we briefly summarize the currently available membrane materials that have been applied in the membrane-EAOPs and the conductive membranes that have been used in wastewater treatment.

1.3.3.1. Non-conductive Membrane Materials. Non-conductive membranes are extensively used in the large-scale water purification applications, and thus they are also the primary constituent in the membrane-EAOPs. In the two-stage membrane-EAOP coupling mode, the membrane process is an stand-alone unit for physical separation, and ceramic membranes and polymer membranes have been used in such applications. On the other hand, in the one-pot membrane-EAOPs, membrane separation and EAOP are carried out simultaneously in the same unit, where, non-conductive membranes are predominately used as the separation media or as a substrate of composite conductive membranes.

Recent studies show that polymeric membranes (e.g., PA, PVDF, PTFE and PS) and ceramic membranes (e.g., Al_2O_3 and TiO_2) are commonly used as non-conductive membranes in the coupling membrane-EAOPs systems. Generally, when non-conductive membranes are used as the separation media in the one-pot coupling systems where they are located between the anode and the cathode, there is an electrical potential gradient across the membrane. Both good water permeability and pollutant retention by the membrane are necessary. For example, NF membranes have a high rejection for dye and tetracycline molecules, and MF membranes are more suitable for NOM-water separation. Besides, the good resistance against electrochemical etch is an essential property of membrane materials to ensure the stability and life span of the membrane. In the case of a composite conductive membrane formed on a substrate, the overall membrane resistance to electrochemical etching is also important. Obviously, the substrate should offer

minimum resistance to water permeation. The PTFE membranes used as a substrate for composite membranes typically have a pore size of 5 μm, which is too big to reject such organic pollutants as phenol methanol, methylene blue and formaldehyde, at the same time, large mass transfer resistance does not occur. In addition, the mechanical strength and thermal stability of the substrate membranes are also critical when they are subjected to a high transmembrane pressure or thermal treatment is needed. In these cases, ceramic membranes such as alumina membranes and TiO_2 membranes are proper choices.

1.3.3.2 Conductive Membrane Materials. At present, the most common types of conductive membrane materials applied for wastewater purification include conductive metal and metal oxide membranes, carbon-based membranes and conductive polymer membranes (CPMs).

(a) Conductive metal and metal oxide membranes. The commonly used porous metal membranes are mainly fabricated by using press forming and sintering of metal powder. Among them, stainless steel membranes and porous titanium membranes are most widely investigated. Owning to their mechanical stability and low costs, stainless steel membranes are also widely used as porous support of composite membranes . However, stainless steel membranes are not stable when a positive potential is applied during the water treatment as a result of the electrochemical etching . On the other hand, porous Ti membranes have attracted attentions because of their good corrosion resistance and the feasibility of loading electro-catalysts. To today, porous Ti membranes have been applied in electrocatalytic membrane reactors (ECMR) where the Ti membranes serve as both an anode and filtration medium simultaneously for wastewater treatment . It is shown that the cell conductivity and mass transfer on the membrane electrode surface are improved, and

the treatment efficiency is considerably enhanced. Besides, the ECMR has also been used for controllable oxidation of such organic chemicals as n-propanol, cyclohexane, glucose, benzyl alcohol, and 2,2,3,3-tetrafluoro-1-propanol. Most metal oxides are non-conductive at room temperature, but the sub-stoichiometric titanium oxides Ti_nO_{2n-1}($n \geq 3$) (Magnéli phase) are an exception. These oxides ($4 \leq n \leq 6$) possess high electrical conductivity ($\sim 166 \Omega^{-1}$ cm^{-1}) at room temperature and good resistance to corrosion making them suitable for use as electrodes. It has been reported that the Ti_4O_7-based electrodes behave as both an active electrode for direct electron transfer reactions and an inactive electrode for producing ·OH via water oxidation. Consequently, the Ti_4O_7 electrode is a promising candidate for electrochemical wastewater remediation applications. Magnéli phase Ti_4O_7 is usually produced by heating titanium oxide at a temperature above 900°C, followed by reduction in hydrogen. The ECMR using Ti_4O_7 based porous membranes for treatment of organic wastewater via electrochemical oxidation has attracted significant interest. Excellent performance has been observed for the removal of such organic compounds as phenols, oily wastewater, humic acid as well as bacteria deactivation.

(b) Carbon-based conductive membranes. Carbon-based membranes (CBMs) are derived from the pyrolysis of carbonaceous materials (e.g., polymers) or fabricated directly from the carbon materials. Due to abundant resources, a wide range of species and good conductivity, CBMs have been investigated for various applications, including gas separation, vapor separation, fuel cells and water treatment. As an important part of conductive membranes, CBMs become promising alternative top other conductive membranes in the electrochemically-assisted membrane processes for wastewater treatment.

Recent studies on CBMs for electrochemical-assisted water purification can be categorized into two groups: (1) carbon-based membranes fabricated from novel nano-carbon materials; (2) carbon-based membranes derived from such conventional granular carbon materials as graphite and coal. Graphene and CNTs are representative nano-structured carbon materials, and their unique physicochemical properties (e.g., high surface area, thermal conductivity, electron mobility and mechanical strength) make them a hot research subject for environmental applications. Conductive membranes derived from these nano-carbon materials are shown to perform well in wastewater treatment. Generally, composite conductive membranes with a nano-carbon conductive layer can be fabricated by deposition under pressure or via vacuum filtration. Free standing nano-carbon based membranes can also be prepared using the phase inversion process, with appropriate polymers such as PVA, PVDF and PVB being used as the binders. The conventional carbon-based membranes derived from graphite and coal have the advantages of low costs of raw material, good chemical and thermal stabilities. In addition, the simple preparation procedure makes them especially suitable for large scale productions. The novel design of membrane reactors that use coal-based carbon membranes (CBCM) as an electrode demonstrated excellent performance in decontamination of organic wastewater.

(c) Conductive polymeric membranes. Polymers with conjugated backbones formed by a series of alternating single and double carbon bonds, tend to exhibit good electrical conductivity. The p-orbitals in the series of π-bonds overlap, allowing the electrons to be easily delocalized and to move freely between the atoms. The most common conductive polymers are polypyrrole(PPy), polyaniline (PANI), polythiophene and

polyacetylene. Due to their unique properties, membrane made from these polymers have attracted considerable attention.

Among the conductive polymer membranes used for water treatment. PPy appears to be the most popular conductive polymer for the preparation of conductive membranes because of its relatively high conductivity and good environmental stability. Having a tight and rigid structure with weakly basic anion-exchangeable groups, PPy can be polymerized easily by chemical or electrochemical oxidation. Moreover, the conducting polymers are not readily soluble in common solvents, and membranes are difficult to cast with the solution casting technique. Thus, PPy conductive membranes are normally prepared via the chemical/electrochemical polymerization deposition method on appropriate porous supports. However, in contrast to carbon-based materials and other inorganic conductive materials (e.g., Ti_4O_7), conductive polymers generally have a low electro-conductivity and weak electrochemical activity. Since these polymers are vulnerable to corrosion by electrochemical oxidation, conductive polymeric membranes are always used to serve as a cathode in water treatment, and the enhancement in foulant rejection is mainly contributed to the electrostatic forces.

CHAPTER 2

FACET DEPENDENT ELECTROCHEMICAL PROPERTIES OF Cu_2O NANOCRYSTALS: EXPERIMENTAL AND THEORETICAL ASSESSMENT

Work of this chapter is related to the publication:
Qingquan Ma, Joshua Young, Sagnik Basuray, Guangming Cheng, Jianan Gao, Nan Yao, Wen Zhang. "Elucidating Facet Dependent Electronic and Electrochemical Properties of Cu_2O Nanocrystals Using AFM/SCEM and DFT." *Nano Today*, 45 (2022): 101538.

2.1 Introduction

It is commonly known that the smaller nanoparticle size becomes, the larger their surface area, resulting in greater reactivity or mass transfer rates. However, recent studies have demonstrated that smaller size does not necessarily correlate with reactivity, suggesting that other aspects such as thoe exposed crystal surfaces or facets begin to govern the nanoparticle reactivity at nanoscale. For instance, metal-oxide nanoparticles such as Cu_2O and Ag_2O in cubic, cuboctahedron, octahedron, and rhombic dodecahedron shapes elicit facet-dependent catalytic, photocatalytic, and molecular adsorption. For example, Amanda et al. discovered that the adsorption of selenium oxyanions onto the [110] hematite facets was higher than that of [012] using extended X-ray absorption fine edge spectroscopy (EXAFS). Chen et al. demonstrated that [111] facets of Pt or Pd NPs are significantly more active than [001] facets toward carbon monoxide (CO) oxidation using diffuse reflectance infrared Fourier transform spectroscopy (DRIFTS). Wu et al. have pointed out reported that the water-splitting reactions on CeO_2 [110] and [111] facets of CeO_2 are 10 ~ 100 times faster than that on CeO_2 [100] facet at temperature (T) < 950 K using DFT simulations. Furthermore, control of surface termination on TiO_2 nanoparticles can enhance the electrochemical reaction selectivity and suppress the competing reaction pathways or byproduct interference. Peng et al. examined the electronic states and structures of TiO_2 on

particular facets such as [001] and [101] using ^{31}P nuclear magnetic resonance (NMR) in combination with trimethylphosphine (TMP) as a surface probe. They found that surface Ti cations on various facets with different Lewis acidities, surface energies, and steric arrangements are different.

Characterizing the influences of surface crystal facets on their properties at nanoscale or an atomic scale still remains challenging, because many surface characterization techniques such as Raman mapping, electrochemical measurements, surface plasmon resonance, and fluorescence microscopy usually resolve the average information of surface properties or at the single nanoparticle level. Only a few techniqeus such as XAFS, NMR, DRIFTS, and liquid cell (high-resolution) transmission electron microscopy (LCTEM) were demonstrated to detect facet-level material properties. For example, Sung et al. reported the different etching redox behavior of [100] for reduction and [111] for oxidation of ceria-based nanocrystals under the control of redox-governing factors using LCTEM. By contrast, traditional electrochemical measurements, such as cyclic voltammetry (CV), linear sweep voltammetry (LSV), and electrochemical impedance spectroscopy (EIS), only resolves average surface information of bulk materials or aggregated nanoparticles. Interpretation of macroscale electrochemical measurement results may be affected by nanoparticle aggregation states or surface coverage of nanoparticles on the electrode surface. Recently, scanning probe techniques such as scanning electrochemical microscopy (SECM), scanning electrochemical cell microscopy (SECCM), scanning ion conductance microscopy (SICM), scanning ion conductance microscopy-scanning electrochemical microscopy (SICM-SECM), electrochemical scanning tunneling microscopy (EC-STM), atomic force microscopy-scanning

electrochemical microscopy (AFM-SECM) are applied for performing electrocatalytic current mapping at a typical spatial resolution of hundreds of nanometers. However, regular scanning electrochemistry microscopy (SCEM) employs microelectrode probes that thus achieves a micrometer resolution.

AFM-SCEM has increasingly been used in simultaneously probing morphology and electrochemically active sites of various nanomaterials, such as dimensionally stable anodes, noble metal nanoparticles, functionalized electrodes, and soft electronic devices. For example, Mediator-tethered AFM-SECM successfully reveals the local electrochemical activity of 20-nm gold nanoparticles/nanodots functionalized by redox-labeled PEG chains deposited on gold surface. Catalytic current mapping of oxygen reduction reaction or hydrogen peroxide generation on individual 300-nm Pt particles was achieved by AFM-SECM. However, imaging at the nanoscale is challenging, as nanoelectrode probes are fragile and subject to destruction by electrostatic effects and vibrations as well as contamination. Positioning and maintaining the tip at nm distances requires high positional stability. Unlike scanning tunneling and atomic force microscopy, in the SECM the tip does not ever contact the surface. This requires a high level of control of the positioners. AFM-SECM is one among the few scanning probe methods that provide independent current and positioning control. Consequently, we can apply any selected potential without interfering with the tip separation distance from the electrode. Thus, the catalytic particles' surface activity under activation controlled and diffusion controlled electrochemical reaction conditions could be measured.

This study employed the AFM-SECM to examine the facet/shape-dependent electrochemical properties of individual cuprous oxide (Cu_2O) nanocrystals of four shapes:

nanocubes with the dominant [100] facet, rhombic dodecahedron with the dominant [110] facet, octahedrons with the dominant [111] facet, and cuboctahedron with [111] and [100] facets. Cu_2O is a p-type semiconductor with a direct band gap of about 2.17 eV, which emerges as a promising material in photocatalysis, catalysis, antibacterial activity, gas sensor, supercapacitors, lithium-ion batteries, ion detection, surface-enhanced Raman scattering (SERS), organocatalysis, and photoelectrochemical water splitting. Here, we performed *in-situ* AFM-SECM mapping on cuprous oxide (Cu_2O) nanoparticles with different shapes or facets. A nanoelectrode probe was used to permit high spatial resolution topographical mapping and electro-chemical activity assessment on the local facet level. To support the facet-dependent electrochemical analysis, kelvin probe force microscopy (KPFM) was also conducted to measure the local work function of the different facets. Finally, density function theory (DFT) simulations were performed to assess the electron transfer at the interface of different cuprous oxide (Cu_2O) nanocrystals and interpret the facet-dependent electrochemical properties.

2.2 Materials and Methods

2.2.1 Preparation of Cuprous Oxide (Cu_2O) Nanoparticles with Different Exposed Facets

Copper (II) chloride dihydrate ($CuCl_2 \cdot 2H_2O$), Sodium hydroxide, Sodium dodecyl sulfate (SDS), and hydroxylamine hydrochloride ($NH_2OH_3 \cdot HCl$) were purchased from Fisher Scientific. The Deionized water was used to prepare all solutions which is produced from a Milli-Q water machine (Direct–Q 3UV, Millipore) that produces ultrapure water with resistivity of 18.2 MΩ·cm at 25 °C. To synthesize Cu_2O nanocrystals with cubic and rhombic dodecahedral structures, 9.55, 9.35, 9.05, and 8.75 mL of deionized water were

respectively added to four sample vials labeled a, b, c, and d, which were placed in a water bath at 32-34 ^{o}C. Then, 0.1 mL of a 0.1-M $CuCl_2$ solution and 0.087 g of SDS powder were added to each vial with vigorous stirring. After complete dissolution of the SDS powder, 0.20 mL of a 1.0-M NaOH solution was added, which turned the solution color into light blue immediately, due to the formation of $Cu(OH)_2$ precipitate. Finally, 0.15, 0.35, 0.65, and 0.95 mL of 0.2 M $NH_2OH_3{\cdot}HCl$ were quickly spiked within 5 s into vials a, b, c, and d, respectively. The total solution volume in each vial was now 10 mL. After the vials were stirred for 20 s, they were kept in the water bath for 2 h for nanocrystal growth. The suspension was centrifuged at 4000 g for 5 min. After the supernatant was decanted, the precipitate was washed with 6 mL of a 1:1 volume ratio of water and ethanol. The precipitate was centrifuged and washed again using the same water/ethanol mixture to remove unreacted chemicals and SDS. The final washing step used 5 mL of ethanol, and the precipitate was dispersed in 0.6 mL of ethanol for storage and analysis.

2.2.2 Bulk Analysis of Particle Sizes, Shapes, Adsorptive and Electrochemical Properties

2.2.2.1 Hydrodynamic Diameter and Zeta Potential. The average hydrodynamic radius with polydispersity index (PDI) and zeta potentials were determined by dynamic light scattering (DLS) on a Zetasizer Nano ZS instrument (Malvern Instruments, UK) using 0.8 mL of 600 $\mu g{\cdot}L^{-1}$ different nanocrystal suspensions that were properly diluted with DI water in a standard macro-cuvette with a pass length of 10 mm. The measurement temperature was maintained at 25°C, and the scattering angle was 173°. A refractive index (RI) of 1.07 and an absorption value of 0.01 were used for the Cu_2O nanocrystals.

2.2.2.2 Morphology, Facet Identification and Facet Area Quantification. Scanning electron microscopy (SEM) images for four kinds of nanocrystal samples were taken by a

field emission scanning electron microscope (FE-SEM) (JSM-7900F, JEOL). Further facet identification and individual facet surface areas were determined statistically by a Verios 460 e Extreme High-Resolution Scanning Electron Microscope (XHR-SEM). At least 50 single nanocrystal particles of one kind were selected for XHR-SEM imaging. Titan Cubed Themis 300 double Cs-corrected Scanning/Transmission Electron Microscope (S/TEM) heir transmission electron microscopy (TEM) were operated to obtain the selected-area electron diffraction (SAED) patterns for facet identification.

2.2.2.3 Adsorption Assay. The adsorption activities of the different shaped Cu_2O nanocrystals were investigated using methyl orange ($C_{14}H_{14}N_3NaO_3S$) as the model adsorbate. Our hypothesis is that methyl orange exhibits a negative charge due to sulfonate ($-SO_3^-$) and may have different interactions with different facets of Cu_2O nanocrystals that render different charge densities. To validate this hypothesis, we conducted facet-related adsorption experiments using methyl orange. Briefly, 50 mg Cu_2O polyhedrons with different shapes were dispersed into the methyl orange solution (100 mL, 15 $mg \cdot L^{-1}$). Under constant stirring in the dark, about 5 mL of the solution was taken out at different intervals. After centrifugation of the liquid samples (4000 ×g for 5 min), the UV-Vis spectrum of the supernatant was recorded at 465 nm to monitor the remaining concentration of the bulk methyl orange and to determine adsorption behavior (e.g., adsorption kinetics) on different shaped Cu_2O. Attenuated total reflection-Fourier transform infrared spectroscopy (ATR-FTIR) was employed to characterize the surface deposition of methyl orange on the Cu_2O nanocrystals. ATR-FTIR spectra were recorded on a bench top FTIR-spectrometer (Cary 670, Agilent Technologies, USA) with a scanning range between 400 and 4000 cm^{-1}, the scanning time of 32 s and the resolution of 2 cm^{-1}.

2.2.2.4 Electrochemical Analysis of Cu_2O Nanocrystals. The Au coated copper electrode (Au/Cu electrode) was used as the substrate to deposit the four kinds of nanocrystal samples. These substrates were firstly polished carefully with 0.3-μm and 0.05-μm alumina slurry (Alumina polish powder, CH Instruments as shown in a tutorial video: https://www.youtube.com/watch?v=B1vndNRUnV4), and then rinsed thoroughly with DI water. Before deposition, the polished electrode was ultrasonicated in ethanol and DI water for 5 min, respectively. Subsequently, 5 μL of a Nafion solution (1%, v/v) in ethanol was first dropped onto the cleaned Au/Cu electrode surface to form a coated area of 0.05 cm^2. Following this step, the Nafion modified electrode was immersed into the suspensions of different shaped Cu_2O nanocrystals (0.2 $mg \cdot mL^{-1}$) for 6 h for forming the electrode with attached one single layer of nanocrystals. The residual nanocrystals were slowly washed away with DI water. Finally, the finished electrodes were stored in a refrigerator at 4°C when not in use.

All electrochemical measurements were performed in a conventional three-electrode cell at ambient temperature using a CHI 700E electrochemical potentiostat (CH Instruments, USA). An Ag/AgCl electrode (CHI112, CH Instruments, in 1.0 M KCl) and a Pt wire (CHI115, CH Instruments) were employed as a reference electrode and counter electrode, respectively. Cyclic voltammetry (CV) measurements were performed at a sweep rate of 50 $mV \cdot s^{-1}$ with 5 mM $K_3[Fe(CN)_6]$ as the redox probe in 0.1 M KCl solution. Before the CV measurements, the electrolyte was deoxygenated by bubbling ultrapure nitrogen (Airgas, Inc.) for 30 min.

To examine the potential interfacial differences, electrochemical impedance spectrometry (EIS) was acquired on the prepared electrodes under open circuit potential

(OCP) at the frequency range of 100 kHz to 0.01 Hz in aqueous solution containing 5 mM $K_3[Fe(CN)_6]$ with 0.1 M KCl solution. The EIS spectra were fitted in an equivalent circuit to determine the interfacial charge-transfer resistance parameters, including the charge-transfer resistance at the electrode/solution interface (R_{ct}, $\Omega \cdot cm^2$), the electrolyte resistance (R_s, $\Omega \cdot cm^2$), and W is the Warburg impedance ($S \cdot s^{1/2}$) where S = siemens =ohm^{-1}, s = second. Instead of an ideal double-layer capacitance (C), the constant phase element (CPE), $Z_{CPE} = \frac{1}{Q(wi)^n}$, is employed due to the inhomogeneity of the interface between the the electrode/solution interface, where Q is capacitance, wi is angular momentum and n is exponential factor (n=1 describes an ideal capacitor while the case n=0 describes a pure resistor).

2.2.3 Facet-Level Analysis of Surface Activity

2.2.3.1 Work Function Determination by Kelvin Probe Force Microscopy (KPFM). Facet-dependent interfacial charge transfer process is influenced by the surface atomic configurations and their corresponding energy band structures on different facets. KPFM has been demonstrated in nanometer-scale imaging and surface potential mapping on a broad range of materials ranging from biomaterials such as proteins and DNA to semiconductor nanomaterials. The measured surface potential is the contact potential difference (CPD) due to the difference in work functions (or Fermi energy levels) between the sample surface and the tip. Surface work function is affected by surface charges, doping levels, defects or grain boundaries. This study employed a Bruker Dimension Icon® with the Frequency modulation KPFM (FM-KPFM) integrated with PeakForce Tapping mode to conduct KPFM on different shaped nanocrystals to reveal facet dependence of work

functions. Briefly, Platinum-Iridium (Pt/Ir) doped silicon cantilever probes (Bruker, USA) were used as the conductive probes that have a relative stable work function (Φ_{tip}), a force constant of approximately 3 $N \cdot m^{-1}$ and a nominal resonance frequency of 75 kHz. Cu_2O nanocrystals were immobilized on Silicon wafers (⌀3" Silicon wafer, Type P/<111>, TED PELLA, Inc.) by depositing 5 μL of the Cu_2O suspensions (10 $mg \cdot L^{-1}$) with ~30 min air drying. During the operation, the microscope was fully contained in an environmental chamber that controls temperature (25 ± 2 ^{o}C) and humidity (<10 %) as measured by a temperature/humidity thermometer. KPFM mapping images were collected in the PeakForce Tapping mode at a scan rate of 0.1 Hz with a scan size of 5×5 μm and a retraction height or the distance between the tip and the sample surface of 50 nm.

Finally, the sample surface's work function (Φ_{sample}) was calculated by CPD= $-(\Phi_{tip} - \Phi_{sample})/e$. To determine the work function of the tip, we utilized three reference substrates, Au [111] substrate, highly oriented pyrolytic graphite (HOPG) and Si [111] substrates, which have stable work functions of 5.20–5.60 eV, 4.4–4.8 eV and 4.60–4.85 eV respectively. Each cantilever tip we used went through the same calibration process to determine the individual work function. At least 50 different facet regions of each shape on the deposited sample were probed to achieve statistical significance of the CPD measurement.

2.2.3.2 Local Surface Electrochemical Activity Measurement. Cu_2O nanocrystals were deposited onto silicon wafers (⌀3" Silicon wafer, Type P/[111], TED PELLA, Inc.) as illustrated in **Figure 2.1a** via spinning coating. Silicon wafer was cut into a single piece of 38 mm×38 mm, followed by washing using ethanol, methanol and DI water to remove organic and inorganic contaminants. The water suspension of the nanocrystals (10 $mg \cdot L^{-1}$)

were dropped in a volume of 10 µL on four different red spots of the silicon wafer substrates as shown in **Figure 2.1b** to repeat the measurement on the same sample. The substrate was vacuum dried at 40°C for 1 hour before the following AMF/SCEM test.

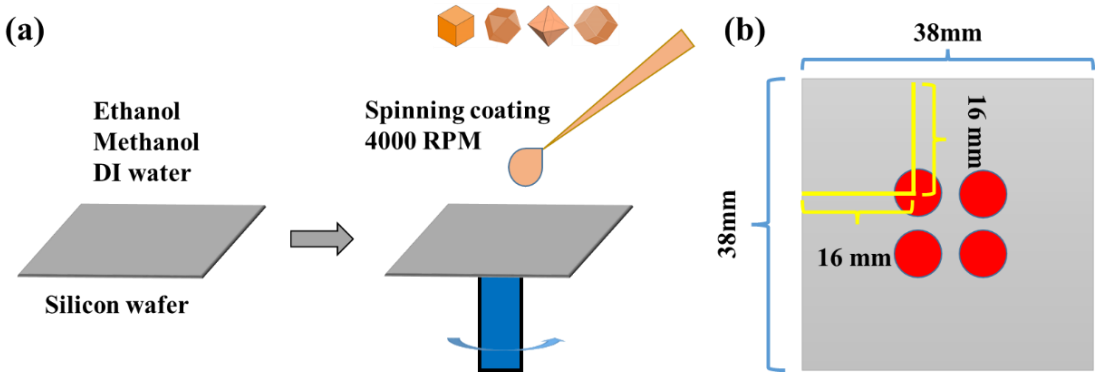

Figure 2.1 Deposition of Cu_2O Nanoparticles on a Silicon Wafer.

The SECM measurements were performed on the same Bruker Dimension Icon® that were equipped with standard PeakForce SECM accessories as detailed elsewhere. Both the probe and the sample are working electrodes sharing the same reference and counter electrodes. Prior to the PeakForce SECM measurement, all PeakForce SECM probes (tip radius of 25 nm and tip height of 215 nm, Bruker Nano Inc, CA, US) were tested by performing a few cyclic voltammetry in a standard three-electrode electrochemical cell with a Pt counter electrode and a standard Ag/AgCl reference electrode (CH Instruments, Inc.). The electrochemical cell was filled with 1.8 ml of 10 mM $[Ru(NH_3)_6]Cl_3$ in 0.1 M KCl. A bipotentiostat (CHI700E, CH Instrument) was connected to the electrochemical cell to perform the cyclic voltammetry analyses with a scanning voltage from 0 to −0.4 V vs. Ag/AgCl at 50 $mV \cdot s^{-1}$ applied to PeakForce SECM probes. Both the probe and the sample on the substrate are working electrodes sharing the same reference and counter electrodes. The probe and the sample are generally biased at different potentials, relative to the reference electrode, to enable different chemical reactions. In this

work, the probe reduces the $[Ru(NH_3)_6]^{3+}$ to $[Ru(NH_3)_6]^{2+}$ at −400 mV versus a pseudo Ag/AgCl reference electrode, while the sample is biased at +100 mV to oxidize $[Ru(NH_3)_6]^{2+}$ back to $[Ru(NH_3)_6]^{3+}$. We hypothesize that different dominant facets of Cu_2O should generate different levels of tip-sample currents at a sensitivity of $nA \cdot V^{-1}$ due to the reactivity differences and thus generate imaging contrast from the background or the silicon substrate that had negligible electrochemical oxidation reactions with $[Ru(NH_3)_6]^{3+}$. The PeakForce SECM scan was performed using an interleaved scan mode with a lift height of typically 40 to 150 nm between the probe and the sample surface. On each line scan during the main scan, the probe scans over the sample surface using the normal PeakForce QNM mode at a scan rate at 0.1 Hz and a scan size at 5×5 µm. After verifying SECM standard test sample (silicon nitride pattern cover on Pt layer) the sample-coated substrate was placed into the same fluidic cell to replace the SECM standard test sample. The same SCEM scanning procedure was performed on the sample surface at a DC bias of −400 mV and +100 mV applied to the probe and the sample substrate at the scan rate of 0.1 Hz and a scan size is 5×5 µm.

2.2.4 DFT Calculations of Surface Properties

The Vienna Ab Initio Simulation Package (VASP) was used to perform all the density functional theory (DFT) calculations within the generalized gradient approximation (GGA) using the Perdew-Burke-Ernzerhof (PBE) formulation. We employed projected augmented wave (PAW) potentials to describe the ionic cores and took valence electrons into account using a plane wave basis set with a kinetic energy cutoff of 500 eV. Partial occupancies of the Kohn−Sham orbitals were allowed using the Gaussian smearing method with a width of 0.05 eV. The electronic energy was considered self-consistent when the energy change

was smaller than 10^{-6} eV. A geometry optimization was considered convergent when the force change was smaller than 0.02 eV·Å^{-1}. Grimme's DFT-D3 methodology was used to describe the dispersion interactions.

The equilibrium lattice constants of Cu_2O unit cell in the cubic $Pm\overline{3}m$ space group were optimized using a 3×3×1 Monkhorst-Pack k-point grid for Brillouin zone sampling. The [100], [110] and [111] surfaces of Cu_2O were constructed with *p*(2×2×2) periodicity in the x, y and the z direction separated by a vacuum layer in the depth of 15 Å in order to separate the surface slab from its periodic duplicates. During structural optimizations, the **Γ** point in the Brillouin zone was used for k-point sampling.

Surface energy is a measure of thermodynamic stability of the surface; a low positive value indicates a stable surface. The surface energy (γ_r) of Cu_2O facets of [100], [110] and [111] was calculated by:) of Cu_2O facets of [100], [110] and [111] was calculated by:

$$\gamma_r = (E_{surf} - nE_{bulk}) / 2A \tag{2.1}$$

where E_{surf} is the total energy of the surface (eV), E_{bulk} is the bulk energy of the unit cell (eV), A is the surface area (m^2), the coefficient is 2 since there have the upper and lower surfaces, and n represents the number of unit cells that the surface contains.

The work function was also computationally calculated by Equation (2.2) to compare with the experimental data from KPFM by:

$$\Phi = E_{vac} - E_f \tag{2.2}$$

where Φ is the work function (eV), E_{vac} is the electrostatic potential of vacuum level (eV), and E_f is the energy of Fermi level (eV) for different species Fermi level (from OUTCAR file).

The density of states (DOS) of the three Cu_2O nanocrystal facets were also calculated with an increased Monkhorst-Pack k-point mesh of 3×3×1. The adsorption energy (E_{ads}) of the adsorbate (i.e., H_2O or $Ru(NH_3)_6]^{3+}$) is calculated by:

$$E_{ads} = E_{A/surf} - E_{surf} - E_{A(g)} \quad (2.3)$$

where $E_{A/surf}$, E_{surf} and $E_{A(g)}$ are the energy of the adsorbate molecules on the surface (eV), the energy of clean surface (eV), and the energy of isolated *A* molecule (eV) in a cubic periodic box with a side length of 20 Å and a 1×1×1 Monkhorst-Pack k-point grid for Brillouin zone sampling, respectively. The atomic charges were obtained from Bader charge calculations and analysis based on the numerical implementation developed by Henkelman et al.

2.2.5 Quality Assurance (QA) and Quality Check (QC)

The following experiments were carried out with triplicate independent sampling or testing: (1) The hydrodynamic diameter and zeta potential measurements of the Cu_2O nanocrystals; (2) Nanoparticle's characterizations including UV-Vis spectrometry, ATR-FTIR and KPFM. (3) Electrochemical testing including CV and EIS; The presented results are presented with average values with standard deviation as error bars.

2.3 Results and Discussion

2.3.1 Size, Morphology, Crystallinity, Absorptivity and Electrochemical Characterization

2.3.1.1 Hydrodynamic Diameters and Zeta potentials of Cu_2O Nanocrystals. Table 2.1 summarizes the average hydrodynamic radii of these nanocrystals are mostly in the range of 400-600 nm with polydispersity index (PDI) of 0.186, 0.156, 0.213, and 0.134 for cube,

cuboctahedron, octahedron and rhombic dodecahedron Cu_2O nanocrystals, respectively. PDI is a dimensionless measure of the broadness of the size distribution. As all of these are less than 0.25, the Cu_2O nanocrystals are considered well dispersed in the suspension without significant aggregation. The zeta potentials of four nanocrystals measured in the DI water ranged from −31.91 ± 0.86 to −34.06 ± 0.80 mV represent them are all electrostatically stabilized suspension.The zeta potentials of four nanocrystals measured in the DI water ranged from −31.91 ± 0.86 to −34.06 ± 0.80 mV represent them are all electrostatically stabilized suspension.

Table 2.1 Average Particle Sizes and Polydispersity Index of Four Cu_2O Nanocrystals

Cu_2O nanocrystals	Average hydrodynamic diameters (nm)	Zeta potential (mV)	Polydispersity index (PDI)
Cube	583 ± 104	−34.06 ± 0.80	0.186
Cuboctahedron	540 ± 67	−31.91 ± 0.86	0.156
Octahedron	460 ± 67	−32.16 ± 0.68	0.213
Rhombic dodecahedron	492 ± 64	−32.09 ± 0.40	0.134

2.3.1.2 Morphology, Crystallographic Facet Indexing and Facet Area Quantification. To avoid the effect of the surface-capping ligands on catalytic activities, we synthesized the different shaped nanocrystals with the same coating molecule of SDS using the seed-mediated approaches. Cube, cuboctahedron, octahedron and rhombic dodecahedron shapes formed due to the increasinge of the volumes of $NH_2OH_3{\cdot}HCl$ that change the amount of reductant added. The top panel of **Figure 2.2** shows high resolution SEM images of Cu2O nanocrystals with different geometriess, which are agreed with previously reported results. For example, cubic nanocrystals are generally composed of six identical square [100] facets. Cuboctahedron nanocrystals have six squares [100] facets in addition to the eight [111] facets. Octahedral nanocrystals are those with an octahedral structure bound by only [111]

facets. There are twelve congruent rhombic [110] facets in a rhombic dodecahedron. Nanocrystals could have a slightly different crystal facet distribution due to the defect formation or other factors (e.g., temperature varies and stabilizers concentration difference).

The second row of **Figure 2.2** illustrates the 3-D models of the four shaped nanocrystals. The third row shows their typical TEM images. The fourth row shows SAED images. For a cubic particle made of six exposed [100] facets, when the electron beam was aligned to be perpendicular to the direction of the [001], a two-dimensional (2-D) square-shaped projection should be observed in the TEM image. Four facets in the [100] family, which are parallel to [001] zone axis, are marked in **Figure 2.2a**. The HR-TEM images (**Figure 2.2a**) and the index of the spots in the SAED patterns indicate that indicate that this Cu_2O nanocrystal product is single crystal, and these cubes mainly have their [100] crystal facets exposed.

As for a cuboctahedron bounded by six square [100] and eight triangle [111] facets, when the electron beam is aligned to be perpendicular to [111], the TEM image exhibits as an equilateral hexagon projection constructed by the edges of [100] and [110]. The corresponding diffraction patterns in **Figure 2.2b** demonstrate the existence of [100] and [111] facets. The SAED pattern of Cu_2O cuboctahedron (**Figure 2.2b**) gives two sets of lattice fringes of 0.21 nm and 0.246 nm with an intersection angle of 60°. These lattice fringes respectively correspond to the lattice fringe of the [-111] and [002] planes of the Cu_2O structure (JCPDS card No. 34-1354).34-1354).

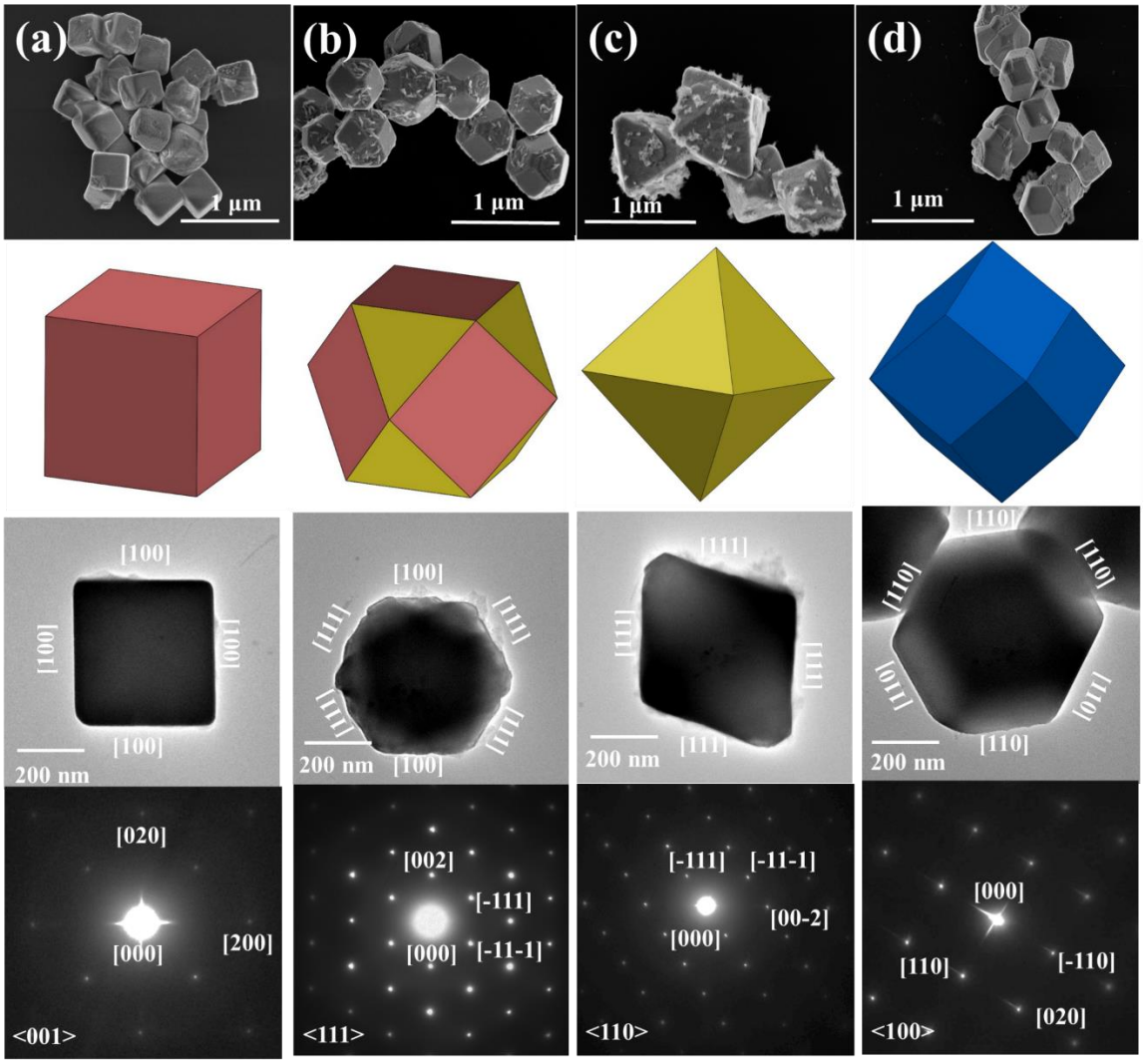

Figure 2.2 SEM images, sketch, bright TEM images and corresponding SAED patterns of the Cu_2O nanocrystals with various morphologies: (a) cube, (b) cuboctahedron, (c) octahedron, and (d) rhombic dodecahedron.

For an octahedral particle in **Figure 2.2c**, the projection is a parallelogram made of the projections of four [111] facets if the electron beam is in parallel with the [110] zone axis. The SAED pattern of Cu_2O octahedron (**Figure 2.2c**) gives two sets of lattice fringes of 0.246 nm with an intersection angle of 60°. These lattice fringes respectively correspond to the lattice fringe of the [-111] and [-11-1] planes of the Cu_2O structure (JCPDS card No. 34-1354), which further indicates that octahedral Cu_2O is composed of single crystals and these crystalline octahedrons mainly have their [111] crystal facets exposed.

For a rhombic dodecahedron particle in **Figure 2.2d**, the TEM projection is a hexagon shape if viewed from [110] zone axis. The six edges of the hexagon correspond to the edge of [110]. The lattice fringe of 0.30 nm of rhombic dodecahedron (**Figure 2.2d**) can be assigned to the [110] plane of the Cu_2O structure. The TEM and SEAD pattern reveal that rhombic dodecahedron which mainly expose [110] facets of the single crystal.

To analyze the distribution (%) of the crystal facets such as [100], [110] and [111], we computed the ratios of the specific facet areas over the total surface area of the nanocrystals of each shape. **Figure 2.3** illustrates the model structures of single crystal units of Cu_2O and the calculations of the volumes and surface areas of each particle shape assuming the same or uniform mass density of 6.0 $g \cdot cm^{-3}$. The number of particles and total surface copper atoms of each particle shape for 50 mg of Cu_2O are summarized in **Table 2.2**. Firstly, we measured the edge of above 50 Cu_2O nanocrystals of each shape and calculated their surface areas and volumes with formulas as shown in **Figure 2.3.** We calculated the number of particles corresponding 50 mg according to the density of Cu_2O is 6 $g \cdot cm^{-2}$. Then we get the total surface area number of particles of 50 mg and correlated surface atoms according the surface copper atom densities of 10.98, 14.27, and 7.76 Cu atoms$\cdot nm^{-2}$ were reported for the (100), (111), and (110) planes of Cu_2O, respectively. according Tthe surface copper atom densities of 10.98, 14.27, and 7.76 Cu atoms$\cdot nm^{-2}$ were reported for the (100), (111), and (110) planes of Cu_2O, respectively.

Table 2.2 Calculated Numbers of Particles and Surface Copper Atoms of Different Morphologies' Cu_2O nanocrystals Weighing 50 mg

	Cube	Cuboctahedron	Octahedron	Rhombic dodecahedron
Average size (nm)	404	295	448	363
Weight (mg)	50	50	50	50
Surface area of each particle (nm^2)	979296	823613	695259	1825844
Volume of each particle corresponding 50 mg (nm^3)	62939264	60510368	42386522	147284815
Number of particles (unitless)	1.26×10^{11}	1.38×10^{11}	1.97×10^{11}	5.66×10^{10}
Total surface area (nm^2)	1.24×10^{17}	1.13×10^{17}	1.37×10^{17}	1.03×10^{17}
Surface atoms (unitless)	1.36×10^{18}	1.38×10^{18}	1.95×10^{18}	8.02×10^{17}

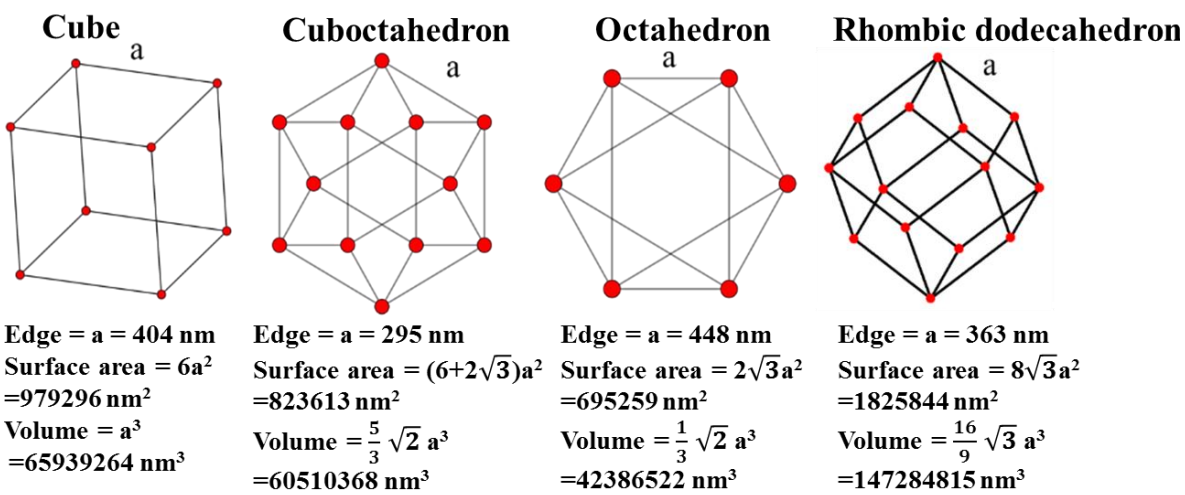

Figure 2.3 Calculations of surface area and volume of a single Cu_2O cube, cuboctahedron, octahedron, and rhombic dodecahedron.

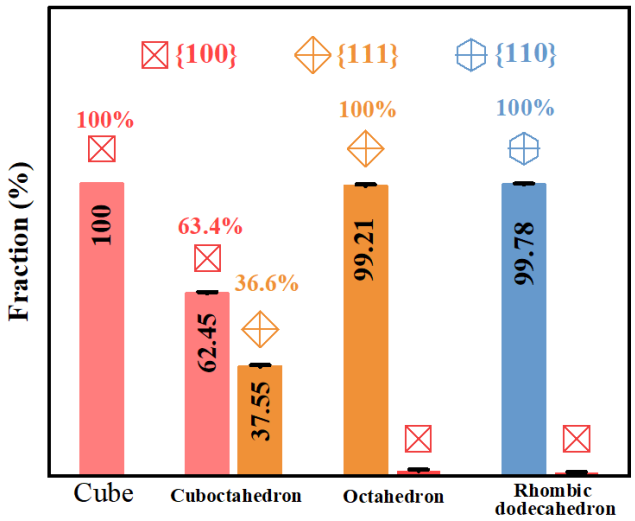

Figure 2.4 Statistics determination of percentage of the predominant facet.

Table 2.3a Calculated Facet Area Quantification (Cube)

Particles	Cube			
	Edge (nm)	Area of Facet [100] (nm^2)	Total area (nm^2)	Ratio of [100] over the total area (%)
1	423	1.07×10^6	1.07×10^6	100
2	443	1.18×10^6	1.18×10^6	100
3	452	1.23×10^6	1.23×10^6	100
4	481	1.39×10^6	1.39×10^6	100
5	352	7.43×10^5	7.43×10^5	100
6	481	1.39×10^6	1.39×10^6	100
7	381	8.71×10^5	8.71×10^5	100
8	384	8.85×10^5	8.85×10^5	100
9	387	8.99×10^5	8.99×10^5	100
10	421	1.06×10^6	1.06×10^6	100
11	369	8.17×10^5	8.17×10^5	100
12	352	7.43×10^5	7.43×10^5	100
13	414	1.03×10^6	1.03×10^6	100
14	505	1.53×10^6	1.53×10^6	100
15	423	1.07×10^6	1.07×10^6	100
16	455	1.24×10^6	1.24×10^6	100
17	432	1.12×10^6	1.12×10^6	100
18	429	1.10×10^6	1.10×10^6	100
19	440	1.16×10^6	1.16×10^6	100
20	379	8.62×10^5	8.62×10^5	100
21	384	8.85×10^5	8.85×10^5	100

Table 2.3b Calculated Facet Area Quantification (Cuboctahedron)

Particles	Cuboctahedron					
	Edge (nm)	Area of Facet [100] (nm^2)	Area of Facet [111] (nm^2)	Total area (nm^2)	Ratio of [100] over the total area (%)	Ratio of [111] over the total area (%)
1	348	7.27×10^5	4.40×10^5	1.17×10^6	62.26	37.74
2	313	5.88×10^5	3.53×10^5	9.41×10^5	62.48	37.52
3	313	5.88×10^5	3.60×10^5	9.48×10^5	62.04	37.96
4	221	2.93×10^5	1.78×10^5	4.71×10^5	62.26	37.74
5	333	6.65×10^5	4.15×10^5	1.08×10^6	61.59	38.41
6	288	4.98×10^5	2.99×10^5	7.96×10^5	62.48	37.52
7	456	1.25×10^6	7.27×10^5	1.98×10^6	63.17	36.83
8	421	1.06×10^6	6.57×10^5	1.72×10^6	61.81	38.19
9	387	8.99×10^5	5.60×10^5	1.46×10^6	61.59	38.41
10	285	4.87×10^5	2.81×10^5	7.69×10^5	63.40	36.60
11	314	5.92×10^5	3.45×10^5	9.37×10^5	63.17	36.83
12	428	1.10×10^6	6.54×10^5	1.75×10^6	62.71	37.29
13	326	6.38×10^5	3.87×10^5	1.02×10^6	62.26	37.74
14	377	8.53×10^5	5.17×10^5	1.37×10^6	62.26	37.74
15	437	1.15×10^6	6.68×10^5	1.81×10^6	63.17	36.83
16	453	1.23×10^6	7.18×10^5	1.95×10^6	63.17	36.83
17	418	1.05×10^6	6.23×10^5	1.67×10^6	62.71	37.29
18	335	6.73×10^5	4.16×10^5	1.09×10^6	61.81	38.19
19	304	5.54×10^5	3.36×10^5	8.91×10^5	62.26	37.74
20	371	8.26×10^5	5.10×10^5	1.34×10^6	61.81	38.19
21	326	6.38×10^5	3.76×10^5	1.01×10^6	62.94	37.06

Table 2.3c Calculated Facet Area Quantification (Octahedron)

Particles	Octahedron					
	Edge (nm)	Area of Facet [111] (nm^2)	Area of Facet [100] (nm^2)	Total area (nm^2)	Ratio of [111] over the total area (%)	Ratio of [100] over the total area (%)
1	476	7.14×10^5	11011.59	7.25×10^5	98.48	1.52
2	506	8.43×10^5	3840.54	8.46×10^5	99.55	0.45
3	400	5.32×10^5	1536.00	5.34×10^5	99.71	0.29
4	469	7.16×10^5	4751.16	7.21×10^5	99.34	0.66
5	501	7.83×10^5	15060.06	7.98×10^5	98.11	1.89
6	466	7.00×10^5	6384.39	7.06×10^5	99.10	0.90
7	492	7.97×10^5	3630.96	8.00×10^5	99.55	0.45
8	540	9.60×10^5	4374.00	9.64×10^5	99.55	0.45
9	455	6.74×10^5	4471.74	6.79×10^5	99.34	0.66
10	569	1.02×10^6	15734.78	1.04×10^6	98.48	1.52
11	557	9.78×10^5	15078.10	9.93×10^5	98.48	1.52
12	563	1.07×10^6	1711.63	1.07×10^6	99.84	0.16
13	304	2.95×10^5	3548.77	2.98×10^5	98.81	1.19
14	539	9.56×10^5	4357.82	9.60×10^5	99.55	0.45
15	466	7.22×10^5	2084.70	7.24×10^5	99.71	0.29
16	490	7.57×10^5	11668.86	7.69×10^5	98.48	1.52
17	483	7.60×10^5	5039.04	7.65×10^5	99.34	0.66
18	404	5.31×10^5	3525.47	5.35×10^5	99.34	0.66
19	553	1.05×10^6	183.49	1.05×10^6	99.98	0.02
20	474	7.32×10^5	4853.00	7.36×10^5	99.34	0.66
21	332	3.59×10^5	2380.84	3.61×10^5	99.34	0.66

Table 2.3d Calculated Facet Area Quantification (Rhombic dodecahedron)

Particles	Rhombic dodecahedron					
	Edge (nm)	Area of Facet [110] (nm^2)	Area of Facet [100] (nm^2)	Total area (nm^2)	Ratio of [110] over the total area (%)	Ratio of [100] over the total area (%)
1	368	1.88×10^6	0	1.88×10^6	100.00	0.00
2	405	2.27×10^6	229.64	2.27×10^6	99.99	0.01
3	416	2.40×10^6	15505.82	2.41×10^6	99.36	0.64
4	434	2.61×10^6	263.70	2.61×10^6	99.99	0.01
5	290	1.17×10^6	1883.84	1.17×10^6	99.84	0.16
6	380	2.00×10^6	3234.56	2.00×10^6	99.84	0.16
7	417	2.41×10^6	243.44	2.41×10^6	99.99	0.01
8	394	2.15×10^6	13909.15	2.16×10^6	99.36	0.64
9	369	1.89×10^6	0.00	1.89×10^6	100.00	0.00
10	360	1.80×10^6	14696.64	1.81×10^6	99.19	0.81
11	364	1.84×10^6	2967.91	1.84×10^6	99.84	0.16
12	418	2.42×10^6	8806.09	2.43×10^6	99.64	0.36
13	441	2.69×10^6	272.27	2.70×10^6	99.99	0.01
14	407	2.30×10^6	14842.15	2.31×10^6	99.36	0.64
15	445	2.74×10^6	277.24	2.74×10^6	99.99	0.01
16	293	1.19×10^6	480.75	1.19×10^6	99.96	0.04
17	393	2.14×10^6	1946.06	2.14×10^6	99.91	0.09
18	287	1.14×10^6	2882.92	1.14×10^6	99.75	0.25
19	359	1.79×10^6	0.00	1.79×10^6	100.00	0.00
20	315	1.37×10^6	5000.94	1.38×10^6	99.64	0.36
21	358	1.78×10^6	4485.74	1.78×10^6	99.75	0.25

2.3.1.3 Adsorption of Methyl Orange (MO) on Different Shaped Cu_2O Nanocrystals.

Figure 2.5a is a plot of adsorption kinetics of MO molecules on four various Cu_2O nanocrystals in the dark. The adsorption rates and capacities of MO exhibited evident shape dependence, following an order of rhombic dodecahedron > octahedron > cuboctahedron > cube. The presented adsorption data were fitted with a pseudo-first-order kinetics model (Equation 2.4) and a modified pseudo-first-order kinetics model (Equation 2.5) to determine the relevant adsorption parameters and analyze their possible shape dependence.

$$\ln\left(q_e - q_t\right) = \ln q_e - k_1 t \tag{2.4}$$

$$\ln\left(q_e^s - q_t^s\right) = \ln q_e^s - k_1^s t \tag{2.5}$$

where q_e is adsorption capacity at adsorption equilibrium (mg·g^{-1}), q_t is adsorption capacity (mg·g^{-1}) at time t (h), k_1 is the pseudo-first-order adsorption rate constant (h^{-1}), q_e^s is adsorption capacity per surface area at equilibrium (mg·m^{-2}), q_t^s is adsorption capacity per surface area (mg·m^{-2}) at time t (h), and k_1^s is the modified pseudo-first-order adsorption rate constant (h^{-1}). q_t and q_t^s were both calculated by experimental data The total surface areas of the spiked Cu_2O nanocrystals (15 mg L^{-1}, 100 mL) shown in **Table 2.2** were used in the calculations of q_e^s and k_1^s .

The fitted values of k_1 , k_1^s, q_e and q_e^s summarized in **Table 2.4 and 2.5**, respectively. The rhombic dodecahedron with [110] facet has the highest adsorption capacity at equilibrium of 9778.70 mg·g^{-1}, which is greater than other morphological Cu_2O nanocrystals. Again, the adsorption capacity per surface area at equilibrium of four different Cu_2O nanocrystals also show that rhombic dodecahedron has the highest value of 100.94 mg·m^{-2}. Guo et al. demonstrated that the adsorption ability of MO to the different shapes of Cu_2O nanocrystals followed the sequence of octahedron > cuboctahedron > cubes. The exposed [111] facets of octahedron-Cu_2O nanocrystals had positively charged "Cu" atoms that inclined to interact with the negatively charged groups $–SO_3^-$ in MO molecules (**Figure 2.5b**). Subsequently, the rhombic dodecahedron-Cu_2O nanocrystals with only exposed [110] facets exhibited an excellent adsorption ability of MO because of the high density of Cu atoms on the surface.

Table 2.4 Pseudo-first-order Adsorption Kinetics Parameters of MO for Different Cu_2O NPs

Cu_2O NPs	Pseudo first-order kinetics equation	Adsorption capacity at equilibrium, q_e, ($mg \cdot g^{-1}$)	Adsorption rate constant, k_1, (h^{-1})	R^2
Cube	$y = 6.73 – 6.13\times10^{-4}x$	836.91	6.13×10^{-4}	0.94
Cuboctahedron	$y = 8.63 – 3.20\times10^{-4}x$	5594.70	3.20×10^{-4}	0.94
Octahedron	$y = 9.03 – 3.16\times10^{-4}x$	8337.77	3.16×10^{-4}	0.99
Rhombic Dodecahedron	$y = 9.19 – 5.42\times10^{-4}x$	9778.70	5.42×10^{-4}	0.99

Table 2.5 Modified Pseudo-first-order Adsorption Kinetics Parameters of MO for Different Cu_2O NPs

Cu_2O NPs	Modified Pseudo first-order kinetics equation	Adsorption capacity per surface area at equilibrium, q_t^s, ($mg \cdot m^{-2}$)	Adsorption rate constant, k_1^s, (h^{-1})	R^2
Cube	$y = 3.62 – 1.13\times10^{-3}x$	37.33	1.13×10^{-3}	0.94
Cuboctahedron	$y = 4.43 – 2.00\times10^{-3}x$	83.92	2.00×10^{-3}	0.94
Octahedron	$y = 4.57 – 3.84\times10^{-3}x$	96.91	3.84×10^{-3}	0.99
Rhombic Dodecahedron	$y = 4.61 – 1.13\times10^{-2}x$	100.94	1.13×10^{-2}	0.99

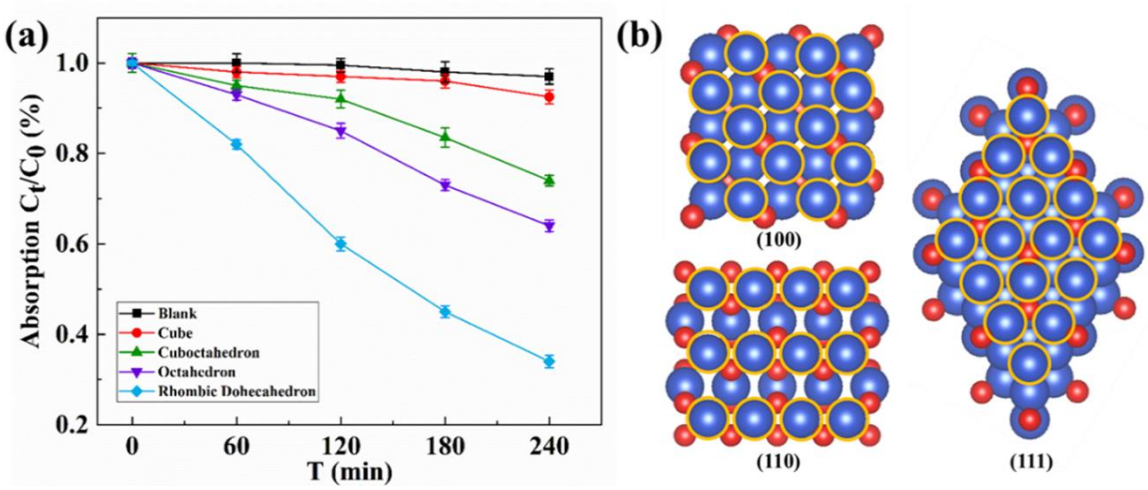

Figure 2.5 (a) Absorption (C_t/C_0) of the aqueous solution of methyl orange (15 $mg \cdot L^{-1}$, 100 mL) in the presence of Cu_2O nanocrystals with different morphologies. (b) Crystal structures of Cu_2O oriented to show the [100], [110], and [111] planes. Surface Cu atoms on the surfaces are shown with yellow circles.

The FTIR spectrum of the Cu_2O nanocrystals before and after adsorption exhibits two strong vibration bands as shown in curve 1 in **Figure 2.6**. The band at 632 cm^{-1} corresponds to the Cu–O bond (optically active lattice vibration in the oxide), and the peak at 1632 cm^{-1} is attributed to the –OH bending vibration, which originates from the surface-adsorbed H_2O. In comparison with the FTIR spectrum of the pure Cu_2O nanocrystals, some new peaks appear in those of Cu_2O NPs after adsorption (curves 1–4 in **Figure 2.6**). Combined with the FTIR of pure MO (curve 5 in **Figure 2.6**, the new peaks can be assigned to the characteristic vibration from MO. The peaks at 1449 cm^{-1} and 1385 cm^{-1} are the signals from the methyl group. The peaks at 697 cm^{-1}, 1039 cm^{-1} and 1118 cm^{-1} come from the vibration of the sulfonic group. Thus, the FTIR characterization provided solid evidence for the MO adsorption by Cu_2O nanocrystals polyhedra.

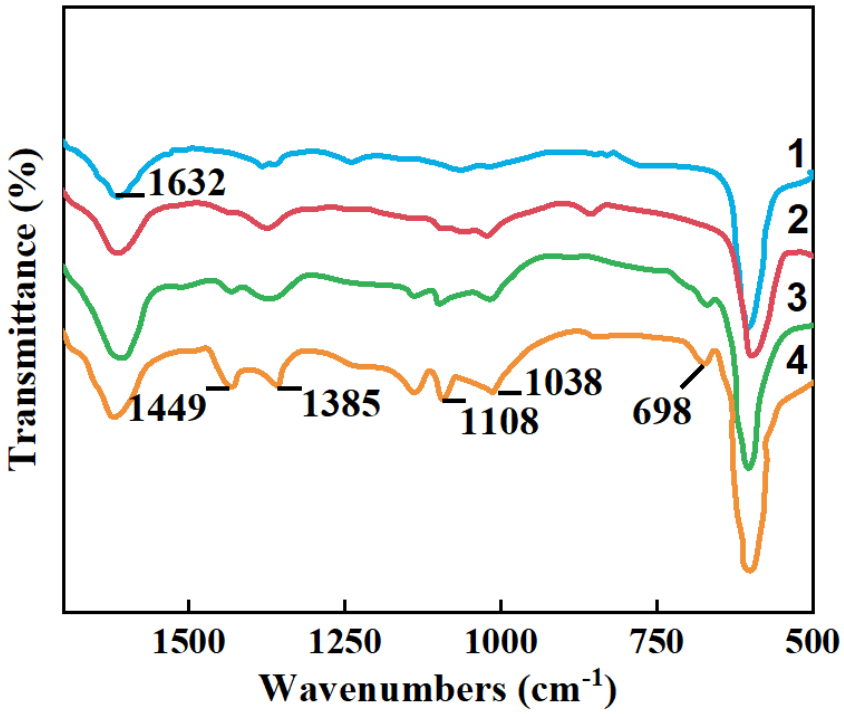

Figure 2.6 FTIR spectra of (1–4) the residual after the MO adsorption by Cu_2O nanocube, cubooctahedron, octahedron, rhombic dodecahedron respectively.

2.3.1.4 Electrochemical Activity Measurement of Cu_2O Nanocrystals. Cyclic voltammetry (CV) has been reported for use in detecting the "fingerprint" of specific lattice planes of nanoparticles such as gold, CeO_2 and Co_3O_4. For instance, the oxidation peak for [100] and [111] of gold nanostructures in 0.01 M aqueous H_2SO_4 were reported to be +1.3 and +1.1 V (vs Ag/AgCl, saturated KCl), respectively. For the four types of Cu_2O nanocrystals, CV curves were obtained by immersing the nanocrystal-covered Au/Cu electrodes in 5 mM $K_3[Fe(CN)_6]$ with 0.1 M KCl solution. **Figure 2.7** shows the typical CV curves that exhibit different peak currents or corresponding applied potentials. For Cu_2O nanocubes, a clear oxidation peak and a reduction peak is noted at around +0.38 V and +0.29 V (vs Ag/AgCl, 1.0 M KCl), respectively. Cu_2O nanocubes have a peak-to-peak potential separation (ΔE_p) of 113 mV (vs. Ag/AgCl) and relatively low redox peak currents, corresponding the presence of dominant [100] facets as shown in the HR-TEM results (**Figure 2.1a**). For cubooctahedron, the characteristic CV peaks reflect the influences from [111] and [100] planes. The oxidation peak current of Cu_2O cuboctahedron is slightly higher that of Cu_2O nanocubes, probably because the Cu_2O's [111] plane promoted the electron transfer or reactivity toward the probe molecules of $[Fe(CN)_6]^{3-/4-}$. On the octahedron, a pair of well-defined redox peaks also appear with the ΔE_p of 103 mV, due to the increase of the [111] plane. Similarly, rhombic dodecahedron had ΔE_p of 87 mV (vs. Ag/AgCl), indicating a more reversible electron transfer process.

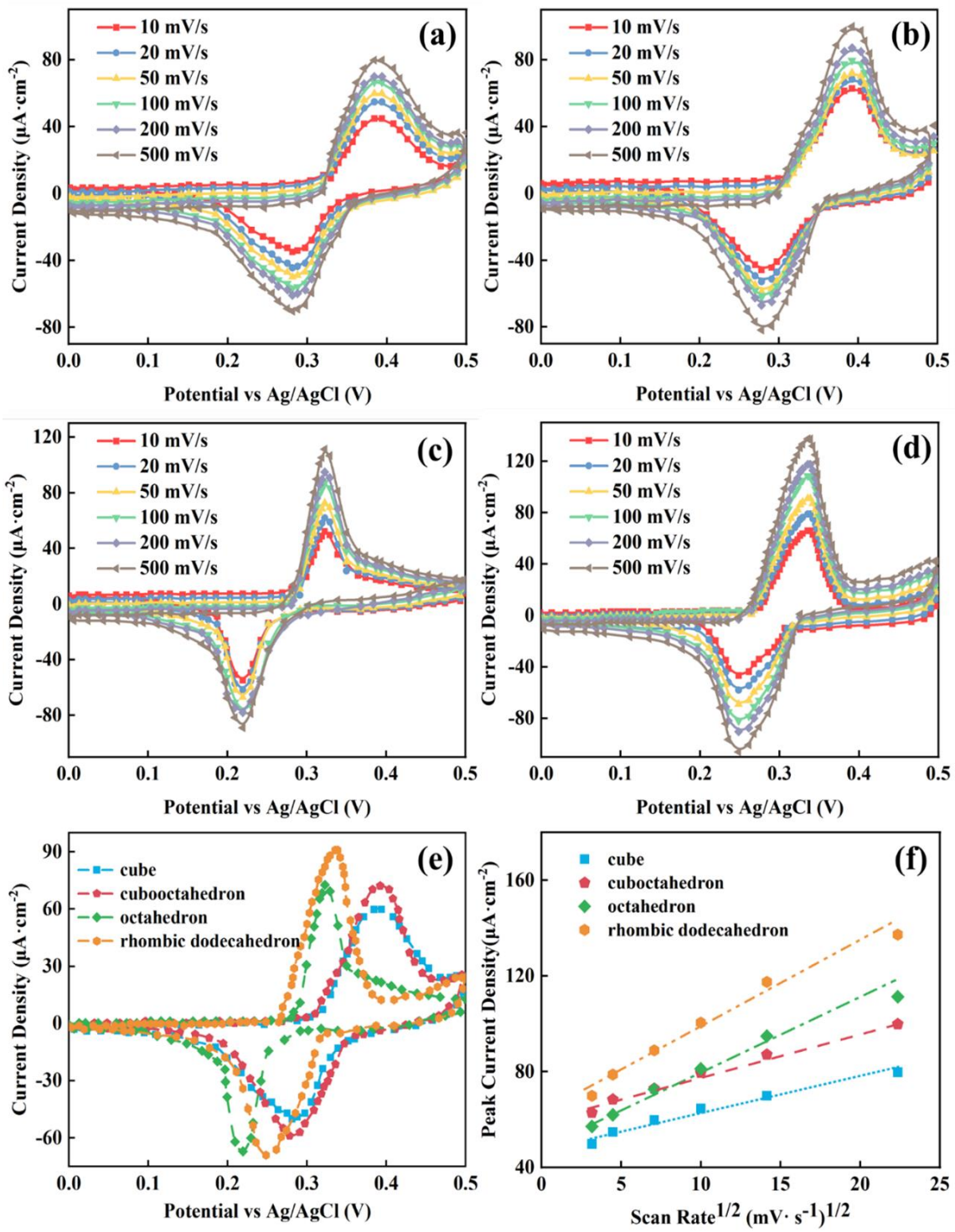

Figure 2.7 Characteristic cyclic voltametric curves of (a) cube, (b) cuboctahedron, (b) octahedron, (d) rhombic dodecahedron under different scan rate (***v***) in 5 mM $K_3[Fe(CN)_6]$ with 0.1 M KCl solution and (e) CV results under 50 mV·s^{-1} of four Cu_2O nanocrystals and (f) The peak current plots versus the square root of scan rates ($v^{1/2}$) (from 10 to 500 mV/s).

The effect of scan rate (***v***) on peak currents of the cyclic voltammograms is also monitored. It is observed that for all the ***v*** studied, the ratio of the cathodic and anodic processes' peak currents is consistently nearing 0.95, indicating the chemical reversibility as expected for the $[Fe(C.N.)_6]^{3-/4-}$ redox process. Furthermore, as shown in **Figure 2.7 (f)**, from 10 to 500 mV/s, peak currents density vs. square root of scan rate ($\boldsymbol{v}^{1/2}$) show good adherence to linearity, demonstrating classical Nernstian diffusion-controlled redox behavior.

Figure 2.8 (**a–e**) shows the EIS complex-plane plots for the four types of Cu_2O nanocrystal-covered Au/Cu electrodes, which were obtained at an open-circuit potential in 5 mM $K_3[Fe(CN)_6]$ with 0.1 M KCl solution in the frequency range from 0.1 to 10^6 Hz. The semicircle portion at high frequencies is due to the electron transfer limited process and the linear portion at lower frequencies results from a diffusion limited process. The distorted semicircle suggests that a double layer could be established at the interface of electrolyte/Cu_2O nanocrystals on Au/Cu electrode. Smaller semicircle usually means faster interfacial charge transfer.).

Figure 2.8 also shows that Cu_2O nanocrystals decorated Au/Cu electrodes possesses smaller semicircle than that after methyl orange (MO) adsorption, which could increase the interfacial electric resistance. To explain these results, the charge transfer resistance (R_{ct}) was obtained by fitting the impedance data to an equivalent electric circuit model (**Figure 2.8e**). **Table 2.6** shows that the R_{ct} value increased from 104.1 ± 0.50 Ω to 112.2 ± 0.36 Ω before and after methyl orange adsorption on the electrode surface covered by the cubic Cu_2O nanocrystals. By contrast, upon deposition of cuboctahedron Cu_2O nanocrystals on the Au/Cu electrode, the R_{ct} value decreased to 89.7 ± 0.10 Ω, indicating

that the increased [111] facet facilitates electron transfer of the interfacial redox reactions. R_{ct} for the rhombic dodecahedron nanocrystal modified Au/Cu electrode further decreased to 70.19 ± 0.18 Ω, suggesting a faster electron transfer at the rhombic dodecahedron Cu_2O nanocrystals interface compared to that for cube, cuboctahedron and octahedron Cu_2O. This result matches the observed facet-dependent photocatalytic properties of Cu_2O nanocrystals, where rhombic dodecahedron with dominant [110] facets was reported to achieve greater efficiency to produce radicals, than octahedron and cube with dominant [111] and [100] facets respectively. The range of n(0.85~0.96) for CPE further supports the hypothesis that these electrode interfaces can be regarded as imperfect capacitors with non-ideal behavior of capacitance, attributed to surface heterogeneity. Moreover, the change ratio [change (%)=(After -Before)/Before] of R_{ct} and *CPE* ($F \cdot s^n$) showed increasing from cube to rhombic dodecahedron which could be ascribed to adsorption ability of MO for four different Cu_2O nanocraystal.

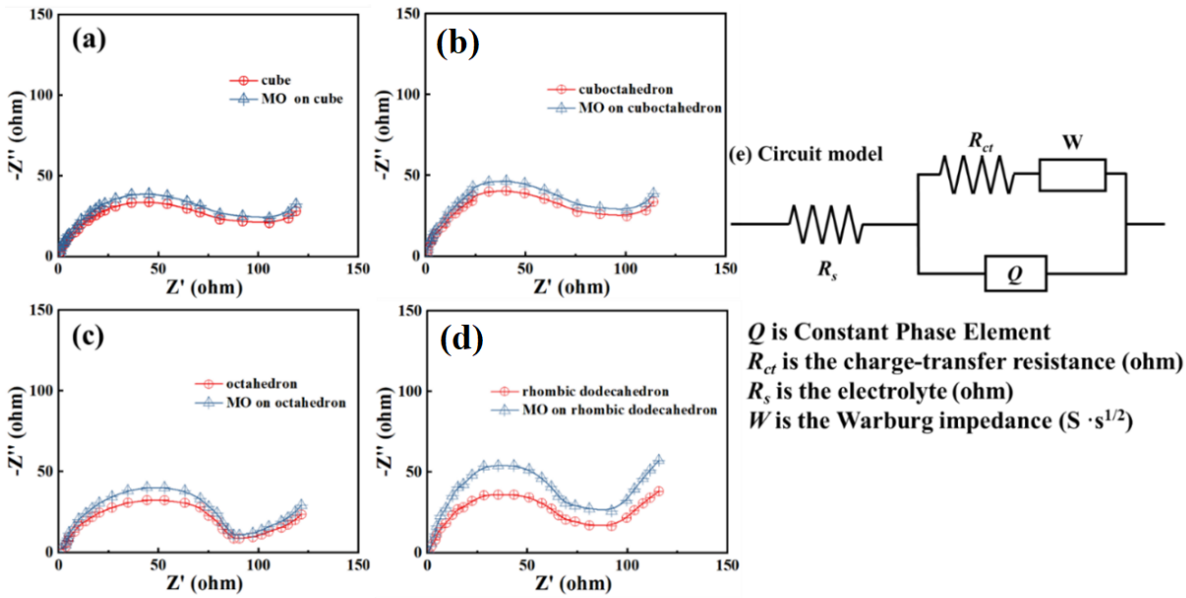

Figure 2.8 Nyquist impedance plots for the pristine Cu_2O nanocrystal-coated electrodes and those after methyl orange (MO)-adsorption: (a) cube, (b) cuboctahedra, (c) octahedra, (d) rhombic dodecahedra and (e) Equivalent circuit used to fit the Nyquist plots obtained via EIS.

2.3.2 Electric and Electrochemical Properties at a Facet Level

2.3.2.1 Measurement of Surface Work Function. First, the work function of the Pt/Ir-coated tip was obtained by measuring the contact potential difference (CPD) between the Pt/Ir-coated tip and the Au [111] substrate, since the Au surface are found to possess a work function of ~5.2 eV. The work function for the AFM probe is 5.5±0.1 eV, which falls in the reported range for Pt (5.12~5.93 eV). To verify this result, we measured the CPD between the probe and HOPG substrate and determiened the work function (Φ_{HOPG}) of ~4.8 eV, which matches the reported range between 4.4 and 4.8 eV. Similarly, the silicon wafer [111] was found to possess a work function of ~4.6 eV that is consistent with the previously reported values between 4.60–4.85 eV. The CPD or work function mapping for different substrate surfaces is shown in **Figure 2.9** with a schematic energy diagram in **Figure 2.9d**. The dotted line indicates the Fermi level of Pt. The cross correlation of data and statistical analysis of the various surface potentials allow us to make a semiquantitative assessment of the work function of the Cu_2O nanocrystals.

Table 2.6 Fitted Results of the Interfacial Charge-Transfer Resistance Parameters in the Equivalent Circuit for Four Cu_2O Nanocrystals Before and After the MO Adsorption

Cu_2O	Parameters	Before adsorption	After adsorption	Change (%)
Cube	R_s (ohm)	5.18 ± 0.14	5.09 ± 0.05	-1.74
	R_{ct} (ohm)	104.1 ± 0.50	112.2 ± 0.36	7.78
	CPE ($F \cdot s^n$)	3.16×10^{-8}	3.56×10^{-9}	-88.73
	n for CPE (1)	0.87	0.85	-2.29
	W ($S \cdot s^{1/2}$)	0.00071	0.00052	-26.76
Cuboctahedron	R_s (ohm)	5.37 ± 0.04	5.66 ± 0.10	5.40
	R_{ct} (ohm)	89.7 ± 0.10	107.7 ± 0.60	20.06
	CPE ($F \cdot s^n$)	3.99×10^{-8}	3.68×10^{-9}	-88.81
	n for CPE (1)	0.868	0.86	-0.92
	W ($S \cdot s^{1/2}$)	0.00083	0.00047	-43.37
Octahedron	R_s (ohm)	5.17 ± 0.02	5.04 ± 0.01	-2.51
	R_{ct} (ohm)	81.54 ± 0.10	99.98 ± 0.60	22.61
	CPE ($F \cdot s^n$)	4.54×10^{-8}	4.37×10^{-9}	-90.37
	n for CPE (1)	0.95	0.86	-9.47
	W ($S \cdot s^{1/2}$)	0.00048	0.00043	-10.42
Rhombic dodecahedron	R_s (ohm)	4.99 ± 0.02	5.05± 0.02	1.20
	R_{ct} (ohm)	70.19 ± 0.18	86.92 ± 0.01	23.83
	CPE ($F \cdot s^n$)	2.07×10^{-7}	1.52×10^{-8}	-92.65
	n for CPE (1)	0.94	0.92	-2.12
	W ($S \cdot s^{1/2}$)	0.00081	0.00073	-9.87

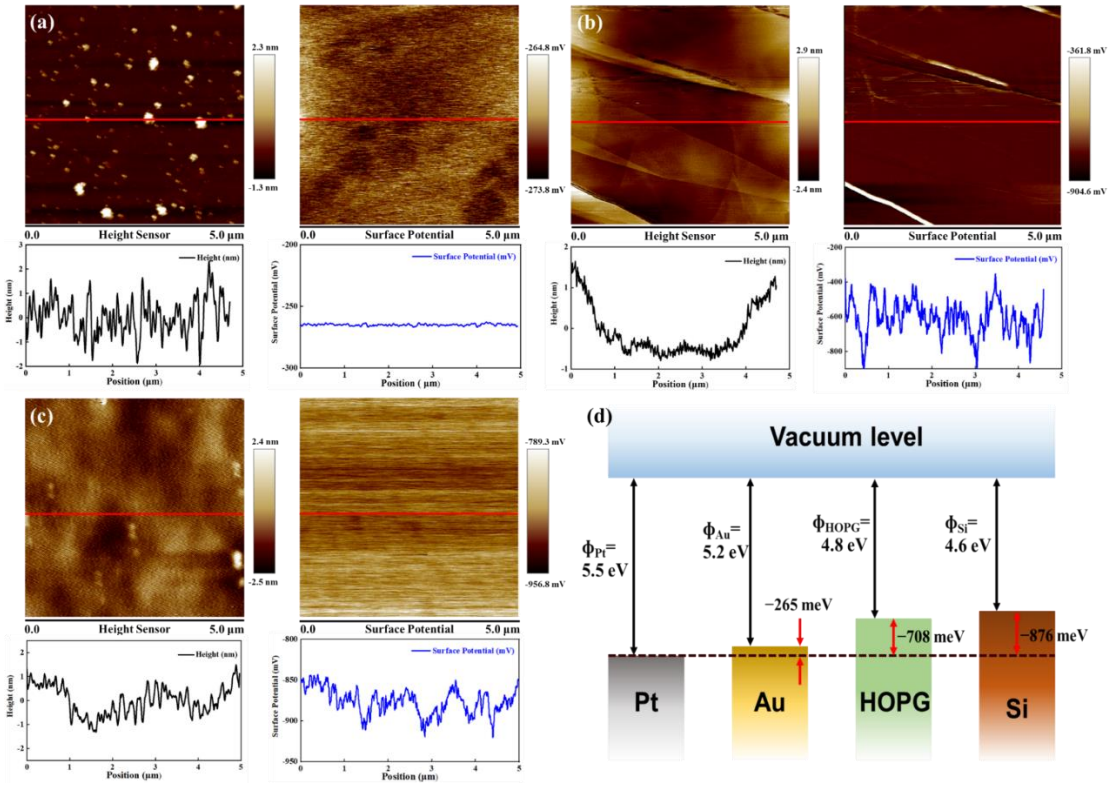

Figure 2.9 High-resolution images of the topography and surface potential of (a) Au surface, (b) HOPG and (c) Silicon [111] wafer. The cross-section profiles of the topography and surface potential were taken along the directions marked with the red dashed lines in each topography and surface potential. (d) Proposed energy band diagram of Pt, Au, HOPG and Si materials.

KPFM was conducted on Cu_2O to reveal the potential different electronic structures or work functions of the [100], [110], and [111] facets. **Figure 2.10** shows the surface potential mapping of different Cu_2O nanocrystals deposited on the silicon wafer. The surface potential of different facets of the Cu_2O nanocrystals can be determined by comparing to the silicon wafer. Based on the analysis of over 15 different samples for each shape, the surface potentials (the CPD levels) correspond to +320±50, +350±70, and +400±58V for the [100], [110], and [111] surfaces, respectively. The corresponding surface work function of [100]-cubic, [110]-rhombic dodecahedral, and [111]-octahedral Cu_2O are 4.92, 4.95, and 5.00 eV, respectively. This result agrees with a study reported by Lee et. al, which indicated that the [100] surfaces and intermediate work functions of the [110] facet

of Cu_2O had the lowest work functions. For the cuboctahedron Cu_2O nanocrystals, we observed a difference between [100] and [111] surfaces of ~80 mV. Comparing with the [100] and [111] facets, the [110] facet possesses the intermediate electronic work function. Practically, the electrochemical processes always combine into two categories: outer-sphere redox processes, where there is little or no physical interaction between the redox species and electrode surface, and where questions relate to the influence of local electronic structure, solvent/electrolyte properties and double layer effects on electrochemical processes, and inner-sphere or catalytic redox processes, where the bonding or adsorption of reactants, intermediates, and/or products to the electrode surface has a profound effect on the electrode reaction kinetics. The DFT simulation results in the following section further investigate that adsorption of reactants on different facets and reveal electrochemical activity of four Cu_2O nanocrystals related to its surface structure (such as DOS and work function) and interaction with probe molecules.

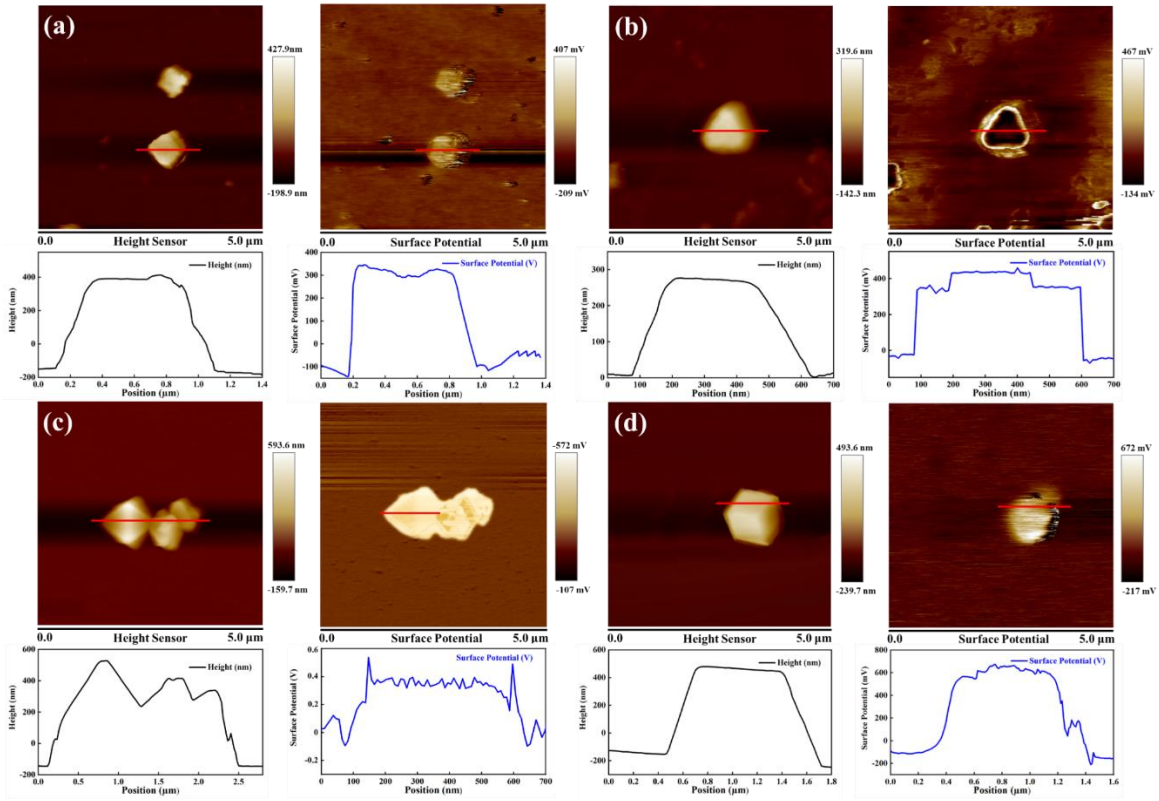

Figure 2.10 KPFM images and corresponding potential for (a) cube, (b) cuboctahedron, (c) octahedron and (d) rhombic dodecahedron Cu_2O nanocrystals.

2.3.2.2 Measurement of Surface Electrochemical Activity of Cu_2O Nanocrystals. AFM-SECM was used to reveal facet/shape-dependent electrochemical properties of Cu_2O nanocrystals immerged in the $[Ru(NH_3)_6]Cl_3$/KCl solution. The topography and tip-sample current images of four types of Cu_2O nanocrystals are presented in **Figure 2.11**. The right column of **Figure 2.11** shows that when the tip approaches or sweeps over the Cu_2O nanocrystals, a higher tip-sample current was achieved. The tip current was generated due to the reduction reaction of $[Ru(NH_3)_6]^{3+}$ to $[Ru(NH_3)_6]^{2+}$ with a DC bias potential at -0.4 V applied to the tip as depicted in **Figure 2.12e**. When the tip approaches the sample surface, the enhanced tip current mainly results from a reaction loop, where the sample surface under a positive DC bias (+0.1 V) enabled oxidation of $[Ru(NH_3)_6]^{2+}$. The oxidized

product then diffused to the tip for reductive reactions, which led to a higher tip current. By contrast, the silicon substrate, though under the same positive DC bias, did not exhibit the same oxidative reactivity toward $[Ru(NH_3)_6]^{2+}$ and thus generate relatively low tip current enhancement.

Furthermore, the tip-sample current exhibited slight dependence on the shape or exposed dominant facets of Cu_2O nanocrystals. Cube, cuboctahedron, octahedron and rhombic dodecahedron of Cu_2O nanocrystals yielded an average tip current of 205.4, 233.4, 279.4 and 318.3 pA, respectively, at the same tip-sample distance of 100 nm. The observed tip current variations could be attributed to the effects of different facet surfaces or surface states (e.g., work functions and electrolyte/electrode interactions) that are further analyzed by DFT. For instance, the diffusion and concentration profile or distribution of the redox mediator from the bulk solution to the probe tip could be affected by the interactions of mediator molecules and facet surfaces. The interplay or overlapping of the two electric double layers of the samples and the probes affects the diffusion transport of the redox mediators and ultimately the redox reactions at the tip (or tip current). For example, the local concentration profile of $[Ru(NH_3)_6]^{3+}$ was reported to be influenced by the tip-sample interactions and could vary with the tip-sample distance, which can be estimated under the approximation of a semi-infinite spherical diffusion:

$$C_d = C_0(1 - \frac{2.3r_{tip}}{d + 2.3r_{tip}}) \tag{2.6}$$

where C_d is the surface concentration at a tip-sample distance (d) following the central axis as shown in **Figure 2.12a**.

Figure 2.12 evaluates the changes of tip current and redox mediator concentration around the tip surface. When the probe was far away (e.g., 1 mm) from an insulating

substrate (**Figure 2.12a**), a constant tip current of 718 pA was calculated using extended Butler–Volmer equation with releant parameters shown in **Table 2.7.** This tip current is also called a steady-state current ($i_{tip,\infty}$), which is acquired when the tip is placed far away from the sample. When the probe is positioned at a distance of greater than 10 times r_{tip}, the probe will be considered to stay in the bulk solution or far away from the sample surface and the measured tip current i_{tip} is equal to the steady-state current $i_{tip,\infty}$. **Figure 2.12b** shows the concentration profile of the redox mediator when the tip was 10 nm away from the insulating surface. The resulting tip current decreased from 718 to 434 pA because inert surface hinder diffusion of redox mediator to the tip by the substrate. **Figure 2.12c** shows that on a conducting substrate under a potential suitable to drive the oxidation reaction bias (+0.2 V), a positive feedback mode is achieved, where the $[Ru(NH_3)_6]^{3+}$ is reduced on the tip and returned to $[Ru(NH_3)_6]^{3+}$ near the conducting substrate. Consequently, the tip current increased from 748 to 1193 pA at the same tip-sample distance of 10 nm. To confirm the dependence of tip current on the tip-sample distance, we measured the tip currents on Au coated Si sample surface at different tip-sample distances (20, 50, 100, 150 and 200 nm). **Figure 2.12d** shows the effective surface concentration (C_d) of the redox mediator calculated by Equation (2.7) using the obtained tip currents.

$$i_{tip,\infty} = 4nDFC_0 r_{tip}\beta \tag{2.7}$$

where the value of $i_{tip,\infty}$ depends linearly on the mediator concentration and the tip radius for a conductive probe with a disk geometry, n is the number of the electrons transferred (n=1), D is the diffusion coefficient of the redox species in solution (3.52×10^{-4} $cm^2\cdot s^{-1}$), F is the faradaic constant (96,485 $C\cdot mol^{-1}$), C_0 is the effective concentration of mediator near

the electrode surface (e.g., 10 mM $[Ru(NH_3)_6]Cl_3$ in 0.1 M KCl), and β is a geometrical factor. If the tip is conical, then β can be calculated by:

$$\beta = 1 + \frac{0.23}{(R_g^{\ 3} - 0.81)^{0.36}} \tag{2.8}$$

Here, R_g is a geometrical factor, which is the radius of the insulating sheath (r_g) divided by the radius of the probe (r_{tip}). Thus, $R_g = r_g / r_{tip}$ (r_g =390 nm and r_{tip} =25 nm).

Table 2.7 Parameters for COMSOL Simulation

Parameters	Value	Unit
Exchange current density (J)	0.5	$A \cdot m^{-2}$
Electrode potential (E)	-0.4	V
Equilibrium potential (E_{eq})	-0.1	V
Absolute temperature (T)	293	K
Number of electrons involved in the reaction (z)	1	unitless
Faraday constant (F)	96485	$C \cdot mol^{-1}$
Universal gas constant (R)	8.314	$J \cdot K^{-1} \cdot mol^{-1}$
Reduction charge transfer coefficient (α_c)	0.5	unitless
Oxidation charge transfer coefficient (α_a)	0.5	unitless
Activation overpotential (η)	-0.3	V

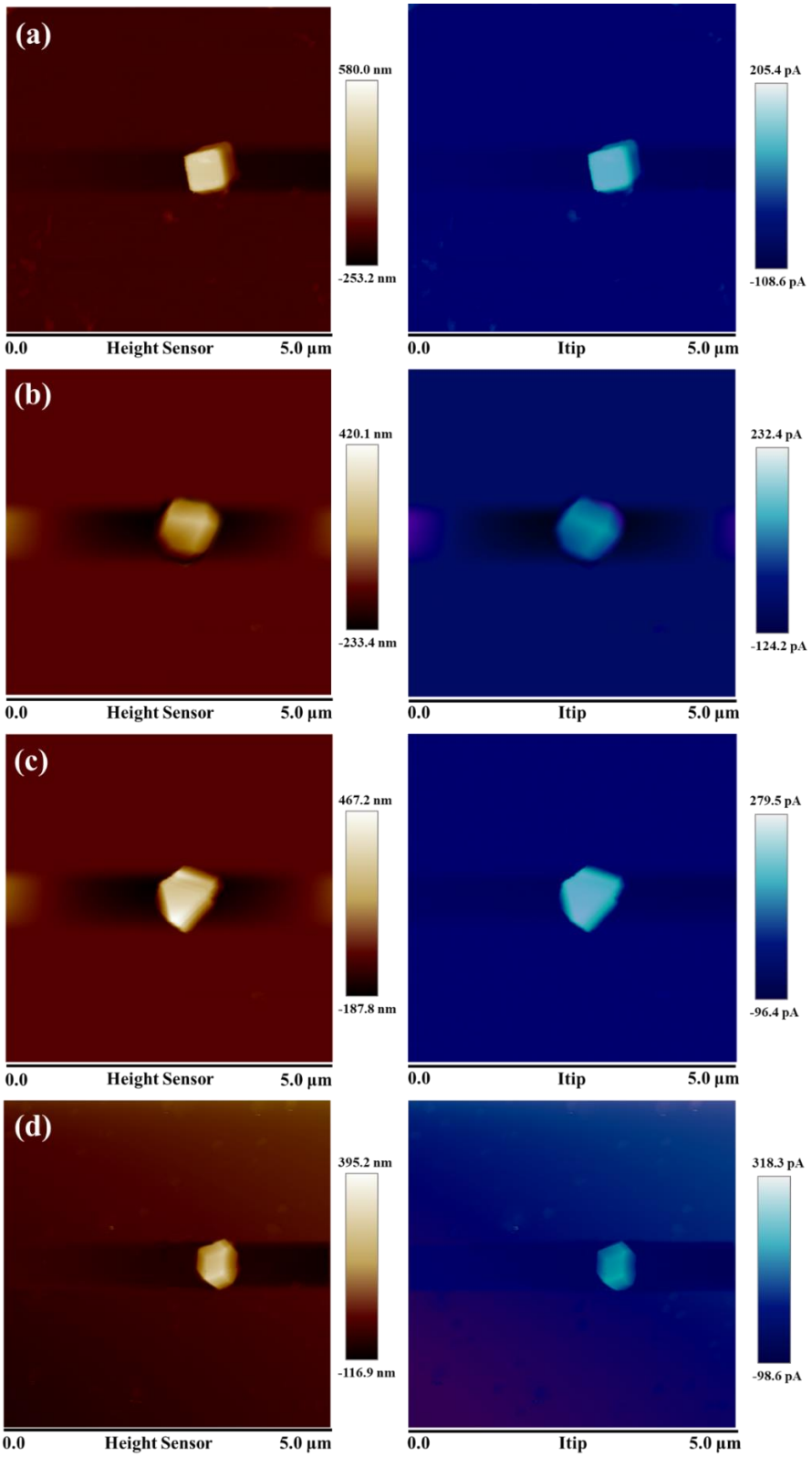

Figure 2.11 Typical topography and tip-sample current images of (a) cube, (b) cuboctahedron, (c) octahedron and (d) rhombic dodecahedron Cu_2O nanocrystals.

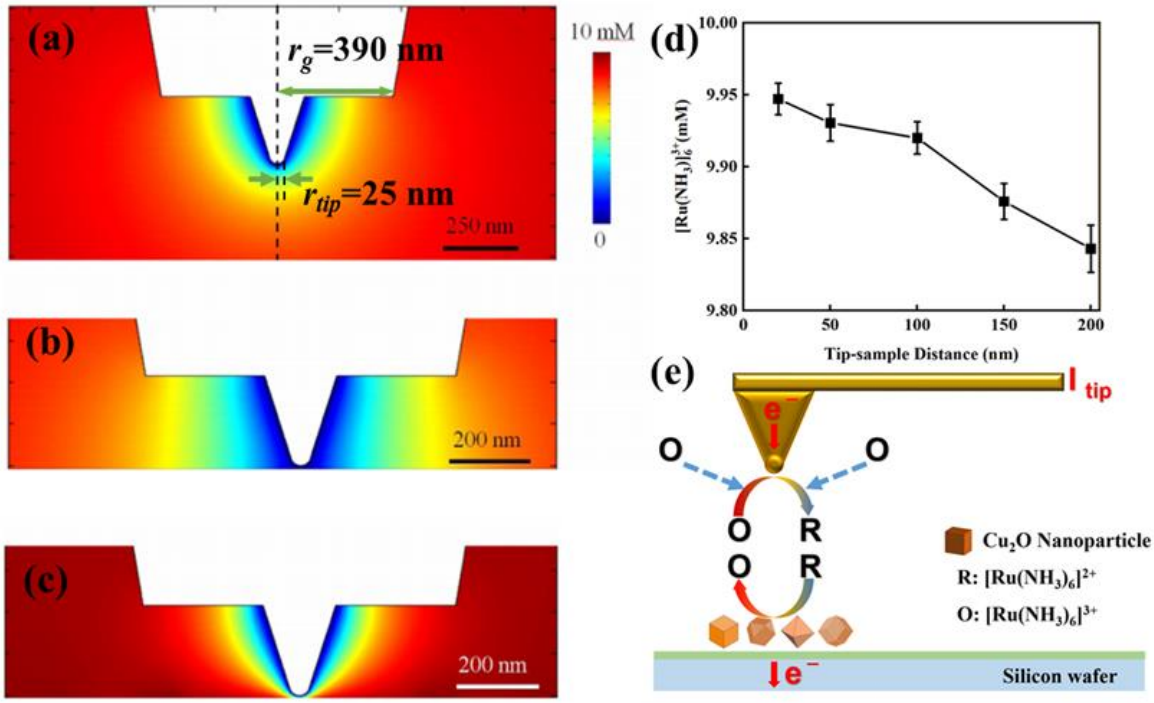

Figure 2.12 Simulation of the concentration profile of 10 mM $[Ru(NH_3)_6]^{3+}$ in 0.1 M KCl electrolyte near the nanoelectrode probe. (a) The probe is 1 mm away from an insulating substrate, (b) and (c) The probe is 10 nm away from an insulating substrate and a conducting substrate, respectively. (d) Different surface concentrations (C_d) on the tip calculated from the tip currents measured at different tip-sample distances. (e) Schematic of the electrochemical reactions at the tip and the sample surface.

2.3.3 DFT Analysis of Facet Properties of Cu_2O Nanocrystals

2.3.3.1 Surface Energy and Work Function. With different facets exposing different surface atoms, tuning Cu_2O morphology correspondingly controls its surface chemistry and reactivity. This is important when considering the (intrinsically linked) structural and electronic factors that contribute to binding target molecules. Depending on the atomic coordination and structural configuration of Cu_2O surfaces, different proportions of cations and anions are accessible for reactant adsorption, thus greatly influencing the charge transfer between sorbent and sorbate and affecting the type and strength of binding and generation of products or reactive species. Furthermore, different atomic coordination results in distinct electron density configurations, also influencing the type and strength of

binding as well as band gap energies and positions. Because these electronic and binding characteristics and behaviors govern the mechanisms in sorption-dependent fields such as heterogeneous catalysis, gas sensing, or molecular reactions.

The three low-index Cu_2O surfaces: [100], [110] and [111], were constructed with each terminated in two ways as illustrated in **Figure 2.13**. The surfaces are denoted first by the facet followed by the species of the terminating atoms; for example, the Cu-terminated [100] facet is denoted as [100]:Cu, the CuO-terminated [110] facet is denoted as [110]:CuO and the O-terminated [111] facet is denoted as [111]:O. We have calculated the surface energies and work function of the six different surface terminations as shown in **Table 2.8**. The surface energy of [100]:Cu and the [100]:O are similar (1.12 and 1.05 $J \cdot m^{-2}$, respectively). Only O atoms are terminated in the [100]:O facet, which has a slightly lower surface energy than the Cu terminated facet. The [110]:Cu and [110]:Cu–O are the most two reactive surfaces with surface energy of 2.12 and 2.09 $J \cdot m^{-2}$. Finally, we found that a surface energy of 1.87 $J \cdot m^{-2}$ for the [111]:O surface that is lower than that of [111]:Cu (2.01 $J \cdot m^{-2}$), which agrees with the result reported by Soon et al. It is well established that the surface energy is closely related to the density of under-coordinated Cu atoms, a trend that we observe here. The [110] surface contains both doubly coordinated Cu atoms and undercoordinated, singly coordinated Cu atoms, with dangling bonds perpendicular to the surface. The [111]:Cu surface similarly exposes both Cu atoms and O atoms, but the density of dangling bonds is much less than the [110] surface. The surface energies of Cu_2O generally follow the density of undercoordinated Cu atoms, [100] < [111] < [110]. A higher surface energy typically indicates a more reactive surface and therefore the highest surface energy of each facet correlates with the observed adsorptive

performance of the Cu_2O nanocrystals, as measured on the cubic [100] crystals, octahedral [111] crystals, and rhombic dodecahedral [110] crystals.[79]

Understanding of the electronic structure of a material is essential for its potential technological applications in numerous devices as it provides a comprehensive description of the optical, electronic and thermoelectric properties. To further determine the surface electronic structure of the three Cu_2O nanocrystals, we calculated the electronic work functions and the electronic band gaps by the slab models of the three facets. The work function is a direct consequence of the electrostatic barrier induced by the dipole double layer at the surface. The presence of highly electronegative atoms, such as oxygen, at the surface increases the contribution of the dipole double layer to this electrostatic barrier, making it harder for an electron to leave the surface. This is reflected in the work functions of both the [100]:O and [110]:Cu-O structures, which have values significantly higher than that of only Cu-terminated surfaces (although the work functions of [111]:Cu and [111]:O are similar). Conversely, the work function of the [110]:Cu structure is smallest in value when compared to that of the other surface which may result in better activity owing to the increased ease of electron transfer.

The electronic band gaps (E_g) of the different surfaces are determined from the density of states (DOS) as the difference between the valence band maximum (VBM) and conduction band minimum (CBM), and the band gap energies for three low-index Cu_2O surfaces with different termination are listed in **Table 2.8**. The [110]:Cu facet has the smallest bandgap due to the unsaturated Cu atoms at the surface giving rise to some gap states which are considered to be the active sites in catalytic reaction. With the decrement

of undercoordinated Cu atoms the bandgap energies increase, which is well consistent with previous findings.

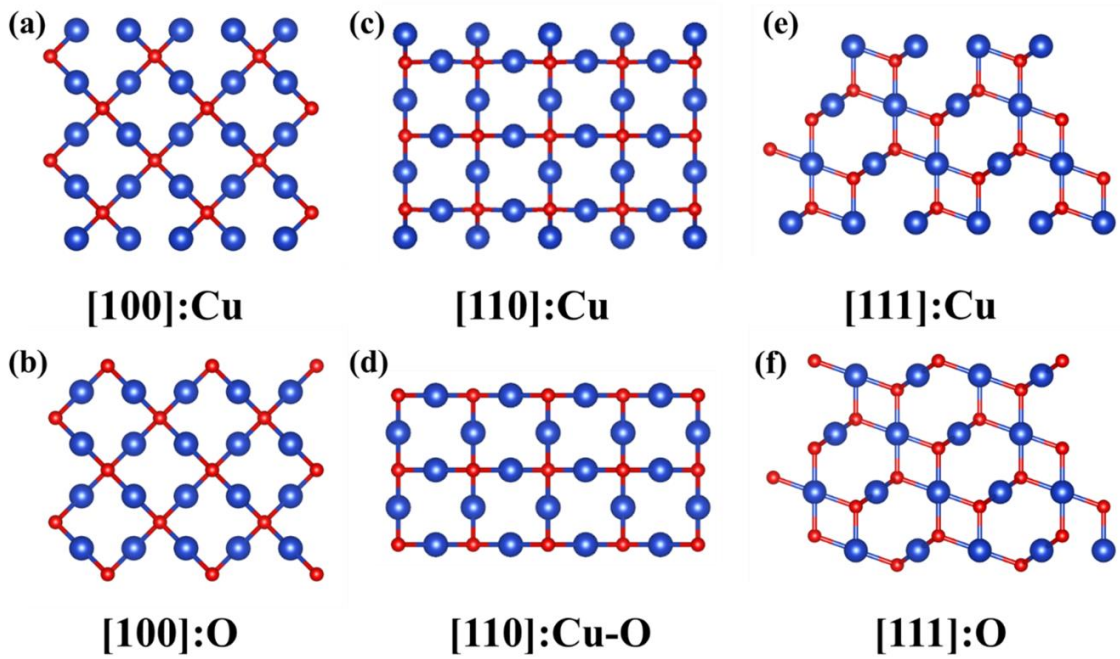

Figure 2.13. Relaxed Cu_2O surfaces. Blue and red balls indicate Cu and O atoms respectively.

Table 2.8 Calculated Relaxed Surface Energies (γ_r), Work Functions (Φ), and the Bandgaps (E_g) of Different Cu_2O Surfaces, the Bandgaps (E^*_g) of the $[Ru(NH_3)_6]^{3+}$ Adsorption on Different Cu_2O Surfaces

Surface	γ_r ($J \cdot m^{-2}$)	Φ (eV)	E_g (eV)	E^*_g (eV)
[100]:Cu	1.12	4.48	0.46	0.14
[100]:O	1.05	5.58	0.97	0.56
[110]:Cu	2.12	3.93	0.16	0.27
[110]:Cu-O	2.09	5.66	1.25	0.36
[111]:Cu	2.01	4.82	0.59	0.32
[111]:O	1.87	4.67	0.49	0.45

2.3.3.2 Density of States. We investigated the electronic density of states (DOS) with Fermi-level set to zero of those six Cu_2O surfaces. The calculated projected DOS shows that both valence band maxima (VBM) and conduction band minima (CBM) mainly consist of O (p) and Cu (d) orbitals, respectively, while contributions from other orbitals

are much less. In the DOS for [100]:Cu (**Figure 2.14a.**), the unsaturated Cu atoms at the surface give rise to some gap states which are considered to be the active sites in catalytic reaction. DOS plots for [100]:O planes show semiconducting band structures. We observed a finite number of states near the Fermi level in the electronic DOS of the [110]:Cu and hence propose that this surface is conducting. The calculated electronic DOS for [110]:Cu–O terminations also exhibits the semiconducting band structures. We calculated the electronic DOS for both terminations and found that the bandgaps for the [111] surfaces are quite low; these two surfaces are also found to be semiconducting. Soon et al. employed the technique of "ab initio atomistic thermodynamics" to identify the surface structures of the [110] and [111] planes, and found that both of them exhibit a metallic character, but their electronic structures are rather different. The [111] plane structure's metallic character is largely bulk-like in nature, whereas that of the [110] plane structure is truly surface like, which may result in better catalytic activity related to the "Cu" dangling bonds of the [110] surfaces.

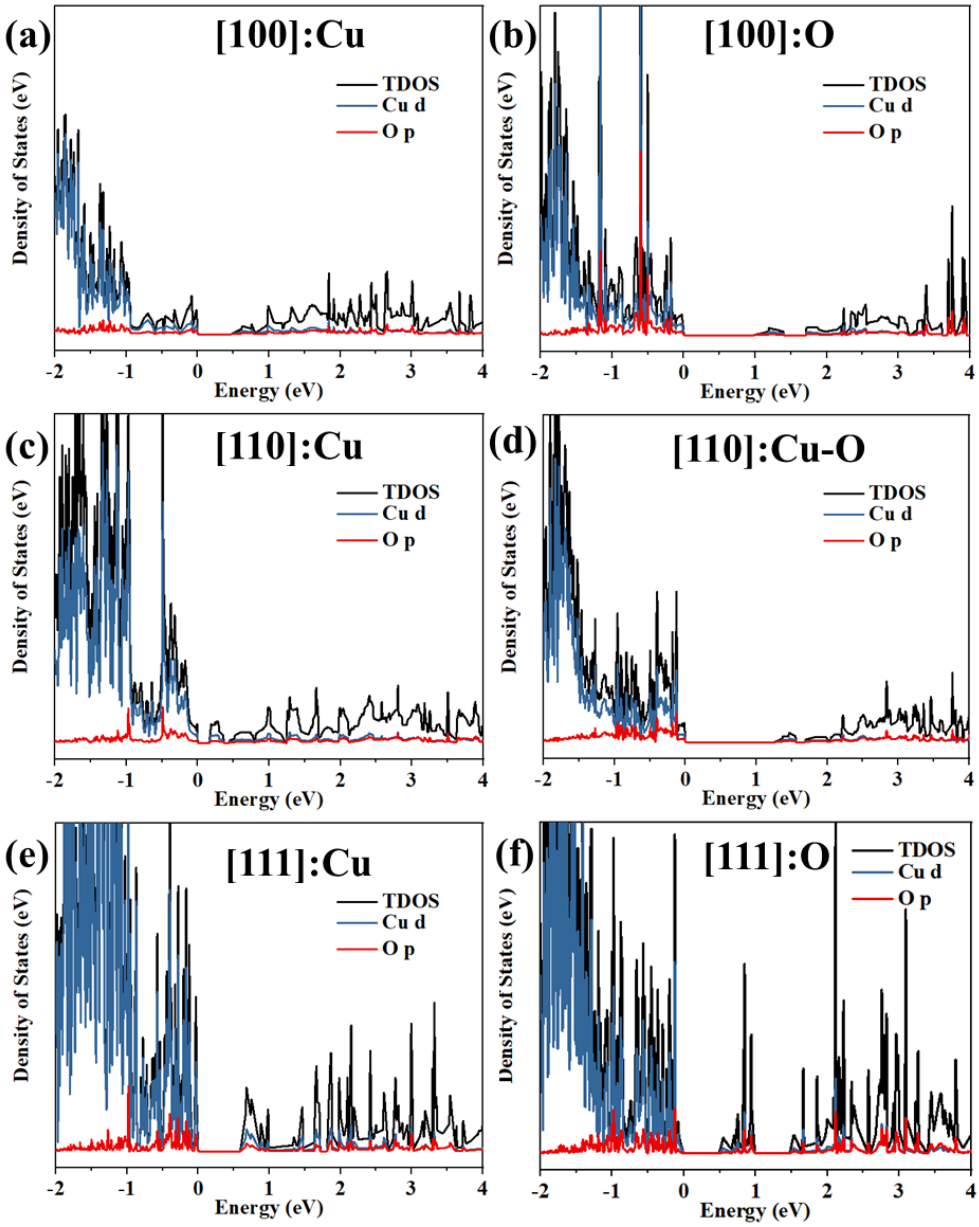

Figure 2.14. Electronic DOS of Cu_2O (a) [100]: Cu, (b) [100]: O, (c) [110]: Cu, (d) [110]: Cu–O, (e) [111]: Cu and (f) [111]: O terminated surfaces.

2.3.3.3 Adsorption energy. To gain further insights into the morphology–electrochemical activity relationship of Cu_2O, we have conducted a series of DFT calculations to address the adsorption mechanism of molecular Hexaammineruthenium (III) cation ($[Ru(NH_3)_6]^{3+}$) on the Cu_2O [100], [110] and [111] surfaces. Ruthenium hexamine ($[Ru(NH_3)_6]^{3+/2+}$) is one of commonly used redox couples for aqueous electrolytes. Its one electron redox process

is a good representation of the fictive species Oxidation and Reduction. The redox couple comes in the form of aqueous solutions from ruthenium hexamine (III) chloride or ruthenium hexamine (II) chloride, with the first one the more common choice. The most stable adsorption configurations are shown in **Figure 2.15**. The adsorption energies are also given in **Table 2.9**. The values of adsorption energies for all of the three crystal facets were negative, suggesting the adsorption processes are exothermic and spontaneous.

We noted that the adsorption energy, E_{ads}, correlates strongly with the surface energy, as shown in **Table 2.8**. The smallest surface energy [110]:Cu-O surface shows weak adsorption, while the largest surface energy [110]:Cu surface shows the strongest binding. Bandgaps of $[Ru(NH_3)_6]^{3+}$ adsorbed on Cu_2O surfaces are shown in **Table 2.8.** The adsorption of $[Ru(NH_3)_6]^{3+}$ will narrow the bandgap mainly due to the presence of the N (p) impurity state, which can be found in the DOS of each Cu_2O surface after $[Ru(NH_3)_6]^{3+}$ adsorption.

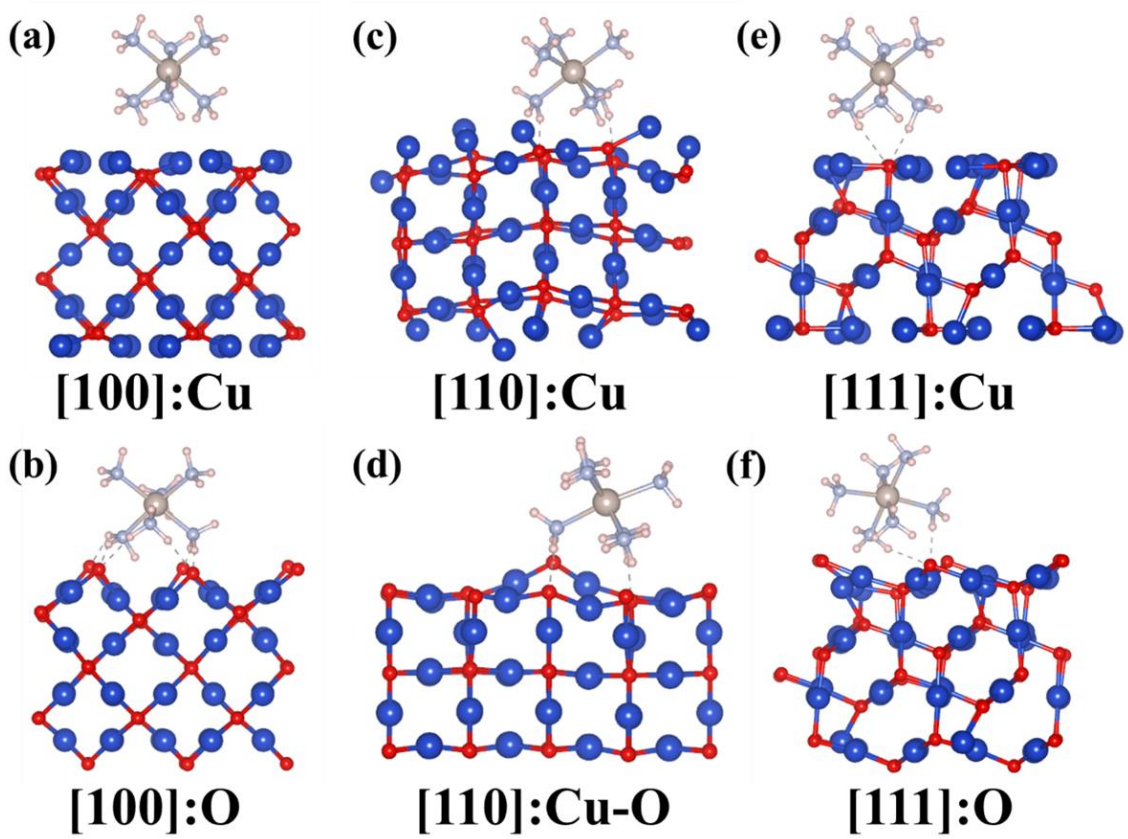

Figure 2.15. $[Ru(NH_3)_6]^{3+}$ cation on Cu_2O surfaces. Blue, red, gray, light blue, pink balls indicate Cu, O, Ru, N and H atoms, respectively.

Table 2.9. Adsorption Energies (E_{ads}) of the H_2O and $[Ru\ (NH_3)_6]^{3+}$ Adsorption on Different Cu_2O Surfaces and the Charge Transfer between $[Ru(NH_3)_6]^{3+}$ Cation and Different Cu_2O Surfaces.

Surface	E_{ads} (H_2O) (eV)	E_{ads} ($[Ru\ (NH_3)_6]^{3+}$) (eV)	Charge transfer (e)
[100]:Cu	−1.28	−4.21	−0.76
[100]:O	−1.72	−4.86	−0.70
[110]:Cu	−2.95	−9.93	−1.11
[110]:Cu-O	−0.75	−4.44	−0.49
[111]:Cu	−1.77	−4.10	−0.58
[111]:O	−1.80	−4.59	−0.52

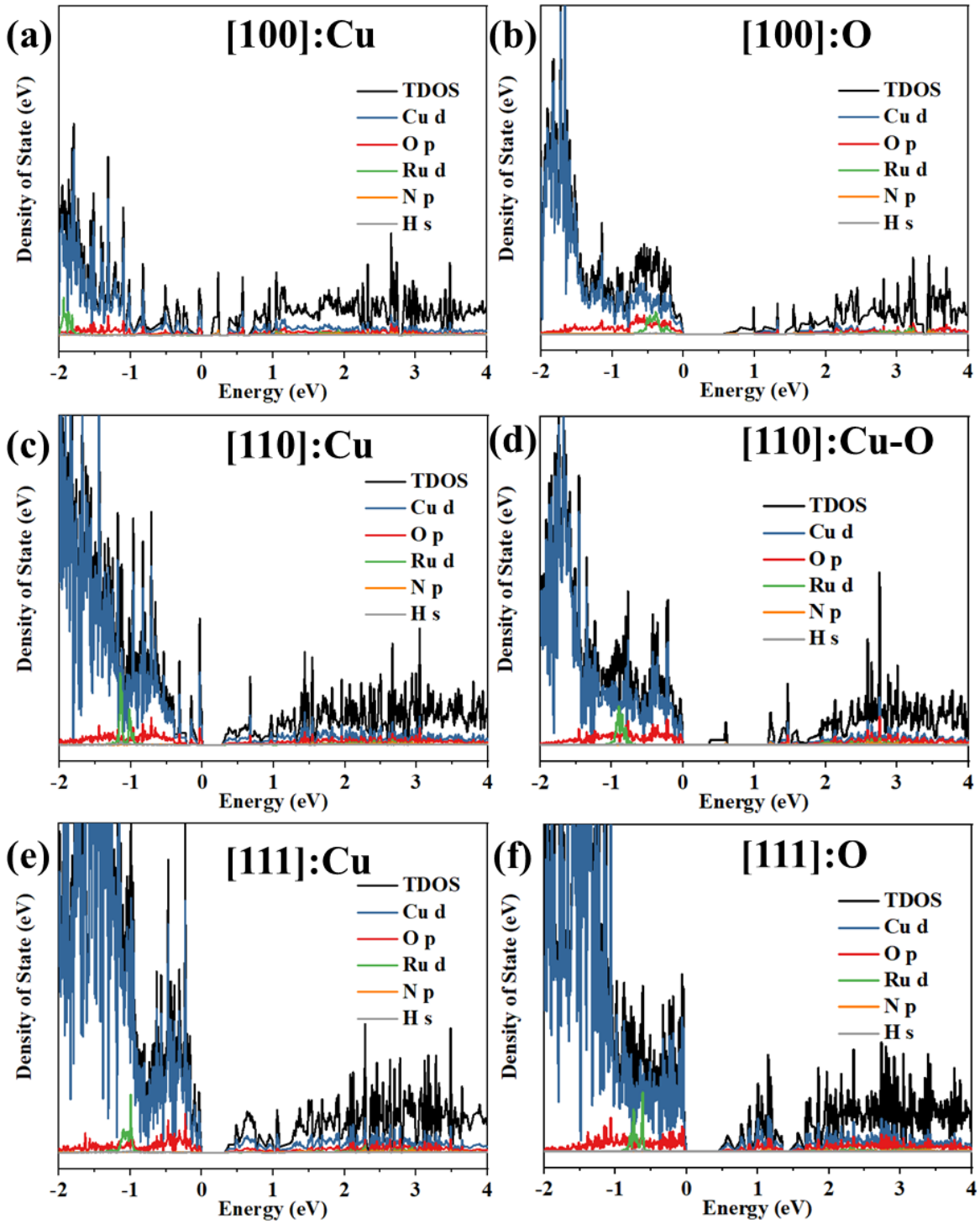

Figure 2.16. Electronic DOS of $[Ru(NH_3)_6]^{3+}$ adsorption on Cu_2O (a) (100): Cu, (b) (100): O, (c) (110): Cu, (d) (110): Cu–O, (e) (111): Cu and (f) (111): O terminated surfaces.

2.3.3.4 Bader Charge Analysis. To further investigate the electronic interactions between $[Ru(NH_3)_6]^{3+}$ cation and different crystal facets of Cu_2O, the charge transfer was also

calculated for the adsorption of $[Ru(NH_3)_6]^{3+}$. There is obvious electron injection from different Cu_2O surfaces to $[Ru(NH_3)_6]^{3+}$ cation (see **Figure 2.17**). The amount of charge transfer is listed in **Table 2.9**; it is found that the strength of electronic interaction between $[Ru(NH_3)_6]^{3+}$ cation and different crystal facets follows the order of [110] facets > [111] facets > [100] facets. The more charge transfer between $[Ru(NH_3)_6]^{3+}$ cation and these surfaces, the stronger the electronic interactions that form, which will lead to better catalytic activity. In this regard, [110] facets may be more suitable for $[Ru(NH_3)_6]^{3+}$ cation adsorption compared with that of [100] and [111] facets. The results may explain the significantly distinct effect of $[Ru(NH_3)_6]^{3+}$ cation decoration on the electrochemical catalytic performance of the different Cu_2O support in our work.

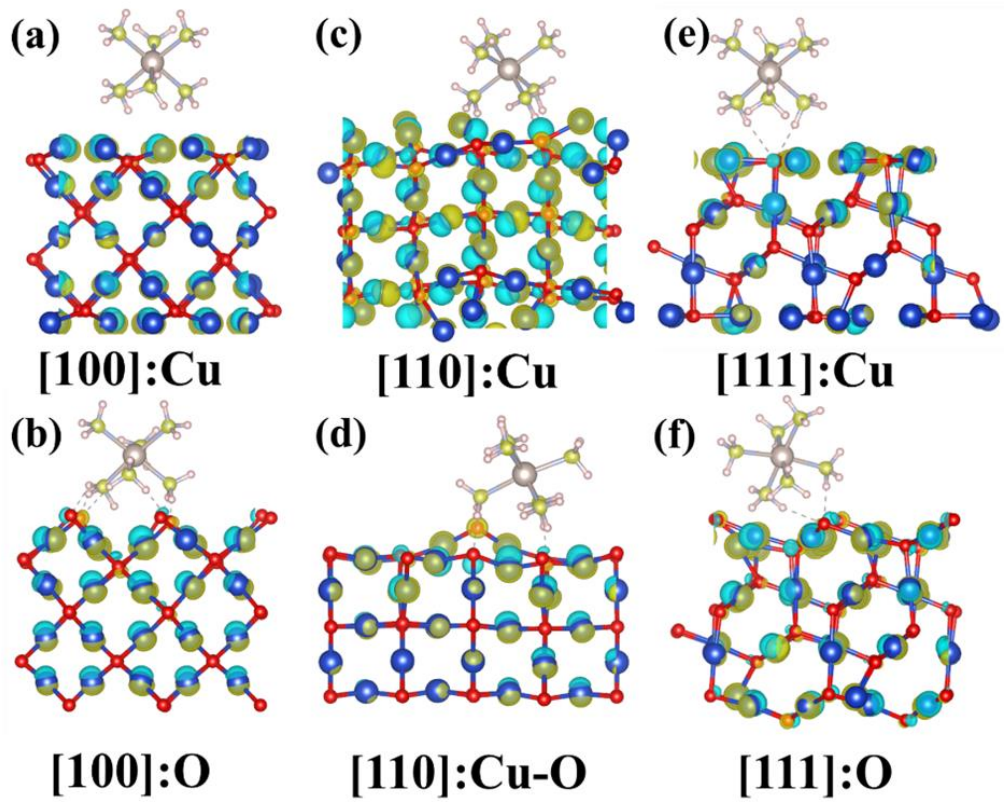

Figure 2.17. Three-dimensional charge density difference maps of $[Ru(NH_3)_6]^{3+}$ cation on Cu_2O surfaces. The regions of charge depletion and charge accumulation are represented by the blue and yellow lobes. Blue, red, gray, light blue, pink balls indicate Cu, O, Ru, N and H atoms, respectively.

In comparison with Cu_2O with [100] and [111] facets, rhombic dodecahedra Cu_2O with [110] facet exhibited relative larger adsorption capacity and adsorption energy, further leading different electrochemical performance. The [110] faces are higher in surface energy and expected to be more catalytically active than the [100] and [111] facets. Furthermore, Cu_2O crystals bounded by the [110] facet contain positively charged copper atoms at the surfaces, whereas those bounded by the [100] faces such as the cubes are electrically neutral.

2.4 Conclusion

In this work, for the first time, *in situ* AFM-SECM demonstrated the nanoscale level probing of the facet dependent electrochemical properties of Cu_2O nanocrystals. AFM−SECM multidimensional imaging on the four different morphology particles unveiled the correlation between facets in Cu_2O nanocrystals and AFM electrochemical images. We employed traditional electrochemical measurement including cyclic voltammetry and electrochemical impedance spectroscopy, and KPFM to improve the addressability of understanding facet dependent electrochemical properties of Cu_2O nanocrystals, however the results do not identify all possible causes and more work is needed to elucidate the mechanisms that facet-dependent activities of different morphology nanoparticles. Lastly, DFT calculations evidenced that the higher surface energy and efficient electron transfer on [110] facet responsible for the higher electrochemical responses. AFM-SECM provides high spatiotemporal resolution, which shows promising potential in the area of energy materials, single-cell imaging, and analysis.

CHAPTER 3

NANOSCALE HYDROPHOBICITY AND ELECTROCHEMICAL MAPPING PROVIDES INSIGHTS INTO FACET DEPENDENT SILVER NANOPARTICLE DISSOLUTION

3.1 Introduction

Morphologies such size and shape largely influence the physicochemical properties of many metal nanomaterials. For example, gold (Au), palladium (Pd), and platinum (Pt) nanomaterials in different shapes such as rods, wires, plates, tetrahedrons, shells, cubes, spheres, stars, and octahedrons have been widely explored in biomedicine, catalysis, surface plasmon resonance, surface-enhanced Raman scattering (SERS), and optoelectronic devices. Silver nanoparticles (Ag NPs) are probably the most widely used commercial nanomaterials, which have increasingly been incorporated in textiles, food containers, cosmetics, toys and medical devices as antimicrobial agents. The amicrobial activity of Ag NPs is largely attributed to the release of silver ions and internalization of Ag NPs that could both bind to thiol groups and disrupt cellular functions. Dissolution of Ag NPs usually occurs through oxidation of metallic silver into silver ions. This process is highly affected by intrinsic physicochemical properties (surface coating, shape and size) and extrinsic conditions such as the solution ionic strength, pH, dissolved oxygen concentration, temperature and dissolved complexing ligands. Studying the dynamic dissolution and ion release process of nanostructured silver and other metallic nanomaterials endows us the opportunity to comprehend the structure-activities relationships and the elicited antimicrobial properties.

Recent studies have explored the toxicity of Ag NPs to a variety of organisms such as plants, algae, fungi, microorganisms, and human cells. The negative impacts of Ag NPs

on the environment and potentially humans may be long lasting and have been recently reviewed. While all of the mechanisms by which Ag NPs elicit a toxic effect remain unclear, it is generally considered that the toxicity of Ag NPs is at least partly driven by Ag^+ ion release. Even if Ag^+ release is only one of many pathways by which Ag NPs elicit toxicity, dissolution remains an important process that alters nanoparticle properties and is thus a critical aspect of Ag NP safety.

Most prior studies examined the dissolution of Ag or other metallic nanoparticles at ensemble level by tracking particle size or shape changes and the released silver ion concentrations. The commonly employed techniques include ultraviolet−visible spectroscopy (UV−vis), dynamic light scattering (DLS), nanoparticle tracking analysis (NTA), inductively coupled plasma−mass spectrometry (ICP−MS), transmission electron microscopy (TEM) and atomic force microscopy (AFM). The relevant results show that the shape and size of Ag NPs both affect the Ag^+ ion release and cytotoxicity. For example, the dissolution of spherical and prism Ag NPs has been evaluated scanning transmission electron microscopy and atomic absorption spectroscopy, the results showed Ag prisms has the faster dissolution than Ag sphere due to its higher surface energy. The aggregation of Ag NPs also decreased the available surface reactivity by at least an order of magnitude and consequently decreased the dissolution rate. Thus, it is critical to accurately unravel the dissolution process of Ag NPs at a single-particle level and eliminate the effects of aggregation and other factors. Atomic Force Microscopy-Scanning Electrochemical Microscopy (AFM-SECM) has been demonstrated as a powerful tool in material science for imaging composite material surfaces exhibiting electrochemically active sites, such as dimensionally stable anodes, noble metal nanoparticles, functionalized electrodes, and soft

electronic devices. AFM-SECM, which directly reveals the local electrochemical information by isolating a nanoscopic portion of the electrode for the electrochemical measurement, holds promising potential to unveil fundamental interfacial properties or activity at nanoscale.

This study aims to elucidate the fundamental mechanisms of dissolution for Ag NPs of three different shapes (nanocube, nanorod, and octahedron) and to determine the facet/shape dependence. The facet/shape effects of Ag NPs on dissolution kinetics were examined by measuring the hydrophobicity and electrochemical activity at local surfaces of Ag NPs using novel approaches. For example, local surface hydrophobicity as a measure of the affinity toward water molecules was mapped to analyze the dissolution sites on different shaped Ag NPs. Furthermore, local reactive sites of Ag NPs were probed by AFM-SECM, which allows us to detect tip-sample currents at a sensitivity of $nA \cdot V^{-1}$ due to the reactivity differences of local facets of Ag NPs. To explain the observed facet-dependent dissolution behavior, density functional theory (DFT) calculations and COMSOL simulations were conducted. The ab initio molecular dynamics (AIMD) simulations were investigated to analyze the stability Ag facets, which aims to provide new insights into the dissolution of Ag nanoparticles and support functional nanomaterial design.

3.2 Materials and Methods

3.2.1 Preparation and Characterization of Ag NPs of Different Shapes

Silver nitrate, sodium chloride, Iron (III) 2,4-pentanedionate, poly(vinylpyrrolidone) (PVP, MW 55000 $g \cdot mol^{-1}$) and anhydrous ethylene glycol were purchased from Fisher Scientific,

USA. All reagents were used as received without further purification. Ultrapure water (Millipore, 18.2 MΩ·cm) was used to prepare all solutions.

Ag NPs are commonly synthesized using a polyol synthesis method that involves the heating of a polyol solution with a salt precursor and a polymeric capping agent to generate metal colloids. To synthesize silver nanorods, ethylene glycol (EG), silver nitrate ($AgNO_3$), and poly(vinyl pyrrolidone) (PVP; MW = 55,000) were used as the polyol, salt precursor, and polymeric capping agent, respectively.-Briefly, 5 mL of EG was heated in an oil bath at 160 °C for 1 h before simultaneously injecting 3 mL of two EG solutions, one containing 48 mg of $AgNO_3$ and the other containing 48 mg of PVP. Nanorod formation also required that the reaction solution contained 60 μM of NaCl and 3 μM of Fe(III) acetylacetonate ($Fe(acac)_3$) that were dissolved in the EG solution containing PVP.

To synthesize silver nanocubes, we employed the same procedure for the nanorod synthesis but without adding 3 μM $Fe(acac)_3$. The reaction mixture was heated at 160°C for 45 min. The product was dominated by cubic nanoparticles, with a small amount (5%) of silver nanorods. For the synthesis of octahedral Ag NPs, 60 μM of NaCl in the silver nanorod synthesis was substituted with 30 μM of NaBr with the rest procedure or materials that are the same as used in the nanorods synthesis.

The average hydrodynamic radius was determined by dynamic light scattering (DLS) on a Zetasizer Nano ZS instrument (Malvern Instruments, UK) using 1.5 mL of the silver nanoparticle suspension in a standard macro-cuvette (pass length: 10 mm). The temperature was maintained at 25°C, and the scattering angle was 173°. A refractive index (RI) of 1.07 and an absorption value of 0.01 were used for Ag NPs. Scanning electron microscopy (SEM) images were taken by a field emission scanning electron microscope

(FE-SEM) (JSM-7900F, JEOL) to analyze morphology. The crystal phases were identified by a Philips, EMPYREAN X-ray powder diffractometer, equipped with a Co KR source. Samples were mounted on a zero-background sample holder. Diffraction patterns were collected in the 2θ range of 10-100° using a step size of 0.067°.

3.2.2 Quantifying Local Surface Hydrophobicity

Surface hydrophobicity of three Ag NPs was probed by a Bruker Dimension Icon AFM (Bruker, USA) using our reported method. The adhesion forces between surface functionalized AFM tips and sample surfaces were measured to indicate the hydrophobic interactions and local hydrophobicity. Briefly, silicon nitride (Si_3N_4) cantilever tips (NPG-10, Bruker, USA) were purchased, which have gold coating both on the reflex side and surface of tip and a radius of curvature at 30 nm. The tips were hydrophobicized by immersion in 1 mM $HS(CH_2)_{11}CH_3$ for 14 h to coat the tip surface with $-CH_3$ groups. Before this hydrophobization, the tips were rinsed with deionized water and then methanol to remove any surface contaminants from probes. Next, gold (111) substrate surfaces (Agilent, USA) were used as a platform to create different hydrophobicity by surface coating with different alkanethiol self-assembled monolayers (SAMs) terminated with OH and CH_3 groups. Briefly, the gold substrates were immersed in ethanol solutions containing 1 mM $HS(CH_2)_{11}CH_3$ and $HS(CH_2)_{11}OH$ in various molar ratios (0:100, 20:80, 40:60, 60:40, 80:20, and 100:0) for 14 h and then rinsed with ethanol before use. The $-CH_3$ groups chemically bound to gold result in different hydrophobicity levels as the surface coverage of CH_3 groups varies. Water contact angles were measured on these functionalized gold substrate surfaces to quantify the hydrophobicity degree. **Table 3.1** shows that the water contact angle increases as molar fractions of CH_3 on the SAM surfaces increase. A

calibration curve (**Figure 3.1**) was established by plotting the adhesion force between the gold substrate surfaces and the functionalized tip against the cosine value of the water contact angles. Due to the small sizes of Ag NPs, water contact angles are difficult to measure on single NPs. Thus, the local surface hydrophobicity of Ag NPs was measured similarly by probing the adhesion force between the surface-functionalized tips and Ag NPs that were spin-coated on a silicon wafer (Type P/<111>, TED PELLA, Inc.) that was pretreated by immersion in 5% (3-mercaptopropyl)-trimethoxysilane in methanol for 12 h to enhance adhesion between deposited NPs and the silicon wafer. For each Ag NPs, at least 40 locations were randomly selected to measure the adhesion force, and three force measurements were performed at each location. Using the measured adhesion forces and the obtained calibration curve, the local surface hydrophobicity was finally quantified using the calculated water contact angles.

Table 3.1 Water Contact Angles for Various SAM-Functionalized Surfaces

SAMs	Molar fractions of CH_3 (%)					
	0	20	40	60	80	100
Contact angle on Au {111} (°)	31.9	45.1	57.6	68.3	78.6	85.1
Standard deviation (°)	0.6	0.3	0.6	0.7	0.5	0.9

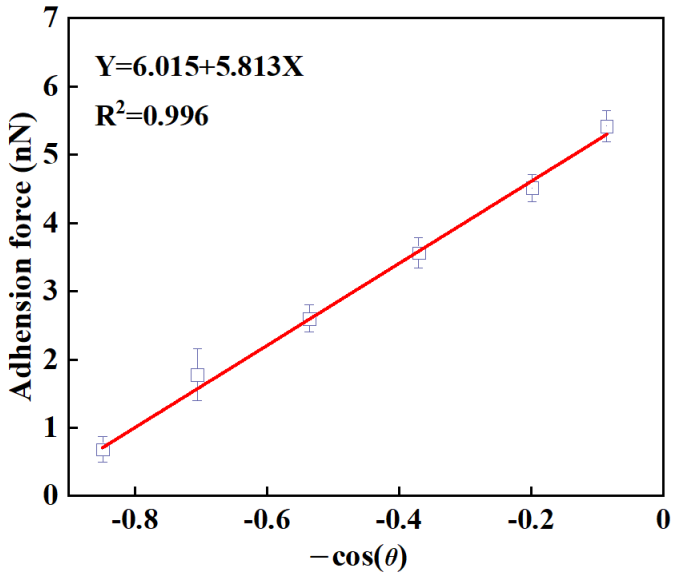

Figure 3.1 Adhesion forces versus –cos(θ) values of different gold {111} substrate surfaces functionalized with alkanethiol self-assembled monolayers (SAMs).

3.2.3 Surface Electrochemical Activity Measurement

AFM-SECM was used to identify electrochemically reactive or active sites to unravel the redox-mediated dissolution mechanisms for Ag NPs. The SECM measurements were performed on the same Bruker Dimension Icon® and FastScan® AFM that is equipped with standard PeakForce SECM accessories as detailed elsewhere. Both the probe and the sample are working electrodes sharing the same reference and counter electrodes. Prior to the SECM measurement, all PeakForce SECM probes (tip radius of 25 nm and tip height of 215 nm, Bruker Nano Inc, CA, US) were tested by performing a few cyclic voltammetry in a standard three-electrode electrochemical cell with a platinum (Pt) counter electrode and a standard Ag/AgCl reference electrode (CH Instruments, Inc.). The electrochemical cell was filled with 1.8 ml of 10 mM $[Ru(NH_3)_6]Cl_3$ (as the reversible redox probe or mediator) in 0.1 M KCl (as the background electrolyte). A bipotentiostat (CHI700E, CH Instrument) was connected to the electrochemical cell to perform the cyclic voltammetry

analyses with a scanning voltage from 0 to −0.4 V vs. Ag/AgCl at 50 mV·s^{-1} applied to PeakForce SECM probes. In this work, the tip probe reduces $[Ru(NH_3)_6]^{3+}$ to $[Ru(NH_3)_6]^{2+}$ at −400 mV versus a pseudo Ag/AgCl reference electrode. We hypothesize that different dominant facets of Ag NPs may generate different levels of tip-sample currents to reflect the reactivity differences and the tip-sample current mapping could generate strong contrast from the background or the silicon substrate that had negligible electrochemical oxidation reactions with $[Ru(NH_3)_6]^{3+}$.

An interleaved scan mode with a lift height of typically 40 to 150 nm between the probe and the sample surface was used in SCEM. On each line scan during the main scan, the probe scans over the sample surface using the normal PeakForce QNM mode at a scan rate at 0.1 Hz and a scan size at 5×5 µm. After verifying SECM on a standard test sample (a surface patterned silicon nitride on Pt), the Ag NPs-coated silicon substrate was placed into the same fluidic cell to replace the standard test sample. The same SCEM scanning procedure was performed on the sample surface at a DC bias of −400 mV and +100 mV applied to the probe and the sample substrate at the scan rate of 0.1 Hz and a scan size is 3×3 µm.

3.2.4 Nanoparticle Dissolution Experiments

To reveal the shape dependent dissolution of Ag NPs, direct mapping of the immobilized Ag NPs was conducted on AFM. A similar approach was used to immobilize Ag NPs on a cleaned silicon wafer substrate, which was moved to 20 mL of the phosphate buffered solution (1 mM NaH_2PO_4; 1 mM Na_2HPO_4, pH=5.8) in a 50-mL polystyrene sample tubes (Fisher Scientific) and sealed with Parafilm. Additionally, NaCl was added at a final concentration of 550 mM to accelerate the dissolution of AgNPs. The PBS solutions with

different pHs (5.0, 7.0 and 9.0) were also prepared to examine the pH effect on dissolution of Ag NPs. pH value was adjusted by 50 mM PBS, the stock solution (100 mM, dissolved in 1 L DI) was prepared as follows: pH 5.2 (0.21 g Na_2HPO_4, 11.82 g NaH_2PO_4); pH 6.3 (1.87 g Na_2HPO_4, 10.42 g NaH_2PO_4); pH 7.2 (8.55 g Na_2HPO_4, 4.77 g NaH_2PO_4); pH 8.0 (13.32 g Na_2HPO_4, 0.74 g NaH_2PO_4) and pH 9.1 (14.10 g Na_2HPO_4, 0.79 g NaH_2PO_4). All dissolution experiments were conducted at room temperature (25 °C) in the dark. The substrates were taken after different times (e.g., 1−4 days) and dried under N_2. The same Bruker Dimension Icon® and FastScan® AFM was used to scan the morphology of the remaining Ag NPs on silicon wafer using the silicon probes (Model: SCANASYST-Air, Bruker, USA) in a PeakForce mode using a 256 × 256-pixel resolution at a scan rate of 0.1−0.5 Hz. An average number of 142 Ag NPs was used to measure the mean particle size at each time point.

3.2.5 DFT Calculation and AIMD Simulation

To identify the stability of different Ag facets and analyze the interactions of H_2O and Cl ions with dominated facets of Ag NPs, the Vienna Ab Initio Simulation Package (VASP) was to perform relevant DFT calculations. A generalized gradient approximation (GGA) using the Perdew-Burke-Ernzerhof (PBE) formulation was employed. The projector augmented wave (PAW) pseudopotentials were used to describe the ionic cores with a plane wave basis set and kinetic energy cutoff of 600 eV to account for the valence electrons. Partial occupancies of the Kohn−Sham orbitals were allowed using the Gaussian smearing method and a width of 0.05 eV. The energy was considered self-consistent when the energy change was smaller than 10^{-6} eV. A geometry optimization was considered converged when the force change was smaller than 0.02 eV·$Å^{-1}$. Grimme's DFT-D3 methodology was used

to describe the dispersion interactions. The atomic charges were obtained from Bader's analysis based on the numerical implementation developed by Henkelman et al.

To construct two dominated surfaces' structures of Ag NPs, firstly, the equilibrium lattice constants of the Ag unit cell in the cubic Fm-3m space group were optimized to be a=4.161 Å, b=4.161 Å, c=4.161 Å, α=90°, β=90°, and γ=90°, when using a 4×4×4 Monkhorst-Pack K-point grid for Brillouin zone sampling. Then, we built a periodic surface with four layers for two different facets. The models contain 32 atoms for {100} facets and 64 atoms for {111} facets. Two typical facets, Ag {100} and {111}, was constructed with *p*(2×2) periodicity in the x, y and 1 stoichiometric layer in the z direction separated by a vacuum layer in the depth of 20 Å in order to separate the surface slab from its periodic duplicates. During structural optimizations, the gamma point in the Brillouin zone was used for K-point sampling. For both the crystalline Ag surfaces (that is, {100} and {111} surface) and adsorption calculations, a K-point grid of 2 × 2 × 1 was used. Models of two facets are shown in **Figure 3.2**. The optimal plane wave cutoff and k-point grid density were found by continually increasing them until the self-consistent energy changed by less than 1 meV/atom. The surface energies (γ) of Ag {100} and {111} surfaces were calculated by Equation (3.1) to assess the stability of the surface (e.g., a low surface energy indicates a stable state).

$$\gamma = (E_{surf} - nE_{bulk}) / 2A \tag{3.1}$$

where E_{surf} is the total energy of {100} or {111} surface (J) as constructed in **Figure 3.2**, E_{bulk} is the bulk energy of the unit cell (J), A is the surface area of the supercell (m^2), the coefficient 2 was used since the upper and lower surfaces are both optimized, and n

represents the number of unit cells that the surface contains. The total energy of the Ag surfaces was calculated using the total free energy in the OUTCAR after optimizations.

The surface adsorption energy between water molecules or Cl^- ions and the identified stable facets or surfaces of Ag NPs were calculated to assess if the facet-dependence of Ag could exert a pivotal effect on the hydrophobicity activity and adsorption. Water molecule (H_2O) was selected for this comparative study as the model molecule. We first optimized the molecular structures by putting the H_2O molecule in a cubic periodic box with a side length of 20 Å and a 1×1×1 Monkhorst-Pack k-point grid for Brillouin zone sampling. Then, the relaxed molecule was place on bare Ag surfaces, and after optimization, the obtained energies were recorded. The adsorption energy (E_{ads}) of the adsorbate (A) on different surfaces that were defined in previous section was calculated by Equation (3.2):

$$E_{ads} = E_{A/surf} - E_{surf} - E_{A(g)} \tag{3.2}$$

where $E_{A/surf}$, E_{surf} and $E_{A(g)}$ are the energy of A adsorbed on the catalyst surface (eV), the energy of a clean catalyst surface (eV), and the energy of an isolated A molecule (eV), respectively. Ultimately, the adsorption sites and adsorption mechanisms (e.g., adsorbate-adsorbent configurations and electron transfer) were evaluated by comparing the energies of different adsorption configurations and taking the lowest energy one as the most favorable.

The Ab-initio molecular dynamics (AIMD) was used to elucidate the mechanisms of the silver dissolution at room temperature (298 K) coexisted with water. We simulated the system consisted of Ag {100} and {111} surfaces by keeping the bottom three layers fixed, H_2O molecules, Cl^- ion and Na^+ cation concerning the ion pairs, PVP molecule as shown in **Figure 3.3**. To allow for the Ag surface−solvent interaction, the top two layers

of the Ag supercell are relaxed along with the solvent for 1000 ps trajectory. Similar methodologies to construct the interphase models have been opted in some of the previous studies and have successfully evaluated the detailed microscopic view of the involved electrochemical reactions. The spin polarization effects were neglected. Three Ag dissolution models are constructed by randomly inserting the optimized H_2O molecules into the 20 Å vacuum of the supercells, maintaining an experimental density of H_2O (1.00 $g \cdot cm^{-3}$). Firstly, 100 H_2O molecules and 65 H_2O molecules are used to fill the empty volume of the Ag {100} and {111} surfaces, respectively. Then, same models with added one chloride ion and sodium cation as shown in **Figure 3.3(e)** and **(f).** Moreover, similar technique has been followed to construct models involving PVP molecule, one more PVP molecule with H_2O molecules were constructed on the Ag surface.

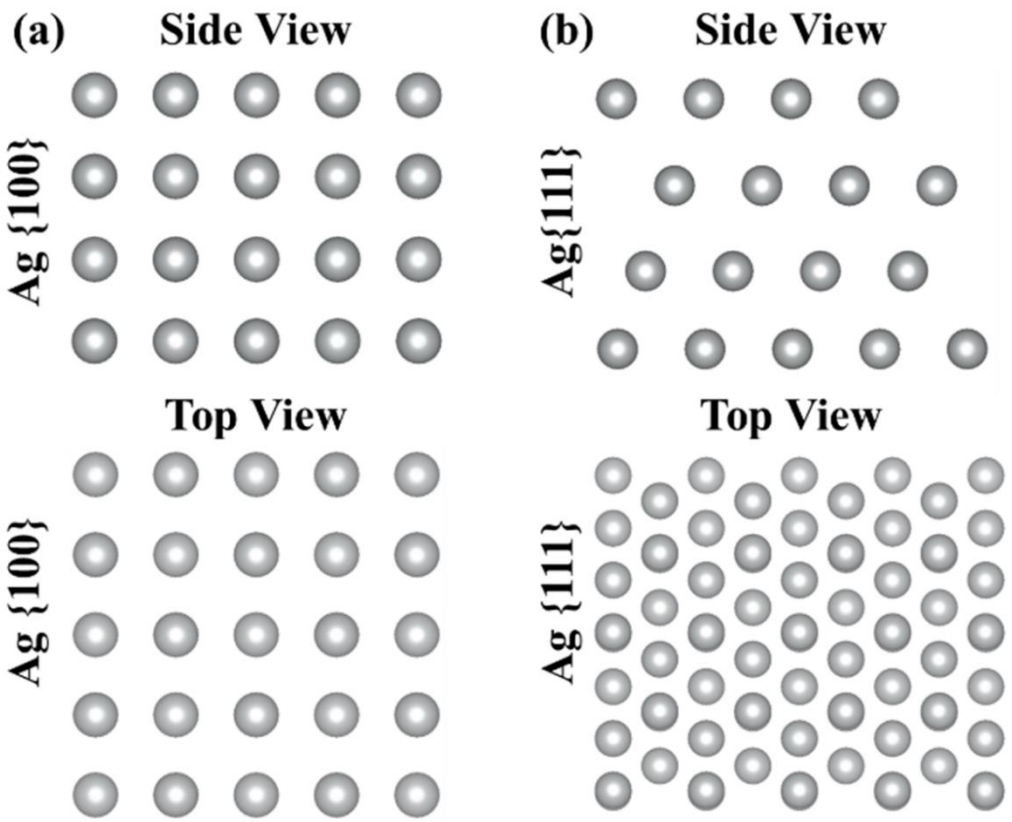

Figure 3.2 Schematic of atomic surface structures of (a) {100} facet and (b) {111} facet of Ag surfaces. Silver atoms are illustrated by silver color spheres.

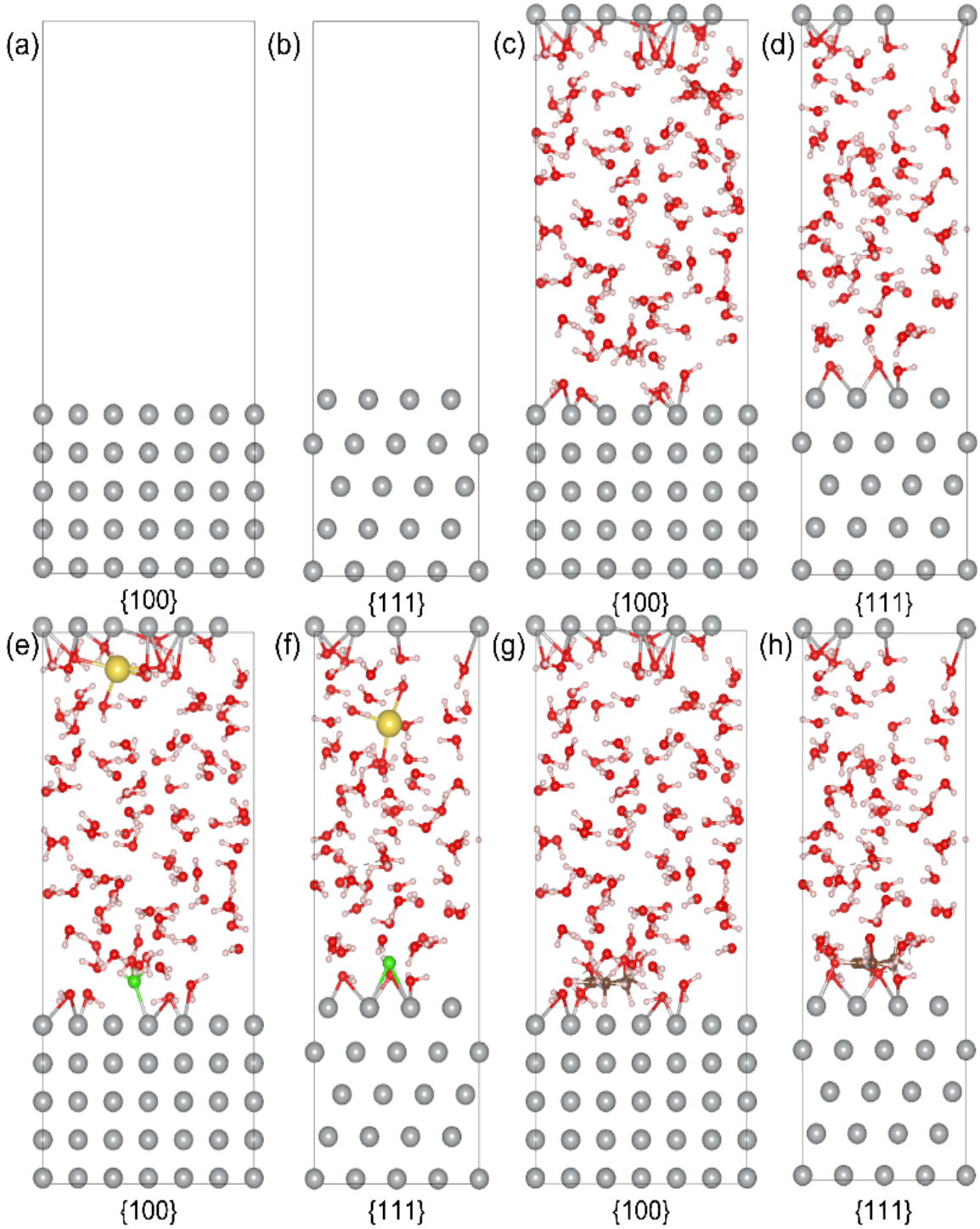

Figure 3.3 Schematic of atomic surface structures of (a) {100} facet and (b) {111} facet of Ag surfaces, 94 and 65 water molecules on {100} facet (c) and {111} facet (d) of Ag surfaces, Cl^- ion and Na^+ cation coexisted with water molecules on {100} facet (e) and {111} facet (f) of Ag surfaces, one PVP molecule coexisted with water molecules on {100} facet (e) and {111} facet (f) of Ag surfaces. Silver, oxygen, carbon, nitrogen, hydrogen, chlorine, and sodium atoms are illustrated by sliver, red, brown, lavender, pink, green and yellow color spheres, respectively.

3.2.6 COMSOL Simulation of Ag NPs Shape-Dependent Dissolution

The shape-dependent dissolution process of Ag NPs was simulated in using COMSOL Multiphysics (6.0) by considering the transport characteristics of dilute species near Ag NPs of three different shapes (such as, cube, rod and octahedron). Transport of dilute species and deformed geometry modules of the COMSOL were used. For two-dimensional (2D) modeling, finer and fine meshes and for the three-dimensional (3D) modeling, normal and finer mesh were used. To describe the mass transport of Ag ions, the diffusion equation in Equation (3.3) was solved using the finite element method to find the concentration profile, c_{Ag}, in the diffusion field after each time step.

$$\frac{\partial c_{Ag}}{\partial t} + \nabla J_{Ag} = 0 \tag{3.3}$$

$$J_{Ag} = -D_{Ag} \nabla c_{Ag} \tag{3.4}$$

J_i is the mass flux diffusive flux of species Ag (mol·m^{-2}·s^{-1}); D_{Ag} is the diffusion coefficient of species Ag (m^2·s^{-1}) which was assumed to be independent of composition; c_{Ag} is the concentration of species Ag (mol·m^{-3}). The initial average Ag concentration was set to zero in this study.

The dimension (S) of the diffusion field for different particle geometries, cube, rod and octahedron, are calculated based on constant volume for the 3D modeling or constant area for the 2D modeling according to Equations (3.5)– (3.7)

$$S^3 = a^3,\ S^2 = a^2 \text{ cube} \tag{3.5}$$

$$S^3 = 1.72a^2 l,\ S^2 = 2al \text{ rod} \tag{3.6}$$

$$S^3 = \frac{\sqrt{2}}{3}a^2,\ S^2 = \frac{\sqrt{3}}{2}a^2 \text{ octahedron} \tag{3.7}$$

where a_c in Equation (3.5) is the edge of cube. Parameter a_r and l_r in Equation (3.6) are the edge of pentagon and the length of the rod, respectively. Parameter a_o in Equation (3.7) is the edge of octahedron.

The model input parameters are presented in **Table 3.2**. c_{Ag} and D_{Ag} in this table are the concentration of Ag at the particle-matrix interface, diffusivity factor, respectively.

Table 3.2 Parameters for COMSOL Simulation

Physical Parameters	Symbols	Value	Unit
Diffusion coefficient	D_{Ag}	1.0×10^{-9}	$m^2 \cdot s^{-1}$
Silver concentration	c_{Ag}	100	mol
Edge length of cube	a_c	1.0×10^{-6}	m
Edge length of rod	a_r	1.0×10^{-6}	m
Length of rod	l_r	5.0×10^{-6}	m
Edge length of octahedron	a_o	1.0×10^{-6}	m

3.3 Results and Discussion

3.3.1 Particle Size and Morphology of Ag NPs

The average hydrodynamic radius and polydispersity index (PDI) of three kinds of Ag NPs are provided in **Table 3.3**. The sizes of these nanoparticles fall mostly in the range of 300-400 nm. PDI is a dimensionless measure of the broadness of the size distribution reported from the Zetasizer Nano ZS instrument. The PDI values are 0.176, 0.213, and 0.134 for nanocube, nanorod, and octahedral Ag nanoparticles, respectively. As the PDI values are less than 0.25, Ag NPs are considered well dispersed in their water suspension without significant aggregation. All three shaped Ag NPs are mostly stabilized by PVP and have a negative zeta potential of around -25 mV.

Table 3.3 Average Particle Sizes and Polydispersity Index of Three different Ag NPs in DI Water

Ag NPs	Average hydrodynamic diameters(nm)	Standard deviations (%)	Polydispersity index (PDI)	Zeta Potential (mV)
Nanocube	375 ± 71	19	0.176	−29.8 ± 5.8
Nanorod	322 ± 56	17	0.213	−25.7 ± 4.3
Octahedron	360 ± 57	16	0.134	−24.9 ± 2.9

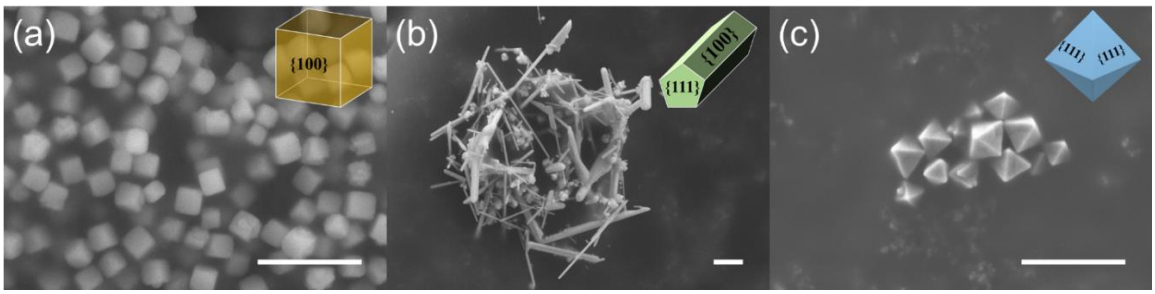

Figure 3.4 SEM images of the three kinds of Ag NPs: (a) nanocube, (b) nanorod, (c) octahedron. Scale bar = 1 μm. The inset figures on top right are 3D models with presumed dominant facets with corresponding indexes.

Figure 3.4 presents the SEM images that compares the morphologies. As PVP can selectively bind to Ag {100} to make its surface free energy lower than that of Ag {111},

the formation of nanocubes or cubic Ag nanocrystals composed of six square {100} facets are facilitated. Similarly, as the nanorod nanoparticles include the {100} and {111} facets, by adjusting the surfactants (PVP) or additives (NaCl or NaCl), the nanorod with two ends of the {111} facets could grow continuously throughout Ostwald ripening . Ag nanorods can elongate because its two end surfaces are largely uncovered and remain to reactive toward new silver atoms as previously reported , while the five rod surface {100} are passivated by PVP. Finally, octahedron Ag NPs formed because less stable {100} facets will gradually be replaced with the more stable {111} facets, leading to the formation of truncated cubes, cuboctahedrons, and finally octahedrons and exposed {111} facets.

3.3.2 Local Surface Hydrophobicity of Three Different Shaped Ag NPs

The local scale surface hydrophobicity of the three Ag NPs were measured using the reported AFM method . **Figure 3.5** shows the calculated water contact angles of three shaped Ag NPs based on the adhesion force measurements using the calibration curve in **Figure 3.1**. In addition to the full distribution of data, this violin plot also displays summary statistics such as mean, interquartile ranges, and median. The measured adhesion forces between the Pt-coated tip and the surface of nanocube and nanorod Ag NPs seem to be significantly different from that on octahedron ($p < 0.05$). This difference may be attributed to the different tip-facet interactions, where the dominant {111} facet of octahedron Ag seems to have a greater adhesion force with the probe tip than the {100} facet on nanocube and nanorod Ag NPs. The Ag NPs used in the Dpresent study were all stabilized by PVP, which binds preferably to {100} facet compared to {111} facet . Since the nanocube and nanorod Ag NPs have more exposed {100} facet surfaces are coated with PVP that is hydrophilic, the hydrophobicized AFM tip thus exhibited a lower adhesion force on

nanocube and nanorod Ag NPs than on octahedron Ag. Shen et al. reported that nanocrystals' facets of TiO_2 and α-Fe_2O_3 with larger surface energies exhibited lower surface hydrophobicity and higher adhesion forces with NOM with different molecular weights.

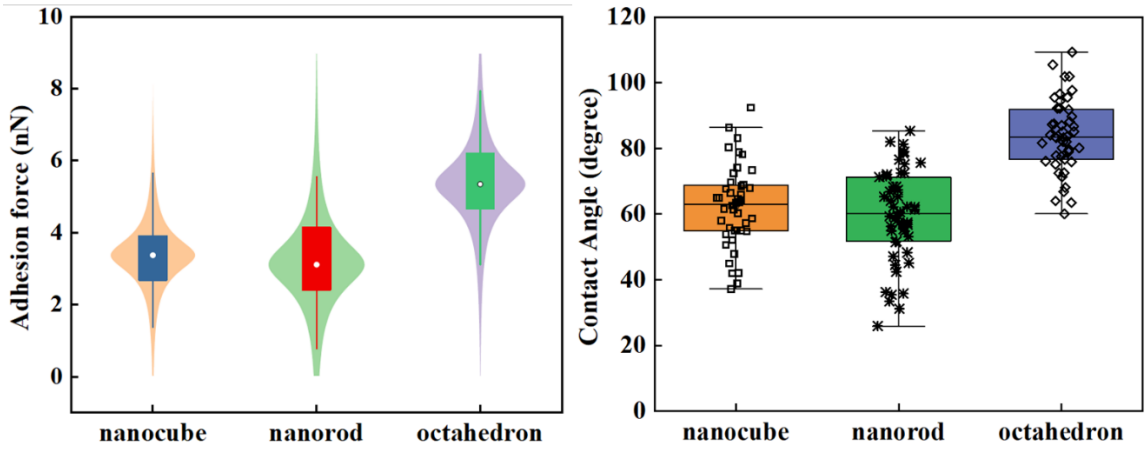

Figure 3.5 Violin graphs of the measured adhesion forces and the calculated the water contact angles for three Ag NPs (nanocube, nanorod and octahedron). Violin plots are a combination of a box plot and density plot. A box indicates the interquartile range, which means that 50% of the data are contained in the box. The white circle represent median the data. The whiskers extended from the box display the lower (min) and upper (max) adjacent values. The shape of the violin plot shows the frequency of values.

3.3.3 Shape-dependent Electrochemical Activity of Three Different Shaped Ag NPs

The metal dissolution is one of the fundamental processes for many applications, including battery, corrosion, electrocatalyst degradation, and material synthesis. However, obtaining detailed structure–activity relationship for these processes at complex material interfaces remains challenging as some of the characterizations such as electrochemical studies are conventionally achieved using ensemble approaches. However, electrochemical behavior at nanomaterial interfaces is inevitably affected by defects, crystal grains of different orientations, and grain boundaries. The kinetics and mechanisms of metal dissolution are also expected to depend on the local surface structure and activity. Scanning probe

microscopy techniques, including scanning tunneling microscopy (STM) and atomic force microscopy (AFM), have been applied to study anodic dissolution reactions in situ, which provide insight into the dissolution mechanism. However, only processes of intermediate kinetics that match the time scale of STM or AFM can be probed directly. In addition, a direct correlation between the measured electrochemical activity (i.e., current) and the local topography changes is often missing due to the mismatched length scale: electrochemical signal (e.g., current) is associated with the entire millimeter-sized electrode, while the topography is only a nanoscopic portion of the entire electrode. AFM-SECM integrates classic SECM and AFM to achieve on-step acquisition of unparalleled high-spatial-resolution surface topology and nanoscale electrochemical images and allows direct structure–activity correlation at complex electrochemical interfaces. Such measurements are crucial for understanding structure-activity relationships relevant to a wide range of applications in material science, life science and chemical processes.

Figure 3.6 shows that the tip-sample current exhibited slight dependence on the shape or exposed facets of Ag NPs. Cube, nanorods and octahedron of Ag NPs yielded an average tip current of 110.5±10.8, 98.8±27.8 and 150.8±13.5 pA, respectively, at the same tip-sample distance of 100 nm. The observed shape dependence of tip currents is attributed to the different facet surface states (e.g., work functions) that caused different electrolyte/electrode interactions. In our operation mode, the tip-sample current is caused by redox reaction originated from different Ag nanoparticles on the substrate. The diffusion and concentration profile or distribution of the redox mediator ($[Ru(NH_3)_6]Cl_3$) from the bulk solution to the probe tip could be affected by the local interactions of mediator molecules and facet surfaces. Moreover, the interplay or overlapping of the two electric

double layers of the samples and the probes affects the diffusion transport of the redox mediators and ultimately the redox reactions at the tip (or tip current). Our results indicate that compared with nanocube and nanorod, the octahedron of Ag NPs yield high electrocatalytic responses can be attributed to the exposed surface facet.

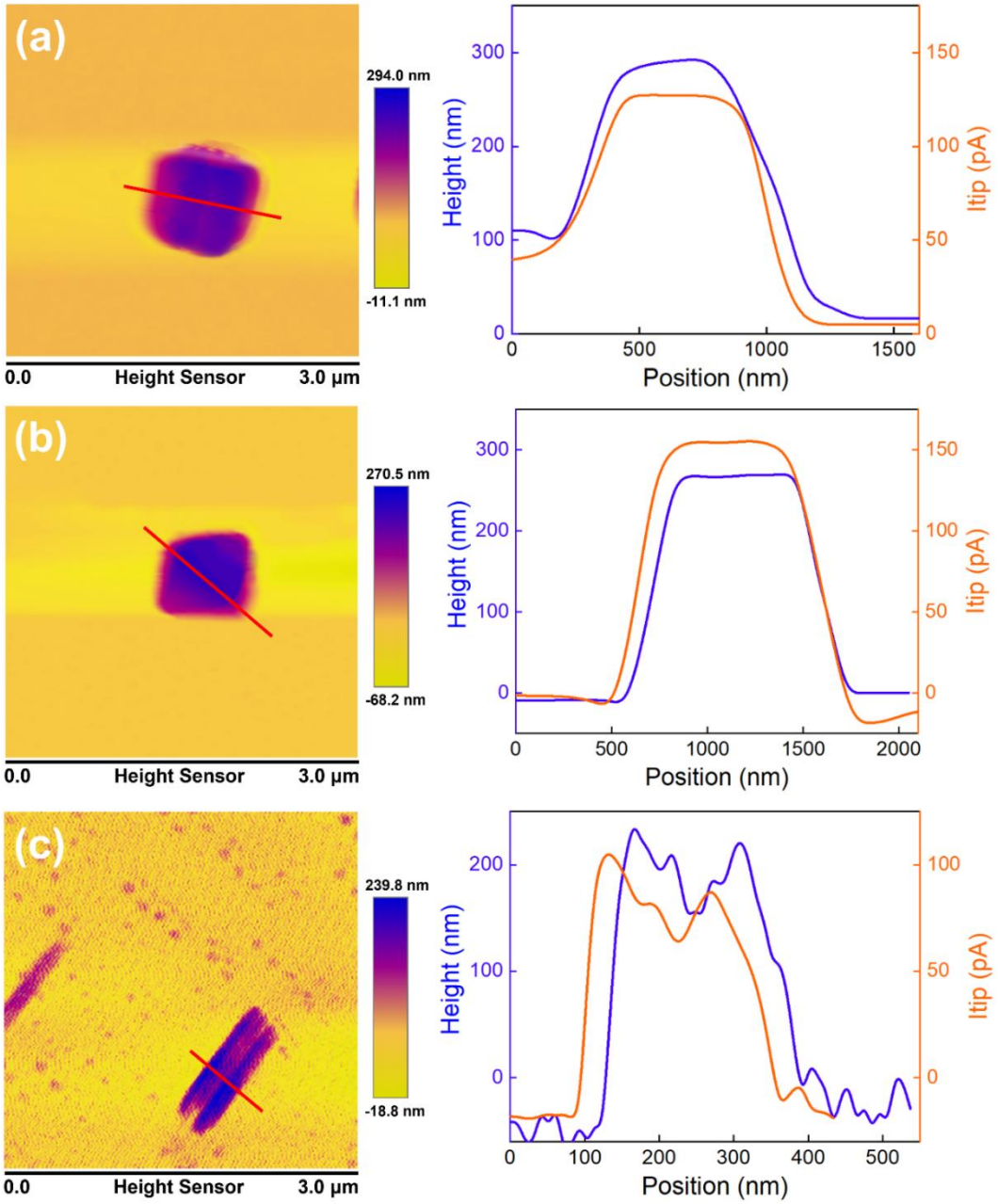

Figure 3.6 Typical topography and AFM-SECM cross-sectional tip-sample current along the red lines in top images for three Ag NPs (a) nanocube, (b) octahedron and (c) nanorods.

3.3.4 Silver Nanoparticle Dissolution Experiments

Dissolution and ion release of ENMs are often evaluated by inductively coupled plasma-mass or optical emission spectrometry (ICP-MS or ICP-OES). Only two recent studies have employed AFM to conduct *in situ* characterization of dissolution of Ag NPs and to assess local morphological changes during dissolution. In this study, we hypothesized that faceted Ag NPs may dissolve differently along particular orientations of facets due to the local surface energies and reactivity of the different crystal facet as mentioned above. To verify this hypothesis, we have measured the high-resolution AFM images of three differently faceted Ag NPs. Briefly, **Figure 3.7a-c** show AFM images of the three different Ag NPs in a phosphate buffered solution (1 mM NaH_2PO_4; 1 mM Na_2HPO_4, pH=5.8). Cubic, nanorod and octahedral shapes are all resolved in AFM images with the measured heights (~300 nm) consistent with the results obtained from SEM images. However, the widths (400–600 nm) are larger than SEM results, possibly due to the tip convolution effect (e.g., the imaged width is a sum of the nanoparticle width and the tip diameter). To promote dissolution of Ag NPs, the PBS was additionally spiked NaCl at a high concentration of 550 mM to induce the chlorination reaction where Ag ions release via oxidative dissolution and then complex with chloride ions . Formation of AgCl creates a core-shell Ag^0-AgCl structure , which then affects the surface properties, reactivity, and bioavailability of Ag NPs. At a high Cl/Ag ratio (Cl/Ag = 26,750), the solid AgCl could be converted to the dissoluble species of $AgCl_x^{(x-1)-}$, which promotes the dissolution of AgNPs . The dissolution process is likely governed by local surface energies due to their geometrical shape and different stabilization of the different crystal faces.

Figure 3.7d present the normalized height changes of three different shaped Ag NPs almost linearly decreased with the dissolution time. The height of cubic and nanorod

Ag NPs reduced to 30–50% after 4 days in the NaCl solution, whereas those of octahedron nanoparticles decrease down to 60–70%. The cross-section image of nanocube Ag NPs (**Figure 3.6a**) indicates that the edges of the cube dissolved to form a truncated cube after 1 day's exposure to the NaCl solution. Height changes and dissolutions are slightly different for three different morphologies of Ag NPs. The result in **Figure 3.7d** shows that the {111} facet of Ag NPs with a lower coordination number dissolves faster than the {100} facet. Thus, Ag NPs with {100} facet have higher resistance to dissolution in NaCl.

Figure 3.7e illustrates the hypothetic shape changes of Ag NPs during dissolution, where the truncated cube is flattened gradually, and then the flat terrace-like structure appears again. Pointed peak of octahedron Ag NPs shrinks rapidly after first day espouse, giving flat terrace-like structure. After the terrace formed on the top, decrease of the height is nearly ceased. Some octahedral NPs, however, were observed to dissolve with the pointed peak of the cross section preserved for four days exposure. For Ag nanorod, the edges of the pentagon first dissolve and then cross section become more roundly like over time and the height was decreasing gradually.

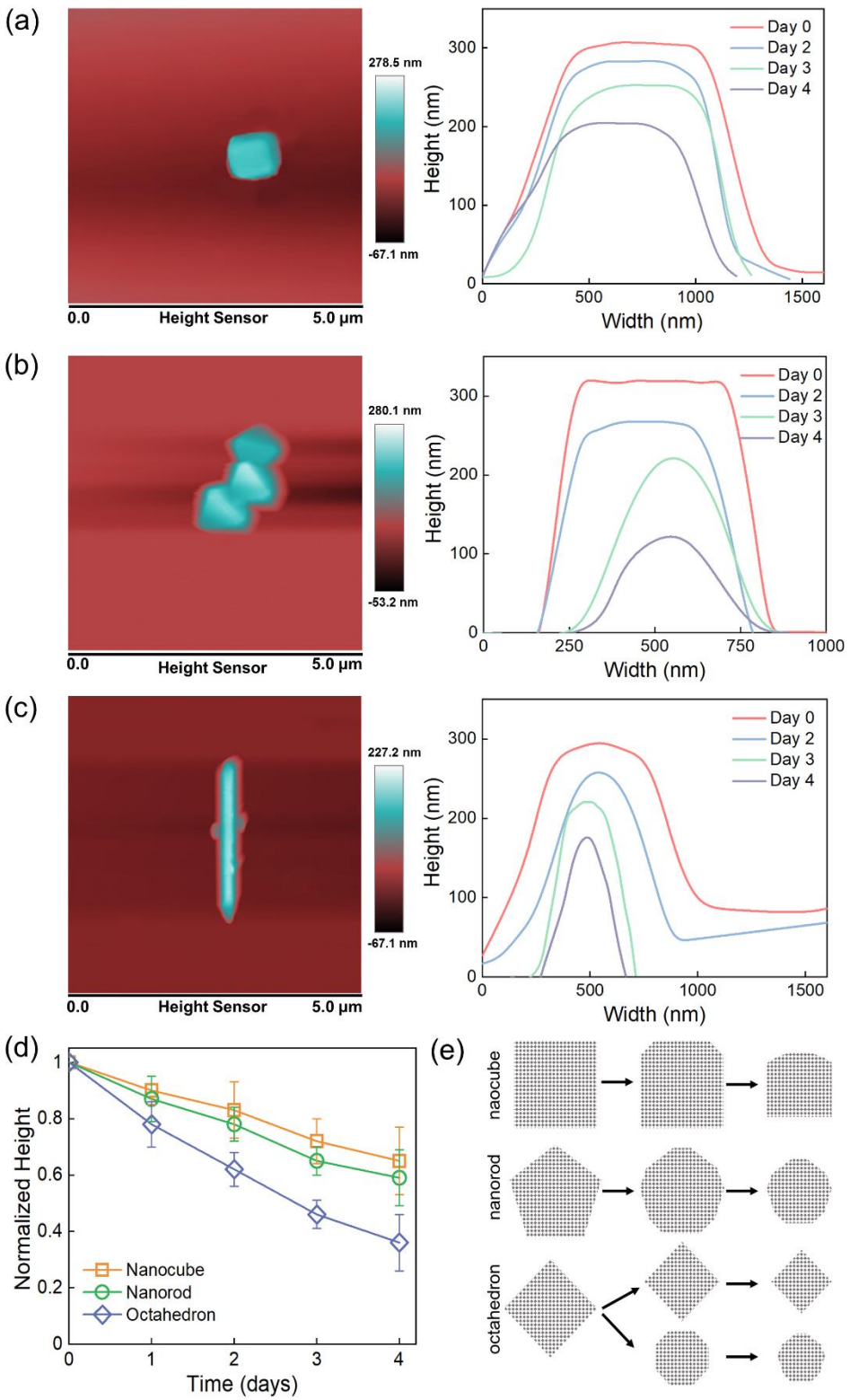

Figure 3.7 The height change images of Ag nanoparticles (a) cube, (b) nanorod, (c) octahedron, (d) normalized mean Ag NPs height at different times and (e) dissolution models of Ag NPs of three different shapes.

3.3.5 Water Molecule Adsorption Configurations and Energies

The surface energies (γ) of the two different low-index Ag surfaces, {100} and {111} , as constructed in **Figure 3.2** were calculated with Equation (3.1). Through structural optimization, the surface energies of the {100} and {111} facets are 1.60 $J \cdot m^{-2}$ and 1.27 $J \cdot m^{-2}$, respectively. In general, the surface with a higher surface energy has a larger proportion of under-coordinated atoms, which can elicit higher reactivity in heterogeneous reactions .

To evaluate the surface reactivity of the two {100} and {111} facets, the interaction behavior between water molecules and different Ag surfaces were investigated. To determine the optimal adsorption configuration of H_2O on the Ag surfaces, the adsorption energy (E_{ads}) of one H_2O molecule on the constructed Ag surface was calculated using Equation (3.2) for several possible positions of H_2O as illustrated in **Figure. 3.8** and the one with the most negative E_{ads} corresponds to the most favorable H_2O adsorption configuration. The calculated adsorption energies at the atop, bridge and hollow sites of {100} facet are −0.94, −0.83 and −0.81 eV, respectively, which are consistent with a previous study that reported the adsorption energies of H_2O on Ag surface follow the order of: atop sites > bridge sites > hollow sites . **Table 3.4** summarizes the adsorption energies of H_2O on the different Ag surfaces. For both {100} and {111} facets, H_2O is always forming a one-coordinated structure with an Ag-O bond length of 2.318 and 2.382 Å, respectively. The most favorable adsorption energies on the {100} and {111} facets were found to be −0.94 and −0.89 eV, respectively, indicating that H_2O has a stronger affinity on the {100} facet than on the {111} facet, which is in agreement with the surface energy calculations.

Both the present work and previous studies found that the water molecule situated on an atop site is the optimum binding configuration. Our results in **Table 3.4** also show that the most favorable binding site on the Ag {111} was atop an Ag atom, followed by the bridge site and then the hollow site, with interaction energies of −0.89, −0.79, and −0.67 eV, respectively. A previous study of water adsorption on an Ag {100} cluster, performed at the configuration interaction level using ab initio embedding approach, obtained the adsorption energies of 50.2−32.2 kJ·mol^{-1}, which are smaller than the values calculated in this study. However, both studies found the hollow site to be the most unfavorable adsorption site.

Table 3.4. Water Molecule Adsorption Energies at Different Positions

Ag facet	Adsorption energy at different positions (eV)			Adsorption energy of Cl ions (eV)
	atop	bridge	hollow	
{100}	−0.94	−0.83	−0.81	−1.35
{111}	−0.89	−0.79	−0.67	−0.27

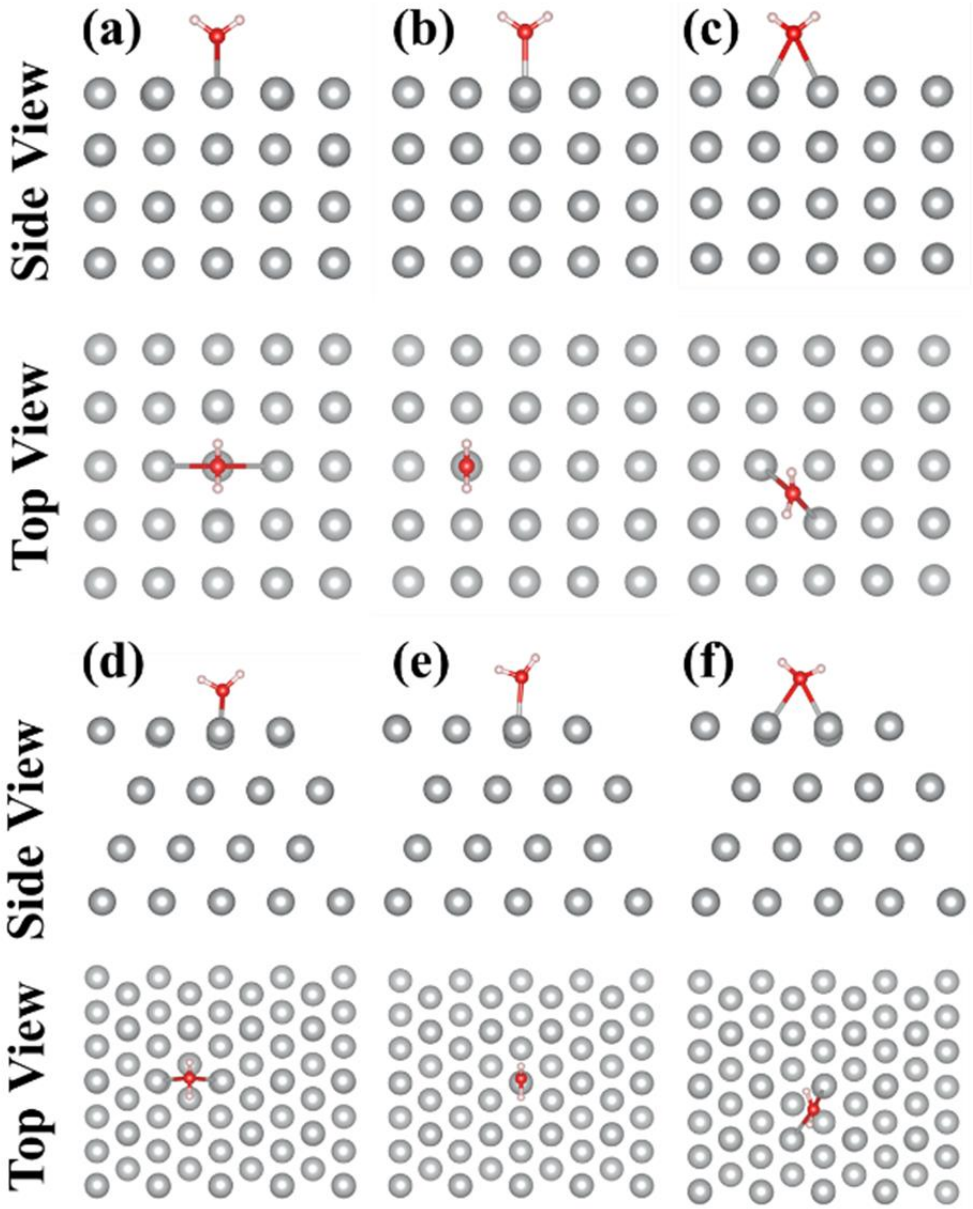

Figure 3.8. Schematic of water molecule adsorption on (a, b, c) (100) facet and (d, e, f) (111) facet of Ag surfaces. Silver, oxygen and hydrogen atoms are illustrated by sliver, red and pink, respectively.

3.3.6 Ag Surface Stability Assessment with AIMD

Ab initio molecular dynamics (AIMD) simulations further explore the stability of different silver facets as indicated by **Figure 3.9.** AIMD follows the trajectories of all atoms while computing interatomic interactions quantum mechanically based on the

Hellmann-Feynman theorem. Three simulation cells containing Ag {100} or {111} surfaces were created with exposure to H_2O (i.e., 100 molecules for {100} and 65 molecules for {111}). Firstly, only water molecules were placed in the simulation cell arbitrarily, and a 1000 ps trajectory was performed. **Figure 3.9** shows that the Ag {111} surface tend to interact with water molecule than Ag {100} surface as indicate by the unfixed two layer became more disordered, which supports the DFT-computed adsorption energies of water molecule on Ag surfaces.

A second simulation cell containing one Cl^- and Na^+ as shown in **Figure 3.9e-f**, and 1000 ps trajectory was performed. This simulation shows that the Ag atoms of on the {100} surface prefer to migrate from Ag surface to phase which containing water molecules than that of Ag {111}. The Cl^- ions (green sphere) tend bind to the one of Ag atoms, which agrees with Cl^- ions is more stable on Ag {100} which found in the DFT-computed adsorption energies of Cl ions on Ag surfaces. Lastly, the third simulation cell contain one PVP molecule as shown in **Figure 3.9g-h**. After PVP bonding to the surface, the Ag {100} surface become more stable than that of {111} as indicated by the Ag atoms mostly kept at its own positions after 1000 ps trajectory simulation. This finding explains the mechanisms of the observed dissolution of facet dependent PVP coated Ag NPs when blended with NaCl and water.

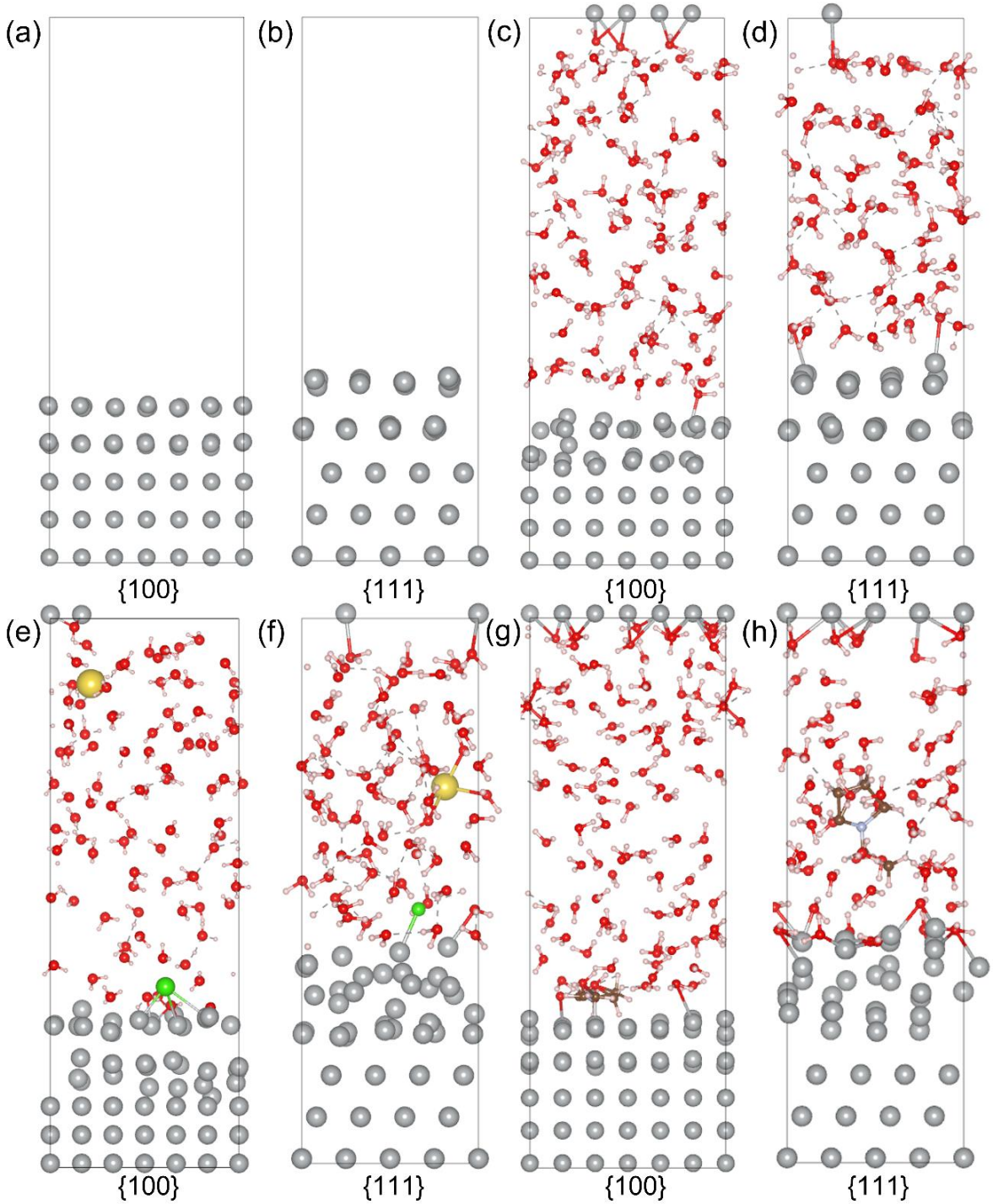

Figure 3.9 Optimized atomic surface structures of (a) {100} facet and (b) {111} facet of Ag surfaces, 94 and 65 water molecules on {100} facet (c) and {111} facet (d) of Ag surfaces, Cl^- ion and Na^+ cation coexisted with water molecules on {100} facet (e) and {111} facet (f) of Ag surfaces, one PVP molecule coexisted with water molecules on {100} facet (e) and {111} facet (f) of Ag surfaces. Silver, oxygen, carbon, nitrogen, hydrogen, chlorine, and sodium atoms are illustrated by sliver, red, brown, lavender, pink, green and yellow color spheres, respectively.

3.3.7 Simulation Analysis of Dissolution Behavior of Ag NPs

The three shaped particles' evolution (nanocube, nanorod, and octahedron) of Ag NPs during dissolution in NaCl (100 mM) were acquired by COMSOL multiphysics simulations (**Figure 3.10**). Ag NPs dissolution is typically modeled using first-order reaction kinetics; however, solid-state reactions are dominated by interfacial interactions. Accordingly, the dissolution process may be affected by surface properties of different facet Ag NPs. The Ag NPs used in the present study are all stabilized by PVP. The dissolution rate of nanocube (as indicated by the volumetric reduction percentage) is lower than that of octahedron. The fast dissolution of the Ag octahedrons can be explained by their high surface energy after PVP binding (see above).

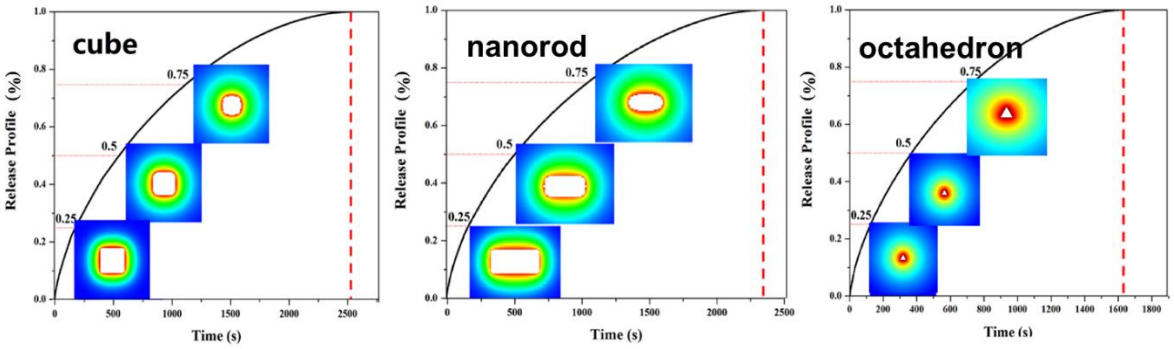

Figure 3.10 Simulated dissolution of volumetric reduction of three different Ag NPs.

3.4 Conclusion

Dissolution of nanoparticles is an important process that alters their properties and affect their environmental fate or applications such as nanomedicine or chemical delivery. Studying nanoparticle dissolution at a crystalline facet level can promote safe-by-design nanomaterials and their applications. In this work, three different morphologies of silver NPs with PVP coating were used to study the facet or shape dependent dissolution

mechanisms. Through mapping the height changes of Ag NPs fabricated on silicon wafer by AFM, we discovered the height of octahedron nanoparticles decrease faster than cubic and nanorod Ag NPs. DFT simulations shows Ag {100} with high surface energy is more likely interactive with water molecule and Cl ion, however, the {100} surface became more stable than {111} after PVP adsorption. Finally, COMSOL simulation also revealed that volumetric reduction percentage of octahedron is faster than cubic or nanorod morphology. The experimental and DFT approaches, and the major findings could be useful to the analysis and prediction of the dissolution behavior of many other common metallic nanomaterials such as Cu, Ni, and Zn NPs.

CHAPTER 4

ELECTROCHEMICAL AGING AND HALOGEN OXIDES FORMATION ON MULTIWALLED CARBON NANOTUBES (MWCNTS) AND Fe_3O_4@g-C_3N_4 COATED CONDUCTIVE MEMBRANES

Work of this chapter is related to the publication:
Qingquan Ma, Jianan Gao, Courtney Potts, Xiao Tong, Wen Zhang. "Electrochemical Aging and Halogen Oxides Formation on Carbon Nanotube (CNT) and Fe_3O_4/g-C_3N_4 coated Conductive Membranes." *Industrial and Engineering Chemistry Research* (2022).

4.1 Introduction

Electrically charged or electrochemically reactive membranes (ERMs) integrate electrochemical advanced oxidation and/or electrochemical reduction reactions into membrane filtration to enhance pollutant degradation, rejection or transformation (e.g., nitrification) . Electrochemical membrane filtration has demonstrated promising concurrent rejection and degradation of diverse contaminants for water purification and wastewater treatment . For example, effective removal of persistent organic pollutants (e.g., polycyclic aromatic hydrocarbons and polychlorinated biphenyls), dyes, pharmaceutical residuals and personal care products, and perfluorochemicals as well as microbial species were reported . In a typical configuration, the constituents of influent serve as the electrolyte and ERMs the dual function of separation unit and electrode. Such a design can improve electrochemical kinetics and efficiencies by the increased electro-active surface area and the enhanced convective mass transfer of pollutants. When the proper electrode potentials (e.g., 1-2 V) are applied to ERMs, anodic or cathodic reactions may take place and generate diffusive radicals or reactive species such as reactive oxygen/chlorine species, causing direct or indirect oxidation or reduction of aqueous species .

Electrochemical membranes are featured for high electrical conductivity, electrochemical activity and water permeability. Various organic and inorganic materials

have been reported to fabricate ERMs, including conductive polymers (e.g., polyaniline, polythiophene and polyacetylene) , carbon-based nanomaterials such as multi-wall carbon nanotubes (MWCNTs) and graphite , metallic membranes (e.g., Cu) , and ceramic/metal oxides membranes such as alumina (Al_2O_3), zirconia (ZrO_2), and titania (TiO_2)), silica (SiO_2), and Magnéli phase Ti_4O_7). Conductive ceramic membranes particularly demonstrate high chemical inertness, excellent thermal stability, outstanding mechanical strength, and long service life. Except for Magnéli phase Ti_4O_7, most ceramic materials (e.g., Al_2O_3, ZrO_2, and TiO_2) are non-conductive and require the construction of a conductive catalyst layer for electrochemical reactions. For example, MWCNTs-based materials and carbon−metal nanohybrids (e.g., Fe_3O_4 conjugated with g-C_3N_4) as a conductive layer were reported due to their high conductivity and reactivity . Zhang et al. coated CNTs onto a ceramic membrane by pyrolysis for organic wastewater treatment . Wang et al. reported that CNT-functionalized ceramic membrane possessed high hydrophilicity, permeability, and conductivity, which promoted the generation of reactive (radical) chlorine species (RCS) through anodization of chloride ions for membrane self-cleaning .

Practical implementations of electrochemical membranes are largely hampered by electrode material stability and operational cost for long-term use . For instance, ERMs are often needed to operate at relatively high overpotentials to effectively degrade persistent pollutants. However, high electrode potentials not only cause high electrical consumption and risks of inducing undesirable water oxidation or oxygen evolution on anode or chlorine or hydrogen gas evolution on cathode . Furthermore, high electrode potentials may lead to detrimental impacts on electrochemical membrane properties (e.g., aging or passivation),

as characterized by the loss of conductivity, reactivity and even mechanical integrity or stability. Conversely, only a few studies have reported the membrane aging on limited materials such as the Magnéli phase Ti_4O_7 that could be oxidized into TiO_2 or other titanium phases in oxidative environments . Halali et al. also reported that CNT/PVA coated electrically conductive membranes were physically unstable during the filtration as indicated by the PVA leaching under 2–4 V vs. Ag/AgCl reference electrode . Three standardized methods such as electrochemical oxidation, surface scratch testing, and pressurized leaching were employed to assess the electrochemical, chemical, and physical stability of such membrane coatings . The related aging mechanisms are not well understood and deserve research efforts to support the rational design and operation of electrochemical membrane systems.

The other important concern is the formation of poisonous halo-oxyanions and halogenated by-products in the electrochemical treatment . Strong anodic oxidation could yield chlorate (ClO_3^-), perchlorate (ClO_4^-), and bromate (BrO_3^-) in the treated water , especially when Cl^- and Br^- concentrations are high (500-4000 mM). ClO_4^- is laborious to reduce to Cl^- once it is formed and presents serious health risks. The halogenation of organic compounds can lead to the production of halogenated by-products such as trihalomethane and polybrominated biphenyl that are significantly more toxic than the precursor compounds. However, electrochemical production of these halogen oxides or halogenated organic matters requires certain reaction times due to relatively low reaction rate constants (e.g., the formation rate constant of ClO_3^- is around $2.4–12\times10^{-6}\ s^{-1}$) . To avoid these byproducts, applying proper electrode potentials is essential to address this critical challenge.

The objectives of this study aim to unravel electrochemical membrane aging mechanisms and byproducts formation using two model electrocatalyst-membranes: hybridized MWCNTs coated ceramic membrane (MWCNTs/CM) and Fe_3O_4@g-C_3N_4 loaded ceramic membrane (Fe_3O_4@g-C_3N_4/CM), which have been reported for the degradation of organic dyes , tetrabromobisphenol A (TBBPA) , and diclofenac . For example, g-C_3N_4 hybrids with Fe_3O_4 composite has been reported owing better electrochemical performance than pure g-C_3N_4 . Membrane filtration experiments were performed in the single pass, permeate flow-through operational mode under variations of the initial concentrations of sodium chloride (NaCl) and sodium bromide (NaBr), solution pH and applied electrode potentials. The membrane aging of the two types of hybridized ERMs were thoroughly characterized by examining the changes of the membrane's physicochemical and electrochemical properties. Halogenated byproducts in the filtrate were analyzed to establish connections with operational factors such as applied current densities and solution pH values. Ultimately, this work promotes the durable design and operations of efficient and safe electrochemical membrane water filtration.

4.2 Materials and Methods

4.2.1 Anode Membrane Preparation and Characterization

4.2.1.1 Preparation of MWCNTs and MWCNTs-Coated Membrane (MWCNTs/CM).

MWCNTs (>99%) were purchased from Fisher Scientific (USA). The illustration outer diameter and length of CNTs are 20−40 nm and 5−15 μm, respectively. To introduce oxygen-containing functional groups, which could interfere the electron transport in the sp^2 carbonaceous structure, we prepared two kinds of MWCNTs, pristine or untreated

MWCNTs (p-MWCNTs) and oxidized MWCNTs (o-MWCNTs). p-MWCNTs were produced by hydrochloric acid treatment of the MWCNTs. Briefly, 0.2 g of the MWCNTs powder was dispersed in 200 mL of HCl (36%) and heated at 70 °C under refluxing for 12 h. After heating, the solid sample was cooled to room temperature, rinsed by DI water, and vacuum-filtered to collect the p-MWCNTs. o-MWCNTs were prepared by the oxidation of the p-MWCNTs using a modified Hummers' method , where 0.1 g of p-MWCNTs were dispersed in 60 mL of H_2SO_4 (78%) with 0.1 g of $NaNO_3$ by stirring at an ice bath for 40 min, followed by the addition of 0.2 g of $KMnO_4$ and sonication at 40 °C for 2 h. 20 mL of H_2O_2 (30%) was then added and the mixture was stirred under reflux at 70 °C for 40 min. After heating, the resulting mixture was centrifuged, diluted, vacuum-filtered, and rinsed with DI water to obtain the o-MWCNTs.

A commercial ceramic membrane (47N014, Sterlitech Corporation, US) was chosen as a membrane support for catalyst coating. This flat-sheet membrane is made of a zirconia/titania (Zr/TiO_2) coating on an alumina (α-Al_2O_3) owing a nominal pore size of 140 nm, a diameter of 4.6 cm and an effective surface area of 17.34 cm^2. The membrane was rinsed rigorously with deionized (DI) water before use to remove loosely attached particles or impurities. To obtain hybridized MWCNTs-coated membrane (MWCNTs/CM), p-MWCNTs and o-MWCNTs were dispersed in DMSO at 0.5 $mg \cdot mL^{-1}$ with a 10:1 mass ratio followed by ultrasonication for 15 min to obtain a hybridized MWCNTs suspension, which was then vacuum filtered through the planar ceramic membrane at a loading rate of 1 $mg \cdot cm^{-2}$. The 10:1 mass ratio of p-MWCNTs and o-MWCNTs was chosen to obtain the optimal surface states of hydrophilicity and conductivity and high water permeability as reported previously . The fabricated membrane was then rinsed by sequential filtering of

50 mL of ethanol, 50 mL of 1:1 DI water/ ethanol, and 100 mL DI water to remove the residual DMSO, followed by desiccating at 70 °C for 60 min.

4.2.1.2 Preparation of Fe_3O_4 NPs, Fe_3O_4 NPs@g-C_3N_4 and Fe_3O_4 NPs@g-C_3N_4-coated Membranes. To synthesize Fe_3O_4 nanoparticles (NPs), 0.67 g of the $FeCl_3$ $6H_2O$ was dissolved in 50 mL of ethylene glycol to form a well-mixed solution. Then, the controlled amount of sodium acetate, (1.08 g) was added to the prepared ethylene glycol solution at room temperature under magnetic stirring. The resultant homogeneous mixture was then transferred to a 100 mL Teflon lined stainless steel autoclave and incubated at 200 ^{o}C for 24 h. After the incubation, the black solid precipitates were collected by magnetic separation and washed with ethanol three times. The final products were dried in a vacuum oven at 40 ^{o}C for 6 h. Fe_3O_4@g-C_3N_4 composites were prepared via a two-step self-assembly . The g-C_3N_4 solid was prepared by heating melamine to 550 ^{o}C for 2 h in N_2 atmosphere. After that, the g-C_3N_4 solid was grounded and mixed with 10 ml methanol under ultrasonic mixing for 30 min. Finally, the mixture of Fe_3O_4 and g-C_3N_4 with a weight ratio of 5 wt% (Fe_3O_4 to g-C_3N_4) was ultrasonicated for 30 min and stirred in a fume hood for 24 h to remove methanol. The obtained solids were calcined in a muffle furnace at 150 °C for 4 h.

The Fe_3O_4@g-C_3N_4 composite was dispersed in Dimethyl sulfoxide (DMSO) at 0.5 $mg \cdot mL^{-1}$ and ultrasonicated for 15 min to obtain a Fe_3O_4@g-C_3N_4 suspension, which was loaded onto the ceramic membrane at 1 $mg \cdot cm^{-2}$ by vacuum filtration of the as-prepared Fe_3O_4@g-C_3N_4 suspension through the pristine ceramic membrane with an effective membrane area of approximately 17.34 cm^2. The membrane was then rinsed by sequential filtering of 50 mL of ethanol, 50 mL of 1:1 DI water/ethanol, and 100 mL DI water to

remove the residual DMSO, followed by desiccation at 70 °C for 60 min.

4.2.2 Membrane Surface Aging and Characterization

Membrane aging experiments were performed by continuously filtering the 100 mM NaCl solution at 350 $L \cdot m^{-2} \cdot h^{-1}$ under pressure of 1.0 bar (14.5 psi) for 5 days (120 hours) through the modified membranes that were applied at an anodic potential of approximately 10 V (corresponding to a current density of 20 $mA \cdot cm^{-2}$). To analyze membrane aging, cyclic voltammetry (CV) was conducted to measure the electroactive properties of the anode membrane materials before and after applications of DC currents and liquid permeate filtration. Briefly, the standard three-electrode system was established with the two anode membranes as working electrode, the Ag/AgCl (in 1.0 M KCl) as reference electrode, and a 3-mm platinum wire as the counter electrode. CV curves will be mapped on a CHI 700E electrochemical workstation (CH Instrument, USA). All the measured electrochemical potentials are referenced to the Ag/AgCl electrode potential (considered as 0 V). The electrolyte solution is 10 mM $K_3Fe(CN)_6$ (a redox mediator) in 0.5 M KCl as a supporting electrolyte. The CV curves were obtained by sweeping from -0.4 to 1 V versus Ag/AgCl at a scan rate of 0.05 $V \cdot s^{-1}$. Chronoamperometry (CA) was also conducted in 100 mM NaCl electrolyte at 10 V versus Ag/AgCl. All electrochemical measurements (CV, CA and EIS) of the ERMs were performed using Ag/AgCl (in 1.0 M KCl) as reference electrode, and a 3-mm platinum wire as the counter electrode.

Electrochemical impedance spectrometry (EIS) will be further conducted to investigate the electrochemical properties of the anode membranes. The anode membranes were performed under open circuit potential (OCP) of 0.3 V vs Ag/AgCl at the frequency range of 100 kHz to 0.01 Hz in aqueous solution containing 10 mM $K_3Fe(CN)_6$ with 0.5

M KCl solution. Furthermore, the obtained EIS data were split/fitted into electrolyte resistance, charge-transfer resistance, and resistance of solid/electrolyte interface to examine the changes in electrode conductivity in detail. During EIS measurements, total impedance of the membrane system (Z_m) is measured as a function of frequency (*f*) and the resulting data is represented on a Nyquist plot and the obtained data is interpreted by using a ZSim 3.0 software.

The morphologies of the MWCNTs and Fe_3O_4@g-C_3N_4 composites or nanohybrids and ceramic membrane with/without catalyst coating were examined using scanning electron microscope coupled with an energy dispersive spectrometer (SEM-EDS, JEOL JSM-7900F). Hydrodynamic particle size distribution (PSD) and zeta potential of the MWCNTs and Fe_3O_4@g-C_3N_4 suspension were measured by dynamic light scattering (DLS) on a Zetasizer nano ZS instrument. Fourier transform infrared spectroscopy (FTIR) of the MWCNTs and Fe_3O_4@g-C_3N_4 nanohybrids were recorded on a bench top FTIR-spectrometer (Cary 670, Agilent Technologies, USA) applied with Diamond ATR at classical transmission method. Raman spectroscopy (DXR2Xi Raman imaging microscope, Thermo Fisher Scientific, Madison, USA) was performed with the laser wavelength of 532 nm and power of 8 mW.

The surface chemical compositions tested using an X-ray photoelectron spectroscope (XPS, Specs Analyzer & Bruker IR, USA). Bulk scale contact angle measurement was conducted on an optical contact angle goniometer (JC2000DM, Powereach, Shanghai, China). The probing liquid selected for this investigation is deionized (DI) water (18.2 MΩ cm at 25 ^{o}C, Direct-Q® UV3 System, EMD Millipore, Bedford, MA, USA). The water contact angle was measured as following procedure. A

drop of DI water (~5 μL) was placed on a dry membrane surface. At least three liquid drops at different locations were used to obtain the average contact angles for each ceramic membrane sample. The image of the liquid drop was taken within 10 s to determine the air–liquid–surface contact angles with the ImageJ software.

4.2.3 Electrochemical Membrane Filtration Assessment

Electrochemical membrane filtration experiments were conducted by a dead-end membrane filtration cell as illustrated in **Figure 4.1**. The Fe_3O_4@g-C_3N_4 loaded ceramic membrane (Fe_3O_4@g-C_3N_4/CM) or MWCNTs coated ceramic membrane (MWCNTs/CM) was served as the anode with a stainless-steel mesh (diameter 4.5 cm) as the cathode. The measured distance between set-up anode and cathode was 8 mm. A copper wire was directly connected to the coating layer of the membrane and then covered by epoxy to prevent exposure to water. Reactive oxygen species (ROSs), reactive chlorine species generation and bromate generation highly depend on the concentrations of chloride or bromide and applied anode potentials. Thus, the feed solution was prepared with the NaCl or NaBr concentrations of 50 mM, 100 mM, 200 mM and 400 mM. These high concentrations were selected to facilitate the detection of the byproducts during electrochemical experiments. Moreover, the high salinity conditions are relevant for the brine wastewater generated from oil and natural gas production, which may contain chloride and bromide at a wide range (e.g., 1~200 $g \cdot L^{-1}$) . The applied cell voltage was applied within 3-15 V, resulting in the current density of 1, 5, 10, and 20 $mA \cdot cm^{-2}$ (corresponding to an anodic potential of approximately 1 V, 2 V, 5 V and 10 V vs Ag/AgCl, respectively). During the electrochemical membrane filtration, the current densities were controlled at fixed levels by a DC power generator (DC power supply YH-302D). The

solution pH value can affect the formation of byproducts and was adjusted to 2.0, 7.0, and 13.0, to compare the changes of byproduct formation. The pH value of the feed solution was adjusted with 1.0 M NaOH solution and 1.0 M HCl solution. Filtration lasted for about one hour. After stabilizing the electrochemical filtration for 15 minutes, the filtered solution was collected for sample testing every 10 minutes.

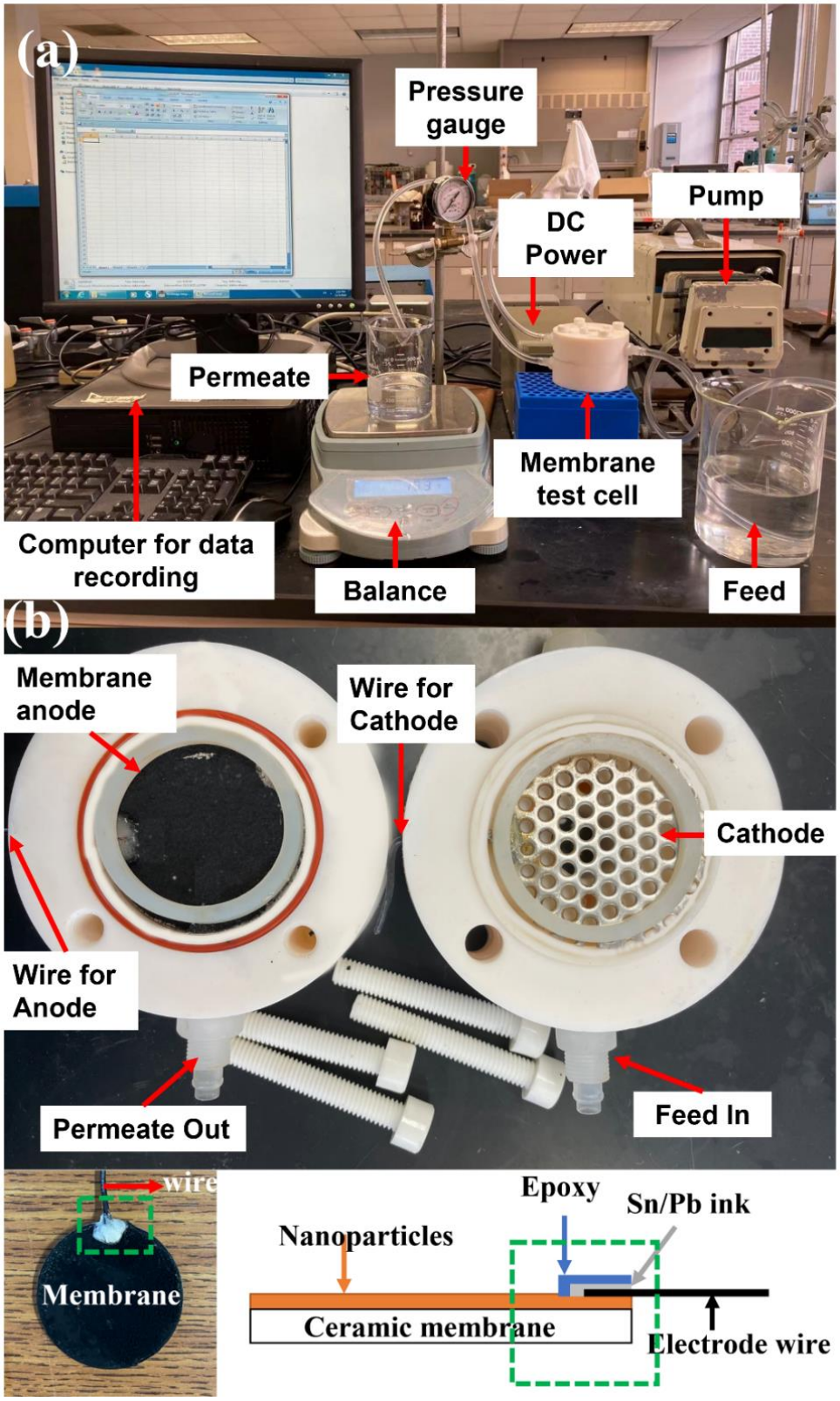

Figure 4.1 (a) Photographs of electrochemical membrane filtration system. (b) The zoom-in photo of the electrochemical membrane cell and detailed illustration of the electrochemical membrane.

The overall porosity (P_r) of the membrane was determined by a gravimetric method. Briefly, the ceramic membranes were immersed in water and fully soaked (or ran filtration to allow water to flow through all pores. Then wet ceramic membranes weight (m_w) was measured and the difference from the dry ceramic membranes (m_d) was determine. This difference represents the weight of pure water in the membrane pores, which can be used to calculate the overall porosity as defined in the following equation:

$$P_r = \frac{m_w - m_d}{\rho AL} \tag{4.1}$$

where m_w is the weight of the wet membrane (after immersed in water for 24 hours); m_d is the weight of the dry membrane; A is the membrane effective area (m^2), ρ is the water density (0.998×10^6 g·m^{-3}), and L is the membrane thickness (m).

In addition, to determine the membrane mean pore radius (r_m), the Guerout–Elford–Ferry equation in Equation (4.2) on the basis of the pure water flux and porosity data was utilized:

$$r_m = \sqrt{\frac{(2.9 - 1.75P_r) \times 8\eta LQ}{P_r \times A \times \Delta P}} \tag{4.2}$$

where η is the water viscosity (8.9×10^{-4} Pa·s), Q is the volume of permeate water per unit time (m^3·s^{-1}), and ΔP is the operation pressure (1.0×10^3 Pa).

The permeate flux was calculated by the Darcy's equation in Equation (4.3), commonly expressed in units of liters per m^2 of membrane per hour (L · m^{-2} · h^{-1}, LMH):

$$Jw = \frac{V}{At} = \frac{TMP}{\mu(R_m + R_f)} = \frac{P_F - P_P}{\mu(R_m + R_f)} \tag{4.3}$$

where J_w is the permeate flux (LMH), V is the permeate volume (L), t is the time of the permeate collection (h) and A is the effective surface area of the membranes (m^2), TMP is

the transmembrane pressures (Pa), which defined the difference of the hydraulic pressure in the feed stream (P_F) and the hydraulic pressure in permeate stream (P_p). P_F was measured by a pressure gauge (PEM-LF SERIES, WINTERS), and P_p was regard as the atmospheric pressure. R_m (the inherent membrane resistance) and R_f (the fouling layer or coating layer resistance) contribute to the total membrane hydraulic resistance (for clean membranes, $R_f = 0$), and μ is the dynamic viscosity of water at 25°C (0.8937×10^{-3} N·s·m^{-2}).

Chloride, chlorite, chlorate, bromide and bromate concentrations in the permeate were measured by a Dionex ICS-1500 Ion Chromatography System (ICS-1500) equipped with the AS50 autosampler, and an IonPac AS22 column coupled to a conductivity detector (31 mA). For separation of those anions, we used 23 mM NaOH as the eluent. Operation was isothermic at 30°C with a flow rate of 1 mL·min^{-1}. All synthetic standard solutions were prepared using deionized water (DI). The stock standard solutions containing 1000 mg L^{-1} of chloride, chlorite, chlorate, bromide and bromate were purchased from Fisher Scientific of SPEX CertiPrep. Working standard solutions of all chemicals were carefully prepared by dilution of stock solutions using an opaque plastic volumetric flask and deionized water. The specific Ion Chromatography filters (IC Acrodisc Syringe Filters,13 mm, 0.2 um) were purchased from Fisher Scientific. All liquid samples were filtered with 0.22-μm IC Acrodisc filters to remove particles and prevent clogging.

Visual MINTEQ (3.1) software was used to simulate the speciation and evolution of chemicals in the aqueous system at different applied potentials or redox potentials. Cl^- ions concentrations at 0.05-0.4 M were used in modeling programs under a temperature of 25 °C. The evaluation of various chlorine species versus redox potentials and solution pH were conducted.

4.3 Results and Discussion

4.3.1 Membrane Filtration Performance Assessment

Table 4.1 summarizes the measurements of permeate fluxes, porosity and pore sizes of the pristine and aged membranes. The electrochemical aging treatment did not result in remarkable changes to the filtration performance of the two membranes. However, the permeate flux increased slightly after the aging treatment due to the minor increase in surface hydrophilicity of the two modified membranes, as indicated by the smaller water contact angles as shown in **Table 4.2**. High surface hydrophilicity improves the water interactions and thus leads to a rise in permeation flux. The overall porosity and pore sizes before and after modification barely changed with variations from 16% to 18%. The mean pore size reduced slightly from 294±12 nm to 258±14 nm and 264±12 nm for MWCNTs/CM and Fe_3O_4@g-C_3N_4/CM respectively, due to the presence the dense layers of MWCNTs or Fe_3O_4@g-C_3N_4/CM. The overall porosity and pore sizes before and after aging treatment did not result in remarkable changes due to the minor electrocatalyst aging.

Table 4.1 Properties of the Membrane Permeate Flux, Porosity and Mean Pore Radius

Membrane	Permeate flux (LMH)	Porosity (%)	Mean pore radius (nm)
CM	1283.60±14	16.65%	294±12
MWCNTs/CM	1300.20±22	18.57%	258±14
Aged MWCNTs/CM	1309.71±20	18.37%	252±11
Fe_3O_4@g-C_3N_4/CM	1328.16±24	18.28%	264±12
Aged Fe_3O_4@g-C_3N_4/CM	1332.04±28	17.87%	260±16

The water contact angle measurements on the pristine CM and two modified CMs are shown in **Table 4.2**. Multiwalled carbon nanotubes (MWCNTs) nanomaterial has hydrophobic nature. However, chemical treatments are usually used to provide hydrophilicity by introducing hydrophilic/functional moieties or macromolecules on a

MWCNTs surface. A hydrophilic MWCNTs modified membrane could produce excellent membrane properties due to higher hydrophilicity, higher porosity, and smoother surface structure. Those excellent membrane properties are followed by remarkable membrane performances such as increased permeability, increased rejection, anti-trade-off between permeability and selectivity. Compared with the pristine ceramic membranes, the presence of MWCNTs significantly increased the hydrophilicity as indicated by the decreased water contact angles. The increased surface hydrophilicity is ascribed to the abundance of hydrophilic oxygen-containing functional groups on the hybrids MWCNTs and hydrophilicity of Fe_3O_4. As shown in **Table 4.2**, the hydrophilicity of two modified membrane slightly increased after the aging treatment as indicated the contact angle decreased. The decreasing contact angle of the modified membranes is mostly due to the presence of hydrophilic hydroxyl groups and carboxylic groups presence after aging.

Table 4.2 Average Contact Angles of the Pristine and Modified Membranes

Membrane	Contact angle of DI Water (°)	
	As prepared	Aged
Pristine CM	62 ± 1	NA
MWCNTs/CM	35 ± 2	33 ± 2
Fe_3O_4@g-C_3N_4/CM	43 ± 3	41 ± 3

4.3.2 Morphological Characterization Before and After Aging Treatment

Figure 4.2 shows the typical SEM figures of the p-MWCNTs, o-MWCNTs, Fe_3O_4 NPs, g-C_3N_4 sheet and Fe_3O_4@g-C_3N_4. The MWCNTs diameter and length distributions are 20−40 nm and 5−15 μm as measured from **Figure 4.2a**. The pure Fe_3O_4 NPs exhibited a spherical morphology with a size diameter in the range of 200-300 nm (**Figure 4.2c**). **Figure 4.2d** shows the pure g-C_3N_4 sample was composed of different sizes crystals stacking layers. **Figure 4.2e** shows the conjugated state of Fe_3O_4@g-C_3N_4, where g-C_3N_4

is expected to be those irregular aggregated particles about several micrometers in size. Moreover, g-C_3N_4 has small pores due to the gas discharge from the melamine decomposition. Fe_3O_4@g-C_3N_4 exhibited a sheet-like structure with spherical Fe_3O_4 NPs deposited on the g-C_3N_4 sheet surfaces as marked in red circles.

The top view and cross-section images of pristine CM, MWCNTs/CM and Fe_3O_4@g-C_3N_4/CM in **Figure 4.3d** show that the surface of pristine ceramic membranes contains pores with hundreds nanometers, which is consistent with the reported 140 nm pore size by the manufacturer. **Figure 4.3e** shows that the coating layer of MWCNTs/CM are in possession of the typical morphology of MWCNTs as shown in **Figure 4.2a and 4.2b**. The cross section images of the MWCNTs/CM indicate that MWCNTs formed a layer with a thickness of ~11 μm. For the Fe_3O_4@g-C_3N_4/CM, **Figure 4.3f** shows the ceramic membrane is covered with many irregularly shaped particles. The cross section image of the Fe_3O_4@g-C_3N_4/CM reveals the layer thickness of ~7 μm.

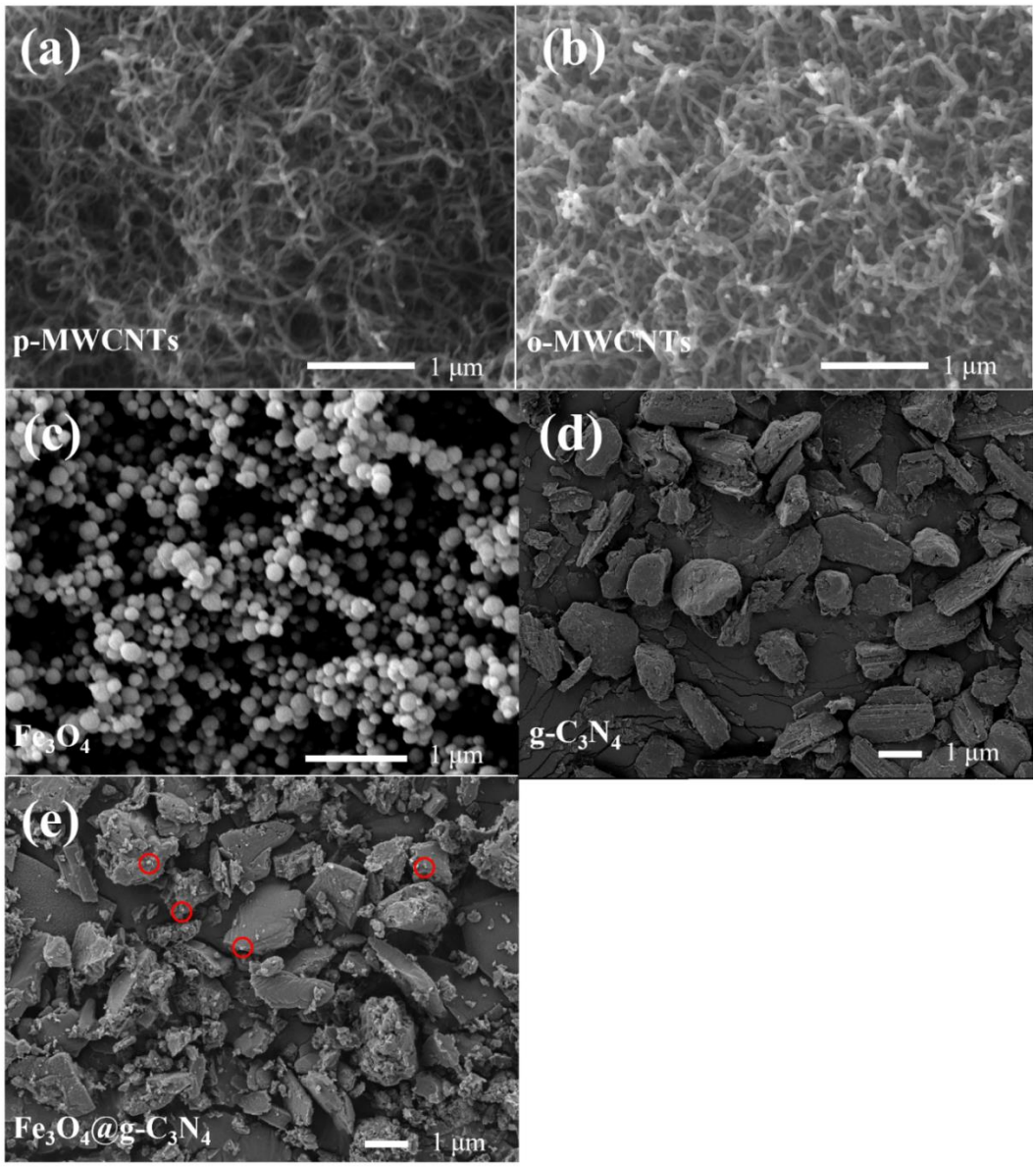

Figure 4.2 SEM images of (a) p-MWCNTs, (b) o-MWCNTs, (c) Fe_3O_4 NPs, (d) g-C_3N_4 sheet and (e) Fe_3O_4@g-C_3N_4.

Figure 4.4 compares the surface morphology of the two functionalized membranes before and after aging treatment. There are no apparent visual differences for MWCNTs/CM, indicating that the aging treatment had no considerable impacts on the physical integrity of hybridized MWCNTs or its coating structure. Electrochemical oxidation of MWCNTs by the BDD anode was previously reported under 710-2840

mA·cm^{-2} . The oxidized MWCNTs has transformed from a highly bundled state to a de-bundled state. The amorphous carbon tends to get smaller and become isolated after oxidation, which is not observed in our study

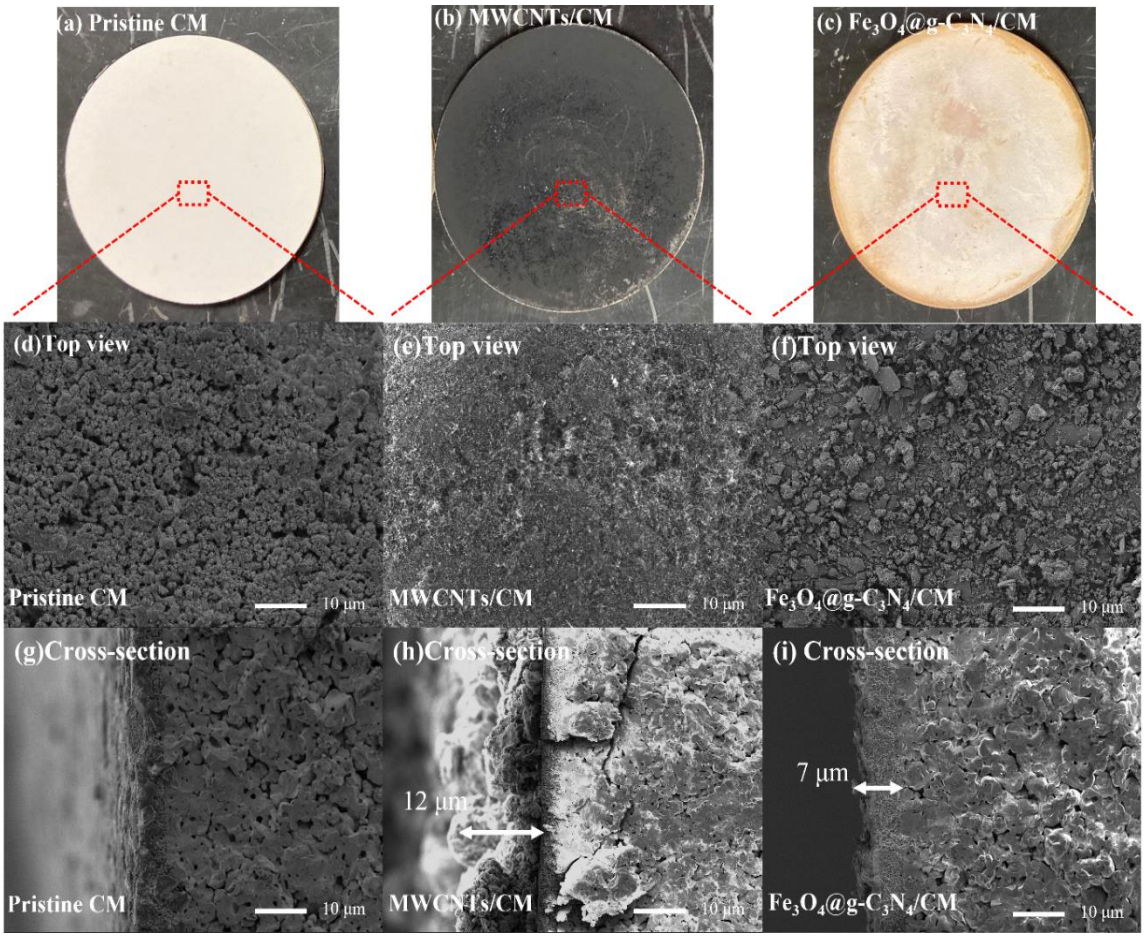

Figure 4.3 (a)-(c) Photographs and (d)-(f) SEM images top view of the pristine CM, MWCNTs/CM, and Fe_3O_4@g-C_3N_4/CM, and (g)-(i) cross-section of the pristine CM, MWCNTs/CM, and Fe_3O_4@g-C_3N_4/CM.

In addition, the SEM images in **Figure 4.4** shows significant differences in surface morphology between the pristine and the aged Fe_3O_4@g-C_3N_4/CM. After aging, the bulk graphitic carbon nitride seems to be fractured and has an increased surface roughness. Oxidation treatment of g-C_3N_4 results in the formation of spherical nanoparticles , which may explain the increased surface roughness of the aged membrane. This morphological

change might be responsible for the formation of the mesoporous graphitic carbon nitride or oxidized g-C_3N_4 .

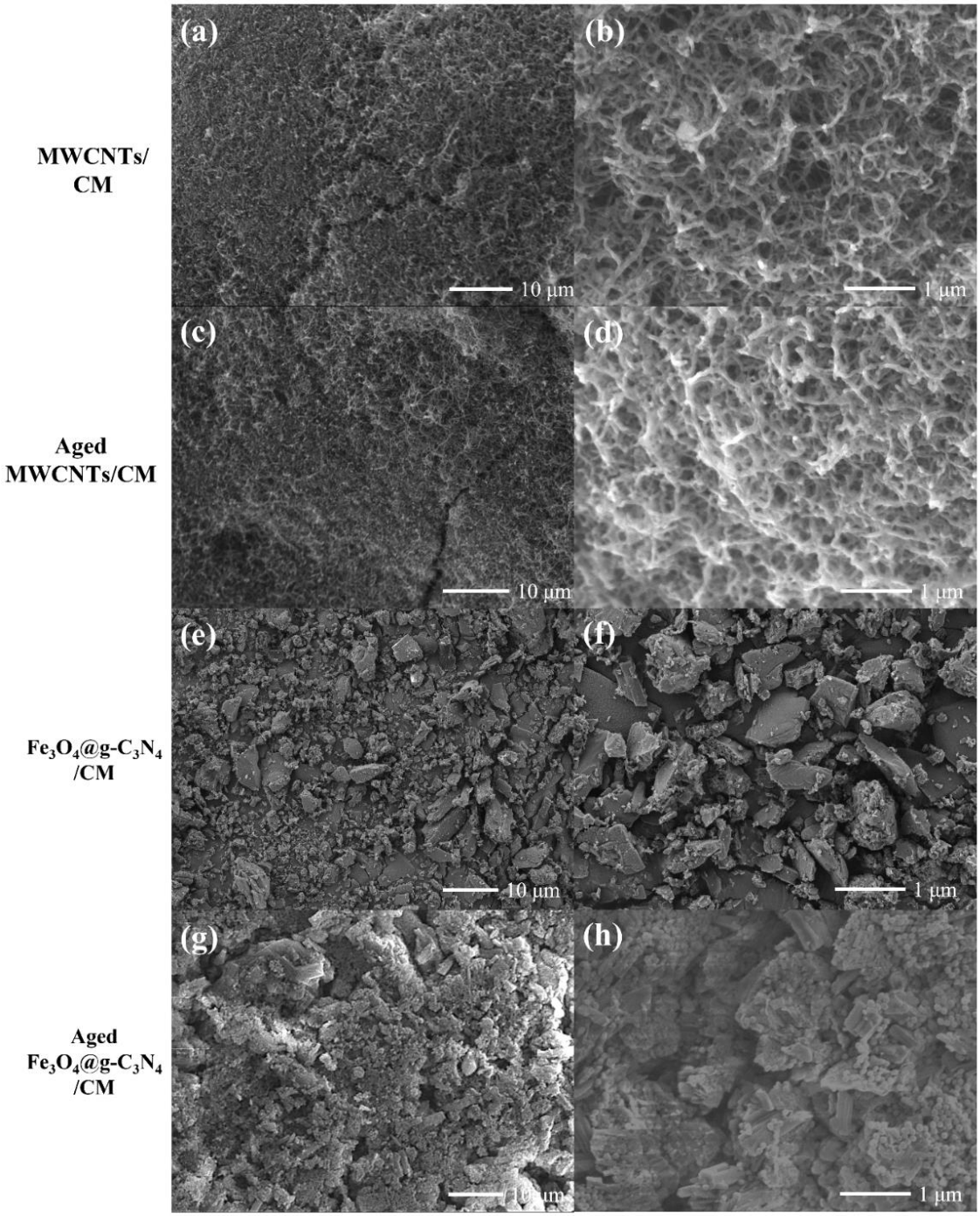

Figure 4.4 Photographs of the pristine and aged MWCNTs/CM and Fe_3O_4@g-C_3N_4/CM. (The left column is obtained at a low magnification and the right column is at a high magnification)

4.3.3 Surface Chemical Characterization Before and After Aging

Figure 4.5a shows the FTIR spectra of Fe_3O_4 that has one strong absorption at 590 cm^{-1} assigned to the Fe-O stretching vibration . However, this peak declined in Fe_3O_4@g-C_3N_4 samples due to the reduced content of Fe_3O_4 (5%). Both g-C_3N_4 and Fe_3O_4@g-C_3N_4 yielded the absorption at 810 cm^{-1}, 1100 cm^{-1}, 1470 cm^{-1} and 1630 cm^{-1} attributed to the breathing and stretching vibrations related to C−N and C=N of triazine units of g-C_3N_4, respectively . Compared with the pristine Fe_3O_4@g-C_3N_4, the aged Fe_3O_4@g-C_3N_4 had an evident decrease of the peak intensity at 1100 cm^{-1} that is assigned to the stretching of C–N bond (**Figure 4.5b**), due to the transformation of C–N into C–O during aging treatment . The FTIR spectra of the p-MWCNTs and o-MWCNTs show a peak at 1670 cm^{-1} that could be associated with the C=O stretch mode of carboxylic groups due to the acid treatment. Additionally, o-MWCNTs show four major peaks at 3230, 1670, 1530, and 1200 cm^{-1}, respectively, which correspond to the hydroxyl groups, the C=C bond stretching, the C=O stretching, and the C–O bond stretching . Moreover, **Figure 4.5b** shows the peak intensities assigned to C=O and C–O bond are slightly higher for aging membrane when compared to that of the pristine membrane, probably because of the increase of the amount of the new functional groups (e.g., COOH). Li et al. reported two possible mechanisms of interactions between hydroxyl radicals and MWCNTs , radical attack on defect sites and unsaturated bonds of MWCNT sidewalls.

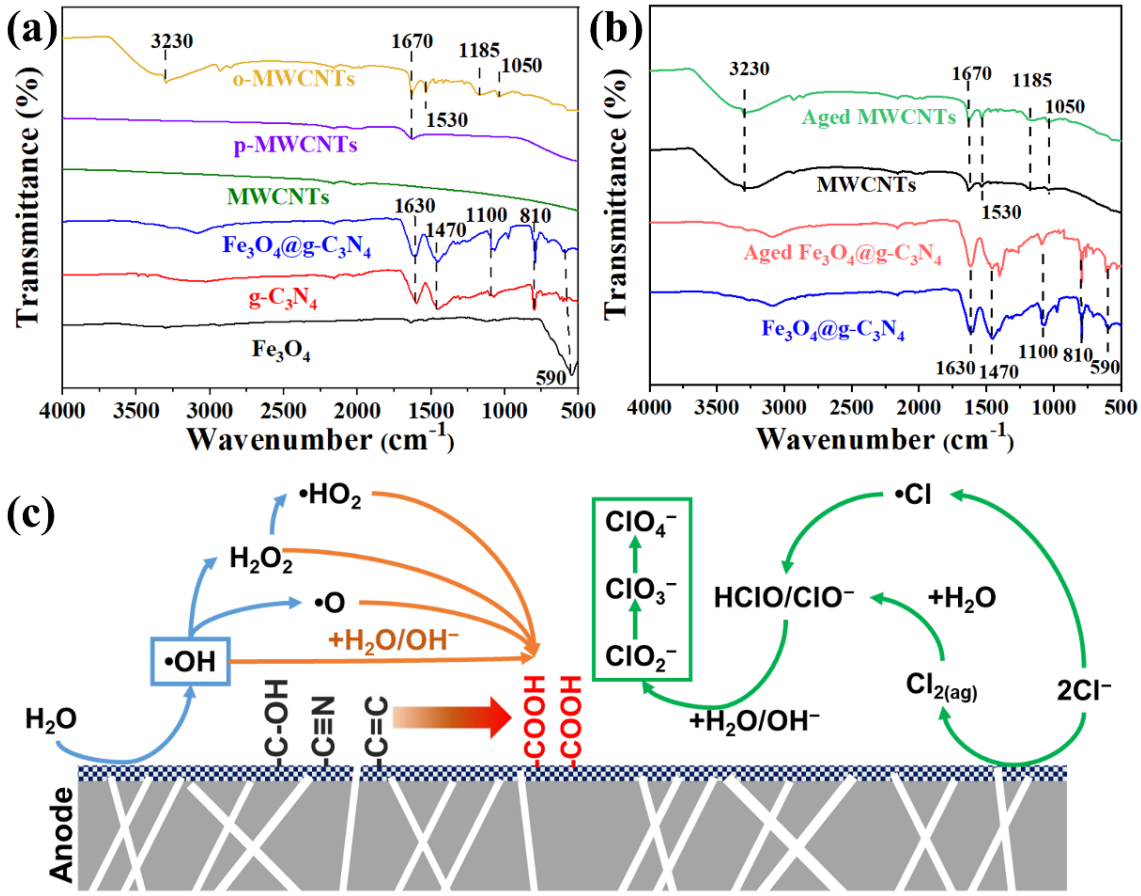

Figure 4.5 (a) FTIR spectra of Fe_3O_4, g-C_3N_4, Fe_3O_4@ g-C_3N_4, MWCNTs, p-MWCNTs and o-MWCNTs. (b) FTIR spectra of the pristine Fe_3O_4@ g-C_3N_4, aged Fe_3O_4@ g-C_3N_4, MWCNTs and aged MWCNTs. (c) Proposed mechanism of membrane aging and byproduct formation in filtration process.

The XPS spectra show the C 1s, N 1s and Fe 2p peaks for the pristine Fe_3O_4@g-C_3N_4 (**Figure 4.7a, 4.7c** and **4.7e**) and the peaks of aged Fe_3O_4@g-C_3N_4 (**Figure 4.7b, 4.7d** and **4.7f**). For instance, **t**he C 1s peak at 284.5 eV is assigned to sp^2 C=C bonds. The appearance peak at 286 eV (C−N or C−O bond) in the aged Fe_3O_4@g-C_3N_4, based on the deconvolution of the C 1s signal is likely related to carboxyl groups formed at the edges of the g-C_3N_4 sheets during aging treatment. The N 1s spectra (**Figure 4.7b** and **4.7d**) are deconvolved into two peaks at 396.5 eV and 398.3 eV, which correspond to the sp^2-hybridized nitrogen in N−C=N groups and the amino function groups. The disappearance

of the N−C=N intensity at 396.5 eV suggests the oxidation of C=N to tertiary nitrogen, secondary amines and nitroso groups or even the loss of N element. **Figure 4.7e** and **4.7f** shows the Fe 2p XPS spectrum of the Fe_3O_4@g-C_3N_4 composite. Two broad peaks at 724.2 and 711.2 eV correspond to Fe $2p_{1/2}$ and Fe $2p_{3/2}$, respectively. The Fe $2p_{3/2}$ spectrum can be divided into two areas, which correspond to Fe^{2+} (710.2 eV) and Fe^{3+} (712.2 eV), respectively. After aging, the percentage of Fe^{3+} (712.2 eV) peak intensity relative to total Fe $2p_{3/2}$ intensity (45.2%) surpassed that of pristine Fe_3O_4@g-C_3N_4 (32.8%), signifying that electrochemical aging led to the transformation of Fe^{2+} to Fe^{3+}. The C 1s spectra of p-MWCNTs and o-MWCNTs can be deconvolved into five peaks at 284.5 eV, 285.4 eV, 286.5 eV, 288.6 eV and 291.0 eV, which correspond to the C=C, C-C, C-O, C=O and C*(π-π*). Compared to the p-MWCNTs, the peaks intensity of oxygen-containing functional groups (−OH, C−O, and C=O) in the o-MWCNTs increased (**Figure 4.6a** and **4.6b**) which indicates that oxygen is introduced to the surface of the o-MWCNTs by the modified Hummers' method. In addition, C1s XPS spectra of hybridized MWCNTs and aged hybridized MWCNTs (**Figure 4.7g** and **4.7h**) also displayed five peaks. After aging, the percentage of carboxyl group peak intensity relative to total C 1s intensity (13.8%) surpassed that of pristine hybridized MWCNTs (10.7%), signifying that electrochemical aging promote the incorporation of carboxyl groups. This result is supported by a previous study reporting that carboxyl (–COOH) group could hinder the electrooxidation of pollutants and increase resistance of charge transfer . Both Fe_3O_4@g-C_3N_4/CM and MWCNTs/CM aging mechanism is depicted in **Figure 4.5c,** C–O, C=N or C=C transfers COOH during aging treatment.

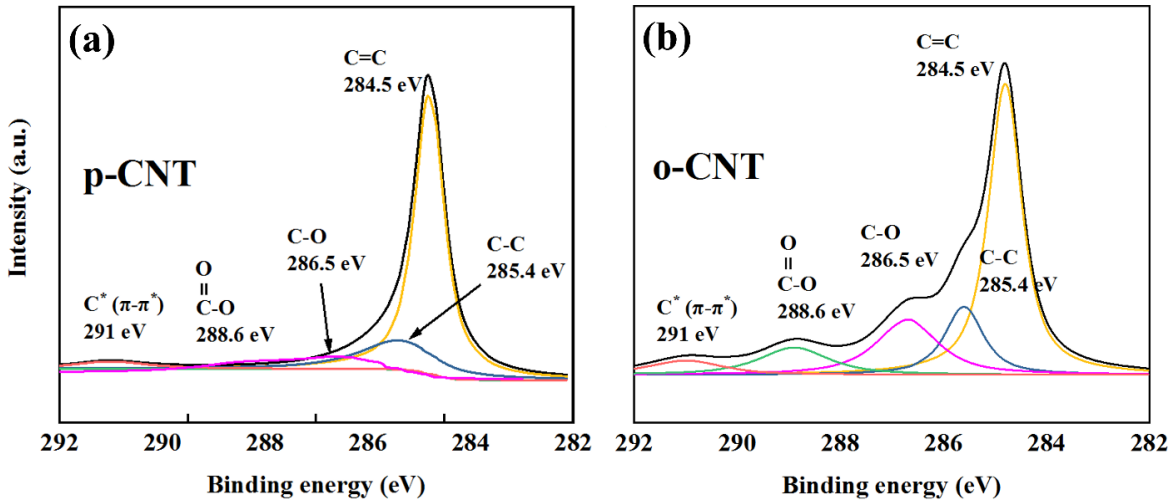

Figure 4.6 XPS spectra of C 1s of (a) p-MWCNTs and (b) o-MWCNTs.

The relative intensity ratio of the D band to the G band (I_D/I_G ratio) represents the degree of disorder in multi-walled carbon nanotube structures. The pristine and electrochemically aged MWCNTs membranes show minor changes in the spectral peak intensity and shape. The aged MWCNTs (blue dotted line) shows a decrease in G band signal relative to the D band signal. The G' bandwidth is also slightly increased due to the formation of defects or hydrogenated amorphous carbon. It is normal to use the D/G intensity ratio as proxy for overall MWCNTs structure order. The observed increase in the D/G band ratio from 0.92 ± 0.08 to 1.25 ± 0.13 (standard deviations at n = 3) indicates a rise in the relative nanotube structure ordering and implies that both disorder structures and the amount of the functional groups after the aging process.

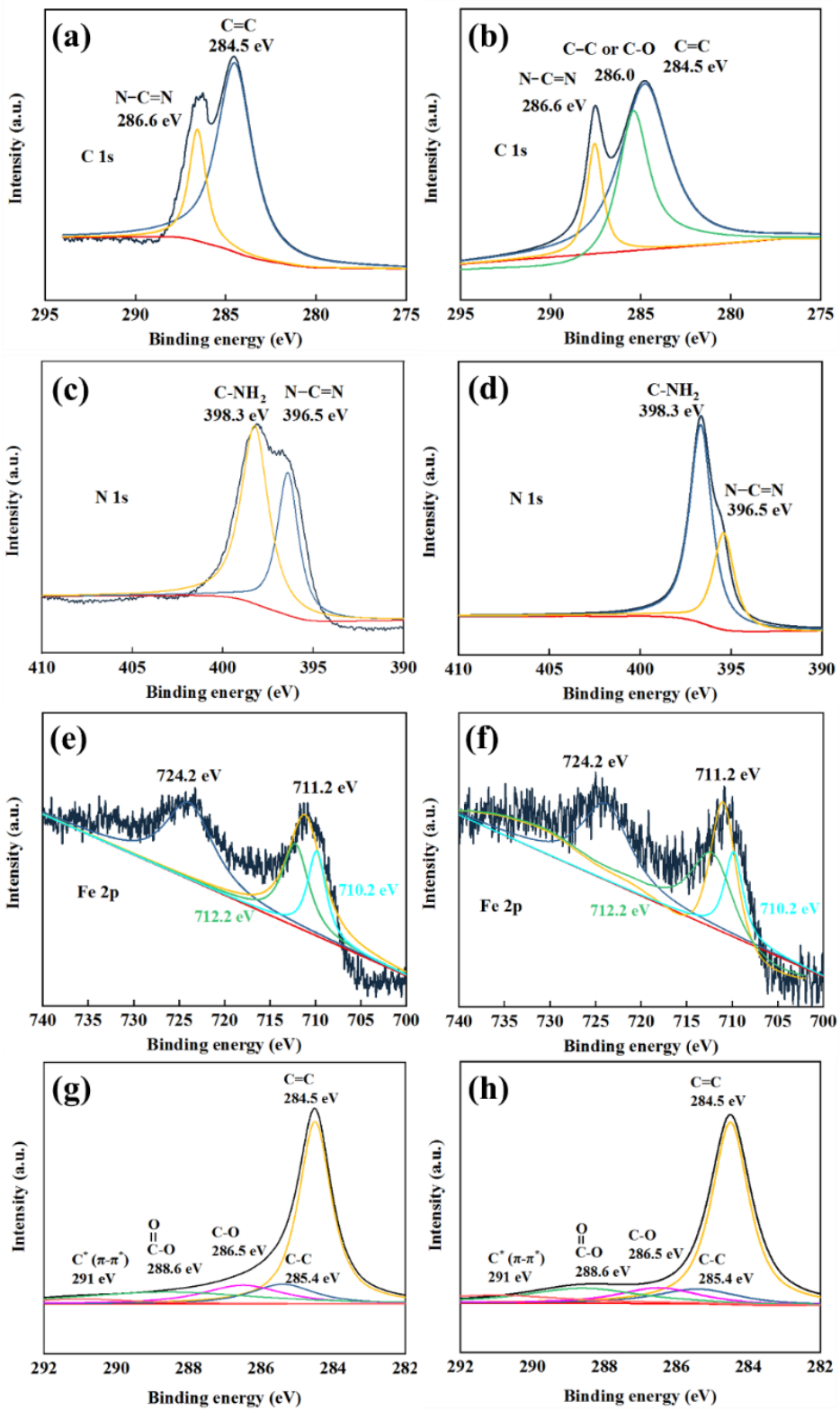

Figure 4.7 XPS spectra of (a) C 1s spectrum of Fe_3O_4@g-C_3N_4 and (b) aged Fe_3O_4@g-C_3N_4, (c) N 1s spectrum of Fe_3O_4@g-C_3N_4 and (d) aged Fe_3O_4@g-C_3N_4, (e) Fe 2p spectrum of Fe_3O_4@g-C_3N_4 and (f) aged Fe_3O_4@g-C_3N_4, (g) C 1s spectrum of hybridized MWCNTs and (f) aged hybridized MWCNTs.

Similarly, magnetite Fe_3O_4 nanoparticles could partially be oxidized under the radical attack or oxygen diffusion that converts Fe^{2+} to Fe^{3+} on the surface. By contrast, g-C_3N_4 has relatively high stability and resistance to electrochemical oxidation largely due to the rich presence of C–N=C and C–NH–C structures. However, continuous oxidation could remove the N element and decrease the surface-active sites. The Raman spectra for Fe_3O_4@g-C_3N_4/CM in **Figure 4.8** consist of two strong Raman modes of D and G around 1342 cm^{-1} and 1564 cm^{-1}, which represents the E_{2g} symmetric vibration mode in the graphite-like structure and disordered sp^2 microdomains introduced by linking with N atoms the presence of defects or disorder in the graphite structure and the stretching vibration modes of C=N and C-N heterocycles. The peak at 680 cm^{-1} is attributed to the conjugated Fe_3O_4 nanoparticles. Similarly, the G band intensity of the aged membrane decreased remarkably similar to the observation on MWCNTs, probably because of the increase of both disorder structures and the amount of the new functional groups (e.g., COOH) on Fe_3O_4@g-C_3N_4 after the aging process. Furthermore, the aged membrane had the reduced D-band and G-band intensities (corresponding to the red region in the Raman mapping in the bottom two rows in **Figure 4.9**).

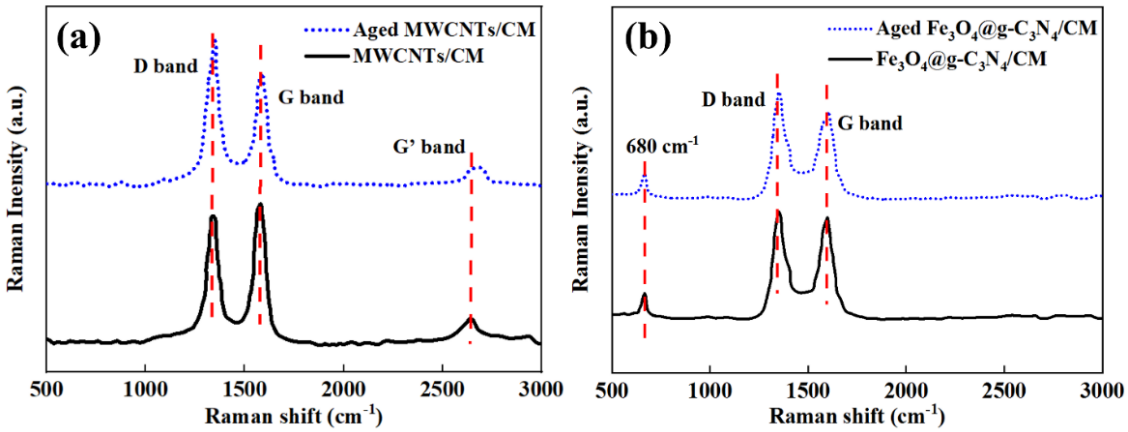

Figure 4.8 Raman spectra of the pristine and aged (a) MWCNTs and (b) Fe_3O_4@g-C_3N_4/ coated on the ceramic membrane (CM).

The surface aging of MWCNTs and Fe_3O_4@g-C_3N_4 modified membranes during electrochemical filtration was studied with Raman spectrometry. The top two rows in **Figure 4.9** compare the surface Raman mapping of the pristine and aged MWCNTs/CM membranes. Pristine MWCNTs/CM samples typically exhibit three characteristic Raman peaks at 1344.5, 1581.2, and 2681.2 cm^{-1}, respectively as shown in **Figure 4.8a**, which correspond to the D band, the G band, and the G' band. The three columns, a, b and c are images generated based on the intensities of D band, G band and the ratio of D/G bands, where some regions have higher intensities (red dots) indicative of the presence of MWCNTs. The aged MWCNTs/CM surface had a remarkable reduction in intensity of these Raman signals compared to that of pristine MWCNTs/CM. The ratio between the intensity of D-band and the G-band is slightly higher for aging membrane when compared to that of the pristine membrane. Moreover, it is possible to identify the locations of the aged MWCNTs on the membrane surface from these mapping images. Similarly, the Raman spectra for the aged Fe_3O_4@g-C_3N_4 in **Figure 4.8b** show the G band intensity decreased remarkably similar to the observation on MWCNTs, probably because of the increase of both disordered structures and the amount of the new functional groups (e.g., -COOH) on Fe_3O_4@g-C_3N_4 after the aging process. Accordingly, the I_D/I_G ratios of MWCNTs/CM and Fe_3O_4@g-C_3N_4/CM were found to increase from 20 % and 25 % to 40 % and 50 %, respectively, indicating that the two electrocatalyst membranes underwent different aging degrees. The I_D/I_G ratio changes also reflect the transformations of C–O, C=N or C=C groups into COOH groups. The loss of N increased the structural defects (e.g., nitrogen vacancies) on g-C_3N_4 as indicated by the relative higher band intensity ratio (I_D/I_G) .

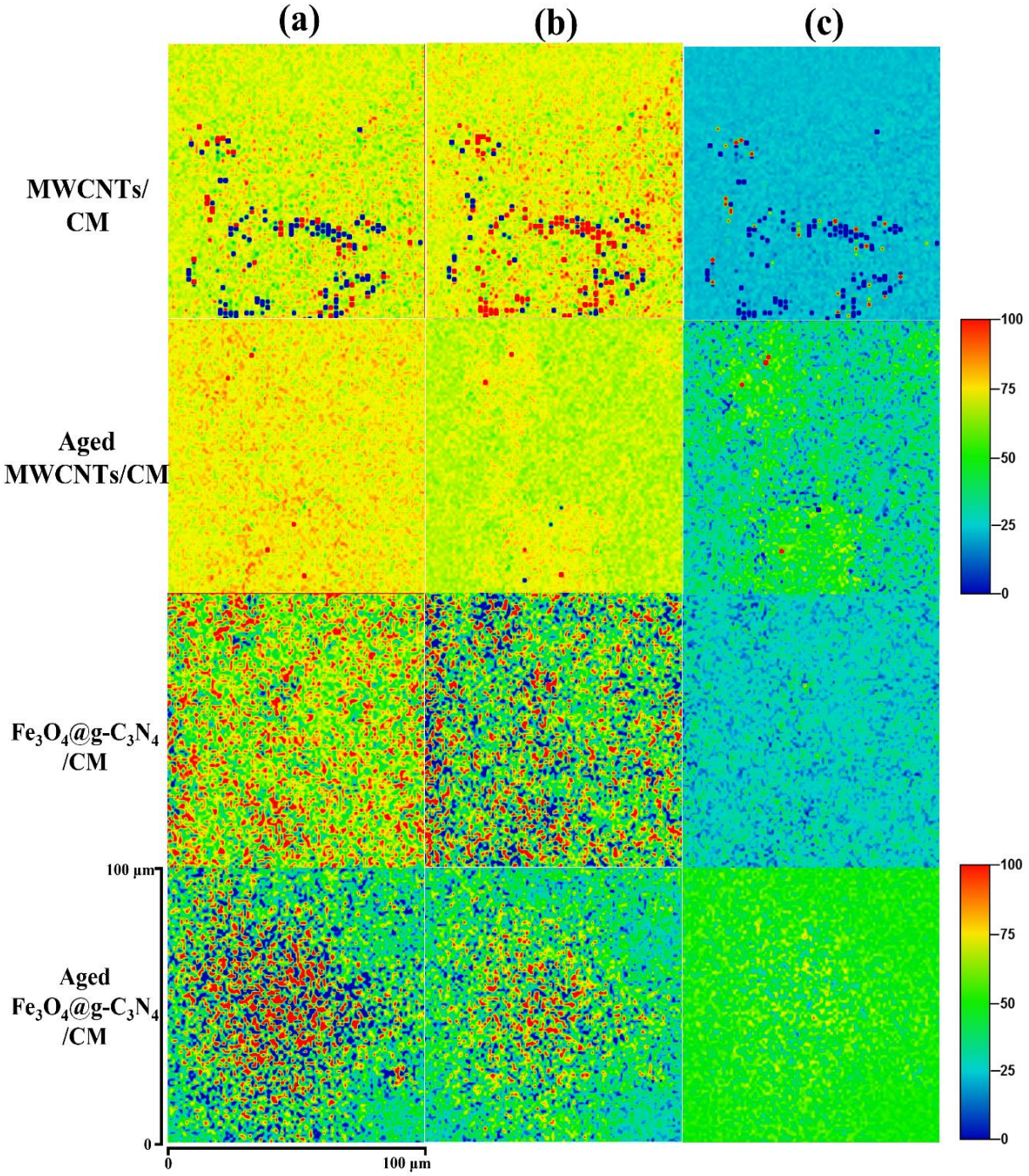

Figure 4.9 Raman mapping of pristine and aged MWCNTs and Fe_3O_4@g-C_3N_4/CM: (a) D band mapping of the membrane surface, (b) G band mapping of the membrane, (c) I_D/I_G ratio contrast imaging of the membrane surface.

4.3.4 Electrochemical Activity Changes

4.3.4.1 Cyclic Voltammetry Assessment for the Pristine and Aged Membranes. The aging degree is often associated with the reduction of the electrochemically active surface area or electroactive sites. Voltametric charge density (Q) is closely related to the amounts of electroactive sites of a porous electrode and was calculated by integrating the CV curves in **Figure 4.10a-4.10d**. Total voltametric charge density (Q_T, mC·cm^{-2}) is the Q value obtained when the scan rate (v, mV·s^{-1}) is zero as indicated by Equation (4.4) and represents the total electroactive surface charge per surface area.

$$(Q)^{-1} = (Q_T)^{-1} + kv^{1/2} \tag{4.4}$$

where k is a constant (no unit). Total voltametric charge density (Q_T) is equal to the sum of the outer voltametric charge density (Q_O) and the inner voltametric charge density (Q_I), which represent the charge related to the outer geometric and the inner unattainable electrode areas, respectively. The ratio between Q_I and Q_T (Q_I/Q_T) is equal to the electrochemical porosity. Q_O is related to the easiest attachable electroactive surface area. Q_T and Q_O for the pristine and aged MWCNTs/CM or Fe_3O_4 NPs@ g-C_3N_4/CM samples were determined using Equation (4.4) and (4.5) with the data in **Figure 4.10e** and **4.10f**, respectively.

$$Q = Q_O + kv^{-1/2} \tag{4.5}$$

The determined voltametric charges, electrochemical porosity, and roughness factor (R_r) are listed in **Table 4.3**, which shows the outer voltametric charge of the pristine MWCNTs/CM was greater than that of the Fe_3O_4 NPs@ g-C_3N_4/CM. Thus, the MWCNTs

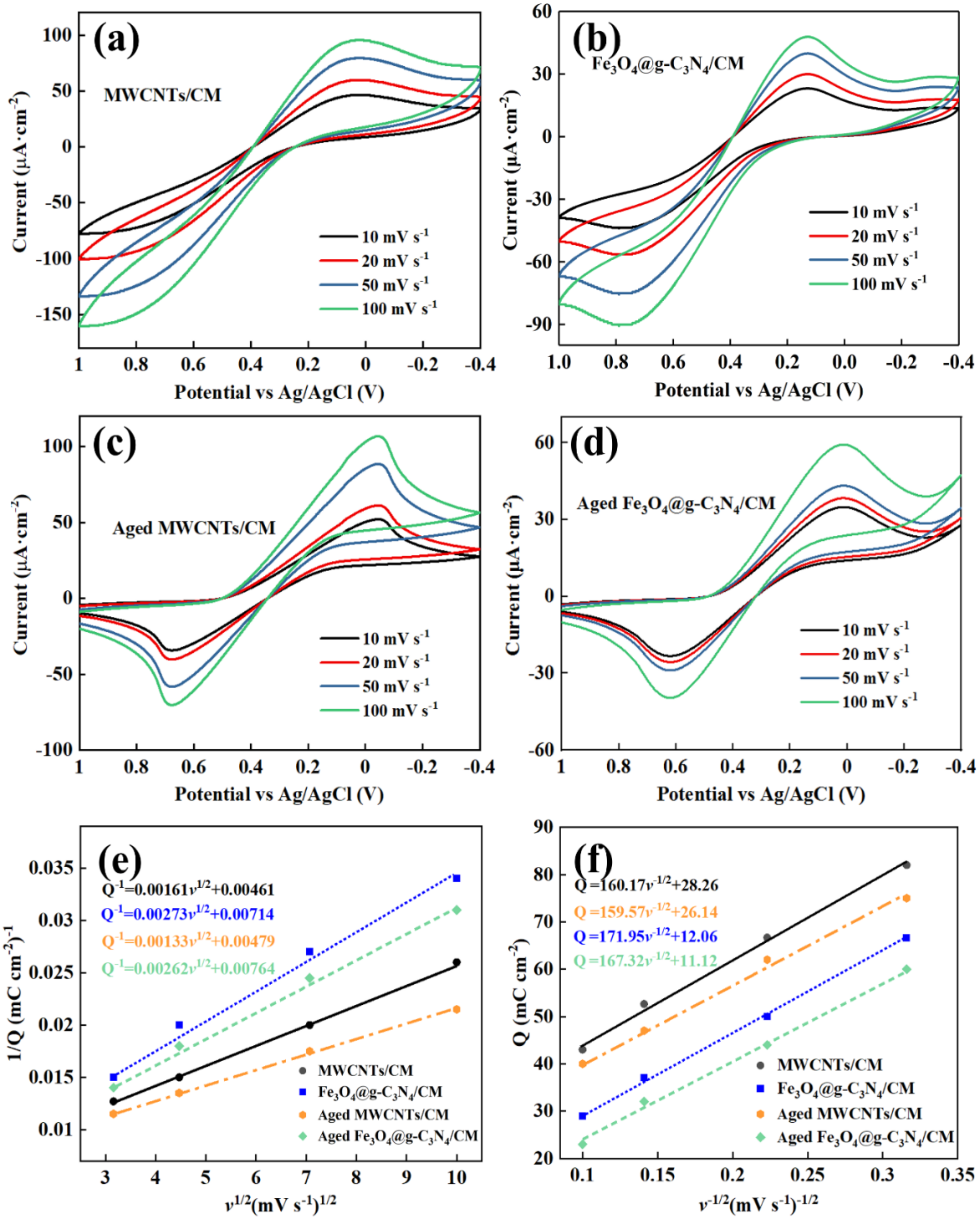

Figure 4.10 (a) and (b) are the CV curves of the pristine MWCNTs/CM and Fe_3O_4 NPs@ g-C_3N_4 /CM at different scan rate; (c) and (d) are the CV curves of the aged MWCNTs/CM and aged Fe_3O_4 NPs@ g-C_3N_4 /CM at different scan rate; (e) Reciprocal voltammetric charge quantity ($1/Q$) *vs*. the square root of scan rate ($v^{1/2}$); (f) Voltametric charge (Q) *vs*. the reciprocal square root of scan rate ($v^{-1/2}$).

/CM yielded a greater number of active sites than Fe_3O_4 NPs@g-C_3N_4/CM. After aging treatment, the outer voltametric charge of the MWCNTs/CM or Fe_3O_4 NPs@g-C_3N_4/CM decreased due to the limited membrane aging. The electrochemical porosity of the MWCNTs/CM or Fe_3O_4 NPs@ g-C_3N_4/CM increase slightly, showing aging process exerts a minor influence on the catalytic behavior of the conductive membrane. R_r as an indicator or electrocatalytic activity is the electroactive surface area (ECSA) divided by the geometrical area of the electrode (i.e., R_r=ECSA/geometrical area) . The ECSA of membrane electrodes is often calculated using the normalization constant of 60 $\mu C \cdot cm^{-2}$. The geometrical area (17.34 cm^2) was then used to calculate the roughness factor. Similar to voltametric charges, R_r of two membrane electrode decreased after aging, suggesting the loss of catalytic activity of the aged membrane .

Table 4.3 Total, Outer and Inner Charge Density, Q_I/Q_T and R_r of the Pristine and Aged MWCNTs and Fe_3O_4 NPs@ g-C_3N_4 Coated Membranes

Membrane	Q_T ($mC \cdot cm^{-2}$)	Q_O ($mC \cdot cm^{-2}$)	Q_I ($mC \cdot cm^{-2}$)	Q_I/Q_T (%)	R_r (unitless)
Pristine MWCNTs/CM	216.91	28.26	188.65	86.97%	3615.17
Aged MWCNTs/CM	208.74	26.14	182.60	87.47%	3479.00
Pristine Fe_3O_4@g-C_3N_4/CM	140.06	12.06	128.00	91.38%	2334.33
Aged Fe_3O_4@g-C_3N_4/CM	130.77	11.11	119.66	91.50%	2179.50

Furthermore, **Figure 4.11a** compares the CVs of the different membrane samples. Without surface coating, the pristine ceramic membrane yielded negligible peak currents at all the sweep potentials, suggesting low electrochemical activity. By contrast, with the coating of MWCNTs or Fe_3O_4@g-C_3N_4, the typical electrochemical reversible current curves are observed. The peak current of MWCNTs/CM is achieved at 0.04 V and is greater than that of Fe_3O_4@g-C_3N_4 at 0.14 V, which indicates a higher interfacial charge transport

on the MWCNTs coating surface. For the aged membrane, the peak currents, especially under the high positive potential bias, decreased significantly for both coated membranes, implying the partial loss of the electrochemical activity or reactive sites on MWCNTs and Fe_3O_4@g-C_3N_4 as mentioned above. To better assess their performance and stability during aging experiments, these two electrochemical membranes were subjected to chronoamperometry at 10 V vs Ag/AgCl. **Figure 4.12** shows that MWCNTs/CM yielded a relatively stable current (~15 mA·cm^{-1}) over time, whereas Fe_3O_4@g-C_3N_4/CM exhibited an initial high current density (~20 mA·cm^{-1}) that progressively declined to 10 mA·cm^{-1} and eventually dropped to 8 mA·cm^{-1} at day 5 due to the oxidative aging. The electrochemical activity of MWCNT/CM generally remained higher than that of Fe_3O_4@g-C_3N_4/CM after the same aging treatment.

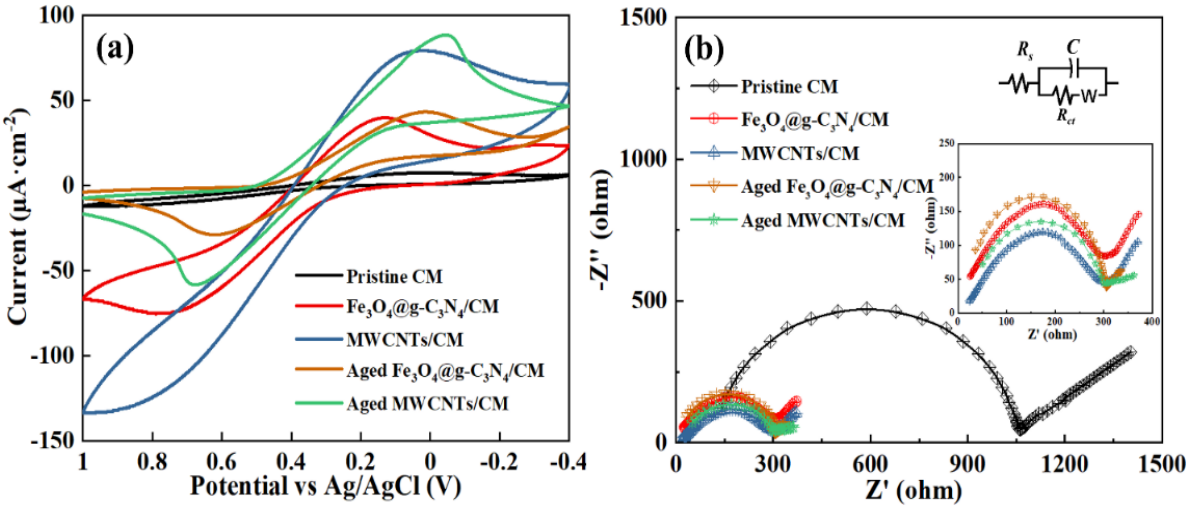

Figure 4.11 (a) CV curves of the pristine and aged MWCNTs/CM and Fe_3O_4@g-C_3N_4/CM obtained at a sweeping rate of 0.05 V·s^{-1}. (b) EIS spectra of the pristine and aged MWCNTs/CM and Fe_3O_4@g-C_3N_4/CM. (All electrochemical testing use Ag/AgCl (in 1.0 M KCl) as reference electrode, and a 3-mm platinum wire as the counter electrode)

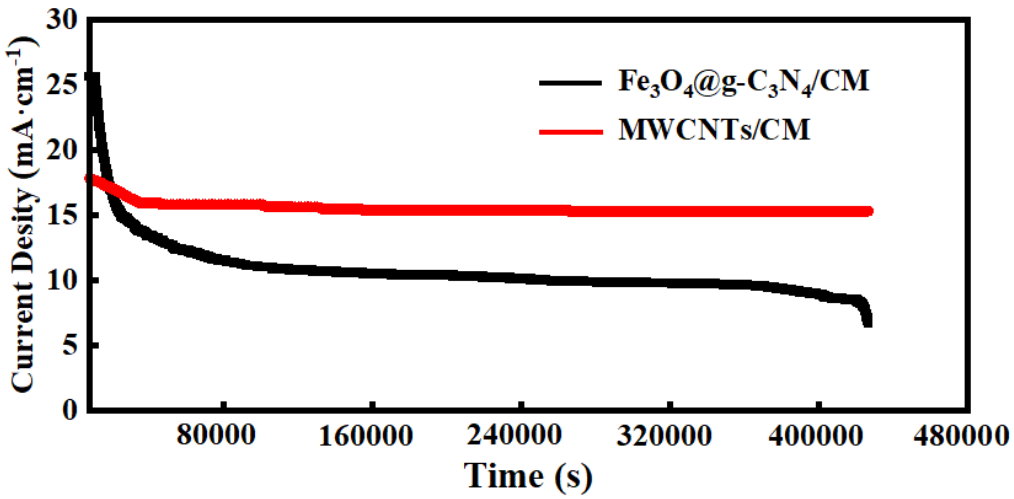

Figure 4.12. Chronoamperometry of MWCNT/CM and Fe_3O_4@g-C_3N_4/CM at 10 V vs Ag/AgCl in 0.1 M NaCl electrolyte for 5 days membrane aging experiments.

4.3.4.2 Electrochemical impedance assessment for the pristine and aged membranes.

To analyze the changes of the interfacial charge-transfer resistance before and after aging treatment, electrochemical impedance spectroscopy (EIS) of the brand-new and aged MWCNTs and Fe_3O_4@g-C_3N_4 modified membranes were studied in the same electrolyte solution (10 mM $K_3Fe(CN)_6$ and 0.5 M KCl) at an open circuit potential (0.3 V). The EIS spectra are presented as a Nyquist plot in **Figure 4.11b**. The diameter of semicircle arc of MWCNTs and Fe_3O_4@g-C_3N_4 modified electrodes were significantly smaller than diameter of semicircle arc of the pristine membrane, suggesting a faster interfacial charge transport on the coated membrane surface than on the pristine membrane surface[68]. The EIS spectra were fitted with an equivalent circuit as shown in the inset of **Figure 4.11b**, where R_{ct} is the charge-transfer resistance at electrode/solution interface, R_s represents the electrolyte resistance, C is the electrode double-layer capacitance formed at electrode/solution interface. W is the Warburg impedance that models the diffusion process in dielectric spectroscopy. The value of R_{ct} was further converted to resistivity (R_{ct}^*) using the surface area and coating thickness of the catalyst layer. The results of R_{ct}, R_{ct}^*, R_s, C

and *W* are summarized in **Table 4.4**. Smaller resistances under MWCNTs composite were obtained compared to Fe_3O_4@g-C_3N_4 composite.

Ceramic membranes made of alumina (Al_2O_3) and zirconia oxides (ZrO_2) also exhibit electrochemical impedance responses as reported previously. Thus, **Table 4.4** demonstrates that the charge transfer resistance (R_{ct}) of the pristine CM reached up to 1000 ohm due to the semiconducting nature of ceramic membranes. The R_{ct} values of MWCNTs (220.3 ± 12) and Fe_3O_4@g-C_3N_4 (290.2± 11ohm) modified membranes were significantly smaller than that of the pristine membrane, suggesting a good conductivity on the coated membrane surface and supporting MWCNTs and Fe_3O_4@g-C_3N_4 coating converted the pristine CM to a conductive CM. Li et al. also have reported CNT coating could covert the charge transfer resistance of the Al_2O_3 CM support around 3000 ohm to the CNT-coated Al_2O_3 CM was only approximately 200 ohm .

By contrast, the charge transfer resistance (R_{ct}) of two aged electrochemical membranes increased from 220.3 ± 12 ohm to 248.1 ± 3 ohm and 290.2± 11ohm to 299.6 ± 3 ohm, respectively. This increase mainly resulted from the restructuring, irreversible phase transition, and reduction of electroactive sites . The decrease of the electrochemically active surface area results in a reduced electrode double-layer capacitance (*C*), which agrees with our results in **Table 4.4**. Warburg impedance (*W*) reflects the diffusion process of electrolyte. **Table 4.4** shows that Warburg impedance increases after aging, implying that the diffusion resistance of the electrolyte within the solid electrode increased. This phenomenon could be caused by the expansion of electrode materials or pore clogging . The electrochemical aging process could have changed the pore size of membranes due to formation of holes, broken layers, partial unzipping and debundling of MWCNTs , which

will hinder efficient diffusion of redox species from the bulk electrolyte into the pores .

Table 4.4 The Fitted Results of the Parameters in the Equivalent Circuit for Pristine CM and Two Modified CM Before and After the Aging Experiments.

Electrode	Parameters	Before aging	After aging
Pristine CM	R_s (ohm)	58 ± 10	NA
	R_{ct} (ohm)	1015 ± 105	NA
	C (F)	8.51×10^{-9}	NA
	W ($S\cdot s^{1/2}$)	0.0012	NA
MWCNTs/CM	R_s (ohm)	37.4 ± 3	35.4 ± 5
	R_{ct} (ohm)	220.3 ± 12	248.1 ± 3
	R_{ct}^* (ohm·cm)	3820.1 ± 69.2	4302.2 ± 53.02
	C (F)	3.95×10^{-7}	3.65×10^{-7}
	W ($S\cdot s^{1/2}$)	0.0056	0.0068
Fe_3O_4@g-C_3N_4/CM	R_s (ohm)	43.5 ± 5	44.5 ± 4
	R_{ct} (ohm)	290.2± 11	299.6 ± 3
	R_{ct}^* (ohm·cm)	5032.1 ± 90.7	5195.2 ± 98.5
	C (F)	3.68×10^{-7}	3.45×10^{-7}
	W ($S\cdot s^{1/2}$)	0.0067	0.0075

4.3.5 Analysis of Halogenated Byproduct Formation

4.3.5.1 Comparison of Halogenated Byproduct Formation on two Electrochemical Membranes. The generation of chlorine related byproducts during electrochemical membrane filtration is initiated by the oxidation of chloride at the anode surface, which follow the general oxidation pathway as shown in **Figure 4.5c** ($Cl^- \rightarrow Cl\cdot \rightarrow HOCl/OCl^- \rightarrow ClO_2^- \rightarrow ClO_3^- \rightarrow ClO_4^-$). However, halogen oxides by-product generation highly depends on the electrode materials .The halogenated byproduct formation on the two presented composite conductive membranes has not been reported elsewhere. **Figure 4.13** shows the halogenated anions such as ClO_2^-, ClO_3^- and BrO_3^- present in the filtrate from the anodic membrane with the feed solutions made of different concentrations of NaCl or NaBr with two MWCNTs/CM and Fe_3O_4@g-C_3N_4/CM electrodes. Perchlorate was not detected in the filtered water under the current experimental conditions. During electrochemical

filtration, Cl^- or Br^- could directly react with the electrode or indirectly with reactive oxygen species (hydroxyl radicals or ozone) to produce oxyanions. Chlorate and bromate formed with a lower level in the Fe_3O_4@g-C_3N_4/CM experiment than that in the MWCNTs/CM experiment. The efficiency of oxidant generation in the electrochemical process depends on the applied anodic potential and adsorption enthalpy of M-OH on electrode materials . During electrolysis, •OH is produced from water as a surficial intermediate. M-OH denotes •OH radicals that are physically adsorbed at a surface site. The results suggest that MWCNTs provide more effective catalytic ability and generate more electrogenerated hydroxyl radicals than Fe_3O_4@g-C_3N_4 under the same anodic potentials. Wu et al. confirmed that carbon nanotubes electrodes could also produce hydroxyl radicals in electrolysis processes . After electrochemical aging process, the concentrations of all halogenated anions decreased due to the loss of catalyst activity or reactive sites. After membrane aging, the introduction of oxygen-containing functional groups, which are capable of interfering with electron transport in the sp2 carbonaceous structure . Fe_3O_4@g-C_3N_4/CM had a relativity higher reduction in halogenated byproduct production than MWCNTs/CM did, due to the relatively lower stability of g-C_3N_4 and Fe_3O_4 than MWCNTs during electrochemical aging as indicated XPS results (Section S4) .

4.3.5.2 Effect of Current Density on Halogenated Byproduct Formation. Figure 4.13a shows the effect of the current density on the oxychloride anions distribution. The produced levels of chlorite, chlorate and bromate increased at high current densities (~20 $mA \cdot cm^{-2}$), which increase the electron transfer rates and favor hydroxyl radicals' formation. Thus, the rate of chloride oxidation to chlorite or chlorate increased. More importantly, high current densities yield high anodic potentials, which is essential for activating the anodic oxidation

reactions of these halogen anions as listed in Equation (4.6)–(4.9). For instance, the Visual MINTEQ simulation indicates that hypochlorous acid (HOCl) and hypochlorite ions (OCl^-) will be involved when the Oxidation/Reduction Potential higher than 1 V as shown in **Figure 4.14**. Even after electrochemical aging process, the concentrations of halogenated anions under a high current density only did not change significantly. By contrast, at low current densities (< 5 $mA \cdot cm^{-2}$), there were almost no chlorite, chlorate or bromate production. The electrochemical aging would significantly cause reduction (above 10%) of the chlorinated or brominated by-products under low current density. However, lowering current densities or anodic potentials could reduce the oxidation efficacy of water micropollutants. For example, anodic potentials of 3-14 V were needed to mineralize 1,4-dioxane on TiO_2 and Ti/IrO_2−Ta_2O_5 . PFASs require even higher anodic potentials (e.g., 4−15 V on Ti/RuO_2) for oxidative degradation. Thus, when treating these recalcitrant micropollutants in saline water, there could be sizable amounts of halogen oxyanions produced.

$$6HClO + 3H_2O \rightarrow 2ClO_3^- + 4Cl^- + 12H^+ + \frac{3}{2}O_2 + 6e^- \quad (4.6)$$

$$6ClO^- + 3H_2O \rightarrow 2ClO_3^- + 4Cl^- + 6H^+ + \frac{3}{2}O_2 + 6e^- \quad (4.7)$$

$$Cl^- + 3H_2O \rightarrow ClO_3^- + 6H^+ + 6e^- \quad (4.8)$$

$$ClO^- + 2OH^- \rightarrow ClO_2^- + H_2O + 2e^- \quad (4.9)$$

$$ClO_2^- + 2OH^- \rightarrow ClO_3^- + H_2O + 2e^- \quad (4.10)$$

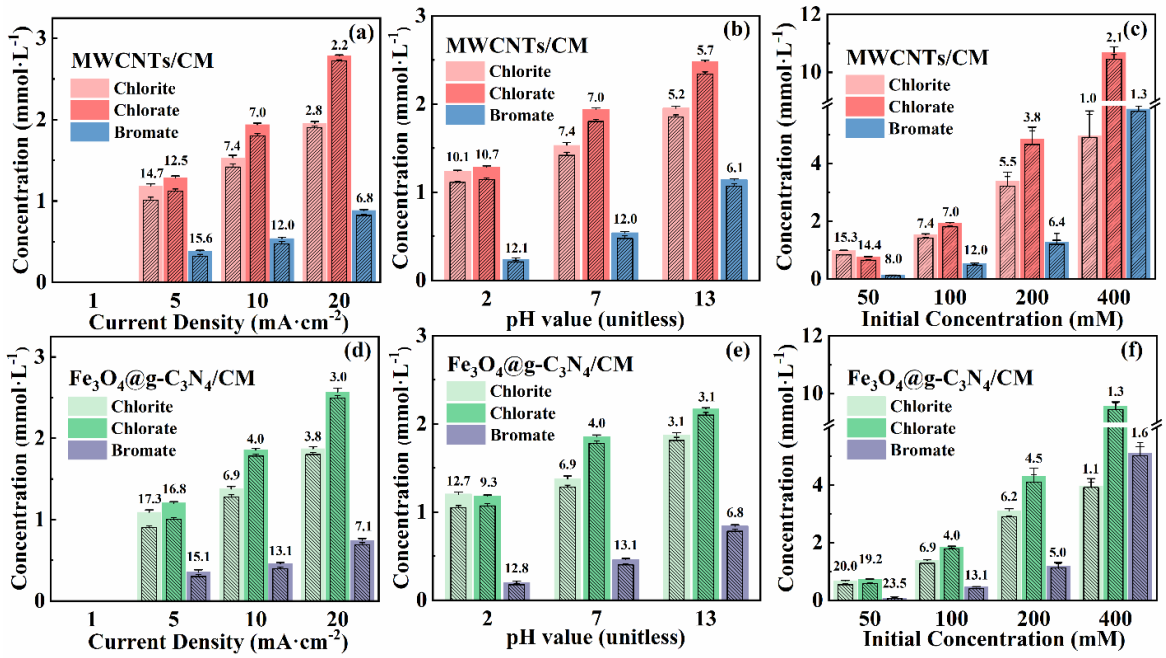

Figure 4.13 Concentrations of chlorite, chlorate and bromate changes of two electrochemical membrane before and after electrochemical aging (a, d) 1-20 mA·cm^{-2} current density with initial concentration 100 mM at pH=7; (b, e) initial pH=2-7 with initial concentration 100 mM and current density=10 mA·cm^{-2} and (c, f) initial concentration 50-400 mM with current density = 10 mA·cm^{-2} at pH=7. (The sub-columns with line pattern are concentrations after aging and the labeled numbers stand for the percentage change after electrochemical aging)

4.3.5.3 Effect of pH on Halogenated Byproduct Formation. The summarized major reactions in **Eq. S5-S9** clearly indicates the involvement of protons in many reactions and thus the solution pH could sensitively affect the formation of oxyanions and their speciation. Our results in **Figure 4.13b** compare the electrochemical byproducts of oxychloride/bromide anions in acidic (pH =2), neutral (pH =7) and basic (pH =13) conditions using 100 mM NaCl or NaBr solutions under a current density of 10 mA cm^{-2}. The formation of ClO_2^- and ClO_3^- increased with an increase in the initial pH values of the solution and remained constant at higher pH conditions. This result is due to the fact that, at acidic pH (pH =2), the dominant chlorine species is hypochlorous acid, and the electrochemical oxidation of HOCl (Eq. S5) would contribute less to the formation of

ClO_3^- than does the OCl^- (**Eq. S6**). If the solution pH is neutral or alkaline, HOCl is likely converted into of ClO_2^- and ClO_3^-, which agrees with experimental observations.

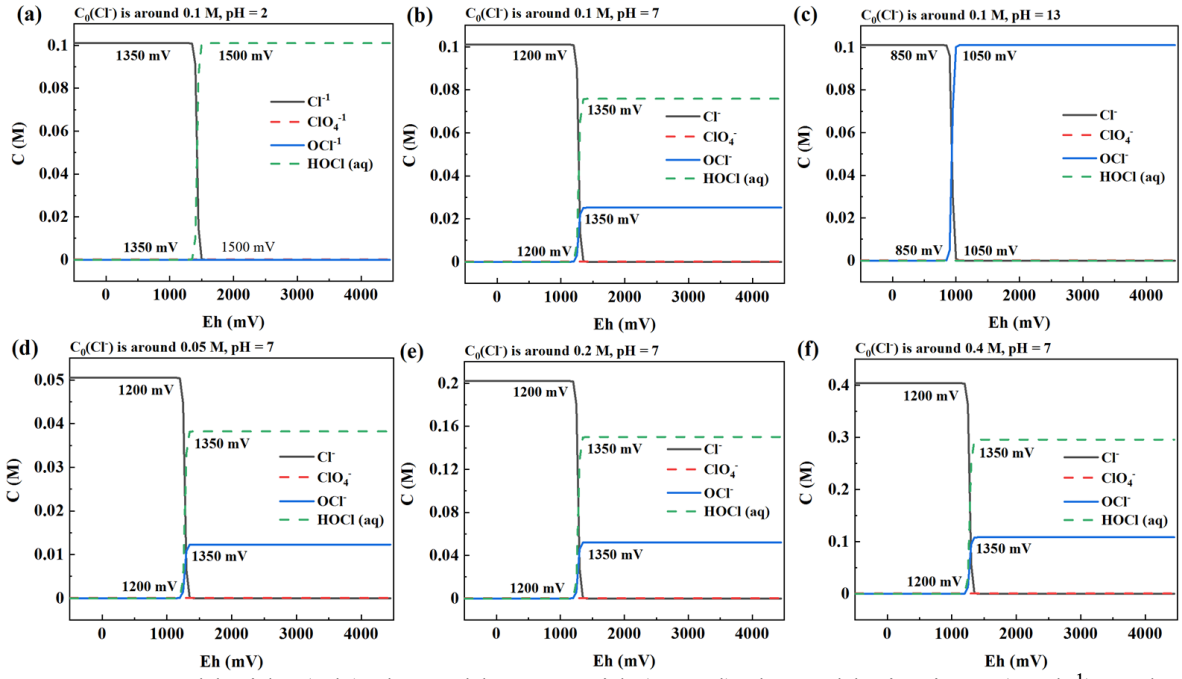

Figure 4.14 Chloride (Cl^-), hypochlorous acid (HOCl), hypochlorite ions (OCl^{-1}) and perchlorate (ClO_4^-) concentration evolution at different applied potential under different pH and initial Cl^- concentration.

The MINTEQ simulations in **Figure 4.14** confirms that the HOCl concentration decreased as a function of pH increase. At acidic pHs, gaseous chlorine could be promoted, reducing available anionic oxychloride species for oxidation reactions and formation of halogenated oxyanions. Thus, for the aged MWCNTs/CM and Fe_3O_4@g-C_3N_4/CM, reducing the solution pH could greatly inhibit the byproduct formation.

4.3.5.4 Effect of the Initial Concentration of Salts. Increasing the initial concentration of Cl^- and Br^- generally increases the reaction kinetics of electrochemical oxidation. **Figure 4.13c** shows the formation of ClO_2^- , ClO_3^- and BrO_3^- during the electrochemical filtration of the solutions with varied initial NaCl or NaBr concentrations (50, 100, 200 and 400 mM). The concentrations of chlorite, chlorate or bromate all increased appreciably with an

increase in the Cl^- or Br^- concentrations, which matches the result reported previously . After electrochemical aging, the percentage change of chlorate concentrations are 19.2, 4.0, 4.5 and 1.3 % for the initial Cl^- concentrations of 50, 100, 200 and 400 mM under MWCNTs/CM, respectively. The electrochemical aging process will not affect the chlorinated or brominated by-products formation when the initial Cl^- concentrations is high. The amount of ClO_2^- could not be precisely measured because the produced ClO_2^- could rapidly react with other oxidants, such as O_3 and •OH, or directly react on the anode to form stable ClO_3^-. Less ClO_4^- could be generated with a higher initial Cl^- content (50−250 $mg \cdot L^{-1}$) due to the limitation in reactive sites on the electrode . The reactive sites on the electrode will be occupied by excessive Cl^- and then inhibit the ClO_3^- to form ClO_4^-.

4. Conclusion

Electrochemical membrane filtration has proven effective for pollutant degradation or chemical conversion in water/wastewater treatment and resource recovery. The high surface area, microporous structures and tunable reactivity of electrochemically reactive membranes garner the enhanced reaction efficiency and pollutant removal. However, the membrane properties could change with time due to the membrane fouling or aging. Particularly, the aging mechanisms for electrochemical membranes remain largely elusive, due to the lack of in-depth research and analysis. Most prior studies only employed limited testing time (1-5 hours) to evaluate the conductive membrane filters (e.g., CNT and β-PbO_2) or employed electrolytes that have different water chemistries from reality . The presented electrochemical assessment (CV and EIS) combined with electron microscope imaging, FTIR, XPS, Raman spectrometry reveals a comprehensive picture of the interfacial

chemical state changes and electrochemical activity reduction of MWCNTs and Fe_3O_4@g-C_3N_4 membranes after filtering high-salinity water under high currents (~20 mA·cm^{-2}) and long-term operation (5 days). This aging assessment is essential for the development of novel electrode filters or membranes to fully understand the membrane aging risks and determine operational limits of the applied currents or potentials. The results lay groundwork to guide the practical and scalable applications of ERM filtration for water/wastewater treatment.

The utilization of electrochemical membrane filtration as decentralized point-of-use and point-of-entry water/wastewater treatment seems to be promising. However, the formation of potentially toxic or carcinogenic organic and inorganic byproducts on electrified filtration must be carefully addressed. The natural water may contain chloride (10-100 ppm) and bromide (1-2 ppm), which leads to inevitable formation of ClO_3^-, ClO_4^- or BrO_3^- if electrochemical oxidation occurs. Our study examined the chlorite, chlorate and bromate byproducts formation under different current densities on different anode materials, different initial solution pHs and salt concentrations. Clearly, proper adjusting operational strategies may limit ClO_3^- or BrO_3^- formation, including lowering the anodic oxidization potential and lowering the feed solution pH values. The use of electrochemical membranes for water/wastewater treatment applications will require optimization of operating conditions and possibly a multi-barrier approach.

CHAPTER 5

ELECTRO-SORPTION, DESORPTION AND OXIDATION OF PERFLUOROALKYL CARBOXYLIC ACIDS (PFCAS, C4&C8) VIA HIGH PERFORMANCE MXENE MEMBRANE

Per- and polyfluoroalkyl substances (PFAS) are bioaccumulative and persistent chemicals that have polluted natural waters and soils globally. The intensity of their concentration and increased frequency of detection around the world raises concerns about their presence in drinking water and the associated health risk. O-terminated MXene-based membrane has significantly higher adsorption capacity (215 $mg \cdot g^{-1}$) and a degradation rate constant (2.8×10^{-2} min^{-1}) compared to those with the F and Cl terminations. Electrochemical oxidation treatment with an applied +6 V potential in the 0.1 M Na_2SO_4 solution yielded >99 % oxidation of the PFOA or PFBA (1 ppm) in 3 hours. The density functional theory (DFT) calculations revel the O-terminated MXene surface on $Ti_3C_2O_2$ yielded the highest PFOA/PFBA adsorption energy. Bader charge analysis shows that when interacting with PFOA, $Ti_3C_2O_2$ with surface defects accept 0.19 |e| and 0.28 |e| more electrons to PFOA relative to $Ti_3C_2F_2$ and $Ti_3C_2Cl_2$, respectively. Moreover, the reaction pathway of PFOA on $Ti_3C_2O_2$ is most favorable among these three MXene structures as indicated by the greater negative free energies.

5.1 Introduction

Per-and poly-fluoroalkyl substances (PFAS) are a group of prevalent anthropogenic micropollutants that show an adverse and severe impacts on environmental and human health due to their intrinsic high toxicity, extraordinary prevalence and persistence, and instant bioaccumulation . The most notable PFASs are perfluorooctanoic acid (PFOA) and

perfluorooctane sulfonate (PFOS) due to their toxicity and recalcitrance to natural weathering processes such as hydrolysis, photolysis, microbial degradation, and metabolism by organisms. The U.S. Environmental Protection Agency (EPA) suggested the health advisory level of the combined PFOA and PFOS in drinking water should not exceed 70 ppt. Furthermore, ultra-short chain PFAS ($C \leqslant 2$, e.g., $C2F_6$, CHF_3, CF_4.) are volatile as well as highly water-soluble, and can easily enter the human body when breathing or consuming food or drinking water. The adverse health effects of PFAS are not only limited to humans; they could be equally harmful to animals and livestock. Therefore, it is an urgent task to develop advanced technologies for PFAS removal from contaminated water.

Recent studies have shown that conventional water or wastewater treatment processes are ineffective at removing perfluorochemicals. At present, large-scale water treatment plants mainly reply on adsorption and ion exchange to remove PFASs. Among various technologies used for PFAS removal from contaminated water such as adsorption, oxidation, UV irradiation, sonochemical, microwave methods, membrane separation, and advanced oxidation/reduction processes (AOPs/ARPs), adsorption is highly favored owing to its simplicity and high efficiency, good selectivity, high flux, high capacity, reusability, and industrial scale-up feasibility in the purification process of contaminated water. Common adsorbents include powdered activated carbon (PAC) or granulated activated carbon (GAC), which are not generally regenerated. The cost of incorporating these adsorbents into existing water treatment processes can be high because a contact column is essential and the adsorbent needs to be continually replaced and purchased. The disposal of the adsorbents is also costly, usually requiring high-temperature incineration. Ion

exchange resin can also remove PFAS efficiently. However, the exhausted ion exchange resin is difficult to regenerate, since it produces high salinity PFAS containing wastewater; if no regeneration is undertaken, considerable solid waste would be produced.

Compared with the adsorption process, electro-sorption can significantly increase the removal rate and capacity by applying an external electric field or electric currents to the conductive adsorbent to enhance the adsorption. Under the action of an external electric field, charged ions in the solution move towards the electrode with the opposite charges. PFAS, though widely detected in various environmental media such as effluents of municipal wastewater treatment plants (WWTP) and industrial wastewaters, often have extremely low concentrations (e.g., 10-100 $ng \cdot L^{-1}$). Thus, enhanced adsorption could sequester and concentrate PFAS for further disposal or degradation treatment. For example, electro-assisted methods with carbonaceous materials were used for the controlled adsorption and desorption of short-chain PFAS. Carbonaceous materials such as activated carbon, carbon nanotubes (CNTs), and reduced graphene oxide (rGO) are commonly used as conductive adsorbents. Most of these conductive nanomaterials are prepared by electrodeposition and require polymer adhesives to bind up these nanomaterials into a stable structure. The chemical binders may reduce the electron transfer efficiency and increase the fabrication cost of the conductive adsorbents. In addition, the surface area and pore size of graphene were also reduced by electrophoretic deposition, which weakened the adsorption capacity of electrodes. Thus, the lack of reactivity and effective adsorbent preparation of carbonous materials lead to the low efficiency of PFAS adsorption.

Recently, MXene, a family of novel atomically thin transition metal carbides/nitrides, have emerged as promising candidates for diverse electrical and

electrochemical applications. MXene are generally synthesized by selectively etching of their parent layered materials, the MAX phases, which have a formula $M_{n+1}AX_n$, where M commonly stands for a transition metal (e.g., Ti, Mo, and V), A is one of group 13 to 16 elements of periodic table (Al, Si, Ga, etc.), X is either carbon and/or nitrogen, and n is an integer from 1 to 4. After the extraction of X atoms from the MAX phase, the outer surfaces of the exfoliated layers are always terminated with F, OH, and/or O groups. The obtained 2D MXenes with negative charge and hydrophilic surface have appealing characteristics to construct membranes with unique properties. Furthermore, MXenes have an excellent electrical conductivity of MXene (e.g., 2.6×10^4 S cm^{-1} for $Ti_3C_2T_x$ MXene) is also beneficial to reducing the Joule loss upon conversion of electricity. Notably, the presence of different functional groups (such as –O and –OH), and high surface area make them ideal candidates for water treatment; further, they have remarkable catalytic performances toward different hazardous pollutants . The key features of MXenes that make them the ideal candidates for various applications are their exceptional structural characteristics like activated metallic hydroxide sites, biocompatibility, ease of functionalization, huge specific surface area, hydrophilicity, large interlayer spacing, remarkable chemical stability, and superior adsorption-reduction capacity.

Etched in HF-containing aqueous solution, the resulting MXene flakes contain surface terminations (T_x), such as =O, −OH, and −F, rendering them hydrophilic and capable of solution processing. MXenes are considered to be composed of metallic conductive transition metal carbide core and electrochemically reactive transition metal oxide-like surface. They hold the unique combination of several excellent properties, such as metallic conductivity (conductivity up to 24 000 $S \cdot cm^{-1}$ for MXene films, much higher

than most carbonous materials), surface plasmons, hydrophilicity, tunable surface groups and work function (theoretically in between 2 and 8 eV), and good water dispersibility without adding surfactants. These properties enable many promising applications of MXenes in energy storage, catalysis, electromagnetic shielding, strain sensing, biosensing, (photo)thermoelectrics, optoelectronics, and electronics. Recently, MXenes have demonstrated excellent adsorption ability for PFAS than a number of anionic ion exchange (IX) resins (A860) or nonionic IX resins (XAD and XAD. A novel MXene− thin-film nanocomposite (TFN) hollow fiber NF membrane was also shown to enhance PFOS removal from water without affecting salt rejection of membranes and enhanced the membrane flux. However, electrochemically assisted adsorption with MXenes has not yet been studied or reported. Moreover, the variations of surface functional group or terminations of MXenes may change the electronic structure and promote electrochemical activity constitutionally. Thus, termination modification of MXene could enhance the adsorption, desorption and degradation performances for PFASs, which has not been well elucidated.

This study demonstrated a novel MXene-based membrane for electro-sorption and desorption of PFAS from water. Briefly, a $Ti_3C_2T_x$ (T= Cl, F or O) layer was coated on a commercial porous Nylon hydrophobic membrane by vacuum filtration. The adsorption capacity and desorption of PFAS were evaluated under different anodic potentials (0−1.2 V vs Ag/AgCl) on the three types of MXenes that are expected to exhibit different interaction affinities toward PFAS. Then, the oxidative degradation of PFOA and PFBA as model perfluoroakly carboxylic acids of C4 and C8 was evaluated on these MXene-based membrane and compared with other reported conductive membranes. Moreover, the

effects of the solution matrix such as pH, organic matter, and co-anions on the PFOA/PFBA removal were evaluated. This study provides new insights into the electro-sorption/desorption with potential concurrent oxidation of PFAS using MXene-based membraness.

5.2 Materials and Methods

5.2.1 Preparation of $Ti_3C_2T_x$ MXenes with Three Different Dominant Termination

Firstly, to prepare $Ti_3C_2T_x$ with the main terminal groups (T) of F, 1 g of LiF powder was added to 20 mL of a 9 M hydrochloric acid solution and stirred for 5 min for complete dissolution. Then, 1 g of Ti_3AlC_2 powder was slowly added to the mixture at room temperature in a duration of over 10 min to prevent overheating. Then, the mixture was magnetice stirred at 500 rpm at 35 °C for 24 h and then, deionized water was added to the mixture for centrifugation at 3000 rpm for 5 min to separate the supernatant from $Ti_3C_2T_x$ sediment. This washing step using DI water was repeated until the pH of the supernatant reached ~6. Then, the sediment was redispersed with deionized water by hand shaking for 10 min and centrifuged at 3000 rpm for 1 h. The collected supernatant contained large $Ti_3C_2T_x$ flakes. The precipitate (multilayered $Ti_3C_2T_x$ powder) was vacuum filtered on a Nylon membrane (mean pore diameter: 0.45 μm, MilliporeSigma) and vacuum dried at room temperature.

To synthesize $Ti_3C_2Cl_2$, 1 g of Ti_3AlC_2 MAX-phase powder and 2.1 g of $CuCl_2$ powder were mixed (in a stoichiometric molar ratio of 1:3) and ground for 10 min. Then 0.6 g of NaCl and 0.76 g of KCl were added to this mixture, which was ground for another 10 min using a mortar under 100% nitrogen atmosphere in a glovebox. The mixture powder

was placed in an alumina crucible that was heated at 750 °C for 24 h in a tube furnace under the argon gas. After the molten-salt etching process, the product was washed with 30 mL deionized water and 20 mL of the 0.1 M ammonium persulfate (APS, $(NH_4)_2S_2O_8$) solution respectively to remove the residual $CuCl_2$ and Cu particles, and the final product was oven dried at 40 °C.

To synthesize $Ti_3C_2O_2$, the $Ti_3C_2Cl_2$ powder (70 mg) was stirred in $Cs_2O/K_2O/Li_2O$ (25:18.9:56.1 molar ratio) solid using a mortar under the nitrogen gas in a glovebox. At least 3 times mole excess of mixed compound was further added to the MXene/salt mixture. The solid mixture was placed the alumina crucible and loaded into a tube furnace for sintering at 600°C (functionalization with O) for 24 h under Ar atmosphere. The solid product was dissolved in a 20 mL anhydrous N_2H_4 solution (or anhydrous formamide) followed by washing with anhydrous acetonitrile and anhydrous Methanol inside the N_2 filled glovebox in to avoid possible oxidation of the surface groups.

Delamination of MXene. 0.1 g one of the above synthesized MXenes was added to 10 mL of TBAOH (tetrabutylammonium hydroxide) (40%) solution and was left in TMAOH for 72 h for delamination, in which the suspension was sonicated for 18 h again in an iced bath. The sonication was accomplished 6 h each day for 3 days and stored inside the freezer during the rest of the time. The suspension was centrifuged at 14000 g for 15 min to precipitate all particles, and the TMAOH solution in the supernatant was removed using a pipet. Finally, the delaminated MXene was centrifuged at 6500 g for 8 min to eliminate the precipitate and obtain the delaminated MXene in the suspension was collected by vacuum filtration on a Nylon membrane (mean pore diameter: 0.45 μm, MilliporeSigma).

5.2.2 Preparation MXene Membrane

Firstly, 1.2 g of the above three kinds of $Ti_3C_2T_x$ was dispersed ultrasonically in a mixture of N-methyl-2-pyrrolidone (NMP) (27.4 g) and 4-methyl piperidine (4-MP) (1 g) for 30 min, and then 0.3 g PANI powder was slowly added into the above suspension. The mixture was vigorously stirred (~300 g) overnight to obtain a $Ti_3C_2T_x$/PANI suspension, which was vacuum filtered on a Nylon membrane (mean pore size=0.45 μm, MilliporeSigma) and vacuum dried at room temperature. The PANI binder was added to strengthen the binding and intern-layer conductivity.

5.2.3 MXene and Membrane Characterization

The morphology and chemical compositions were analyzed by JSM-7900F field emission scanning electron microscope (FE-SEM) (JEOL, Japan) at 15 kV with coupled energy-dispersive X-ray (EDX). The phase composition of the MXene materials was analyzed by XRD (Philips, EMPYREAN, PANalytical Almelo, The Netherlands) with a Co Ka radiation (λ =1.789 Å). XRD patterns were collected with 2θ steps of 0.02° with a collection time of 1 s per step. The chemical composition and bonding states were measured by X-ray photoelectron spectroscope (XPS, Specs Analyzer & Bruker IR, USA) with a monochromatic Al Kα radiation (*hv* =1486.6 eV) at a power of 96 W for the X-ray spot size of 700 × 300 μm. The pass energy of the XPS analyzer was set at 20 eV. The pressure of the analysis chamber was kept below 5×10^{-9} torr. All spectra were calibrated using the binding energy of C 1s (284.8 eV) as a reference. High-resolution TEM images were obtained using a Tecnai F20 (FEI) electron microscope at an acceleration voltage of 200 kV. Structural and chemical analysis was carried out by high-resolution STEM imaging and STEM-EDS within Titan Cubed Themis 300 double Cs-corrected

Scanning/Transmission Electron Microscope (S/TEM) operated at 300 kV; STEM energy-dispersive X-ray analysis was recorded with the embedded high-sensitivity Super-X detector. The sample for the STEM-EDS analysis was ultrasonically suspended in the ethanol solvent, and one or two droplets of this slurry were deposited on a copper grid.

The morphologies of the MXene membranes were examined using atomic force microscopy (AFM, Dimension Icon, Bruker, USA) in the tapping mode in air. The height profile of a 10.0 μm × 10.0 μm sample region was acquired by AFM to estimate the root mean-square-roughness and mean roughness. To measure the membrane surface hydrophilicity, the static water contact angle was measured by a contact angle goniometer (JC2000DM, Powereach, Shanghai, China) equipped with a video camera using the sessile drop method. A 2 μL water droplet was used to minimize the gravity effect. At least 6 various locations were chosen on one membrane surface, to get a reliable contact angle value.

5.2.4 Electrochemical Tests of the MXene Membranes

All electrochemical measurements were performed in a conventional three-electrode cell at ambient temperature by using a CHI700E electrochemical potentiostat (CH Instruments, USA). The MXene membranes (Diameter=4 cm; thickness=0.2 mm), an Ag/AgCl electrode (in 1.0 M KCl) and a Pt wire were employed as the working electrode, the reference electrode and counter electrode, respectively. Cyclic voltammetry (CV) measurements of the three different terminated MXene membranes were performed with a CHI 700E electrochemical workstation at a series of sweep rate (10−500 $mV \cdot s^{-1}$) in 60 mL of 0.1 M Na_2SO_4. Before the CV measurements, the electrolyte (0.1 M Na_2SO_4) was

degassed by bubbling nitrogen for 30 min. The capacitance of the MXene membrane was calculated using the following equation:

$$C = \frac{\int_{E1}^{E2} i(E)dE}{2\Delta V \nu A} \tag{5.1}$$

where C is the capacitance of a membrane unit area ($F \cdot cm^{-2}$), E_1 and E_2 are the cutoff potentials in used during CV, *i(E)* is the instantaneous current, $\int_{E1}^{E2} i(E)dE$ is the total voltammetric charge obtained by integration of the positive and negative CV scan, ΔV is the potential window in the CV scan, v ($V \cdot s^{-1}$) is the CV scan rate, and A is the membrane area. Electrochemical impedance spectroscopy (EIS) was also conducted on these MXene membranes to obtain the Nyquist plots at open circuit potential (OCP) of 0.2 V in the frequency range of 100 kHz to 0.01 Hz in aqueous solution containing 0.1 M Na_2SO_4.

5.2.5 Batch Electro-sorption and Desorption Experiments

To compare the adsorption and desorption on MXenes, PFCAs with two different carbon lengths, PFBA (C=4) and PFOA (C=8), were purchased from Fisher Scientific (all purity >98%). The electro-sorption PFCAs was conducted in 100 mL Teflon beakers equipped with magnetic stir bars. The MXene membrane (diameter = 4 cm) served as the anode and was placed at a distance of 10 mm to a titanium rod as the cathode with a thickness of 1.3 mm and a diameter of 4.6 cm. Each electro-sorption PFCAs removal batch experiments were run in triplicate. To find the suitable applied potential, the electro-sorption kinetics of 1000 µg $L^{-1}$of PFCAs solution will be carried out in 60 mL 0.1 M Na_2SO_4 aqueous solution (pH 7.00 ± 0.10) with a voltage 0 V, 0.2, 0.4, 0.6 V, 0.8, 1.0 and 1.2 V, respectively. The pH of the solution was adjusted to 7.0 ± 0.1 by either 0.1M NaOH or 0.1M HCl. A series of PFCAs concentrations (100, 200, 400, 600, 800, 1000 and 10 000

μg·L^{-1}) were used to evaluate the electro-sorption capacity of MXene membrane using an anodic potential of + 0.8 V. The electro-sorption equilibrium time was 3h, which was determined based on the electro-sorption kinetic. 60 mL 0.1 M Na_2SO_4 aqueous solutions containing 100, 200, 400, 600, 800, 1000 and 10 000 μg·L^{-1} PFCAs were added into Teflon beaker. The whole process was carried out under shading condition. A maximum initial PFCAs concentration of 10 mg·L^{-1} was used to avoid precipitation of PFCAs during batch studies. Other electro-sorption conditions were as the same as that of electro-sorption kinetic experiment.

The amount of PFOA and PFBA absorbed at equilibrium (q_e, mg·g^{-1}) was calculated by Equation (5.2).

$$q_e = \frac{(C_0 - C_e) \times V}{m} \tag{5.2}$$

where V is the volume of the treated solution (L), m is the mass of loaded MXene (20 mg), and C_0 and C_e (mg·L^{-1}) are the initial and final equilibrium concentrations of PFCAs in solution, respectively. The sorption data were fitted by Freundlich isotherm in Equation (5.3) as PFCAs are most likely multi-layer adsorption behaviours on MXene membrane.

$$q_e = K_f C_e^{1/n} \tag{5.3}$$

where K_f is the Freundlich isotherm constant (mg·g^{-1}), n is adsorption intensity, C_e is the equilibrium concentration of PFCAs (mg·L^{-1}), and q_e is the amount of PFCAs adsorbed per gram of the MXene at equilibrium (mg·g^{-1}).

To study the electro-assisted desorption kinetics, desorption experiments were performed in the same batch cell by adding cathodic potential of −1.0 V vs Ag/AgCl to the MXene membrane. First, the MXene membrane reached the adsorption equibrlium or capacity in a solution with an initial PFCAs concentration of 10000 μg·L^{-1} under a

potential bias of +0.8 V for 4 h in 0.1 M Na_2SO_4. After that, those MXene membranes were transferred to a 0.1 M Na_2SO_4 solution (no spiked PFAS) for desorption by applying a cathodic potential of −1.0 V to the MXene electrode for 1 h.

5.2.6 Electro-sorption of PFBA and PFOA in Continuous Filtration

In a typical continuous-flow electrosorption experiment, a modified syringe pump was used to transfer the feed solution of PFCAs (100 $\mu g \cdot L^{-1}$) and 10 mM Na_2SO_4 through a dead-end membrane filtration cell at various flow rates (200-500 LMH) as illustrated in **Figure 5.4f**. A positive voltage (0.8 V vs Ag/AgCl) was applied to the MXene membrane (surface area = 12.56 cm^2) as the anode with a Ti mesh (diameter 4.6 cm) as the counter electrode and a Ag/AgCl reference electrode. As shown in **Figure 5.4h**, the distance between the working anode and counter electrode was also 10 mm.

Each filtration experiments last four hours, where in the first hour, no potential was applied to the membrane surface and the baseline PFCAs removal of the membrane was determined by measuring the difference the PFCAs concentration in the feed (C_F) and permeate (C_P) stream using Equation (5.4). After the first hour, a +0.8 V potential was applied to the membrane electrode (with a corresponding cell potential of +1.0 V and a cell density of 0.5 $mA \cdot cm^2$ on the MXene membrane). All experiments were at least duplicated to obtain the mean PFCA removal (η) under different conditions.

$$\eta(\%) = \left(1 - \frac{C_p}{C_F}\right) \times 100\% \tag{5.4}$$

5.2.7 Adsorption Test on eQCM

To accurately monitor the electro-sorption kinetics of PFCAs on MXene, we conducted the adsorption tests on an Electrochemical quartz crystal microbalance (eQCM, 10M,

GAMRY Instrument), which combines the QCM with a potentiostat (CH Instruments 760E) as shown in **Figure 5.1**. A typical three-electrode system was constructed with a gold crystal sensor (5 MHz, GAMRY Instrument), a platinum (Pt) wire, and an Ag/AgCl electrode as working electrode, counter electrode, and reference electrode respectively. The MXene suspension (10 mg·L^{-1}) were dropped cast on the gold crystal sensor surface and air-dried overnight to form a layer of 0.001 g·cm^{-2}. The catalyst-coated gold sensor was placed in a static cell filled with 0.1 M Na_2SO_4**.** Then, a constant voltage (+ 0.8 V) was applied to the gold sensor to enable PFCAs adsorption. The vibration frequency shift of the gold sensor was caused by the PFCA sorption that caused the mass changes. The frequency shift of the sensor was used to calculate the interfacial mass changes on a gold surface (e.g., gold) at an ng·cm^{-2} level based on the Sauerbrey equation in Equation (5.4) by the supporting software (Echem Analyst, GAMRY INSTRUMENT).

$$\Delta f = -\frac{2 f_0^2}{A\sqrt{\rho_q \mu_q}} \Delta m \tag{5.4}$$

where Δf is the frequency change (Hz), Δm is the mass change (g), f_0 is the resonant frequency (Hz), A is the piezoelectrically active crystal area (0.95 cm^2), ρ_q is the density of quartz (13.92 g·cm^{-3}), and μ_q is the shear modulus of quartz for AT-cut crystal (2.9 × 10^{11} g·cm^{-1}·s^{-2}).

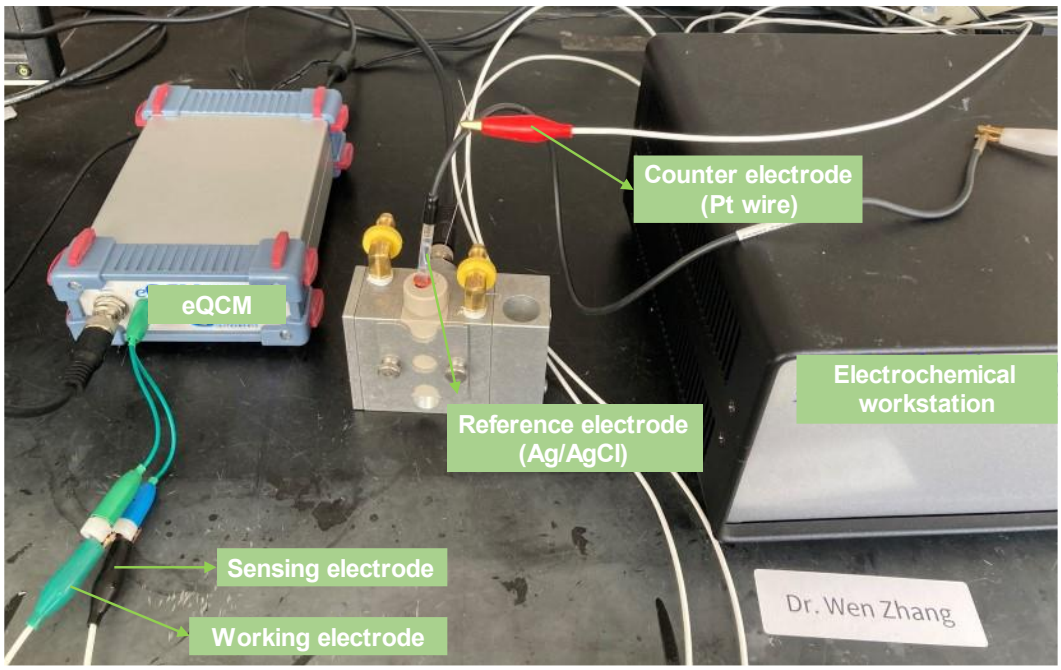

Figure 5.1 The electrochemical quartz crystal microbalance (e-QCM) coupling with an electrochemical workstation system.

5.2.8 DFT Calculation

We have employed the Vienna Ab Initio Package (VASP) to perform all the density functional theory (DFT) calculations within the generalized gradient approximation (GGA) using the Perdew-Burke-Ernzerhof (PBE) formulation. We employed projected augmented wave (PAW) potentials to describe the ionic cores and took valence electrons into account using a plane wave basis set with a kinetic energy cutoff of 600 eV. Partial occupancies of the Kohn−Sham orbitals were allowed using the Gaussian smearing method and a width of 0.05 eV. The electronic energy was considered self-consistent when the energy change was smaller than 10^{-6} eV. A geometry optimization was considered convergent when the force change was smaller than 0.02 eV/Å. Grimme's DFT-D3 methodology was used to describe the dispersion interactions.Bader technique was used for quantifying the loss or gain of charges by the host material and adsorbed PFAS species.

The $Ti_3C_2T_x$ (T = F, O, Cl) unit cell in the cubic $P6_3/mmc$ space group were optimized, which using a 2×2×1 Monkhorst-Pack k-point grid for Brillouin zone sampling. $Ti_3C_2T_x$ with different termination surface model was constructed with *p*(4×4×2) periodicity in the x, y and 1 stoichiometric layer in the z direction separated by a vacuum layer in the depth of 20 Å in order to separate the surface slab from its periodic duplicates. During structural optimizations, the gamma point in the Brillouin zone was used for k-point sampling. A Monkhorst-Pack k-point mesh of 2× 2×1 was also used for calculation of the density of states (DOS).

Surface energy is a measure of thermodynamic stability of the surface; a low positive value indicates a stable surface. The surface energy (γ) of $Ti_3C_2T_x$ (T = F, O, Cl) can be calculated according to the following equation:

$$\gamma = (E_{surf} - nE_{bulk}) / 2A \tag{5.5}$$

where E_{surf} is the total energy of the surface, E_{bulk} is the bulk energy of the unit cell, A is the surface area, the coefficient is 2 since both the upper and lower surfaces are optimized, and n represents the number of unit cells that the surface contains.

The adsorption energies (E_{ads}) of adsorbate PFBA and PFOA were defined as

$$E_{ads} = E_{A/surf} - E_{surf} - E_{A(g)} \tag{5.6}$$

where $E_{A/surf}$, E_{surf} and $E_{A(g)}$ are the energy of adsorbate PFBA or PFOA adsorbed on the surface, the energy of clean surface, and the energy of isolated A molecule in a cubic periodic box with a side length of 20 Å and a 1×1×1 Monkhorst-Pack k-point grid for Brillouin zone sampling, respectively.

The work function is defined as the value of the lowest amount of energy required to relocate the electron from the Fermi level to vacuum level. This parameter can be calculated via the following formula:

$$\Phi = E_{vac} - E_f \tag{5.7}$$

where Φ is the work function, E_{vac} is the electrostatic potential of vacuum level, and E_f is the energy of Fermi level for different species Fermi level (from OUTCAR file).

5.2.9 Determination Method of the PFCA Concentrations

An Agilent 6470A triple quadrupole LC/QQQ system was used to detect the concentrations of PFCAs and intermediates (C_2–C_7) during degradation based on USEPA Method 537. A C18 column (Agilent poroshell 120 EC, 50 × 3 mm, 1.8 μm) was used at 40°C using a mobile phase of solvent A (5 mM ammonium acetate in distilled water) and B (5 mM ammonium acetate in 100% methanol). The injection volume of each sample is 5 μL with a flow rate of 0.5 $ml \cdot min^{-1}$. The compounds were analyzed in an electrospray negative ionization mode. The mode of multiple reaction monitoring with −4.5 kV of ion spray voltage was used to perform the analysis. The fluoride ion in the solution was analyzed by Metrohm 881 Compact Ion chromatography (IC) Pro coupled with a Metrosep A Supp 5–250 column. A solvent gradient was applied to separate different components in solution: 0~5 min, NaOH (1.0 mM); 5.1~32 min, NaOH (15 mM); 32.1~36 min, NaOH (50 mM); 36.1~46 min, NaOH (1 mM). The flow rate and temperature are kept at 1.5 $mL \cdot min^{-1}$ and 30°C, respectively.

5.3 Results and Discussion

5.3.1 Characterization of MXene and MXene-coated Membranes

Figure 5.2a illustrates the preparation process of 2D MXene with different terminations. For example, the fluorine terminated MXene ($Ti_3C_2F_2$) was obtained from etching of Ti_3AlC_2 MAX powder and subsequent liquid-phase delamination in the aqueous solution of hydrochloric acid and lithium fluoride . The synthesis of $Ti_3C_2Cl_x$ from Ti_3AlC_2 is analogous to that of chemical etching of Ti_3AlC_2 in a HF solution, where Cu^{2+} and Cl^- act as H^+ and F^-, respectively. The $Ti_3C_2Cl_2$ powder were further immersed in ammonium persulfate (APS) solution to remove Cu particles from the $Ti_3C_2Cl_2$. The Cl-MXene act similarly during the substitution/elimination reaction for the O-terminated MXene preparation.

Figure 5.2b, 5.2c and **5.2d** display the typical SEM image of the prepared three MXene materials ($Ti_3C_2Cl_2$, $Ti_3C_2F_2$, $Ti_3C_2O_2$) and the respective EDX element mappings. The three MXene show the typical nanosheet structure with a rough surface and a multilayered structure. Element mappings reveal that Ti, C, Cl and O are uniformly distributed throughout the entire structure of $Ti_3C_2Cl_2$ (**Figure 5.2b**). **Table 5.1** indicates that the elemental ratio of Ti/C/Cl = 43.2:21.5:25.3 with small amounts of Cu (0.7 atom %), Al (2.9 atom %), and O (6.3 atom %). The presence of oxygen is probably ascribed to the reisdual Al $(OH)_3$, which is the hydrolysis product of $AlCl_3$. Moreover, a few Cl terminations might be replaced by O-containing terminals during processes such as water washing, which could also contribute to the oxygen element on the surface. EDX mapping also confirms the uniform distribution of Ti, C, F, and O for $Ti_3C_2F_2$ (**Figure 5.2c**), which has Ti 42.1atom %, C 22.5 atom %, F 20.2 atom% and O 13.0 atom%. The O content

increased to 13.0 atom%, probably due to the water absortpion during the synthesis in the LiF-HCl solution. Finally, the $Ti_3C_2O_2$ Mxene (**Figure 5.2d**) is verified to have elements of Ti, C, O and small amounts of Cl (5.8 atom%).

Figure 5.2e-h shows the SEM images of the pristine Nylon membrane and F-MXene-coated membrane surface and cross-section structures. The Nylon membrane surface had homogeneous pores with a mean pore diameter of 0.45 μm. The dense MXene layer on the membrane rendered a thickness of ~10 μm and reduced the effective pore diameter down to 0.12 μm as measured by the water permeability test. The cross-section SEM image also suggests the MXene layer has a laminar structure with narrow and regular interlayers that provide adsorption sites and molecular transport channels.

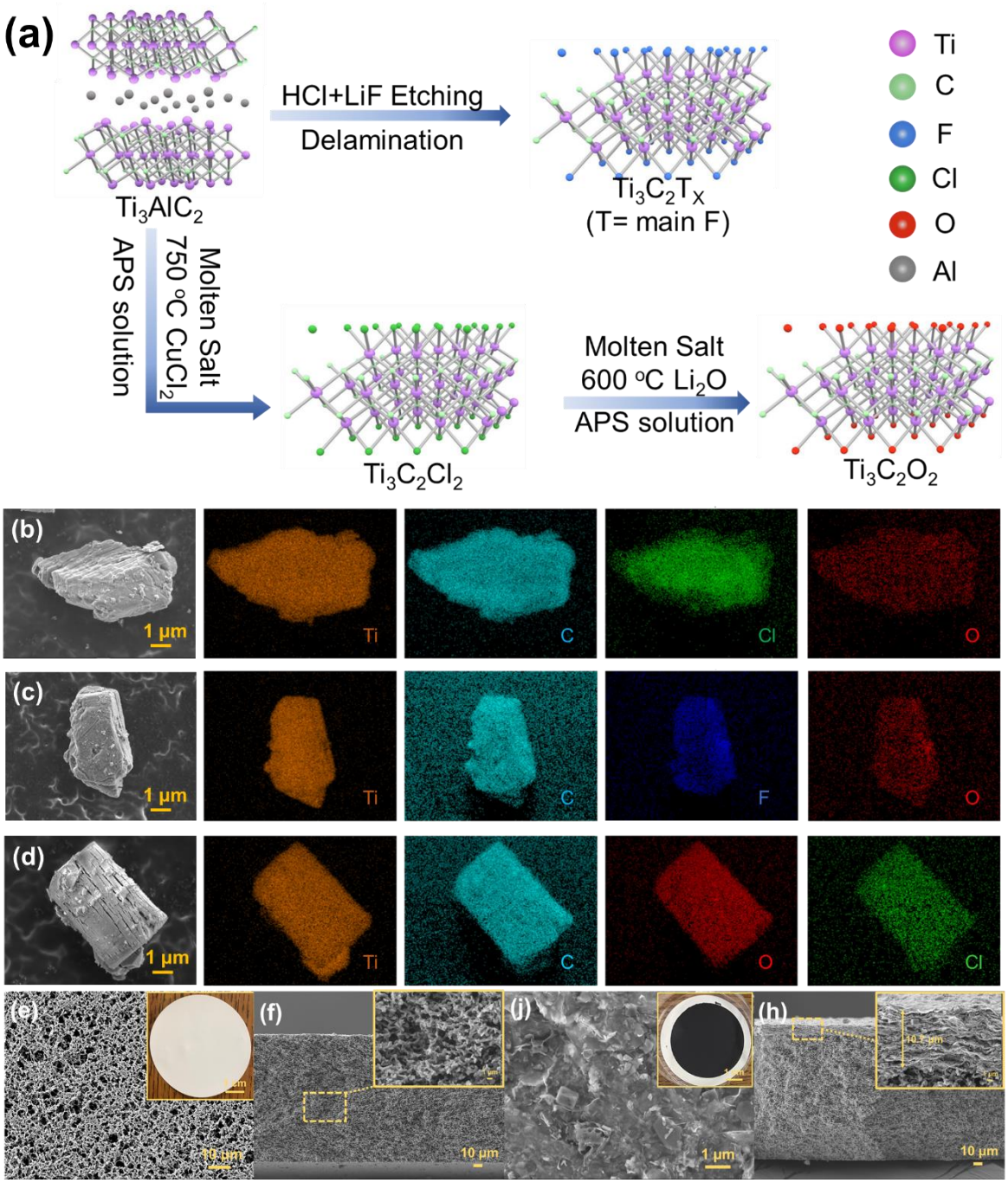

Figure 5.2 (a) Scheme of the synthesis of three different terminated MXene. Typical SEM images and corresponding EDX mapping of (b) $Ti_3C_2Cl_2$, (c) $Ti_3C_2F_2$, and (d) $Ti_3C_2O_2$. SEM images of a Nylon membrane support (e) surface and (f) cross-section. (j) surface and (h) cross-section SEM images MXene membrane, respectively.

Table 5.1 Average Chemical Composition (atom %) of Ti_3AlC_2, $Ti_3C_2Cl_2$, $Ti_3C_2F_2$, and $Ti_3C_2O_2$ MXene

EDS analysis	Ti	Al	C	Cl	O	F
Ti_3AlC_2	51.2	14.8	33.6	NA	0.4	NA
$Ti_3C_2Cl_2$	42.2	3.0	21.5	25.3	7.2	NA
$Ti_3C_2F_2$	42.1	1.2	22.4	NA	13.0	20.3
$Ti_3C_2O_2$	45.6	NA	23.8	5.8	23.1	NA

Figure 5.3a shows the XRD patterns of the pristine Ti_3AlC_2 and the produced $Ti_3C_2Cl_2$, $Ti_3C_2F_2$ and $Ti_3C_2O_2$, respectively. Compared to Ti_3AlC_2, most of the diffraction peaks such as the (107) peak at 39° disappeared in the final products with only the (00l) peaks as well as several broad and low-intensity peaks in the 2θ range from 5° to 60°; these features indicate the successful reduction of Ti_3AlC_2 into layered $Ti_3C_2T_x$, where the Al layers in Ti_3AlC_2 have been etched out by using the Lewis acid molten salt. The different terminal atoms also result in the different structure factors and caused the various relative intensity of the (00l) peaks of the MXenes. In addition, the (002) peak of $Ti_3C_2Cl_2$ MXene shifted to a lower angle, indicates that the lattice spacing has increased due to the removal of the Al layer. $Ti_3C_2F_2$ and $Ti_3C_2Cl_2$ both have the intense (002) peaks corresponding to the interlayer spacing values of respectively 20.90 and 22.22 Å, which agree with previous reports. The increased interlayer spacing in $Ti_3C_2Cl_2$ and $Ti_3C_2O_2$ may result from the larger radii of oxygen and chlorine atoms that replaced the fluorine atoms.

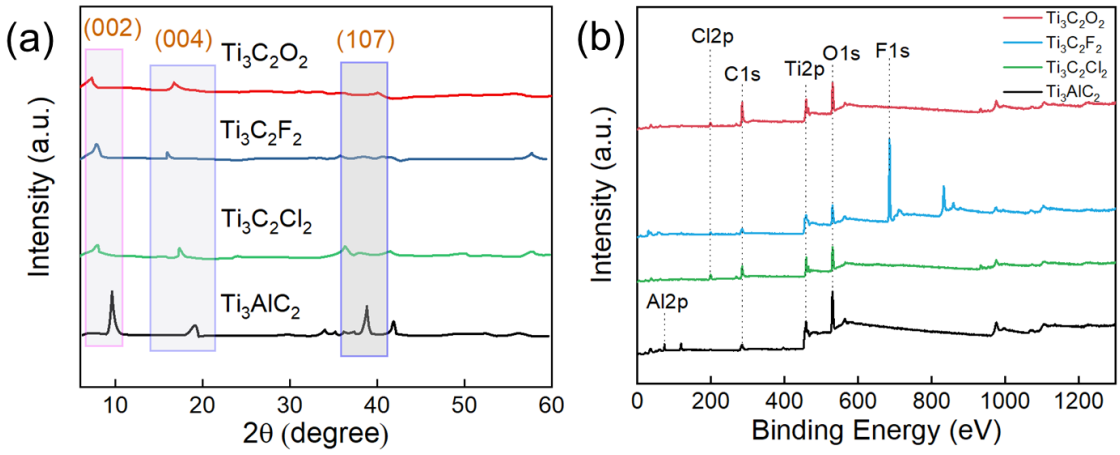

Figure 5.3 (a) XRD patterns and (b) XPS surveys of the Ti_3AlC_2, $Ti_3C_2Cl_2$, $Ti_3C_2F_2$ and $Ti_3C_2O_2$ MXenes.

Figure 5.3b shows the XPS spectra of Ti_3AlC_2 (black) and three different terminated MXenes (–Cl, –F, and –O). For Ti_3AlC_2, the signals of Al 2p, C 1s, Ti 2p, and O 1s were found at 74.2, 284.1, 458.1, and 530.9 eV, respectively. The peak at 74.2 eV is assigned to $Al(OH)_3$, which may be produced from the reaction of Ti_3AlC_2 with water. After etching by $HF/CuCl_2/LiO_2$ and further immersion in APS solution, only the signals of Ti 2p, O 1s, Cl 2p, F 1s and C 1s were detected on the three MXenes, suggesting the no significant amounts of Al, Cu and Li element remained.

Figure 5.4 shows the deconvolution of XPS spectra for Ti 2p, C 1s, O 1s, F 1s and Cl 2p for Cl-, F- and O-terminated MXenes. In the Ti 2p region, the peaks at 455.4 and 461.8 eV are assigned to the Ti−C bond. The peaks at 456.2 and 462.5 eV correspond to Ti−O, the peaks at 458.2 and 464.2 eV corresponding to the Ti−F bond, and the peak at 458.8 eV attributed to the high-valency Ti compound, is assigned to the Ti-Cl bonds. The absence of a peak at around 459 eV indicates that no TiO_2 formed during the sample preparation or the annealing process. The C 1s region is deconvoluted into four peaks at binding energies of 281.3, 284.3, 286.1 and 288.8, which are assigned to C–Ti, C–C, C–O

and O–C=O bonds, respectively. The peaks at 198.3 eV and 200.1 eV are associated with Cl-Ti ($2p_{1/2}$) and Cl-Ti ($2p_{3/2}$) bonds, which indicated the presence of Ti-Cl bonds in Cl-terminated MXene. **Figure 5.4f** shows single XPS peak in the F 1s core level (Ti–F bonds at 685.5 eV), clearly identifies the fluorine to be solely adsorbed on the A site. In the O 1s region (**Figure 5.4i**), the peaks at 530.8 eV, 531.7 eV, and 533.7 eV are assigned to the Ti-O, Ti-C-O, and C-Ti-$(OH)_X$ bonds, respectively.

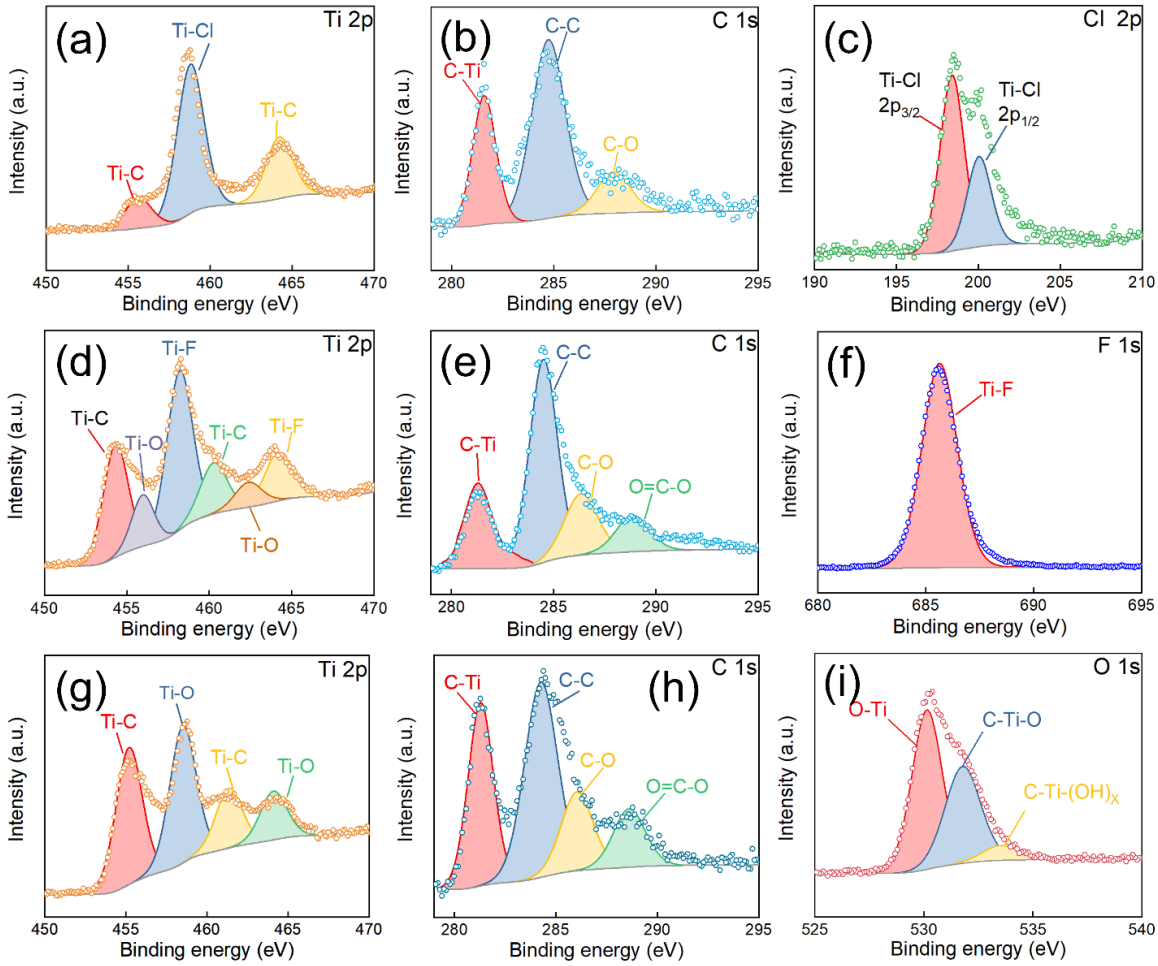

Figure 5.4 XPS Spectra of Three MXene in the Ti 2p, C 1s, O 1s, F 1s and Cl 2p regions.

Figure 5.5a presents the cyclic voltammetry (CV) curves of the different MXenes at the scan rate of 50 $mV \cdot s^{-1}$ with the voltage range of −0.4–0.8 V (vs. Ag/AgCl). The electrochemical capticatance of O-MXene is obviously larger than F-MXene and Cl-

MXene as indicated by higher current respone at same potential. O-MXene also yielded a relatively higher specific capacitance (111.9 mF·cm^{-2}) than Cl-MXene membrane (52.9 mF·cm^{-2}) and F-MXene membrane (79.7 mF·cm^{-2}). **Figure 5.6** also shows cyclic voltammetry (CV) of three MXene electrode with a mass loading of 20 mg at scan rates ranging from 10 mV·s^{-1} to 500 mV·s^{-1}. **Figure 5.5b** shows that the specific capacitance had a linear relationship with square root of scan rate ($v^{-1/2}$), demonstrating the classical Nernstian diffusion-controlled redox behavior. The shape of the CV curve barely changes as the scan rate gradually increases, indicating that the MXenes exhibited excellent capability and a low internal resistance.

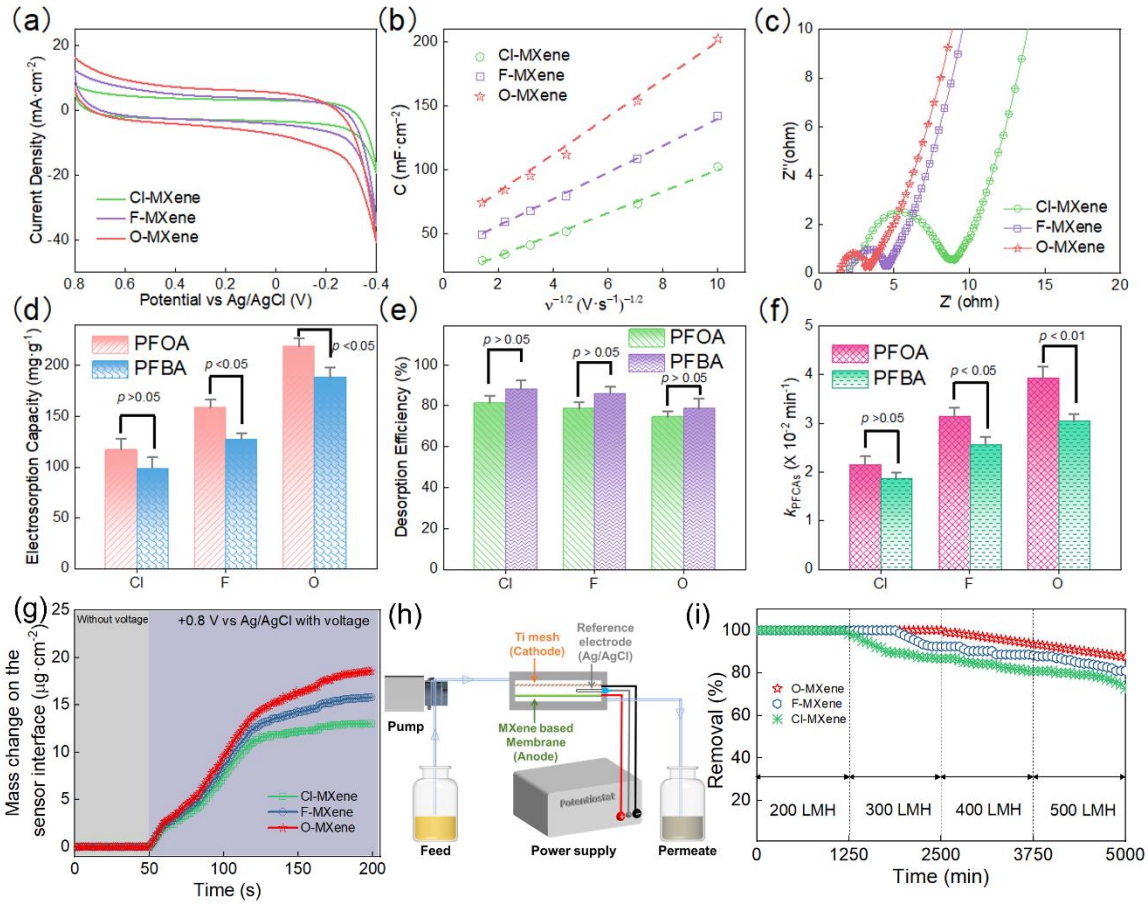

Figure 5.5 (a) Cyclic voltammograms of three different terminated MXenes in 0.1 M Na_2SO_4 with scan rate of 50 mV·s^{-1}, (b) EIS plots of three different terminated MXenes under an open circuit potential, (c) Specific capacitance (*C*) *vs*. the reciprocal square root of scan rate ($v^{-1/2}$) 10 to 500 mV·s^{-1}, (d) PFCAs adsorption capacity and on three different

terminated MXenes in 0.1 M Na_2SO_4 with 10 ppm PFCAs at +0.8 V for 2 h, (e) regeneration efficiency via desorption in 0.1 M Na_2SO_4 at −1.0 V for 0.5 h, (f) The apparent PFCAs degradation rate constant (k_{PFCAS}) on three different terminated MXenes in a batch mode (PFCAs = 1 ppm, anodic potential = +6 V and current density = 10 $mA \cdot cm^{-2}$), (f) The mass changes of MXene-coated Au sensor with/without the potential bias of 0.8 V, (h) Schematics of the MXene-based continuous filtration system and (i) PFOA in continuous filtration mode using three different MXene membranes (the initial concentration of PFOA was 100 $\mu g \cdot L^{-1}$). *p* indicates significance threshold in *t*-test (if $p < 0.05$, then that result is said to be statistically significant. If $p > 0.05$, then the result is insignificant.)

To further reveal the electrical conductivity and capacitance of the three MXenes, the Nyquist plots in **Figure 5.5c** show a typical semicircle for three samples at high frequencies, which reflects the charge transfer resistance (R_{ct}). The inclined line at the low frequency region corresponds to a Warburg diffusion process (*W*), which is associated with the ion diffusion in the porous electrode. The $Ti_3C_2O_2$ electrode (O-MXene) showed a smaller semicircle than that of the other two MXene electrodes, suggesting the faster charge transport and lowest charge transfer resistance.

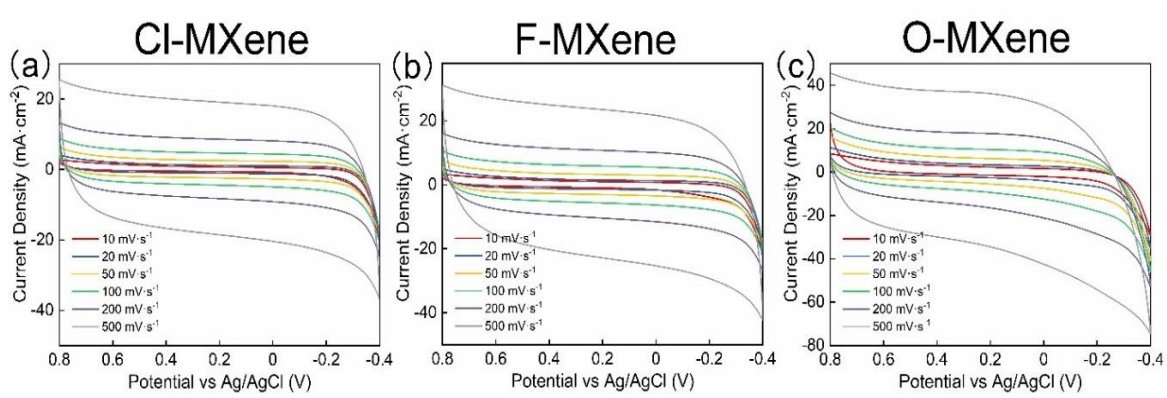

Figure 5.6 CV curves performed on Cl-MXene Membrane, F-MXene Membrane and O-MXene Membrane at Different Scan Rates (10 $mV \cdot s^{-1}$ to 500 $mV \cdot s^{-1}$).

5.3.2 Effect of Termination on the PFCAs Adsorption and Desorption of MXene membrane

The electrosorption capacities of two PFCAs on three MXenes are compared in **Figure 5.5d**. The O-terminated MXene absorbed greater PFACs than F- and Cl-terminated

MXenes did (p<0.05). The Cl-MXene membrane achieved a relateively low electrosorption capacity of 117.3 ± 10.6 mg·g^{-1} for PFOA. In contrast, the F-terminated MXene and O-terminated MXene obviously both had increased electrosorption capacities of 158.8 ± 7.8 mg·g^{-1} and 215.9 ± 8.5 mg·g^{-1}, respectively. The three MXenes consistently exhibited lightly lower adsorption capacities for PFBA especially on O-MXene (p<0.05), probably because the different hydrophobicity of PFBA and PFOA due to different chain length. For all cases, however, applying +0.8 V of positive potential led to greatly improved uptake, with O-terminated MXene membrane having the highest increase with the positive potential.

To further confirm the adsorption behavior of PFCAs on three different terminated MXenes, the eQCM measurements were conducted to sensitively detect the interfacial adsorption of PFOA (1000 ppm) on the MXene-coated gold sensor or chips. **Figure 5.5g** shows that no mass changes were observed in the initial 50 s as indicated by the stable horizontal baselines when no positive potential was applied, suggesting the background adsorption of PFOA on MXene is negligible. After applying a positive voltage (0.8 V vs Ag/AgCl) to the sensor, the mass of gold chips dramatically increased and reached a stable level of 12, 15, and 18 μg·cm^{-2}, respectively, which correspond to 120, 150 and 180 mg·g^{-1} and match the results in **Figure 5.5d**.

Figure 5.5f shows the electrodesorption efficiency of PFCAs from three MXenes at −1.0 V vs Ag/AgCl. Both PFOA and PFBA were found to desorb from MXene and reach the maximum dissolved concentrations within 1 h as compared in **Figure 5.5d**. About 80% of PFOA and 87% PFBA was released into the solution. The desorption efficiency seems to be lower for PFOA than for PFBA probably due to the greater hydrophobic binding

strength for PFOA on MXene. Similarly, the O-terminated MXene shows a lower desorption efficiency (75%) than the other MXenes due to its stronger adsorption capacity and affinity.

After the electro-sorption of PFCAs at the initial concentration of 1 $mg \cdot L^{-1}$ in 0.1 mM Na_2SO_4, the *in situ* degradation of PFOA and PFBA on the MXenes was evaluated by elevating the anoidic potential from 0.8 V to 6.0 V at 10 mA cm^{-2}. **Figure 5.5f** compares the pseudo-first-order rate constants (k_{PFOA}), which increased from 2.14 ± 0.28 min^{-1} for Cl-MXene to 3.92 ± 0.54 min^{-1} for O-MXene and 3.14 ± 0.68 min^{-1} for F-MXene. The electro-oxidation performance of MXene membranes on PFBA and PFOA were investigated by using 1 $mg \cdot L^{-1}$ PFBA or PFOA in 0.1 mM Na_2SO_4. In order to confirm the oxidation of PFBA or PFOA instead of electrosoprtion, desorption experiments were also performed after oxidation experiments. No PFOA or PFBA was found in the desorption electrolyte, implying complete degradation of PFOA or PFBA.

5.3.3 Mechanism of Surface Termination

To better understand the fundamental mechanisms for adsorption and degradation of PFCAs on different terminated MXenes, we further conducted the DFT simulations to compare the adsorption energies of PFOA and PFBA on MXene sheets. **Figure 5.7–5.9** show four different adsorption configurations on three different terminated MXenes. The adsorption energies of PFBA and PFOA on MXene surfaces are summarized in **Table 5.2**, which indicate that surface vacancies are needed to get the PFCAs molecules to adsorb (they won't adsorb on pristine surfaces); because such defects form spontaneously from the synthesis, it is likely this that leads to the good adsorption of PFCAs. Interestingly, we found that the PFCAs won't adsorb on a Cl- MXene either with or without defects. Finally,

we found that the deprotonated PFCAs anions (which are typically present in water) adsorb more strongly that the protonated version, meaning these materials should perform very well in aqueous environments.

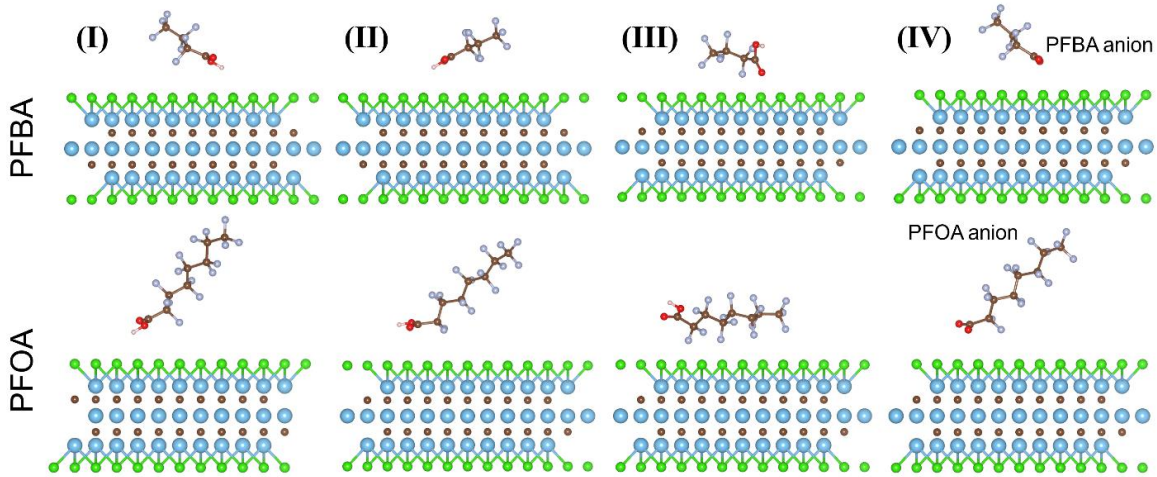

Figure 5.7 The optimized different configurations of PFBA and PFOA adsorption on $Ti_3C_2Cl_2$. Hydrogen, carbon, oxygen, fluorine, chlorine, and titanium atoms are shown in pink, brown, red, lavender, green and cyan spheres, respectively.

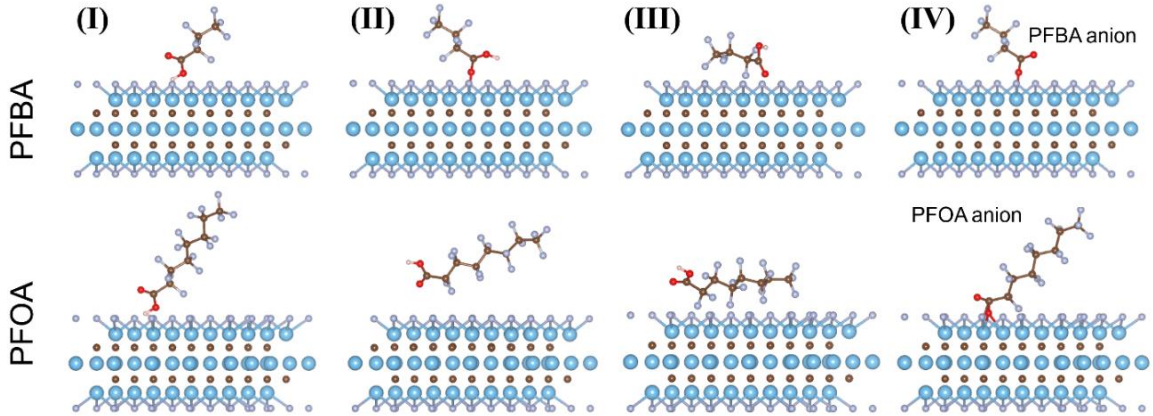

Figure 5.8 The optimized different configurations of PFBA and PFOA adsorption on $Ti_3C_2F_2$. Hydrogen, carbon, oxygen, fluorine, titanium atoms are shown in pink, brown, red, lavender and cyan spheres, respectively.

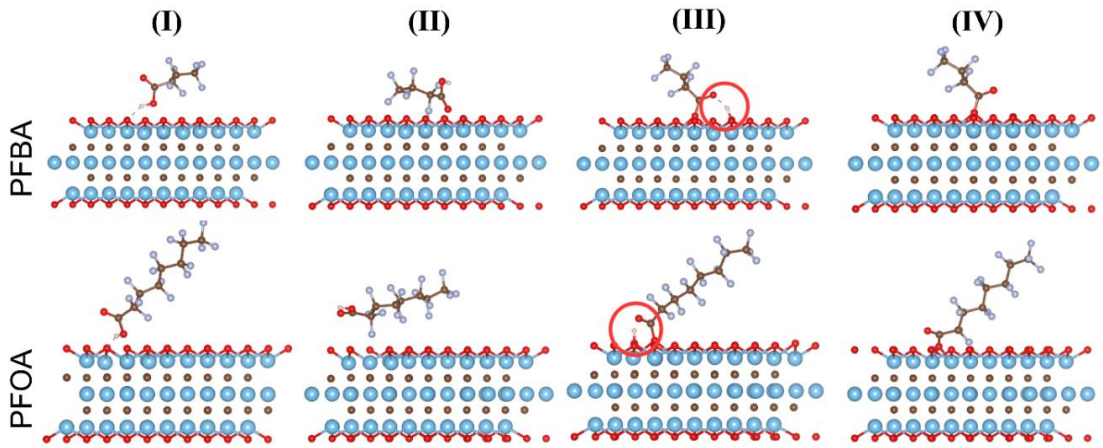

Figure 5.9 The optimized different configurations of PFBA and PFOA adsorption on $Ti_3C_2O_2$. Hydrogen, carbon, oxygen, fluorine, titanium atoms are shown in pink, brown, red, lavender and cyan spheres, respectively.

Table 5.2 PFBA and PFOA Adsorption Energies (eV) on Different Terminated MXene

	Configurations	Materials		
		$Ti_3C_2Cl_2$	$Ti_3C_2O_2$	$Ti_3C_2F_2$
PFBA	(I)	1.64	0.81	1.47
	(I) with defect	1.24	−1.08	−0.80
	(II)	1.32	0.79	−0.75
	(II) with defect	0.55	−1.33	−1.62
	(III)	1.63	0.80	1.47
	(III) with defect	1.11	−1.03	−1.64
	(IV)	1.89	1.07	1.24
	(IV) with defect	0.40	−3.30	−3.07
PFOA	(I)	2.34	0.05	3.31
	(I) with defect	0.31	−1.41	−0.63
	(II)	0.63	2.22	2.89
	(II) with defect	0.34	−1.43	1.56
	(III)	1.84	3.64	6.46
	(III) with defect	1.45	1.75	4.18
	(IV)	1.47	3.08	5.80
	(IV) with defect	−0.04	−1.26	−0.83

The properties of MXene change with surface functionalization and its compositions. For example, the electronic work function (WF), the energy difference between the Fermi level and the vacuum level that depicts the minimum energy required to withdraw an electron from the MXene surface, is found to strongly depend on the

composition of the functional groups . Our calculated work functions for the −Cl, −F and −O terminated MXene are 4.54, 4.92 and 6.20 eV, respectively. The results agree with the previous studies showing that the work function of MXenes follows this trend: −O> −F > bare > −OH functionalized MXene . **Table 5.3** summarizes the variations of the work functions for defected MXenes. The changes of work function could be associated with induced surface dipoles caused by the functional groups as well as by shifts in the Fermi level of the material due to electronic redistribution. Komsa et al. reported that work function depends linearly on the concentration of O, F, and OH . Different work functions of Ti_3C_2Tx with different surface termination may result from the alternation of direction and magnitude of electron transfer at the graphene/MXene interface . The resulting polarization of the interface enhanced the strength of interfacial adhesion and modified the band structure of graphene.

Table 5.3 Calculated Work Function and Bader Charge of Three Different MXene.

Sureface	Work Function (eV)	Bader Charge (e)
Cl-MXene	4.54	0.12
d-Cl-MXene	4.53	0.34
F-MXene	4.92	0.56
d-F-MXene	4.80	0.63
O-MXene	6.20	0.61
d-O-MXene	6.05	0.82

To describe the electrochemical properties more comprehensively, we also calculated the density of states (DOS) of three different terminated MXenes. As shown in **Figure 5.10**, all three MXenes is metallic with the Fermi energy falling into a continuum of energy states. The DOS in the range from −2 to 2 eV are mainly contributed by the Ti 3d orbitals and the DOS located between −5 and −2 eV come from the hybridization of Ti 3d and C 2p orbitals. Moreover, the band structures of $Ti_3C_2Cl_2$ and $Ti_3C_2F_2$ are more

similar compared to $Ti_3C_2O_2$. This is because both Cl and F groups demand receiving one more electron to be stabilized, whereas O is capable of receiving two more. According to the DOS of $Ti_3C_2Cl_2$, $Ti_3C_2F_2$ and $Ti_3C_2O_2$ the p orbitals of surface functionalization groups all hybrid with the Ti 3d orbitals and shift the Fermi level downward to varying degrees. It is to be mentioned that the overlap DOS areas between O 2p and Ti 3d orbitals are much larger than those of Cl or F in the range from −5 to −2 eV, indicating much stronger hybridization between O 2p orbitals and Ti 3d orbitals. Consequently, the much stronger hybridization between O and Ti significantly reduces the number of delocalized/free electrons in pristine Ti_3C_2 MXenes, which finally results in a metal–semiconductor transition of Ti_3C_2 after O functionalization ($Ti_3C_2O_2$). Nevertheless, the continuous electronic states crossing Fermi level for O-terminated MXene indicate that its conductivity is still good. Hence, three different terminated MXenes owe retains outstanding electrical conductivity, implying its exceptional capability to transport electrons. We believe this unique merit of MXene renders it a superior co-catalyst outperforming its counterparts, such as graphene and carbon nanotubes,

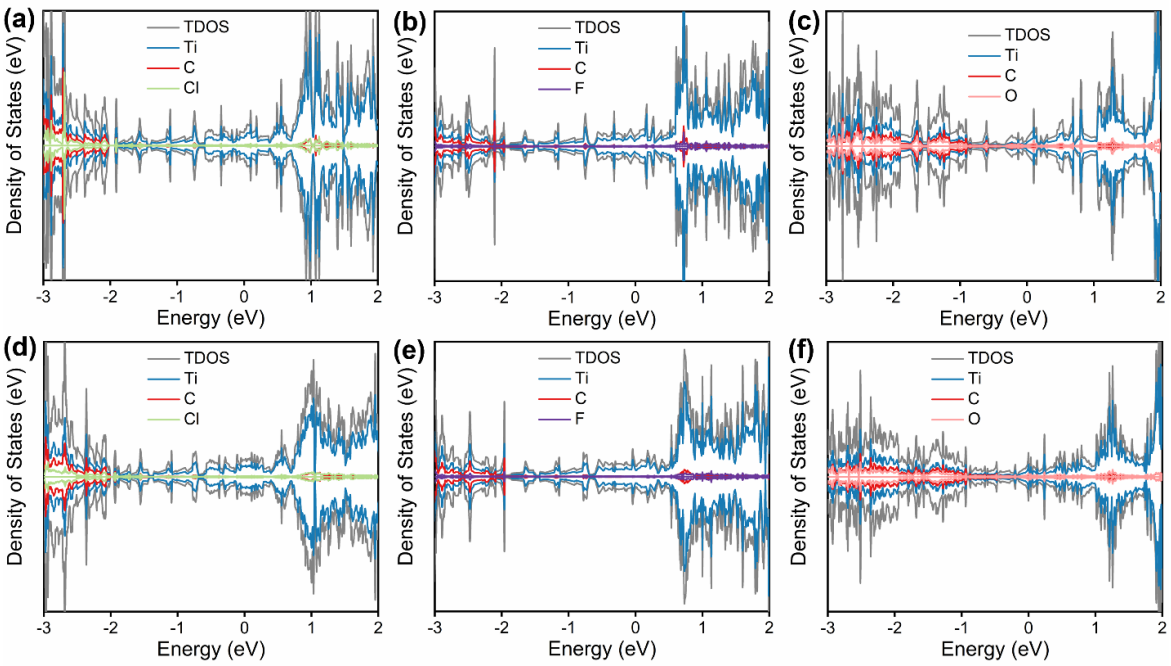

Figure 5.10 The calculated density of states of three different terminated MXene, where the Fermi energy is set to zero.

DFT simulation is capable of computing the charge distribution, according to which the charge transfer could be precisely determined using Bader analysis. Further insights which the enhanced adsorption and degradation for the PFOA on different terminated MXenes can be gained from the charge distribution behavior of anionic PFOA adsorption on $Ti_3C_2Cl_2$, $Ti_3C_2F_2$ and $Ti_3C_2O_2$, Bader charge analysis as shown **Table 5.3** also reveals that defect $Ti_3C_2O_2$ donates 0.19 |e| and 0.28 |e| more electrons to $C_7F_{15}COO^-$ relative to $Ti_3C_2F_2$ and $Ti_3C_2Cl_2$, respectively. Moreover, it is proposed that the –O functional group in Ti_3C_2 MXene is more active in the redox reaction than –Cl and –F. The valence state of Ti element is also a very important parameter affecting pseudocapacitance. It was concluded that the Ti element in $Ti_3C_2O_2$ possesses the most unfilled orbitals, followed by that of $Ti_3C_2Cl_2$ and $Ti_3C_2F_2$, which suggests that the chemical activity of Ti element in Ti_3C_2 MXene is significantly hindered by the –Cl and –F functional groups.

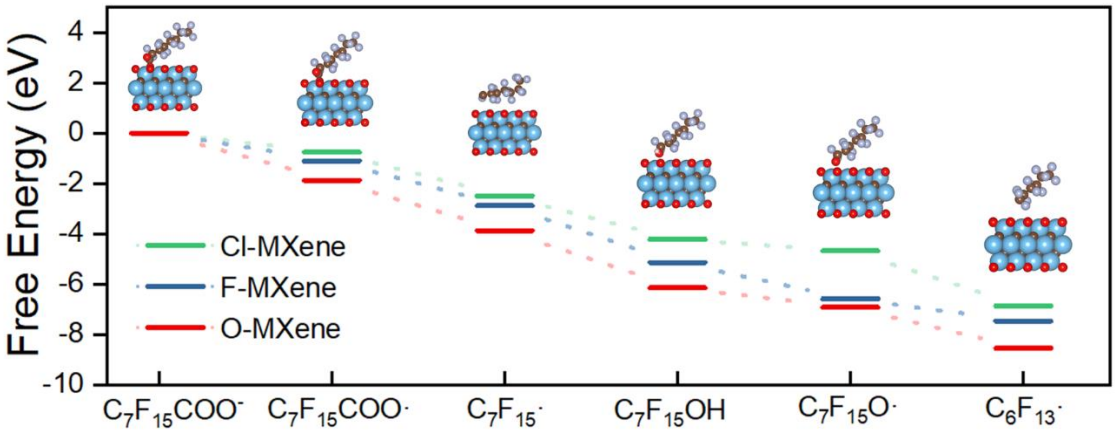

Figure 5.11 Reaction paths for the degradation of PFOA over $Ti_3C_2Cl_2$, $Ti_3C_2F_2$ and $Ti_3C_2O_2$ surface.

Furthermore, we also investigated the effect of surface termination on perfluorooctanoic acid (PFOA) degradation by DFT calculations. We screened possible intermediates and optimal paths for PFOA decomposition over three models ($Ti_3C_2Cl_2$, $Ti_3C_2F_2$ and $Ti_3C_2O_2$). As we mentioned before, for $Ti_3C_2O_2$, anionic PFOA ($C_7F_{15}COO^-$) exhibited a chemical adsorption configuration with an adsorption energy of −1.26eV, followed by the dissociation of CO_2 to form C_7F_{15}• radical. Loss of carbon from PFOA to produce CO_2 is consistent with the first step of anodic oxidation of PFOA following the Kolbe one electron-transfer reaction. Conversion of C_7F_{15}• radical to $C_7F_{15}OH$ has been proposed to involve •OH (C_7F_{15}• +•OH→$C_7F_{15}OH$) in an electrocatalytic system where abundant •OH formation was observed. Loss of fluorine through C−F bond breakage is believed to involve this unstable intermediate: perfluoroheptanol ($C_7F_{15}OH$). One electron from the terminal −OH function group will lose, leading to the formation of C_6F_{13} COF. Based on the above analysis, perfluoroheptanol ($C_7F_{15}OH$) is an important intermediate in destructing of perfluorooctanoic acid. Moreover, the pathway of $Ti_3C_2O_2$ was most favourable among three of different model which also indicates that O-terminated surface was much more effective than Cl- and F-terminated surface.

5.4 Conclusion

We have demonstrated three different termination MXene ($Ti_3C_2Cl_2$, $Ti_3C_2F_2$ and $Ti_3C_2O_2$) to adsorption, desorption and oxidation PFCAs (PFBA and PFOA). In addition, the oxygen functionalized on the surface of the Ti_3C_2 MXene nanosheets ($Ti_3C_2O_2$), which can greatly reduce the interface resistance to accelerate the overall electron transport and improve the electrochemical reaction kinetics. Density functional theory (DFT) calculation shows that the excellent adsorption and interfacial interaction performance of the $Ti_3C_2O_2$ with PFOA and PFBA, which may be result from the generation of numerous electrochemical active sites and the improvement of electronic conductivity. The electrochemical behaviors of the four MXene membrane electrodes suggest that the total capacitance can be divided into two parts: the diffusion-controlled part relating with the redox reaction from the bulk element, mainly dependent on the oxidation state of Ti element in Ti_3C_2 MXene, and the capacitor-like part consisting of electrochemical double layer mechanisms, which are strongly affected by interlayer spacing, surface absorption, and functional groups.

CHAPTER 6

PERSPECTIVE FOR FUTURE RESEARCH

Water treatment technologies with multipurpose, modular, scalable, robust, chemical-free, and energy-efficient are necessary to address the unresolved issues of worldwide water scarcity and water pollution. Developing conductive membranes for water purification and wastewater treatment has become the topic of numerous studies. Reactive electrochemical membrane systems have a limited commercial application due to a few issues, despite the increased treatment efficiency brought on by the synergetic effect of membrane filtration and electrochemical behaviors. For example, (1) trade-offs between electrode material performance, stability and cost, (2) formation of toxic halo-oxyanion and halogenated organic byproducts, (3) the limitations of mass transfer from the bulk solution to the electrode, and (4) improving energy efficiency by optimizing reactor design. The process of producing membrane active layers with high electrical conductivity and porosity is known as reactive electrochemical membrane preparation. Carbonaceous materials, metals, metal oxides, and polymers are the main conductive materials employed in the production of reactive electrochemical membranes. Although materials like CNTs and Magnéli phase Ti_4O_7, which are frequently utilized to prepare reactive electrochemical membranes, there are still some problems like corrosion, passivation, membrane fouling, complicated material synthesis conditions, and high cost. More efforts are required to develop electrochemical membranes that are superior in terms of porosity, conductivity, reactivity, and stability over a long-term operation. Electrochemical membrane fabrication techniques should also be simple, economical, and environmentally friendly. Beyond the development

of proper electrochemical membrane materials, it may be possible to embed specialized catalysts or nanomaterials into the conductive layer to provide quick and selective removal of target contaminants in complex water matrices.

Facet engineering of functional nanocrystalline materials is an area of major scientific and technological interest. This is because in many important applications which rely on surface structure and chemistry, such as heterogeneous catalysis, gas sensing, and energy conversion and storage, the properties of the materials can be tailored by controlling the crystal structure, and morphology of the external surfaces of the constituent particles. For heterogeneous catalysis, scaling down the particle size not only increases the number of catalytic sites, but also modifies the electronic properties. Furthermore, the catalytic reactivity and selectivity changes by modifying the arrangement and coordination of the surface atoms, thus becoming very sensitive to the enclosing crystal facets. Constructed with inorganic metal-based centers and bridging organic linkers, metal–organic frameworks (MOFs) have attracted tremendous attention over the past two decades. Their unique characteristics such as unsaturated metal sites, high surface areas, and well-defined single active sites provide platforms for the scientific research in catalytic applications. Similar to other nanomaterials, the precise fabrication of crystal facets of MOFs is crucial for the catalytic performance due to the difference of the atomic arrangement among their crystal facets. Therefore, facet engineering on MOFs with specific catalytic activity and selectivity should be pay considerable attention in future heterogeneous catalysis.

Metal-organic frameworks (MOFs) emerged as promising candidates for electrocatalysts owing to their large surface area, tunable porosity, as well as diverse compositions and metal centers. However, most of the MOFs are burdened with the

intrinsic poor electroconductivity due to the insulating properties of organic ligands and the poor conjugation of metal-organic connection. A variety of methods have been proposed to solve these issues, such as the exfoliation of MOFs into ultrathin layers, design of complicated linkers to obtain conductive MOFs, carbonization of MOFs, and so on. However, so far the electrocatalytic activities of MOF-based catalysts are still unsatisfied in comparison to state-of-the-art noble metal-based catalysts. In future work, it is a strategy to strongly enhance the catalytic performance of poorly conductive MOFs by confining them into two-dimensional MXene monolayer or few multilayers. MXenes possess a 2D morphology exhibiting a large surface area, elevated electrical conductivity, redox activity, and tunable physicochemical properties by altering the interlayer spacing. Their use as binders, fillers, and precursors for other materials finds a wide spectrum of applications. However, MXenes suffer from stability issues because of its oxidation and restacking, limiting their surface area and physicochemical and electrochemical properties. On the other hand, MOFs are well-known for their large surface area, tunable pore features, uniform pore size, and large redox activity. These properties have made them apt for applications in the field of electrochemical energy storage, sensing, electrocatalysis, water treatment, and various biomedical purposes. However, MOFs are challenged by mediocre stability, limited pore sizes, and most importantly their limited electrical conductivity. Interestingly, the intercalation of MOF scaffolds into MXene galleries has presented the possibility to improve the overall stability as well as physicochemical properties of the formed composite materials. MXene@MOF composites amalgamate the advantages of both MXene and MOFs with different structures, resulting in the further elevation of

specific surface area, electrical conductivity, mechanical/hydrolytic stability, porosity, and physicochemical as well as electrochemical properties in the resulting composite material.

A number of novel materials (GO, TMDs, MXenes, MOFs, COFs, Liquid crystal polymers, vertically aligned CNTs or MXene) have shown promise as high selectivity membranes for desalination, water purification and resource recovery. In particular, materials that are prepared using the bottom-up approach demonstrate great versatility and tuneability necessary for removing the wide range of chemicals encountered in water and wastewater treatment. Nevertheless, the development of these novel membrane materials is still in its infancy and needs to transcend a number of challenges before practical application can be achieved. In particular, developing scalable fabrication methods to produce large, high quality, mechanically robust, and chemically stable water treatment membranes using these novel materials remains a critical research need. High selectivity membrane materials will play a major role in future water systems, where the vision of "one water" is realized by integrated water management with distributed, fit-for-purpose water treatment. In such integrated water management systems, high-rate, precise separation of chemicals from water is necessary not only for pollution control, but also for minimization of chemical and energy consumption, and for recycling and reuse of resources.

Quantum chemical modeling is a powerful approach to developing new catalysts and chemical processes because it provides a fundamental description of atomistic systems and can accurately predict their properties ab initio. Electrochemical reactions are related to the events that occur in the electrochemical interface when an electric potential is applied and current passes. The applied electric potential may cause two different kinds of

processes: faradaic processes, the ones that involve charge transfers (redox reactions), and non-faradaic processes, such as adsorption or desorption. Both processes modify the electrochemical interface not only in its atomic structure but also in its electronic properties. Precise control of electrochemical processes, from energy conversion and storage to electrochemical wastewater treatment, corrosion, and electrodeposition, relies on understanding and manipulating the properties of the electrochemical interface. Computational design of new materials for these applications requires an accurate description of both chemical interactions from first-principles calculations and the effects of the electrochemical environment. For instance, the effects of pH value, ion solvation, electrolyte bonding, and potential at the solid-electrolyte interface must be considered when designing energy materials with increased operating voltage windows and energy storage capacity.

Grand-canonical DFT (GC-DFT) provides a fundamentally correct description of electrified interfaces and a correct model of electrocatalysis when coupled with a sufficiently detailed solvent model of the solvent and electrolyte. GC-DFT calculates the grand free energy at an arbitrary potential by optimizing the grand free energy while self-consistently solving for the number of electrons that matches the applied potential rather than calculating the electronic energy of the system with a fixed number of electrons. The grand free energy is defined as $\Phi = A - \mu N$, where A, μ, and N are the Helmholtz free energy, chemical potential, and total number of electrons, respectively. GC-DFT enables accurate calculation of the electronic energy and adsorbate geometry and should thus provide a reliable prediction of the energetics of electrochemical reaction pathways. Furthermore, it enables the comparison of various possible reaction mechanisms at different applied

potentials. Combining computational and experimental methods is a powerful approach to understand the variables that govern catalyst performance and ultimately design improved materials. However, the effectiveness of this approach rests on the strength of the relationships between calculated parameters and experimental measurements. These relationships are complicated by the intricacy and dynamic behaviors of catalytic active sites, and by the non-trivial relationship between calculated reaction energetics and observed rates. As experimental and computational methods continue to become more powerful, clear connections between the two will maximize their utility to guide the design of efficient and selective electrocatalysts.

In addition to water decontamination (organic pollutants, heavy metals, bacteria, virus) and fouling control (organic, inorganic and biofouling) through electrochemical oxidation, electrochemical reduction, electroadsorption and electrorepulsion, electrochemical membranes are also promising for environmental sensing and resource recovery. For example, incorporating electrochemical technique (CV, EIS, DPV) electrochemical membranes could provide superior sensitivity, flexibility, robustness, and selectivity as membrane-based electrochemical sensors. A variety of stimuli, including organic molecules, inorganic ions, and bacteria, could interact with the responsive sites on electrochemical membranes to enable on-site, real-time monitoring of pollutant removal, byproduct generation, fouling formation, and membrane wetting during filtration processes. Additionally, electrochemical membranes also provide opportunities to reclaim multiple valuable resources (such as, phosphorus recovery, nitrate reduction. H_2O_2 generation and heavy metals) from wastewaters by integrating electrochemical resource recovery methods into membrane processes. By transforming aqueous contaminants into nutrients or other

useful materials, rather than removing them and creating additional waste streams, electrochemical membranes for resource recovery could add economic value to the water treatment process.

Finally, the success of these membrane materials for practical application not only depends electrode porosity, conductivity and stability (aging, corrosion and passivation), but also strongly on the availability, cost, safety, and environmental friendship of raw materials as well as that of the cost and scalability of the fabrication processes. Non-toxic, earth-abundant raw materials and environment-friendly synthesis methods should be used whenever possible to avoid health and environmental risks; secure immobilization of functional additives (e.g., engineered nanomaterials) is critical to not only product safety but also longevity. Despite the fact that electrochemical membranes have shown to have a number of important benefits, there are still a number of obstacles in the way of their deployment. Overall, strategies for using electrochemical membranes in actual water/wastewater circumstances must be developed for practical applications. Further research should focus on reducing the occurrence of competing reactions and improving the selectivity and stability of electrocatalysts during long-term operation, especially in complicated water matrices, in order to produce sustainable and energy-efficient processes. Moreover, it's important to prevent the generation of harmful DBPs such oxyhalides and chlorinated organic compounds (like ClO_4^-). It also is important to evaluate if electrochemical membranes are applicable to waters with relatively low salt contents when treating water for potable consumption or municipal wastewaters. The efficiency of EMs for pollutant removal should be 100% with high current efficiency and low energy consumption. Proper filtration operating mode plays an important role in prevent

membrane fouling, lowing operation and maintenance costs and minimizing the impacts of electrochemical side-reactions. To achieve membrane antifouling and appropriate water production, continual electrification of the membrane surface induces a potential-induced energy barrier to foulant attachment. However, the operation mode for continuous electro filtration uses a lot of energy. For practical applications, an intermittent application of voltage is more feasible. To prevent the membrane surface from developing an irreversible fouling layer, voltage must be applied when the water flux starts to fall. According to studies, irreversible organic foulants can be removed by short-term (1–10 min) in situ electrified membrane self-cleaning. A CNT-functionalized ceramic membrane obtained a nearly full water flux recovery under repeated fouling, backwashing, and self-cleaning cycles when combined with a quick backwashing process for eliminating reversible foulants. In order to integrate electrochemical membrane modules with conventional membrane processes or applications for decentralized water treatment, the design of the modules needs to be enhanced.

REFERENCES

HSS"7th Annual Report on Carcinogens." *US Department of Health and Human Services*, no. PB95-109781 (1994), Washington, D.C..

Abdel-Shafy, Hussein I, and Mona SM Mansour. "Green Synthesis of Metallic Nanoparticles from Natural Resources and Food Waste and Their Environmental Application." *Green Metal Nanoparticles* (2018): 321-85, WILEY.

Abdullah, M, and Siti Kartom Kamarudin. "Titanium Dioxide Nanotubes (Tnt) in Energy and Environmental Applications: An Overview." *Renewable and Sustainable Energy Reviews* 76 (2017): 212-25.

Abdullah, N, Siti Kartom Kamarudin, LK Shyuan, and NA Karim. "Synthesis and Optimization of Ptru/TiO2-Cnf Anodic Catalyst for Direct Methanol Fuel Cell." *International Journal of Hydrogen Energy* 44, no. 58 (2019): 30543-52.

Ackerman, David M, and James W Evans. "Boundary Conditions for Burton–Cabrera–Frank Type Step-Flow Models: Coarse-Graining of Discrete 2D Deposition-Diffusion Equations." *Multiscale Modeling and Simulation* 9, no. 1 (2011): 59-88.

Adachi, Motonari, Masaru Sakamoto, Jinting Jiu, Yukio Ogata, and Seiji Isoda. "Determination of Parameters of Electron Transport in Dye-Sensitized Solar Cells Using Electrochemical Impedance Spectroscopy." *The Journal of Physical Chemistry B* 110, no. 28 (2006): 13872-80.

Ahmed, Farah Ejaz, Boor Singh Lalia, Nidal Hilal, and Raed Hashaikeh. "Electrically Conducting Nanofiltration Membranes Based on Networked Cellulose and Carbon Nanostructures." *Desalination* 406 (2017): 60-66.

Ahmed, Farah, Boor Singh Lalia, Victor Kochkodan, Nidal Hilal, and Raed Hashaikeh. "Electrically Conductive Polymeric Membranes for Fouling Prevention and Detection: A Review." *Desalination* 391 (2016): 1-15.

Ahn, Hyo-Yong, Hye-Eun Lee, Kyoungsuk Jin, and Ki Tae Nam. "Extended Gold Nano-Morphology Diagram: Synthesis of Rhombic Dodecahedra Using CTAB and Ascorbic Acid." *Journal of Materials Chemistry C* 1, no. 41 (2013): 6861-68.

Alekseeva, Olga K, Artem I Mikhalev, Elena K Lutikova, Vladimir I Porembsky, Mikhail Yu Presnyakov, Vladimir N Fateev, Boris L Shapir, and Sergey A Grigoriev. "Structural and Electrocatalytic Properties of Platinum and Platinum-Carbon Layers Obtained by Magnetron-Ion Sputtering." *Catalysts* 8, no. 12 (2018): 665.

Alqadi, M, O Abo Noqtah, F Alzoubi, J Alzouby, and K Aljarrah. "PH Effect on the Aggregation of Silver Nanoparticles Synthesized by Chemical Reduction." *Materials Science Poland* 32, no. 1 (2014): 107-11.

Ames, Richard L, Elizabeth A Bluhm, J Douglas Way, Annette L Bunge, Kent D Abney, and Stephen B Schreiber. "Physical Characterization of 0.5 MM Cut-Off Sintered Stainless Steel Membranes." *Journal of Membrane Science* 213, no. 1-2 (2003): 13-23.

Amooaghaie, Rayhaneh, Mohammad Reza Saeri, and Morteza Azizi. "Synthesis, Characterization and Biocompatibility of Silver Nanoparticles Synthesized from Nigella Sativa Leaf Extract in Comparison with Chemical Silver Nanoparticles." *Ecotoxicology and Environmental Safety* 120 (2015): 400-08.

An, Geon-Hyoung, Hyun-Gi Jo, and Hyo-Jin Ahn. "Platinum Nanoparticles on Nitrogen-Doped Carbon and Nickel Composites Surfaces: A High Electrical Conductivity for Methanol Oxidation Reaction." *Journal of Alloys and Compounds* 763 (2018): 250-56.

Anasori, B, M Lukatskaya, and Y Gogotsi. "2d Metal Carbides and Nitrides (Mxenes) for Energy Storage. *Nature Reviews Materials* 2, no. 2 (2017): 1-17.

Anglada, Ángela, Ane Urtiaga, Inmaculada Ortiz, Dionissios Mantzavinos, and Evan Diamadopoulos. "Boron-Doped Diamond Anodic Treatment of Landfill Leachate: Evaluation of Operating Variables and Formation of Oxidation by-Products." *Water Research* 45, no. 2 (2011): 828-38.

Anis, Shaheen F, Boor S Lalia, Alain Lesimple, Raed Hashaikeh, and Nidal Hilal. "Electrically Conductive Membranes for Contemporaneous Dye Rejection and Degradation." *Chemical Engineering Journal* 428 (2022): 131184.

Antunes, EF, AO Lobo, EJ Corat, and VJ Trava-Airoldi. "Influence of Diameter in the Raman Spectra of Aligned Multi-Walled Carbon Nanotubes." *Carbon* 45, no. 5 (2007): 913-21.

Arneson, Claire, Zachary D Wawrzyniakowski, Jack T Postlewaite, and Ying Ma. "Lithiation and Delithiation Processes in Lithium–Sulfur Batteries from Ab Initio Molecular Dynamics Simulations." *The Journal of Physical Chemistry C* 122, no. 16 (2018): 8769-79.

AshaRani, PV, Grace Low Kah Mun, Manoor Prakash Hande, and Suresh Valiyaveettil. "Cytotoxicity and Genotoxicity of Silver Nanoparticles in Human Cells." *ACS Nano* 3, no. 2 (2009): 279-90.

Asif, Muhammad Bilal, and Zhenghua Zhang. "Ceramic Membrane Technology for Water and Wastewater Treatment: A Critical Review of Performance, Full-Scale Applications, Membrane Fouling and Prospects." *Chemical Engineering Journal* 418 (2021): 129481.

Athanasekou, Chrysoula P, Nikolaos G Moustakas, Sergio Morales-Torres, Luisa M Pastrana-Martínez, José L Figueiredo, Joaquim L Faria, Adrián MT Silva, *et al.* "Ceramic Photocatalytic Membranes for Water Filtration under Uv and Visible Light." *Applied Catalysis B: Environmental* 178 (2015): 12-19.

Ayadi, Saloua, Ilyes Jedidi, Matthieu Rivallin, Frédéric Gillot, Stella Lacour, Sophie Cerneaux, Marc Cretin, and Raja Ben Amar. "Elaboration and Characterization of New Conductive Porous Graphite Membranes for Electrochemical Advanced Oxidation Processes." *Journal of Membrane Science* 446 (2013): 42-49.

Bagheripour, E, AR Moghadassi, F Parvizian, SM Hosseini, and B Van der Bruggen. "Tailoring the Separation Performance and Fouling Reduction of Pes Based Nanofiltration Membrane by Using a PVA/Fe3O4 Coating Layer." *Chemical Engineering Research and Design* 144 (2019): 418-28.

Bao, Ningzhong, Liming Shen, Wei An, Prahallad Padhan, C Heath Turner, and Arunava Gupta. "Formation Mechanism and Shape Control of Monodisperse Magnetic CoFe2O4 Nanocrystals." *Chemistry of Materials* 21, no. 14 (2009): 3458-68.

Bastús, Neus G, Joan Comenge, and Víctor Puntes. "Kinetically Controlled Seeded Growth Synthesis of Citrate-Stabilized Gold Nanoparticles of up to 200 Nm: Size Focusing Versus Ostwald Ripening." *Langmuir* 27, no. 17 (2011): 11098-105.

Becker, Richard, Bo Liedberg, and Per-Olov Käll. "Ctab Promoted Synthesis of Au Nanorods–Temperature Effects and Stability Considerations." *Journal of Colloid and Interface Science* 343, no. 1 (2010): 25-30.

Bejan, Dorin, Elena Guinea, and Nigel J Bunce. "On the Nature of the Hydroxyl Radicals Produced at Boron-Doped Diamond and Ebonex® Anodes." *Electrochimica Acta* 69 (2012): 275-81.

Bergmann, ME Henry, and Johanna Rollin. "Product and by-Product Formation in Laboratory Studies on Disinfection Electrolysis of Water Using Boron-Doped Diamond Anodes." *Catalysis Today* 124, no. 3-4 (2007): 198-203.

Bergmann, ME Henry, Johanna Rollin, and Tatiana Iourtchouk. "The Occurrence of Perchlorate During Drinking Water Electrolysis Using Bdd Anodes." *Electrochimica Acta* 54, no. 7 (2009): 2102-07.

Bergner, Stefan, Preety Vatsyayan, and Frank-Michael Matysik. "Recent Advances in High Resolution Scanning Electrochemical Microscopy of Living Cells–a Review." *Analytica Chimica Acta* 775 (2013): 1-13.

Biacchi, Adam J, and Raymond E Schaak. "The Solvent Matters: Kinetic Versus Thermodynamic Shape Control in the Polyol Synthesis of Rhodium Nanoparticles." *ACS Nano* , no. 10 (2011): 8089-99.

Bin, Deshan, Hong Wang, Jianxin Li, Hui Wang, Zhen Yin, Jianli Kang, Benqiao He, and Zhenhuan Li. "Controllable Oxidation of Glucose to Gluconic Acid and Glucaric Acid Using an Electrocatalytic Reactor." *Electrochimica Acta* 130 (2014): 170-78.

Bindhu, MR, M Umadevi, M Kavin Micheal, Mariadhas Valan Arasu, and Naif Abdullah Al-Dhabi. "Structural, Morphological and Optical Properties of Mgo Nanoparticles for Antibacterial Applications." *Materials Letters* 166 (2016): 19-22.

Biswas, Abhijit, Ilker S Bayer, Alexandru S Biris, Tao Wang, Enkeleda Dervishi, and Franz Faupel. "Advances in Top–Down and Bottom–up Surface Nanofabrication: Techniques, Applications and Future Prospects." *Advances in Colloid and Interface Science* 170, no. 1-2 (2012): 2-27.

Black, Charles T, Stephen M Gates, Christopher B Murray, and Shouheng Sun. "Magnetic Storage Medium Formed of Nanoparticles." Google Patents, 2000, US6162532A.

Blochl, P E. "Projector Augmented-Wave Method." *Physical Revivw B Condensed Matter* 50 (1994): 17953-79.

Blöchl, Peter E. "Projector Augmented-Wave Method." *Physical review B* 50, no. 24 (1994): 17953.

Bogart, Lara K, Cristina Blanco-Andujar, and Quentin A Pankhurst. "Environmental Oxidative Aging of Iron Oxide Nanoparticles." *Applied Physics Letters* 113, no. 13 (2018): 133701.

Bossi, R., J. Strand, O. Sortkjær, and M. M. Larsen. "Perfluoroalkyl Compounds in Danish Wastewater Treatment Plants and Aquatic Environments." *Environment International* 34, no. 4 (2008): 443-50.

Bozon-Verduraz, François, Fernand Fiévet, Jean-Yves Piquemal, Roberta Brayner, Kaoutar El Kabouss, Yaghoub Soumare, Guillaume Viau, and Georges Shafeev. "Nanoparticles of Metal and Metal Oxides: Some Peculiar Synthesis Methods, Size and Shape Control, Application to Catalysts Preparation." *Brazilian Journal of Physics* 39, no. 1A (2009): 134-40.

Buchman, Joseph T, Natalie V Hudson-Smith, Kaitlin M Landy, and Christy L Haynes. "Understanding Nanoparticle Toxicity Mechanisms to Inform Redesign Strategies to Reduce Environmental Impact." *Accounts of Chemical Research* 52, no. 6 (2019): 1632-42.

Bucko, Tomas, Jurgen Hafner, Sébastien Lebegue, and János G Angyán. "Improved Description of the Structure of Molecular and Layered Crystals: Ab Initio DFT Calculations with Van Der Waals Corrections." *The Journal of Physical Chemistry A* 114, no. 43 (2010): 11814-24.

Bukka, Santhosh, Rajashekar Badam, Raman Vedarajan, and Noriyoshi Matsumi. "Photo-Generation of Ultra-Small Pt Nanoparticles on Carbon-Titanium Dioxide Nanotube Composites: A Novel Strategy for Efficient Orr Activity with Low Pt Content." *International Journal of Hydrogen Energy* 44, no. 10 (2019): 4745-53.

Bulgarini, Gabriele, Michael E Reimer, Tilman Zehender, Moïra Hocevar, Erik PAM Bakkers, Leo P Kouwenhoven, and Valery Zwiller. "Spontaneous Emission Control of Single Quantum Dots in Bottom-up Nanowire Waveguides." *Applied Physics Letters* 100, no. 12 (2012): 121106.

Buonsanti, Raffaella, Vincenzo Grillo, Elvio Carlino, Cinzia Giannini, Fabia Gozzo, Mar Garcia-Hernandez, Miguel Angel Garcia, Roberto Cingolani, and P Davide Cozzoli. "Architectural Control of Seeded-Grown Magnetic− Semicondutor Iron Oxide− TiO2 Nanorod Heterostructures: The Role of Seeds in Topology Selection." *Journal of the American Chemical Society* 132, no. 7 (2010): 2437-64.

Buscio, Valentina, María García-Jiménez, Mercè Vilaseca, Victor López-Grimau, Martí Crespi, and Carmen Gutiérrez-Bouzán. "Reuse of Textile Dyeing Effluents Treated with Coupled Nanofiltration and Electrochemical Processes." *Materials* 9, no. 6 (2016): 490.

Cai, Meng, Han Yan, Yuting Li, Wen Li, Hao Li, Xiaoqiang Fan, and Minhao Zhu. "Ti3c2tx/Pani Composites with Tunable Conductivity Towards Anticorrosion Application." *Chemical Engineering Journal* 410 (2021): 128310.

Calaza, Florencia C, Ye Xu, David R Mullins, and Steven H Overbury. "Oxygen Vacancy-Assisted Coupling and Enolization of Acetaldehyde on CeO2 (111)." *Journal of the American Chemical Society* 134, no. 43 (2012): 18034-45.

Carchini, Giuliano, Max García-Melchor, Zbigniew Łodziana, and Núria López. "Understanding and Tuning the Intrinsic Hydrophobicity of Rare-Earth Oxides: A DFT+ U Study." *ACS Applied Materials and Interfaces* 8, no. 1 (2016): 152-60.

Castro-Alarcón, Natividad, José Luis Herrera-Arizmendi, Luis Alberto Marroquín-Carteño, Iris Paola Guzmán-Guzmán, Armando Pérez-Centeno, and Miguel Ángel Santana-Aranda. "Antibacterial Activity of Nanoparticles of Titanium Dioxide, Intrinsic and Doped with Indium and Iron." *Microbiol Reserach International* 4, no. 4 (2016): 55-62.

Cathcart, Nicole, and Vladimir Kitaev. "Multifaceted Prismatic Silver Nanoparticles: Synthesis by Chloride-Directed Selective Growth from Thiolate-Protected Clusters and Sers Properties." *Nanoscale* 4, no. 22 (2012): 6981-89.

Chanda, Kaushik, Sourav Rej, and Michael H Huang. "Facet-Dependent Catalytic Activity of Cu2O Nanocrystals in the One-Pot Synthesis of 1, 2, 3-Triazoles by Multicomponent Click Reactions." *Chemistry–A European Journal* 19, no. 47 (2013): 16036-43.

Chang, Han-Wei, Yu-Chen Tsai, Chung-Wei Cheng, Cen-Ying Lin, and Ping-Han Wu. "Preparation of Graphene-Supported Platinum Nanoparticles in Aqueous Solution by Femtosecond Laser Pulses for Methanol Oxidation." *Journal of Power Sources* 239 (2013): 164-68.

Chang, Jin, and Eric R Waclawik. "Colloidal Semiconductor Nanocrystals: Controlled Synthesis and Surface Chemistry in Organic Media." *RSC Advances* 4, no. 45 (2014): 23505-27.

Chang, Wengui, Yuhua Shen, Anjian Xie, and Xue Liu. "Facile Controlled Synthesis of Micro/Nanostructure Mcro4 (M= Ba, Pb) by Using Gemini Surfactant C12-Peg-C12 as a Soft Template." *Applied Surface Science* 256, no. 13 (2010): 4292-98.

Chaplin, Brian P. "Critical Review of Electrochemical Advanced Oxidation Processes for Water Treatment Applications." *Environmental Science: Processes and Impacts* 16, no. 6 (2014): 1182-203.

Chen, Bor-Rong, Lawrence A Crosby, Cassandra George, Robert M Kennedy, Neil M Schweitzer, Jianguo Wen, Richard P Van Duyne, *et al.* "Morphology and Co Oxidation Activity of Pd Nanoparticles on SrTiO3 Nanopolyhedra." *ACS Catalysis* 8, no. 6 (2018): 4751-60.

Chen, Feng, Yinde Xie, Jianjun He, and Jincai Zhao. "Photo-Fenton Degradation of Dye in Methanolic Solution under Both Uv and Visible Irradiation." *Journal of Photochemistry and Photobiology A: Chemistry* 138, no. 2 (2001): 139-46.

Chen, Kunfeng, and Dongfeng Xue. "Ph-Assisted Crystallization of Cu2O: Chemical Reactions Control the Evolution from Nanowires to Polyhedra." *CrystEngComm* 14, no. 23 (2012): 8068-75.

Chen, Liang, Yu Zhang, Pengli Zhu, Fengrui Zhou, Wenjin Zeng, Daoqiang Daniel Lu, Rong Sun, and Chingping Wong. "Copper Salts Mediated Morphological Transformation of Cu2O from Cubes to Hierarchical Flower-Like or Microspheres and Their Supercapacitors Performances." *Scientific Reports* 5 (2015): 9672.

Chen, Shilong, Tian Cao, Yuxian Gao, Dan Li, Feng Xiong, and Weixin Huang. "Probing Surface Structures of CeO2, TiO2, and Cu2O Nanocrystals with Co and CO2 Chemisorption." *The Journal of Physical Chemistry C* 120, no. 38 (2016): 21472-85.

Chen, Tzu-Ning, Jui-Cheng Kao, Xin-Yan Zhong, Shang-Ju Chan, Anindya S Patra, Yu-Chieh Lo, and Michael H Huang. "Facet-Specific Photocatalytic Activity Enhancement of Cu2O Polyhedra Functionalized with 4-Ethynylanaline Resulting from Band Structure Tuning." *ACS Central Science* 6, no. 6 (2020): 984-94.

Chen, Wushuang, Jia Xue, Yufei Bao, and Ligang Feng. "Surface Engineering of Nano-Ceria Facet Dependent Coupling Effect on Pt Nanocrystals for Electro-Catalysis of Methanol Oxidation Reaction." *Chemical Engineering Journal* 381 (2020): 122752.

Chen, Xialin, Haixia Lü, Qilang Lin, Xiang Zhang, Dongyang Chen, and Yuying Zheng. "Partially Fluorinated Poly (Arylene Ether) S Bearing Long Alkyl Sulfonate Side Chains for Stable and Highly Conductive Proton Exchange Membranes." *Journal of Membrane Science* 549 (2018): 12-22.

Chen, Xuejun, Zhemin Shen, Xiaolong Zhu, Yaobo Fan, and Wenhua Wang. "Advanced Treatment of Textile Wastewater for Reuse Using Electrochemical Oxidation and Membrane Filtration." *Water SA* 31, no. 1 (2005): 127-32.

Chen, Zhu, Coleman X Kronawitter, and Bruce E Koel. "Facet-Dependent Activity and Stability of Co3O4 Nanocrystals Towards the Oxygen Evolution Reaction." *Physical Chemistry Chemical Physics* 17, no. 43 (2015): 29387-93.

Cheng, CY, and GH Kelsall. "Models of Hypochlorite Production in Electrochemical Reactors with Plate and Porous Anodes." *Journal of Applied Electrochemistry* 37, no. 11 (2007): 1203-17.

Cheng, Min, Guangming Zeng, Danlian Huang, Cui Lai, Piao Xu, Chen Zhang, and Yang Liu. "Hydroxyl Radicals Based Advanced Oxidation Processes (AOPs) for Remediation of Soils Contaminated with Organic Compounds: A Review." *Chemical Engineering Journal* 284 (2016): 582-98.

Chennit, Khalil, Jorge Trasobares, Agnès Anne, Edmond Cambril, Arnaud Chovin, Nicolas Clément, and Christophe Demaille. "Electrochemical Imaging of Dense Molecular Nanoarrays." *Analytical Chemistry* 89, no. 20 (2017): 11061-69.

Chien, Yi-Hsin, Ming-Fong Tsai, Vijayakumar Shanmugam, Kripasindhu Sardar, Cheng-Liang Huang, and Chen-Sheng Yeh. "Escape from the Destruction of the Galvanic Replacement Reaction for Solid→ Hollow→ Solid Conversion Process in One Pot Reaction." *Nanoscale* 5, no. 9 (2013): 3863-71.

Choi, Geun-Hyoung, Deuk-Young Lee, Dong-Kyu Jeong, Saranya Kuppusamy, Yong Bok Lee, Byung-Jun Park, and Jin-Hyo Kim. "Perfluorooctanoic Acid (PFOA) and Perfluorooctanesulfonic Acid (PFOS) Concentrations in the South Korean Agricultural Environment: A National Survey." (2017).

Choi, Jong Young, You-Jin Lee, Jina Shin, and Ji-Won Yang. "Anodic Oxidation of 1, 4-Dioxane on Boron-Doped Diamond Electrodes for Wastewater Treatment." *Journal of Hazardous Materials* 179, no. 1-3 (2010): 762-68.

Choi, Myunghoon, Natasha P Siepser, Soojin Jeong, Yi Wang, Gargi Jagdale, Xingchen Ye, and Lane A Baker. "Probing Single-Particle Electrocatalytic Activity at Facet-Controlled Gold Nanocrystals." *Nano letters* 20, no. 2 (2020): 1233-39.

Chu, Chieh-Yu, and Michael H Huang. "Facet-Dependent Photocatalytic Properties of Cu2O Crystals Probed by Using Electron, Hole and Radical Scavengers." *Journal of Materials Chemistry A* 5, no. 29 (2017): 15116-23.

Clara, Manfred, S Scharf, S Weiss, O Gans, and C Scheffknecht. "Emissions of Perfluorinated Alkylated Substances (PFAS) from Point Sources—Identification of Relevant Branches." *Water Science and Technology* 58, no. 1 (2008): 59-66.

Cummings, L, N Nelson, F Sickels, and CT Storms. "Recommendation on Perfluorinated Compound Treatment Options for Drinking Water New Jersey Drinking Water Quality Institute." (2015).

Czelej, Kamil, Marcin Roland Zemła, Piotr Śpiewak, Tomasz Wejrzanowski, and Krzysztof Jan Kurzydłowski. "Atomic-Scale Computational Design of Hydrophobic Re Surface-Doped Al2O3 and TiO2." *Physical Chemistry Chemical Physics* 19, no. 31 (2017): 21119-26.

Das, Suman, and Avner Ronen. "A Review on Removal and Destruction of Per-and Polyfluoroalkyl Substances (PFAS) by Novel Membranes." *Membranes* 12, no. 7 (2022): 662.

Dauthal, Preeti, and Mausumi Mukhopadhyay. "Noble Metal Nanoparticles: Plant-Mediated Synthesis, Mechanistic Aspects of Synthesis, and Applications." *Industrial and Engineering Chemistry Research* 55, no. 36 (2016): 9557-77.

Davarcioglu, Burhan. "Nanotechnology Applications in Food Packaging Industry." In *Nanotechnology*, 87-113: Springer, 2017.

David, Oana, Youri Gendel, and Matthias Wessling. "Tubular Macro-Porous Titanium Membranes." *Journal of Membrane Science* 461 (2014): 139-45.

De Jong, Wim H, and Paul JA Borm. "Drug Delivery and Nanoparticles: Applications and Hazards." *International Journal of Nanomedicine* 3, no. 2 (2008): 133.

Death, Clare, Cameron Bell, David Champness, Charles Milne, Suzie Reichman, and Tarah Hagen. "Per-and Polyfluoroalkyl Substances (PFAS) in Livestock and Game Species: A Review." *Science of The Total Environment* 774 (2021): 144795.

Deng, Shubo, Qiang Yu, Jun Huang, and Gang Yu. "Removal of Perfluorooctane Sulfonate from Wastewater by Anion Exchange Resins: Effects of Resin Properties and Solution Chemistry." *Water Research* 44, no. 18 (2010): 5188-95.

Derry, Gregory N, Megan E Kern, and Eli H Worth. "Recommended Values of Clean Metal Surface Work Functions." *Journal of Vacuum Science and Technology A: Vacuum, Surfaces, and Films* 33, no. 6 (2015): 060801.

DeSantis, Christopher J, Rebecca G Weiner, Andjela Radmilovic, Matthew M Bower, and Sara E Skrabalak. "Seeding Bimetallic Nanostructures as a New Class of Plasmonic Colloids." *The Journal of Physical Chemistry Letters* 4, no. 18 (2013): 3072-82.

Devi, L, S Kumar, and K Reddy. "Photo Fenton Like Process Fe3+/(Nh4) 2S2O8/Uv for the Degradation of Di Azo Dye Congo Red Using Low Iron Concentration." *Open Chemistry* 7, no. 3 (2009): 468-77.

Diogo, João C, António Morão, and Ana Lopes. "Persistent Aromatic Pollutants Removal Using a Combined Process of Electrochemical Treatment and Reverse Osmosis/Nanofiltration." *Environmental Progress and Sustainable Energy* 30, no. 3 (2011): 399-408.

Dixit, Fuhar, Gabriel Munoz, Mahboubeh Mirzaei, Benoit Barbeau, Jinxia Liu, Sung Vo Duy, Sébastien Sauvé, Balasubramanian Kandasubramanian, and Madjid Mohseni. "Removal of Zwitterionic Pfas by Mxenes: Comparisons with Anionic, Nonionic, and Pfas-Specific Resins." *Environmental Science and Technology* (2022).

Duan, Wenyan, Avner Ronen, Sharon Walker, and David Jassby. "Polyaniline-Coated Carbon Nanotube Ultrafiltration Membranes: Enhanced Anodic Stability for in Situ Cleaning and Electro-Oxidation Processes." *ACS Applied Materials and Interfaces* 8, no. 34 (2016): 22574-84.

Dudchenko, Alexander V, Julianne Rolf, Kyle Russell, Wenyan Duan, and David Jassby. "Organic Fouling Inhibition on Electrically Conducting Carbon Nanotube–Polyvinyl Alcohol Composite Ultrafiltration Membranes." *Journal of Membrane Science* 468 (2014): 1-10.

Dumée, Ludovic, Vincent Germain, Kallista Sears, Jürg Schütz, Niall Finn, Mikel Duke, Sophie Cerneaux, David Cornu, and Stephen Gray. "Enhanced Durability and Hydrophobicity of Carbon Nanotube Bucky Paper Membranes in Membrane Distillation." *Journal of Membrane Science* 376, no. 1-2 (2011): 241-46.

Eguchi, Miharu, Daisuke Mitsui, Hsin-Lun Wu, Ryota Sato, and Toshiharu Teranishi. "Simple Reductant Concentration-Dependent Shape Control of Polyhedral Gold Nanoparticles and Their Plasmonic Properties." *Langmuir* 28, no. 24 (2012): 9021-26.

Fan, Feng-Ru, Yong Ding, De-Yu Liu, Zhong-Qun Tian, and Zhong Lin Wang. "Facet-Selective Epitaxial Growth of Heterogeneous Nanostructures of Semiconductor and Metal: ZnO Nanorods on Ag Nanocrystals." *Journal of the American Chemical Society* 131, no. 34 (2009): 12036-37.

Fan, Feng-Ru, De-Yu Liu, Yuan-Fei Wu, Sai Duan, Zhao-Xiong Xie, Zhi-Yuan Jiang, and Zhong-Qun Tian. "Epitaxial Growth of Heterogeneous Metal Nanocrystals: From Gold Nano-Octahedra to Palladium and Silver Nanocubes." *Journal of the American Chemical Society* 130, no. 22 (2008): 6949-51.

Fan, Xinfei, Yanming Liu, Xie Quan, and Shuo Chen. "Highly Permeable Thin-Film Composite Forward Osmosis Membrane Based on Carbon Nanotube Hollow Fiber Scaffold with Electrically Enhanced Fouling Resistance." *Environmental Science and Technology* 52, no. 3 (2018): 1444-52.

Fan, Xinfei, Huimin Zhao, Yanming Liu, Xie Quan, Hongtao Yu, and Shuo Chen. "Enhanced Permeability, Selectivity, and Antifouling Ability of CNTs/Al2O3 Membrane under Electrochemical Assistance." *Environmental Science and Technology* 49, no. 4 (2015): 2293-300.

Fane, Anthony G, Rong Wang, and Matthew X Hu. "Synthetic Membranes for Water Purification: Status and Future." *Angewandte Chemie International Edition* 54, no. 11 (2015): 3368-86.

Fang, C, M Megharaj, and R Naidu. "Electrochemical Advanced Oxidation Processes (EAOPs) to Degrade Per-and Polyfluoroalkyl Substances (PFASs)." *Journal of Advanced Oxidation Technologies* 20, no. 2 (2017).

Fang, Wen-Chien, Fu-Rong Chen, Ming-Chi Tsai, Huei-Yu Chou, Hsuan-Chung Wu, and Chien-Kuo Hsieh. "Electrochemical Deposited High-Crystallinity Vertical Platinum Nanosheets onto the Carbon Nanotubes Directly Grown on Carbon Paper for Methanol Oxidation." *Surface and Coatings Technology* 320 (2017): 584-89.

Fang, Xiao, Zhen Yin, Hong Wang, Jianxin Li, Xiaoping Liang, Jianli Kang, and Benqiao He. "Controllable Oxidation of Cyclohexane to Cyclohexanol and Cyclohexanone by a Nano-MnOx/Ti Electrocatalytic Membrane Reactor." *Journal of Catalysis* 329 (2015): 187-94.

Fang, Yimin, Hui Wang, Hui Yu, Xianwei Liu, Wei Wang, Hong-Yuan Chen, and NJ Tao. "Plasmonic Imaging of Electrochemical Reactions of Single Nanoparticles." *Accounts of Chemical Research* 49, no. 11 (2016): 2614-24.

Farjoo, Afrooz, and Steven M Kuznicki. "H2 Separation Using Tubular Stainless Steel Supported Natural Clinoptilolite Membranes." *The Canadian Journal of Chemical Engineering* 94, no. 11 (2016): 2219-24.

Feigl, Christopher A, Amanda S Barnard, and Salvy P Russo. "Modelling Polar Wurtzite Zns Nanoparticles: The Effect of Sulphur Supersaturation on Size-and Shape-Dependent Phase Transformations." *Journal of Materials Chemistry* 22, no. 36 (2012): 18992-98.

Filipe, Vasco, Andrea Hawe, and Wim Jiskoot. "Critical Evaluation of Nanoparticle Tracking Analysis (NTA) by Nanosight for the Measurement of Nanoparticles and Protein Aggregates." *Pharmaceutical Research* 27, no. 5 (2010): 796-810.

Flemming, H-C, G Schaule, T Griebe, J Schmitt, and A Tamachkiarowa. "Biofouling—the Achilles Heel of Membrane Processes." *Desalination* 113, no. 2-3 (1997): 215-25.

Formoso, Patrizia, Elvira Pantuso, Giovanni De Filpo, and Fiore Nicoletta. "Electro-Conductive Membranes for Permeation Enhancement and Fouling Mitigation: A Short Review." *Membranes* 7, no. 3 (2017): 39.

Franci, Gianluigi, Annarita Falanga, Stefania Galdiero, Luciana Palomba, Mahendra Rai, Giancarlo Morelli, and Massimiliano Galdiero. "Silver Nanoparticles as Potential Antibacterial Agents." *Molecules* 20, no. 5 (2015): 8856-74.

Friedl, Jochen, and Ulrich Stimming. "Determining Electron Transfer Kinetics at Porous Electrodes." *Electrochimica Acta* 227 (2017): 235-45.

Fu, Wanyi, Christina Carbrello, Xiaosong Wu, and Wen Zhang. "Visualizing and Quantifying the Nanoscale Hydrophobicity and Chemical Distribution of Surface Modified Polyethersulfone (Pes) Membranes." *Nanoscale* 9, no. 40 (2017): 15550-57.

Fu, Wanyi, and Wen Zhang. "Measurement of the Surface Hydrophobicity of Engineered Nanoparticles Using an Atomic Force Microscope." *Physical Chemistry Chemical Physics* 20, no. 37 (2018): 24434-43.

Fuji, Masayoshi, Takahiro Shin, Hideo Watanabe, and Takashi Takei. "Shape-Controlled Hollow Silica Nanoparticles Synthesized by an Inorganic Particle Template Method." *Advanced Powder Technology* 23, no. 5 (2012): 562-65.

Galeano, Yohana Martínez, Laura Cornaglia, and Ana M Tarditi. "Naa Zeolite Membranes Synthesized on Top of APTEs-Modified Porous Stainless Steel Substrates." *Journal of Membrane Science* 512 (2016): 93-103.

Ganiyu, Soliu O, Nihal Oturan, Stéphane Raffy, Marc Cretin, Roseline Esmilaire, Eric van Hullebusch, Giovanni Esposito, and Mehmet A Oturan. "Sub-Stoichiometric Titanium Oxide (Ti4O7) as a Suitable Ceramic Anode for Electrooxidation of Organic Pollutants: A Case Study of Kinetics, Mineralization and Toxicity Assessment of Amoxicillin." *Water Research* 106 (2016): 171-82.

Ganiyu, Soliu O, Nihal Oturan, Stéphane Raffy, Giovanni Esposito, Eric D Van Hullebusch, Marc Cretin, and Mehmet A Oturan. "Use of Sub-Stoichiometric Titanium Oxide as a Ceramic Electrode in Anodic Oxidation and Electro-Fenton Degradation of the Beta-Blocker Propranolol: Degradation Kinetics and Mineralization Pathway." *Electrochimica Acta* 242 (2017): 344-54.

Ganiyu, Soliu O, Eric D Van Hullebusch, Marc Cretin, Giovanni Esposito, and Mehmet A Oturan. "Coupling of Membrane Filtration and Advanced Oxidation Processes for Removal of Pharmaceutical Residues: A Critical Review." *Separation and Purification Technology* 156 (2015): 891-914.

Gao, Changfei, Lifen Liu, Tingting Yu, and Fenglin Yang. "Development of a Novel Carbon-Based Conductive Membrane with in-Situ Formed MnO2 Catalyst for Wastewater Treatment in Bio-Electrochemical System (Bes)." *Journal of Membrane Science* 549 (2018): 533-42.

Gao, Dangli, Wei Gao, Peng Shi, and Long Li. "Ph-and Surfactant-Mediated Tunable Morphology and Upconversion of Rare-Earth Doped Fluoride Microcrystals." *RSC Advances* 3, no. 34 (2013): 14757-65.

Gao, Guandao, Meilan Pan, and Chad D Vecitis. "Effect of the Oxidation Approach on Carbon Nanotube Surface Functional Groups and Electrooxidative Filtration Performance." *Journal of Materials Chemistry A* 3, no. 14 (2015): 7575-82.

Gao, Guandao, and Chad D Vecitis. "Doped Carbon Nanotube Networks for Electrochemical Filtration of Aqueous Phenol: Electrolyte Precipitation and Phenol Polymerization." *ACS Applied Materials and Interfaces* 4, no. 3 (2012): 1478-89.

Gao, Guandao, and Chad D. Vecitis. "Electrocatalysis Aqueous Phenol with Carbon Nanotubes Networks as Anodes: Electrodes Passivation and Regeneration and Prevention." *Electrochimica Acta* 98 (2013): 131-38.

Gao, Guandao, and Chad D. Vecitis. "Electrochemical Carbon Nanotube Filter Oxidative Performance as a Function of Surface Chemistry." *Environmental Science and Technology* 45, no. 22 (2011): 9726-34.

Gao, Guandao, and Chad D. Vecitis "Reactive Depth and Performance of an Electrochemical Carbon Nanotube Network as a Function of Mass Transport." *ACS Applied Materials and Interfaces* 4, no. 11 (2012): 6096-103.

Gao, Guandao, Qiaoying Zhang, and Chad D Vecitis. "CNT–PVDF Composite Flow-through Electrode for Single-Pass Sequential Reduction–Oxidation." *Journal of Materials Chemistry A* 2, no. 17 (2014): 6185-90.

Gao, Rui, Jinzhen Zhu, Xiaoling Xiao, Zhongbo Hu, Jianjun Liu, and Xiangfeng Liu. "Facet-Dependent Electrocatalytic Performance of Co3O4 for Rechargeable LiO2 Battery." *The Journal of Physical Chemistry C* 119, no. 9 (2015): 4516-23.

Gao, Yaowen, Yue Zhu, Lai Lyu, Qingyi Zeng, Xueci Xing, and Chun Hu. "Electronic Structure Modulation of Graphitic Carbon Nitride by Oxygen Doping for Enhanced Catalytic Degradation of Organic Pollutants through Peroxymonosulfate Activation." *Environmental Science and Technology* 52, no. 24 (2018): 14371-80.

Gao, Yuanyuan, Min Chen, Ting Zhang, and Xiaoming Zheng. "A Novel Method for the Growth of Zsm-5 Zeolite Membrane on the Surface of Stainless Steel." *Materials Letters* 65, no. 17-18 (2011): 2789-92.

Garcia-Segura, Sergi, Xiaolei Qu, Pedro JJ Alvarez, Brian P Chaplin, Wei Chen, John C Crittenden, Yujie Feng, *et al.* "Opportunities for Nanotechnology to Enhance Electrochemical Treatment of Pollutants in Potable Water and Industrial Wastewater–a Perspective." *Environmental Science: Nano* 7, no. 8 (2020): 2178-94.

Garg, Niti, Clark Scholl, Ashok Mohanty, and Rongchao Jin. "The Role of Bromide Ions in Seeding Growth of Au Nanorods." *Langmuir* 26, no. 12 (2010): 10271-76.

Geng, Ping, and Guohua Chen. "Antifouling Ceramic Membrane Electrode Modified by Magnéli Ti4O7 for Electro-Microfiltration of Humic Acid." *Separation and Purification Technology* 185 (2017): 61-71.

Geng, Ping, Jingyang Su, Caroline Miles, Christos Comninellis, and Guohua Chen. "Highly-Ordered Magnéli Ti4O7 Nanotube Arrays as Effective Anodic Material for Electro-Oxidation." *Electrochimica Acta* 153 (2015): 316-24.

Ghaemi, Negin, Sayed S Madaeni, Parisa Daraei, Hamid Rajabi, Sirus Zinadini, Abdolhamid Alizadeh, Rouhollah Heydari, Mojtaba Beygzadeh, and Sohrab Ghouzivand. "Polyethersulfone Membrane Enhanced with Iron Oxide Nanoparticles for Copper Removal from Water: Application of New Functionalized Fe3O4 Nanoparticles." *Chemical Engineering Journal* 263 (2015): 101-12.

Giannakoudakis, Dimitrios A, Mykola Seredych, Enrique Rodríguez-Castellón, and Teresa J Bandosz. "Mesoporous Graphitic Carbon Nitride-Based Nanospheres as Visible-Light Active Chemical Warfare Agents Decontaminant." *ChemNanoMat* 2, no. 4 (2016): 268-72.

Giannakoudakis, Dimitrios A, Nikolina A Travlou, Jeff Secor, and Teresa J Bandosz. "Oxidized G-C3N4 Nanospheres as Catalytically Photoactive Linkers in Mof/G-C3N4 Composite of Hierarchical Pore Structure." *Small* 13, no. 1 (2017): 1601758.

Giese, Bernd, Fred Klaessig, Barry Park, Ralf Kaegi, Michael Steinfeldt, Henning Wigger, Arnim von Gleich, and Fadri Gottschalk. "Risks, Release and Concentrations of Engineered Nanomaterial in the Environment." *Scientific Reports* 8, no. 1 (2018): 1-18.

Gilroy, Kyle D, Robert A Hughes, and Svetlana Neretina. "Kinetically Controlled Nucleation of Silver on Surfactant-Free Gold Seeds." *Journal of the American Chemical Society* 136, no. 43 (2014): 15337-45.

Gliga, Anda R, Sara Skoglund, Inger Odnevall Wallinder, Bengt Fadeel, and Hanna L Karlsson. "Size-Dependent Cytotoxicity of Silver Nanoparticles in Human Lung Cells: The Role of Cellular Uptake, Agglomeration and Ag Release." *Particle and fibre toxicology* 11, no. 1 (2014): 1-17.

Goh, PS, and AF Ismail. "A Review on Inorganic Membranes for Desalination and Wastewater Treatment." *Desalination* 434 (2018): 60-80.

Gómez-Graña, Sergio, Bart Goris, Thomas Altantzis, Cristina Fernández-López, Enrique Carbó-Argibay, Andrés Guerrero-Martínez, Neyvis Almora-Barrios, *et al.* "Au@ Ag Nanoparticles: Halides Stabilize {100} Facets." *The Journal of Physical Chemistry Letters* 4, no. 13 (2013): 2209-16.

Gomez-Ruiz, Beatriz, Sonia Gómez-Lavín, Nazely Diban, Virginie Boiteux, Adeline Colin, Xavier Dauchy, and Ane Urtiaga. "Efficient Electrochemical Degradation of Poly- and Perfluoroalkyl Substances (PFASs) from the Effluents of an Industrial Wastewater Treatment Plant." *Chemical Engineering Journal* 322 (2017): 196-204.

Gouveia, Rubia F., and Fernando Galembeck. "Electrostatic charging of hydrophilic particles due to water adsorption." *Journal of the American chemical society* 131, no. 32 (2009): 11381-11386.

Goy-López, Sonia, Emilio Castro, Pablo Taboada, and Víctor Mosquera. "Block Copolymer-Mediated Synthesis of Size-Tunable Gold Nanospheres and Nanoplates." *Langmuir* 24, no. 22 (2008): 13186-96.

Graf, Christina, Daniel Nordmeyer, Christina Sengstock, Sebastian Ahlberg, Jörg Diendorf, Jörg Raabe, Matthias Epple, *et al.* "Shape-Dependent Dissolution and Cellular Uptake of Silver Nanoparticles." *Langmuir* 34, no. 4 (2018): 1506-19.

Grimme, Stefan, Jens Antony, Stephan Ehrlich, and Helge Krieg. "A Consistent and Accurate Ab Initio Parametrization of Density Functional Dispersion Correction (DFD-C) for the 94 Elements H-Pu." *Journal of Chemical Physics* 132, no. 15 (2010): 154104.

Grzelczak, Marek, Jorge Pérez-Juste, Paul Mulvaney, and Luis M Liz-Marzán. "Shape Control in Gold Nanoparticle Synthesis." *Chemical Society Reviews* 37, no. 9 (2008): 1783-91.

Guo, Lun, Kai Ding, Karl Rockne, Metin Duran, and Brian P Chaplin. "Bacteria Inactivation at a Sub-Stoichiometric Titanium Dioxide Reactive Electrochemical Membrane." *Journal of Hazardous Materials* 319 (2016): 137-46.

Guo, Lun, Yin Jing, and Brian P Chaplin. "Development and Characterization of Ultrafiltration TiO2 Magnéli Phase Reactive Electrochemical Membranes." *Environmental Science and Technology* 50, no. 3 (2016): 1428-36.

Habouti, Salah, Mária Mátéfi-Tempfli, Claus-Henning Solterbeck, Martha Es-Souni, Stefan Mátéfi-Tempfli, and Mohammed Es-Souni. "Self-Standing Corrugated Ag and Au-Nanorods for Plasmonic Applications." *Journal of Materials Chemistry* 21, no. 17 (2011): 6269-73.

Halali, Mohamad Amin, and Charles-François de Lannoy. "Methods for Stability Assessment of Electrically Conductive Membranes." *MethodsX* 9 (2022): 101627.

Halali, Mohamad Amin, Melissa Larocque, and Charles-François de Lannoy. "Investigating the Stability of Electrically Conductive Membranes." *Journal of Membrane Science* 627 (2021): 119181.

Hamelin, A. "Cyclic Voltammetry at Gold Single-Crystal Surfaces. Part 1. Behaviour at Low-Index Faces." *Journal of Electroanalytical Chemistry* 407, no. 1-2 (1996): 1-11.

Han, Hye Ji, Ju Hyun Park, Jin Kyoung Park, Imanuel Kristanto, Bum Jun Park, Sang Kyu Kwak, and Sang Hyuk Im. "Uniform Ag Nanocubes Prepared by Agcl Particle–Mediated Heterogeneous Nucleation and Disassembly and Their Mechanism Study by DFT Calculation." *Small* 15, no. 43 (2019): 1904031.

Han, Lin, Penglei Cui, Hongyan He, Hui Liu, Zhijian Peng, and Jun Yang. "A Seed-Mediated Approach to the Morphology-Controlled Synthesis of Bimetallic Copper–Platinum Alloy Nanoparticles with Enhanced Electrocatalytic Performance for the Methanol Oxidation Reaction." *Journal of Power Sources* 286 (2015): 488-94.

Han, Miaomiao, Gang Zhang, Ke Shao, Hongtao Li, Yang Zhang, Mingyu Li, Shuang Wang, and Hui Na. "Carboxyl-Terminated Benzimidazole-Assisted Cross-Linked Sulfonated PolyS for Highly Conductive Pem with Low Water Uptake and Methanol Permeability." *Journal of Materials Chemistry* 20, no. 16 (2010): 3246-52.

Han, Yucui, Shaohua Liu, Min Han, Jianchun Bao, and Zhihui Dai. "Fabrication of Hierarchical Nanostructure of Silver Via a Surfactant-Free Mixed Solvents Route." *Crystal Growth and Design* 9, no. 9 (2009): 3941-47.

Hansen, Wilford N., and Galen J. Hansen. "Standard Reference Surfaces for Work Function Measurements in Air." *Surface Science.* 481, no. 1-3 (2001): 172-84.

Hanus, Leo H, Kelly Sooklal, Catherine J Murphy, and Harry J Ploehn. "Aggregation Kinetics of Dendrimer-Stabilized Cds Nanoclusters." *Langmuir* 16, no. 6 (2000): 2621-26.

Harn, Yeu-Wei, Tung-Han Yang, Tsung-Yeh Tang, Miao-Chun Chen, and Jenn-Ming Wu. "Facet-Dependent Photocatalytic Activity and Facet-Selective Etching of Silver (I) Oxide Crystals with Controlled Morphology." *ChemCatChem* 7, no. 1 (2015): 80-86.

Hart, James L, Kanit Hantanasirisakul, Andrew C Lang, Babak Anasori, David Pinto, Yevheniy Pivak, J Tijn van Omme, *et al.* "Control of Mxenes' Electronic Properties through Termination and Intercalation." *Nature Communications* 10, no. 1 (2019): 1-10.

He, Pin-Jing, Zhong Zheng, Hua Zhang, Li-Ming Shao, and Qiong-Yao Tang. "Paes and Bpa Removal in Landfill Leachate with Fenton Process and Its Relationship with Leachate Dom Composition." *Science of the Total Environment* 407, no. 17 (2009): 4928-33.

Hench, Larry L, and Julia M Polak. "Third-Generation Biomedical Materials." *Science* 295, no. 5557 (2002): 1014-17.

Henkelman, Graeme, Andri Arnaldsson, and Hannes Jónsson. "A Fast and Robust Algorithm for Bader Decomposition of Charge Density." *Computational Materials Science* 36, no. 3 (2006): 354-60.

Ho, Chien-Hsin, Chih-Pin Tsai, Chia-Chi Chung, Chun-Ying Tsai, Fu-Rong Chen, Hong-Ji Lin, and Chih-Huang Lai. "Shape-Controlled Growth and Shape-Dependent Cation Site Occupancy of Monodisperse Fe3O4 Nanoparticles." *Chemistry of Materials* 23, no. 7 (2011): 1753-60.

Hodges, Brenna C, Ezra L Cates, and Jae-Hong Kim. "Challenges and Prospects of Advanced Oxidation Water Treatment Processes Using Catalytic Nanomaterials." *Nature Nanotechnology* 13, no. 8 (2018): 642.

Holmes, Stuart M, Christian Markert, Richard J Plaisted, James O Forrest, Jonathon R Agger, Michael W Anderson, Colin S Cundy, and John Dwyer. "A Novel Method for the Growth of Silicalite Membranes on Stainless Steel Supports." *Chemistry of Materials* 11, no. 11 (1999): 3329-32.

Hossain, Fahim, Oscar J Perales-Perez, Sangchul Hwang, and Felix Roman. "Antimicrobial Nanomaterials as Water Disinfectant: Applications, Limitations and Future Perspectives." *Science of the Total Environment* 466 (2014): 1047-59.

Hou, Wanda, Xuejian Dong, Yu Li, Hua Zhang, Linlin Xu, Yue Tian, Anxin Jiao, and Ming Chen. "Ultraviolet Laser Beam-Assisted One-Step Synthesis of Clean Ptpd Nanoarchitectures with Excellent Electrocatalytic Properties for Direct Methanol Fuel Cells." *Materials Chemistry and Physics* 221 (2019): 409-18.

Hu, Jiayue, Mingjuan Sun, Xiaoyan Cai, Chunyang Zhai, Junying Zhang, and Mingshan Zhu. "Two Dimensional Perovskite La2Ti2O7 Nanosheet as Pt Catalyst Support for Photo-Assisted Methanol Oxidation Reaction." *Journal of the Taiwan Institute of Chemical Engineers* 80 (2017): 231-38.

Hu, Xindi C., David Q. Andrews, Andrew B. Lindstrom, Thomas A. Bruton, Laurel A. Schaider, Philippe Grandjean, Rainer Lohmann, *et al.* "Detection of Poly- and Perfluoroalkyl Substances (PFASs) in U.S. Drinking Water Linked to Industrial Sites, Military Fire Training Areas, and Wastewater Treatment Plants." *Environmental Science and Technology Letters* 3, no. 10 (2016/10/11 2016): 344-50.

Hua, Likun, Lun Guo, Megha Thakkar, Dequan Wei, Michael Agbakpe, Liyuan Kuang, Maraha Magpile, *et al.* "Effects of Anodic Oxidation of a Substoichiometric Titanium Dioxide Reactive Electrochemical Membrane on Algal Cell Destabilization and Lipid Extraction." *Bioresource Technology* 203 (2016): 112-17.

Huang, Chih-Ching, Zusing Yang, and Huan-Tsung Chang. "Synthesis of Dumbbell-Shaped Au− Ag Core− Shell Nanorods by Seed-Mediated Growth under Alkaline Conditions." *Langmuir* 20, no. 15 (2004): 6089-92.

Huang, Jian, Zhiwei Wang, Junyao Zhang, Xingran Zhang, Jinxing Ma, and Zhichao Wu. "A Novel Composite Conductive Microfiltration Membrane and Its Anti-Fouling Performance with an External Electric Field in Membrane Bioreactors." *Scientific Reports* 5 (2015): 9268.

Huang, Kai, Agnes Anne, Mohamed Ali Bahri, and Christophe Demaille. "Probing Individual Redox Pegylated Gold Nanoparticles by Electrochemical–Atomic Force Microscopy." *ACS Nano* 7, no. 5 (2013): 4151-63.

Huang, Wan-Chen, Lian-Ming Lyu, Yu-Chen Yang, and Michael H Huang. "Synthesis of Cu2O Nanocrystals from Cubic to Rhombic Dodecahedral Structures and Their Comparative Photocatalytic Activity." *Journal of the American Chemical Society* 134, no. 2 (2012): 1261-67.

Huang, Xiao, Xiaoying Qi, Yizhong Huang, Shaozhou Li, Can Xue, Chee Lip Gan, Freddy Boey, and Hua Zhang. "Photochemically Controlled Synthesis of Anisotropic Au Nanostructures: Platelet-Like Au Nanorods and Six-Star Au Nanoparticles." *ACS Nano* 4, no. 10 (2010): 6196-202.

Huang, Xiaopeng, Ying Chen, Eric Walter, Meirong Zong, Yang Wang, Xin Zhang, Odeta Qafoku, Zheming Wang, and Kevin M Rosso. "Facet-Specific Photocatalytic Degradation of Organics by Heterogeneous Fenton Chemistry on Hematite Nanoparticles." *Environmental Science and Technology* 53, no. 17 (2019): 10197-207.

Hubler, David K, James C Baygents, Brian P Chaplin, and James Farrell. "Understanding Chlorite, Chlorate and Perchlorate Formation When Generating Hypochlorite Using Boron Doped Diamond Film Electrodes." *ECS Transactions* 58, no. 35 (2014): 21.

Huo, Ying, Yunguang Zhu, Jian Xie, Gaoshao Cao, Tiejun Zhu, Xinbing Zhao, and Shichao Zhang. "Controllable Synthesis of Hollow A-Fe2O3 Nanostructures, Their Growth Mechanism, and the Morphology-Reserved Conversion to Magnetic Fe3O4/C Nanocomposites." *RSC Advances* 3, no. 41 (2013): 19097-103.

Huynh, Khanh An, and Kai Loon Chen. "Aggregation Kinetics of Citrate and Polyvinylpyrrolidone Coated Silver Nanoparticles in Monovalent and Divalent Electrolyte Solutions." *Environmental Science and Technology* 45, no. 13 (2011): 5564-71.

Ibáñez, Maria, Pablo Guardia, Alexey Shavel, Doris Cadavid, Jordi Arbiol, Joan Ramon Morante, and Andreu Cabot. "Growth Kinetics of Asymmetric Bi2S3 Nanocrystals: Size Distribution Focusing in Nanorods." *The Journal of Physical Chemistry C* 115, no. 16 (2011): 7947-55.

Ibragimova, Rina, Paul Erhart, Patrick Rinke, and Hannu-Pekka Komsa. "Surface Functionalization of 2d Mxenes: Trends in Distribution, Composition, and Electronic Properties." *The Journal of Physical Chemistry Letters* 12, no. 9 (2021): 2377-84.

Ihsanullah, Ihsanullah. "Mxenes (Two-Dimensional Metal Carbides) as Emerging Nanomaterials for Water Purification: Progress, Challenges and Prospects." *Chemical Engineering Journal* 388 (2020): 124340.

Im, Mi Eun, De Pham-Cong, Ji Yoon Kim, Hun Seok Choi, Jae Hyun Kim, Jong Pil Kim, Jinwoo Kim, Se Young Jeong, and Chae Ryong Cho. "Enhanced Electrochemical Performance of Template-Free Carbon-Coated Iron (II, III) Oxide Hollow Nanofibers as Anode Material for Lithium-Ion Batteries." *Journal of Power Sources* 284 (2015): 392-99.

Ingale, Arun G, and AN Chaudhari. "Biogenic Synthesis of Nanoparticles and Potential Applications: An Eco-Friendly Approach." *J Nanomed Nanotechol* 4, no. 165 (2013): 1-7.

Jabir, Majid Sakhi, Uday Muhsen Nayef, and Waleed Kamel Abdul Kadhim. "Polyethylene Glycol-Functionalized Magnetic (Fe3O4) Nanoparticles: A Novel DNA-Mediated Antibacterial Agent." *Nano Biomedicine and Engineering* 11, no. 1 (2019): 18-27.

Jain, Aditi, Shivendu Ranjan, Nandita Dasgupta, and Chidambaram Ramalingam. "Nanomaterials in Food and Agriculture: An Overview on Their Safety Concerns and Regulatory Issues." *Critical Reviews in Food Science and Nutrition* 58, no. 2 (2018): 297-317.

Janas, Dawid, and Grzegorz Stando. "Unexpectedly Strong Hydrophilic Character of Free-Standing Thin Films from Carbon Nanotubes." *Scientific Reports* 7, no. 1 (2017): 1-13.

Jasmann, Jeramy R, Thomas Borch, Tom C Sale, and Jens Blotevogel. "Advanced Electrochemical Oxidation of 1, 4-Dioxane Via Dark Catalysis by Novel Titanium Dioxide (TiO2) Pellets." *Environmental Science and Technology* 50, no. 16 (2016): 8817-26.

Jasmann, Jeramy R, Phillip B Gedalanga, Thomas Borch, Shaily Mahendra, and Jens Blotevogel. "Synergistic Treatment of Mixed 1, 4-Dioxane and Chlorinated Solvent Contaminations by Coupling Electrochemical Oxidation with Aerobic Biodegradation." *Environmental Science and Technology* 51, no. 21 (2017): 12619-29.

Jasmann, Jeramy R., Thomas Borch, Tom C. Sale, and Jens Blotevogel. "Advanced Electrochemical Oxiddation of 1,4-Dioxane Via Dark Catalysis by Novel Titanium Dioxide (TiO2) Pellets." *Enviornmental Science and Technology* (July 15, 2016 2016)..

Jeong, Joonseon, Choonsoo Kim, and Jeyong Yoon. "The Effect of Electrode Material on the Generation of Oxidants and Microbial Inactivation in the Electrochemical Disinfection Processes." *Water Research* 43, no. 4 (2009): 895-901.

Jeong, Young-IL, Da Hye Kim, Kyu Don Chung, Yoon Hyuk Kim, Yeon Soo Lee, and Ki-Choon Choi. "Antitumor Activity of Trigonelline-Incorporated Chitosan Nanoparticles." *Journal of Nanoscience and Nanotechnology* 14, no. 8 (2014): 5633-37.

Jhaveri, Jainesh H, and ZVP Murthy. "A Comprehensive Review on Anti-Fouling Nanocomposite Membranes for Pressure Driven Membrane Separation Processes." *Desalination* 379 (2016): 137-54.

Jia, Chong, Yao Cheng, Feng Bao, Daqin Chen, and Yuansheng Wang. "Ph Value-Dependant Growth of A-Fe2O3 Hierarchical Nanostructures." *Journal of Crystal Growth* 294, no. 2 (2006): 353-57.

Jiang, Jingjing, Zhuangqun Huang, Chengxiang Xiang, Rakesh Poddar, Hans-Joachim Lewerenz, Kimberly M Papadantonakis, Nathan S Lewis, and Bruce S Brunschwig. "Nanoelectrical and Nanoelectrochemical Imaging of Pt/P-Si and Pt/P+-Si Electrodes." *ChemSusChem* 10, no. 22 (2017): 4657-63.

Jiang, Li, Tingting You, Penggang Yin, Yang Shang, Dongfeng Zhang, Lin Guo, and Shihe Yang. "Surface-Enhanced Raman Scattering Spectra of Adsorbates on Cu2O Nanospheres: Charge-Transfer and Electromagnetic Enhancement." *Nanoscale* 5, no. 7 (2013): 2784-89.

Jiang, Xiantao, Artem V Kuklin, Alexander Baev, Yanqi Ge, Hans Ågren, Han Zhang, and Paras N Prasad. "Two-Dimensional Mxenes: From Morphological to Optical, Electric, and Magnetic Properties and Applications." *Physics Reports* 848 (2020): 1-58.

Jiang, Yu, Tong Xia, Liuxue Shen, Junlin Ma, Hongting Ma, Tongrui Sun, Fengjuan Lv, and Nan Zhu. "Facet-Dependent Cu2O Electrocatalysis for Wearable Enzyme-Free Smart Sensing." *ACS Catalysis* 11, no. 5 (2021): 2949-55.

Jing, Hao, Qingfeng Zhang, Nicolas Large, Chunmei Yu, Douglas A Blom, Peter Nordlander, and Hui Wang. "Tunable Plasmonic Nanoparticles with Catalytically Active High-Index Facets." *Nano Letters* 14, no. 6 (2014): 3674-82.

Jiu, Jinting, Katsuaki Suganuma, and Masaya Nogi. "Effect of Additives on the Morphology of Single-Crystal Au Nanosheet Synthesized Using the Polyol Process." *Journal of Materials Science* 46, no. 14 (2011): 4964-70.

Kaegi, Ralf, Brian Sinnet, Steffen Zuleeg, Harald Hagendorfer, Elisabeth Mueller, Roger Vonbank, Markus Boller, and Michael Burkhardt. "Release of Silver Nanoparticles from Outdoor Facades." *Environmental Pollution* 158, no. 9 (2010): 2900-05.

Kang, Hyunho, Joseph T Buchman, Rebeca S Rodriguez, Hattie L Ring, Jiayi He, Kyle C Bantz, and Christy L Haynes. "Stabilization of Silver and Gold Nanoparticles: Preservation and Improvement of Plasmonic Functionalities." *Chemical Reviews* 119, no. 1 (2018): 664-99.

Karim, NA, Siti Kartom Kamarudin, and Kee Shyuan Loh. "Performance of a Novel Non-Platinum Cathode Catalyst for Direct Methanol Fuel Cells." *Energy Conversion and Management* 145 (2017): 293-307.

Ke, Fu-Sheng, Bryan Solomon, Yong Ding, Gui-Liang Xu, Shi-Gang Sun, Zhong Lin Wang, and Xiao-Dong Zhou. "Enhanced Electrocatalytic Activity on Gold Nanocrystals Enclosed by High-Index Facets for Oxygen Reduction." *Nano Energy* 7 (2014): 179-88.

Kedia, Abhitosh, and Pandian Senthil Kumar. "Solvent-Adaptable Poly (Vinylpyrrolidone) Binding Induced Anisotropic Shape Control of Gold Nanostructures." *The Journal of Physical Chemistry C* 116, no. 44 (2012): 23721-28.

Kent, Ronald D, and Peter J Vikesland. "Controlled Evaluation of Silver Nanoparticle Dissolution Using Atomic Force Microscopy." *Environmental Science and Technology* 46, no. 13 (2012): 6977-84.

Khan, Ibrahim, Khalid Saeed, and Idrees Khan. "Nanoparticles: Properties, Applications and Toxicities." *Arabian Journal of Chemistry* 12, no. 7 (2019): 908-31.

Khan, Zaheer, and Fawziya M Al-Nowaiser. "Effect of Poly (Vinyl Alcohol) on the Size, Shape, and Rate of Silver Nanoparticles Formation." *Journal of Dispersion Science and Technology* 32, no. 11 (2011): 1655-60.

Kim, Jae-Hun, Seungbo Ryu, Ju-Young Lee, and Seung-Hyeon Moon. "Preparation of High-Conductivity Qppo (Quaternary-Aminated Poly (2, 6-Dimethyl-1, 4-Phenyleneoxide)) Membranes by Electrical Treatment." *Journal of Membrane Science* 553 (2018): 82-89.

Kim, Jungah, Soonchang Hong, Hee-Jeong Jang, Yoonjung Choi, and Sungho Park. "Influence of Iodide Ions on Morphology of Silver Growth on Gold Hexagonal Nanoplates." *Journal of Colloid and Interface Science* 389, no. 1 (2013): 71-76.

Kim, Kwan, Hyoung Kun Park, and Nam Hoon Kim. "Silver-Particle-Based Surface-Enhanced Raman Scattering Spectroscopy for Biomolecular Sensing and Recognition." *Langmuir* 22, no. 7 (2006): 3421-27.

Kleiner, Karin, Julia Melke, Michael Merz, Peter Jakes, Peter Nagel, Stefan Schuppler, Verena Liebau, and Helmut Ehrenberg. "Unraveling the Degradation Process of Electrodes in Commercial Lithium Ion Batteries by Electronic Structure Investigations." *ACS Applied Materials and Interfaces* 7, no. 35 (2015): 19589-600.

Knittel, Peter, Boris Mizaikoff, and Christine Kranz. "Simultaneous Nanomechanical and Electrochemical Mapping: Combining Peak Force Tapping Atomic Force Microscopy with Scanning Electrochemical Microscopy." *Analytical Chemistry* 88, no. 12 (2016): 6174-78.

Kobayashi, Makoto, Hideki Kato, and Masato Kakihana. "Synthesis of Spindle and Square Bipyramid-Shaped Anatase-Type Titanium Dioxide Crystals by a Solvothermal Method Using Ethylenediamine." *Journal of the Ceramic Society of Japan* 120, no. 1407 (2012): 494-99.

Kočí, Kamila, Martin Reli, Ivana Troppová, Marcel Šihor, Jana Kupková, P Kustrowski, and Petr Praus. "Photocatalytic Decomposition of N2O over TiO2/G-C3N4 Photocatalysts Heterojunction." *Applied Surface Science* 396 (2017): 1685-95.

Kokura, Satoshi, Osamu Handa, Tomohisa Takagi, Takeshi Ishikawa, Yuji Naito, and Toshikazu Yoshikawa. "Silver Nanoparticles as a Safe Preservative for Use in Cosmetics." *Nanomedicine: Nanotechnology, Biology and Medicine* 6, no. 4 (2010): 570-74.

Kolagatla, Srikanth, Palaniappan Subramanian, and Alex Schechter. "Catalytic Current Mapping of Oxygen Reduction on Isolated Pt Particles by Atomic Force Microscopy-Scanning Electrochemical Microscopy." *Applied Catalysis B: Environmental* 256 (2019): 117843.

Kresse, G, and Furthmüller J. "Efficient Iterative Schemes for Ab Initio Total-Energy Calculations Using a Plane-Wave Basis Set." *Physical Review B Condensed Matter* 54, no. 16 (1996): 11169-86.

Kresse, G., and J. Furthmüller. "Efficiency of Ab-Initio Total Energy Calculations for Metals and Semiconductors Using a Plane-Wave Basis Set." *Compuational Matter* 6, no. 1 (1996): 15-50.

Kresse, G., and D. Joubert. "From Ultrasoft Pseudopotentials to the Projector Augmented-Wave Method." *Physical Review B* 59, no. 3 (1999): 1758-75.

Kresse, Georg, and Jürgen Furthmüller. "Efficient Iterative Schemes for Ab Initio Total-Energy Calculations Using a Plane-Wave Basis Set." *Physical Review B* 54, no. 16 (1996): 11169.

Kresse, Georg, and Daniel Joubert. "From Ultrasoft Pseudopotentials to the Projector Augmented-Wave Method." *Physical Review b* 59, no. 3 (1999): 1758.

Kumar, Santosh, Bharat Kumar, Arabinda Baruah, and Vishnu Shanker. "Synthesis of Magnetically Separable and Recyclable G-C3N4–Fe3O4 Hybrid Nanocomposites with Enhanced Photocatalytic Performance under Visible-Light Irradiation." *The Journal of Physical Chemistry C* 117, no. 49 (2013): 26135-43.

Kummara, Sivaiah, Mrityunjaya B Patil, and Tiewlasubon Uriah. "Synthesis, Characterization, Biocompatible and Anticancer Activity of Green and Chemically Synthesized Silver Nanoparticles–a Comparative Study." *Biomedicine and Pharmacotherapy* 84 (2016): 10-21.

Kuo, Chun-Hong, and Michael H Huang. "Morphologically Controlled Synthesis of Cu2O Nanocrystals and Their Properties." *Nano Today* 5, no. 2 (2010): 106-16.

Kuo, Ping-Lin, Chi-Chang Chen, and Mei-Wen Jao. "Effects of Polymer Micelles of Alkylated Polyethylenimines on Generation of Gold Nanoparticles." *The Journal of Physical Chemistry B* 109, no. 19 (2005): 9445-50.

Kwon, Yongwoo, Aloysius Soon, Haksoo Han, and Hyunjoo Lee. "Shape Effects of Cuprous Oxide Particles on Stability in Water and Photocatalytic Water Splitting." *Journal of Materials Chemistry A* 3, no. 1 (2015): 156-62.

Labille, Jérôme, Jinghuan Feng, Céline Botta, Daniel Borschneck, Magali Sammut, Martiane Cabie, Mélanie Auffan, Jérôme Rose, and Jean-Yves Bottero. "Aging of Tio2 Nanocomposites Used in Sunscreen. Dispersion and Fate of the Degradation Products in Aqueous Environment." *Environmental Pollution* 158, no. 12 (2010): 3482-89.

LaMer, Victor K, and Robert H Dinegar. "Theory, Production and Mechanism of Formation of Monodispersed Hydrosols." *Journal of the American Chemical Society* 72, no. 11 (1950): 4847-54.

Le, Tin, Elnaz Jamshidi, Majid Beidaghi, and Milad Rabbani Esfahani. "Functionalized-Mxene Thin-Film Nanocomposite Hollow Fiber Membranes for Enhanced PFAS Removal from Water." *ACS Applied Materials and Interfaces* (2022).

Lee, Anna, Jeffrey W Elam, and Seth B Darling. "Membrane Materials for Water Purification: Design, Development, and Application." *Environmental Science: Water Research and Technology* 2, no. 1 (2016): 17-42.

Lee, Sang Hun, and Bong-Hyun Jun. "Silver Nanoparticles: Synthesis and Application for Nanomedicine." *International Journal of Molecular Sciences* 20, no. 4 (2019): 865.

Lee, Sungki, Chen-Wei Liang, and Lane W Martin. "Synthesis, Control, and Characterization of Surface Properties of Cu2O Nanostructures." *ACS Nano* 5, no. 5 (2011): 3736-43.

Li, Chen, Chengwen Song, Ping Tao, Menghan Sun, Zonglin Pan, Tonghua Wang, and Mihua Shao. "Enhanced Separation Performance of Coal-Based Carbon Membranes Coupled with an Electric Field for Oily Wastewater Treatment." *Separation and Purification Technology* 168 (2016): 47-56.

Li, Chen, Meihan Zhang, Chengwen Song, Ping Tao, Menghan Sun, Mihua Shao, and Tonghua Wang. "Enhanced Treatment Ability of Membrane Technology by Integrating an Electric Field for Dye Wastewater Treatment: A Review." *Journal of AOAC International* 101, no. 5 (2018): 1341-52.

Li, Duo, Jingyan Tang, Xiezhen Zhou, Jiansheng Li, Xiuyun Sun, Jinyou Shen, Lianjun Wang, and Weiqing Han. "Electrochemical Degradation of Pyridine by Ti/SnO2–Sb Tubular Porous Electrode." *Chemosphere* 149 (2016): 49-56.

Li, Jiao, Jianxin Li, Hong Wang, Bowen Cheng, Benqiao He, Feng Yan, Yang Yang, Wenshan Guo, and Huu Hao Ngo. "Electrocatalytic Oxidation of N-Propanol to Produce Propionic Acid Using an Electrocatalytic Membrane Reactor." *Chemical Communications* 49, no. 40 (2013): 4501-03.

Li, Jiayi, Jinxing Ma, Ruobin Dai, Xueye Wang, Mei Chen, T David Waite, and Zhiwei Wang. "Self-Enhanced Decomplexation of Cu-Organic Complexes and Cu Recovery from Wastewaters Using an Electrochemical Membrane Filtration System." *Environmental Science and Technology* 55, no. 1 (2020): 655-64.

Li, Jinghong, and Jin Z Zhang. "Optical Properties and Applications of Hybrid Semiconductor Nanomaterials." *Coordination Chemistry Reviews* 253, no. 23-24 (2009): 3015-41.

Li, Lin, Tonghua Wang, Qingling Liu, Yiming Cao, and Jieshan Qiu. "A High CO2 Permselective Mesoporous Silica/Carbon Composite Membrane for CO2 Separation." *Carbon* 50, no. 14 (2012): 5186-95.

Li, Mian, Xinliang Li, Guifang Qin, Kan Luo, Jun Lu, Youbing Li, Guojin Liang, *et al.* "Halogenated Ti3C2 Mxenes with Electrochemically Active Terminals for High-Performance Zinc Ion Batteries." *ACS Nano* 15, no. 1 (2021): 1077-85.

Li, Pu, Chao Yang, Feiyun Sun, and Xiao-yan Li. "Fabrication of Conductive Ceramic Membranes for Electrically Assisted Fouling Control During Membrane Filtration for Wastewater Treatment." *Chemosphere* 280 (2021): 130794.

Li, Qilin, Shaily Mahendra, Delina Y Lyon, Lena Brunet, Michael V Liga, Dong Li, and Pedro JJ Alvarez. "Antimicrobial Nanomaterials for Water Disinfection and Microbial Control: Potential Applications and Implications." *Water Research* 42, no. 18 (2008): 4591-602.

Li, Rui, Shefa Alomari, Timur Islamoglu, Omar K Farha, Sujan Fernando, Selma Mededovic Thagard, Thomas M Holsen, and Mario Wriedt. "Systematic Study on the Removal of Per-and Polyfluoroalkyl Substances from Contaminated Groundwater Using Metal–Organic Frameworks." *Environmental Science and Technology* 55, no. 22 (2021): 15162-71.

Li, Rui, Weiwei Sun, Cheng Zhan, Paul RC Kent, and De-en Jiang. "Interfacial and Electronic Properties of Heterostructures of Mxene and Graphene." *Physical Review B* 99, no. 8 (2019): 085429.

Li, Xiang, Guohe Huang, Xiujuan Chen, Jing Huang, Mengna Li, Jianan Yin, Ying Liang, Yao Yao, and Yongping Li. "A Review on Graphitic Carbon Nitride (G-C3N4) Based Hybrid Membranes for Water and Wastewater Treatment." *Science of The Total Environment* (2021): 148462.

Li, Xiaojie, Hongji Li, Mingji Li, Cuiping Li, Dazhi Sun, Yingjie Lei, and Baohe Yang. "Preparation of a Porous Boron-Doped Diamond/Ta Electrode for the Electrocatalytic Degradation of Organic Pollutants." *Carbon* 129 (2018): 543-51.

Li, Xiaolong, Fengqin Zhang, Chao Ma, Yan Deng, Zhifei Wang, Sauli Elingarami, and Nongyue He. "Controllable Synthesis of ZnO with Various Morphologies by Hydrothermal Method." *Journal of Nanoscience and Nanotechnology* 12, no. 3 (2012): 2028-36.

Li, Xinyang, Guicheng Liu, Mei Shi, Jiao Li, Juan Li, Caiyang Guo, Joong Kee Lee, and Jianzhong Zheng. "Using TiO2 Mesoflower Interlayer in Tubular Porous Titanium Membranes for Enhanced Electrocatalytic Filtration." *Electrochimica Acta* 218 (2016): 318-24.

Li, Yang, Jian Zhao, Enxiang Shang, Xinghui Xia, Junfeng Niu, and John Crittenden. "Effects of Chloride Ions on Dissolution, ROS Generation, and Toxicity of Silver Nanoparticles under Uv Irradiation." *Environmental Science and Technology* 52, no. 8 (2017): 4842-49.

Liakakos, Nikos, Benoît Cormary, Xiaojian Li, Pierre Lecante, Marc Respaud, Laurent Maron, Andrea Falqui, *et al.* "The Big Impact of a Small Detail: Cobalt Nanocrystal Polymorphism as a Result of Precursor Addition Rate During Stock Solution Preparation." *Journal of the American Chemical Society* 134, no. 43 (2012): 17922-31.

Liang, Shangtao, Hui Lin, Xiufen Yan, and Qingguo Huang. "Electro-Oxidation of Tetracycline by a Magneli Phase Ti4O7 Porous Anode: Kinetics, Products, and Toxicity." *Chemical Engineering Journal* 332 (2018): 628-36.

Liang, Shaolei, Guangfen Li, and Run Tian. "Multi-Walled Carbon Nanotubes Functionalized with a Ultrahigh Fraction of Carboxyl and Hydroxyl Groups by Ultrasound-Assisted Oxidation." *Journal of Materials Science* 51, no. 7 (2016): 3513-24.

Liao, Yuwei, Guohong Wang, Juan Wang, Kai Wang, Suding Yan, and Yaorong Su. "Nitrogen Vacancy Induced in Situ G-C3N4 Pn Homojunction for Boosting Visible Light-Driven Hydrogen Evolution." *Journal of Colloid and Interface Science* 587 (2021): 110-20.

Lim, Teik-Thye, and Ronn Goei. "Combined Photocatalysis–Separation Processes for Water Treatment Using Hybrid Photocatalytic Membrane Reactors." In *Photocatalysis*, 130-56, 2016.

Lin, Hai-xin, Zhi-chao Lei, Zhi-yuan Jiang, Chang-ping Hou, De-yu Liu, Min-min Xu, Zhong-qun Tian, and Zhao-xiong Xie. "Supersaturation-Dependent Surface Structure Evolution: From Ionic, Molecular to Metallic Micro/Nanocrystals." *Journal of the American Chemical Society* 135, no. 25 (2013): 9311-14.

Lin, Hui, Hanjun Peng, Xingwei Feng, Xiaojing Li, Jinbo Zhao, Kui Yang, Jianbo Liao. "Energy-Efficient for Advanced Oxidation of Bio-Treated Landfill Leachate Effluent by Reactive Electrochemical Membranes (REMs): Laboratory and Pilot Scale Studies." *Water Research* 190 (2021): 116790.

Lin, Meng-Hsuan, Devon Manley Bulman, Christina K Remucal, and Brian P Chaplin. "Chlorinated Byproduct Formation During the Electrochemical Advanced Oxidation Process at Magnéli Phase Ti4O7 Electrodes." *Environmental Science and Technology* 54, no. 19 (2020): 12673-83.

Lin, Ming, Hui Ru Tan, Joyce Pei Ying Tan, and Shiqiang Bai. "Understanding the Growth Mechanism of A-Fe2O3 Nanoparticles through a Controlled Shape Transformation." *The Journal of Physical Chemistry C* 117, no. 21 (2013): 11242-50.

Lin, Xiaohui, Guangbin Ji, Yousong Liu, Qihui Huang, Zhihong Yang, and Youwei Du. "Formation Mechanism and Magnetic Properties of Hollow Fe3O4 Nanospheres Synthesized without Any Surfactant." *CrystEngComm* 14, no. 24 (2012): 8658-63.

Lin, Zhi-jie, Xiaomei Chen, Zhimin Cai, Munetaka Oyama, Xi Chen, and Xiaoru Wang. "The Initial Transformation Mechanism of Gold Seeds on Indium Tin Oxide Surfaces." *Crystal Growth and Design* 8, no. 3 (2008): 863-68.

Lindim, Claudia, J Van Gils, and Ian T Cousins. "Europe-Wide Estuarine Export and Surface Water Concentrations of Pfos and Pfoa." *Water Research* 103 (2016): 124-32.

Liscio, Andrea, Vincenzo Palermo, Klaus Müllen, and Paolo Samorì. "Tip− Sample Interactions in Kelvin Probe Force Microscopy: Quantitative Measurement of the Local Surface Potential." *The Journal of Physical Chemistry C* 112, no. 44 (2008): 17368-77.

Liu, Dong, Libo Li, and Tianyan You. "Superior Catalytic Performances of Platinum Nanoparticles Loaded Nitrogen-Doped Graphene toward Methanol Oxidation and Hydrogen Evolution Reaction." *Journal of Colloid and Interface Science* 487 (2017): 330-35.

Liu, Gang, Hua Gui Yang, Jian Pan, Yong Qiang Yang, Gao Qing Lu, and Hui-Ming Cheng. "Titanium Dioxide Crystals with Tailored Facets." *Chemical Reviews* 114, no. 19 (2014): 9559-612.

Liu, Jiadong, Lifen Liu, Bo Gao, and Fenglin Yang. "Cathode Membrane Fouling Reduction and Sludge Property in Membrane Bioreactor Integrating Electrocoagulation and Electrostatic Repulsion." *Separation and Purification Technology* 100 (2012): 44-50.

Liu, Jie, Bo Xu, Chao Song, Hongde Luo, Xing Zou, Lixian Han, and Xibin Yu. "Shape-Controlled Synthesis of Monodispersed Nano-/Micro-Nay (MoO4)2 (Doped with Eu3+) without Capping Agents Via a Hydrothermal Process." *CrystEngComm* 14, no. 8 (2012): 2936-43.

Liu, Jingyu, and Robert H Hurt. "Ion Release Kinetics and Particle Persistence in Aqueous Nano-Silver Colloids." *Environmental Science and Technology* 44, no. 6 (2010): 2169-75.

Liu, Juncheng, Jennifer N Duggan, Joshua Morgan, and Christopher B Roberts. "Seed-Mediated Growth and Manipulation of Au Nanorods Via Size-Controlled Synthesis of Au Seeds." *Journal of Nanoparticle Research* 14, no. 12 (2012): 1289.

Liu, Licheng, Ting Wei, Xiao Guan, Xuehong Zi, Hong He, and Hongxing Dai. "Size and Morphology Adjustment of PVP-Stabilized Silver and Gold Nanocrystals Synthesized by Hydrodynamic Assisted Self-Assembly." *The Journal of Physical Chemistry C* 113, no. 20 (2009): 8595-600.

Liu, Lifen, Jiadong Liu, Bo Gao, Fenglin Yang, and Shankar Chellam. "Fouling Reductions in a Membrane Bioreactor Using an Intermittent Electric Field and Cathodic Membrane Modified by Vapor Phase Polymerized Pyrrole." *Journal of Membrane Science* 394 (2012): 202-08.

Liu, Siqi, Yi Wang, Xiezhen Zhou, Weiqing Han, Jiansheng Li, Xiuyun Sun, Jinyou Shen, and Lianjun Wang. "Improved Degradation of the Aqueous Flutriafol Using a Nanostructure Macroporous PbO2 as Reactive Electrochemical Membrane." *Electrochimica Acta* 253 (2017): 357-67.

Liu, Yanbiao, Han Liu, Zhi Zhou, Tianren Wang, Choon Nam Ong, and Chad D Vecitis. "Degradation of the Common Aqueous Antibiotic Tetracycline Using a Carbon Nanotube Electrochemical Filter." *Environmental Science and Technology* 49, no. 13 (2015): 7974-80.

Liu, Zhaolin, Leong Ming Gan, Liang Hong, Weixiang Chen, and Jim Yang Lee. "Carbon-Supported Pt Nanoparticles as Catalysts for Proton Exchange Membrane Fuel Cells." *Journal of Power Sources* 139, no. 1-2 (2005): 73-78.

Liu, Zhimeng, Mengfu Zhu, Lei Zhao, Cheng Deng, Jun Ma, Zheng Wang, Hongbin Liu, and Hong Wang. "Aqueous Tetracycline Degradation by Coal-Based Carbon Electrocatalytic Filtration Membrane: Effect of Nano Antimony-Doped Tin Dioxide Coating." *Chemical Engineering Journal* 314 (2017): 59-68.

Liu, Zhong-Gang, Yu-Feng Sun, Wen-Kai Chen, Yuan Kong, Zhen Jin, Xing Chen, Xiao Zheng, *et al.* "Facet-Dependent Stripping Behavior of Cu2O Microcrystals toward Lead Ions: A Rational Design for the Determination of Lead Ions." *Small* 11, no. 21 (2015): 2493-98.

Lizandara-Pueyo, Carlos, Maria Carmen Morant-Minana, Martin Wessig, Michael Krumm, Stefan Mecking, and Sebastian Polarz. "Biomimetic Crystallization of Anisotropic Zinc Oxide Nanoparticles in the Homogeneous Phase: Shape Control by Surface Additives Applied under Thermodynamic or Kinetic Control." *RSC Advances* 2, no. 12 (2012): 5298-306.

Long, Nguyen Viet, Nguyen Duc Chien, Hirohito Hirata, Takashi Matsubara, Michitaka Ohtaki, and Masayuki Nogami. "Highly Monodisperse Cubic and Octahedral Rhodium Nanocrystals: Their Evolutions from Sharp Polyhedrons into Branched Nanostructures and Surface-Enhanced Raman Scattering." *Journal of Crystal Growth* 320, no. 1 (2011): 78-89.

López, Fausto, M Pilar Bernal, Reyes Mallada, Joaquín Coronas, and Jesús Santamaría. "Preparation of Silicalite Membranes on Stainless Steel Grid Supports." *Industrial and Engineering Chemistry Research* 44, no. 20 (2005): 7627-32.

Lounsbury, Amanda W, Ranran Wang, Desiree L Plata, Nicholas Billmyer, Christopher Muhich, Kiyoshi Kanie, Tadao Sugimoto, Derek Peak, and Julie B Zimmerman. "Preferential Adsorption of Selenium Oxyanions onto {110} and {012} Nano-Hematite Facets." *Journal of Colloid and Interface Science* 537 (2019): 465-74.

Lu, Zhuoxuan, Yuanfu Huang, Liming Zhang, Kai Xia, Yan Deng, and Nongyue He. "Preparation of Gold Nanorods Using 1, 2, 4-Trihydroxybenzene as a Reducing Agent." *Journal of Nanoscience and Nanotechnology* 15, no. 8 (2015): 6230-35.

Luo, Xiliang, Aoife Morrin, Anthony J Killard, and Malcolm R Smyth. "Application of Nanoparticles in Electrochemical Sensors and Biosensors." *Electroanalysis: An International Journal Devoted to Fundamental and Practical Aspects of Electroanalysis* 18, no. 4 (2006): 319-26.

Luo, Yongsong, Suqin Li, Qinfeng Ren, Jinping Liu, Lanlan Xing, Yan Wang, Ying Yu, Zhijie Jia, and Jialin Li. "Facile Synthesis of Flowerlike Cu2O Nanoarchitectures by a Solution Phase Route." *Crystal Growth and Design* 7, no. 1 (2007): 87-92.

Lv, Hualiang, Guangbin Ji, Wei Liu, Haiqian Zhang, and Youwei Du. "Achieving Hierarchical Hollow Carbon@ Fe@ Fe3O4 Nanospheres with Superior Microwave Absorption Properties and Lightweight Features." *Journal of Materials Chemistry C* 3, no. 39 (2015): 10232-41.

Ma, Jun, Yuanyuan Wang, Hang Xu, Mingmei Ding, and Li Gao. "Mxene (Ti3C2Tx)-Reinforced Thin-Film Polyamide Nanofiltration Membrane for Short-Chain Perfluorinated Compounds Removal." *Process Safety and Environmental Protection* 168 (2022): 275-84.

Ma, Li-Li, Jia-Lin Li, Hai-Zhen Sun, Ming-Qiang Qiu, Jian-Bo Wang, Jin-Yi Chen, and Ying Yu. "Self-Assembled Cu2O Flowerlike Architecture: Polyol Synthesis, Photocatalytic Activity and Stability under Simulated Solar Light." *Materials Research Bulletin* 45, no. 8 (2010): 961-68.

Ma, Rui, Clement Levard, Stella M Marinakos, Yingwen Cheng, Jie Liu, F Marc Michel, Gordon E Brown Jr, and Gregory V Lowry. "Size-Controlled Dissolution of Organic-Coated Silver Nanoparticles." *Environmental Science and Technology* 46, no. 2 (2012): 752-59.

Ma, Rui, Clément Levard, Stella M. Marinakos, Yingwen Cheng, Jie Liu, F. Marc Michel, Gordon E. Brown, and Gregory V. Lowry. "Size-Controlled Dissolution of Organic-Coated Silver Nanoparticles." *Environmental Science and Technology* 46, no. 2 (2012/01/17 2011): 752-59.

Mabande, GTP, G Pradhan, W Schwieger, M Hanebuth, R Dittmeyer, T Selvam, A Zampieri, H Baser, and R Herrmann. "A Study of Silicalite-1 and Al-Zsm-5 Membrane Synthesis on Stainless Steel Supports." *Microporous and Mesoporous Materials* 75, no. 3 (2004): 209-20.

Manawi, Yehia, Victor Kochkodan, Muataz Ali Hussein, Moe A Khaleel, Marwan Khraisheh, and Nidal Hilal. "Can Carbon-Based Nanomaterials Revolutionize Membrane Fabrication for Water Treatment and Desalination?". *Desalination* 391 (2016): 69-88.

Mann, Amanda K. P., Zili Wu, Florencia C. Calaza, and Steven H. Overbury. "Adsorption and Reaction of Acetaldehyde on Shape-Controlled CeO2 Nanocrystals: Elucidation of Structure–Function Relationships." *ACS Catalysis* 4, no. 8 (2014/08/01 2014): 2437-48.

Miller, Daniel J, Daniel R Dreyer, Christopher W Bielawski, Donald R Paul, and Benny D Freeman. "Surface Modification of Water Purification Membranes." *Angewandte Chemie International Edition* 56, no. 17 (2017): 4662-711.

Mishra, Abhaya Kumar, and Debabrata Pradhan. "Morphology Controlled Solution-Based Synthesis of Cu2O Crystals for the Facets-Dependent Catalytic Reduction of Highly Toxic Aqueous Cr(Vi)." *Crystal Growth and Design* 16, no. 7 (2016): 3688-98.

Mitra, Sangha, Chaitanya Krishna Kamaja, and Monica Katiyar. "Facile Formation of Porous, Multilayer Reduced Graphene Oxide Electrodes Using Electrophoretic Deposition and Flash Sintering." *Carbon* (2022).

Mittal, Amit Kumar, Yusuf Chisti, and Uttam Chand Banerjee. "Synthesis of Metallic Nanoparticles Using Plant Extracts." *Biotechnology advances* 31, no. 2 (2013): 346-56.

Monteiro-Riviere, NA, AO Inman, and LW Zhang. "Limitations and Relative Utility of Screening Assays to Assess Engineered Nanoparticle Toxicity in a Human Cell Line." *Toxicology and Applied Pharmacology* 234, no. 2 (2009): 222-35.

Moreira, Francisca C, Rui AR Boaventura, Enric Brillas, and Vítor JP Vilar. "Electrochemical Advanced Oxidation Processes: A Review on Their Application to Synthetic and Real Wastewaters." *Applied Catalysis B: Environmental* 202 (2017): 217-61.

Morris, Jeff, and Jim Willis. "Us Environmental Protection Agency Nanotechnology White Paper." *US Environmental Protection Agency, Washington, DC* (2007).

Naguib, Michael, Murat Kurtoglu, Volker Presser, Jun Lu, Junjie Niu, Min Heon, Lars Hultman, Yury Gogotsi, and Michel W Barsoum. "Two-Dimensional Nanocrystals Produced by Exfoliation of Ti3AlC2." *Advanced Materials* 23, no. 37 (2011): 4248-53.

Nayak, Sasmita, and Brian P Chaplin. "Fabrication and Characterization of Porous, Conductive, Monolithic Ti4O7 Electrodes." *Electrochimica Acta* 263 (2018): 299-310.

Nellist, Michael R, Yikai Chen, Andreas Mark, Sebastian Gödrich, Christian Stelling, Jingjing Jiang, Rakesh Poddar, *et al.* "Atomic Force Microscopy with Nanoelectrode Tips for High Resolution Electrochemical, Nanoadhesion and Nanoelectrical Imaging." *Nanotechnology* 28, no. 9 (2017): 095711.

Nguyen, Thanh-Dinh. "From Formation Mechanisms to Synthetic Methods toward Shape-Controlled Oxide Nanoparticles." *Nanoscale* 5, no. 20 (2013): 9455-82.

Nguyen, Thanh-Dinh, Cao-Thang Dinh, and Trong-On Do. "A General Procedure to Synthesize Highly Crystalline Metal Oxide and Mixed Oxide Nanocrystals in Aqueous Medium and Photocatalytic Activity of Metal/Oxide Nanohybrids." *Nanoscale* 3, no. 4 (2011): 1861-73.

Nguyen, Thanh-Dinh, Driss Mrabet, Cao-Thang Dinh, and Trong-On Do. "Biomolecule-Assisted Route for Shape-Controlled Synthesis of Single-Crystalline Mnwo 4 Nanoparticles and Spontaneous Assembly of Polypeptide-Stabilized Mesocrystal Microspheres." *CrystEngComm* 13, no. 5 (2011): 1450-60.

Niederberger, Markus, Georg Garnweitner, Jelena Buha, Julien Polleux, Jianhua Ba, and Nicola Pinna. "Nonaqueous Synthesis of Metal Oxide Nanoparticles: Review and Indium Oxide as Case Study for the Dependence of Particle Morphology on Precursors and Solvents." *Journal of Sol-Gel Science and Technology* 40, no. 2-3 (2006): 259-66.

Niesz, Krisztian, Christie Reji, James R Neilson, Ryan C Vargas, and Daniel E Morse. "Unusual Evolution of Ceria Nanocrystal Morphologies Promoted by a Low-Temperature Vapor Diffusion Based Process." *Crystal Growth and Design* 10, no. 10 (2010): 4485-90.

Nishiyama, Norikazu, Akihiro Koide, Yasuyuki Egashira, and Korekazu Ueyama. "Mesoporous Mcm-48 Membrane Synthesized on a Porous Stainless Steel Support." *Chemical Communications*, no. 19 (1998): 2147-48.

Nisticò, Roberto, Paola Rivolo, and Fabrizio Giorgis. "Tips and Tricks for the Surface Engineering of Well-Ordered Morphologically Driven Silver-Based Nanomaterials." *ChemistryOpen* 8, no. 4 (2019): 508-19.

Njaramba, Lewis Kamande, Sewoon Kim, Yejin Kim, Byungjun Cha, Nahyun Kim, Yeomin Yoon, and Chang Min Park. "Remarkable Adsorption for Hazardous Organic and Inorganic Contaminants by Multifunctional Amorphous Core–Shell Structures of Metal–Organic Framework-Alginate Composites." *Chemical Engineering Journal* 431 (2022): 133415.

O'brien, Niall Joseph, and Enda J Cummins. "A Risk Assessment Framework for Assessing Metallic Nanomaterials of Environmental Concern: Aquatic Exposure and Behavior." *Risk Analysis: An International Journal* 31, no. 5 (2011): 706-26.

Obare, Sherine O, Nikhil R Jana, and Catherine J Murphy. "Preparation of Polystyrene- and Silica-Coated Gold Nanorods and Their Use as Templates for the Synthesis of Hollow Nanotubes." *Nano Letters* 1, no. 11 (2001): 601-03.

Okitsu, Kenji, Kohei Sharyo, and Rokuro Nishimura. "One-Pot Synthesis of Gold Nanorods by Ultrasonic Irradiation: The Effect of Ph on the Shape of the Gold Nanorods and Nanoparticles." *Langmuir* 25, no. 14 (2009): 7786-90.

Omi, Farah R, Mahbuboor R Choudhury, Nawrin Anwar, Ahmed R Bakr, and Md Saifur Rahaman. "Highly Conductive Ultrafiltration Membrane Via Vacuum Filtration Assisted Layer-by-Layer Deposition of Functionalized Carbon Nanotubes." *Industrial and Engineering Chemistry Research* 56, no. 30 (2017): 8474-84.

Ong, Yee Kang, Gui Min Shi, Ngoc Lieu Le, Yu Pan Tang, Jian Zuo, Suzana P Nunes, and Tai-Shung Chung. "Recent Membrane Development for Pervaporation Processes." *Progress in Polymer Science* 57 (2016): 1-31.

Orel, Zorica Crnjak, Alojz Anžlovar, Goran Dražić, and Majda Žigon. "Cuprous Oxide Nanowires Prepared by an Additive-Free Polyol Process." *Crystal Growth and Design* 7, no. 2 (2007): 453-58.

Oturan, Nihal, Soliu O Ganiyu, Stephane Raffy, and Mehmet A Oturan. "Sub-Stoichiometric Titanium Oxide as a New Anode Material for Electro-Fenton Process: Application to Electrocatalytic Destruction of Antibiotic Amoxicillin." *Applied Catalysis B: Environmental* 217 (2017): 214-23.

Pace, Heather E, Nicola J Rogers, Chad Jarolimek, Victoria A Coleman, Evan P Gray, Christopher P Higgins, and James F Ranville. "Single Particle Inductively Coupled Plasma-Mass Spectrometry: A Performance Evaluation and Method Comparison in the Determination of Nanoparticle Size." *Environmental science and technology* 46, no. 22 (2012): 12272-80.

Pan, Yanqiu, Wei Wang, Tonghua Wang, and Pinjing Yao. "Fabrication of Carbon Membrane and Microfiltration of Oil-in-Water Emulsion: An Investigation on Fouling Mechanisms." *Separation and Purification Technology* 57, no. 2 (2007): 388-93.

Pan, Zonglin, Chengwen Song, Lin Li, Hong Wang, Yanqiu Pan, Chunlei Wang, Jianxin Li, Tonghua Wang, and Xianshe Feng. "Membrane Technology Coupled with Electrochemical Advanced Oxidation Processes for Organic Wastewater Treatment: Recent Advances and Future Prospects." *Chemical Engineering Journal* 376 (2019): 120909.

Pan, Zonglin, Fangpeng Yu, Lin Li, Ming Liu, Chengwen Song, Jiawei Yang, Hanxu Li, *et al.* "Low-Cost Electrochemical Filtration Carbon Membrane Prepared from Coal Via Self-Bonding." *Chemical Engineering Journal* 385 (2020): 123928.

Paneri, Abhilash, Yunseon Heo, Gregory Ehlert, Anton Cottrill, Henry Sodano, Peter Pintauro, and Saeed Moghaddam. "Proton Selective Ionic Graphene-Based Membrane for High Concentration Direct Methanol Fuel Cells." *Journal of Membrane Science* 467 (2014): 217-25.

Panizza, Marco, Cristina Bocca, and Giacomo Cerisola. "Electrochemical Treatment of Wastewater Containing Polyaromatic Organic Pollutants." *Water Research* 34, no. 9 (2000): 2601-05.

Papadopoulou, Evanthia, and Steven EJ Bell. "Structure of Adenine on Metal Nanoparticles: Ph Equilibria and Formation of Ag+ Complexes Detected by Surface-Enhanced Raman Spectroscopy." *The Journal of Physical Chemistry C* 114, no. 51 (2010): 22644-51.

Pendergast, MaryTheresa M, and Eric MV Hoek. "A Review of Water Treatment Membrane Nanotechnologies." *Energy and Environmental Science* 4, no. 6 (2011): 1946-71.

Peng, Yung-Kang, Yichen Hu, Hung-Lung Chou, Yingyi Fu, Ivo F Teixeira, Li Zhang, Heyong He, and Shik Chi Edman Tsang. "Mapping Surface-Modified Titania Nanoparticles with Implications for Activity and Facet Control." *Nature Communications* 8, no. 1 (2017): 1-13.

Peng, Yung-Kang, and SC Edman Tsang. "Facet-Dependent Photocatalysis of Nanosize Semiconductive Metal Oxides and Progress of Their Characterization." *Nano Today* 18 (2018): 15-34.

Perdew, John P, Kieron Burke, and Matthias Ernzerhof. "Generalized Gradient Approximation Made Simple." *Physical Review Letters* 77, no. 18 (1996): 3865.

Perdew, John P., Kieron Burke, Matthias Ernzerhof, and Erratum. "Generalized Gradient Approximation Made Simple." *Physical Review Letters* (1996).

Perreault, François, Andreia Fonseca De Faria, and Menachem Elimelech. "Environmental Applications of Graphene-Based Nanomaterials." *Chemical Society Reviews* 44, no. 16 (2015): 5861-96.

Peters, Ruud JB, Greet van Bemmel, Zahira Herrera-Rivera, Hans PFG Helsper, Hans JP Marvin, Stefan Weigel, Peter C Tromp, *et al.* "Characterization of Titanium Dioxide Nanoparticles in Food Products: Analytical Methods to Define Nanoparticles." *Journal of Agricultural and Food Chemistry* 62, no. 27 (2014): 6285-93.

Petosa, Adamo R, Deb P Jaisi, Ivan R Quevedo, Menachem Elimelech, and Nathalie Tufenkji. "Aggregation and Deposition of Engineered Nanomaterials in Aquatic Environments: Role of Physicochemical Interactions." *Environmental Science and Technology* 44, no. 17 (2010): 6532-49.

Piccinno, Fabiano, Fadri Gottschalk, Stefan Seeger, and Bernd Nowack. "Industrial Production Quantities and Uses of Ten Engineered Nanomaterials in Europe and the World." *Journal of Nanoparticle Research* 14, no. 9 (2012): 1109.

Pietrobon, Brendan, and Vladimir Kitaev. "Photochemical Synthesis of Monodisperse Size-Controlled Silver Decahedral Nanoparticles and Their Remarkable Optical Properties." *Chemistry of Materials* 20, no. 16 (2008): 5186-90.

Pimentel, D, Bonnie Berger, D Filiberto, M Newton, B Wolfe, Elizabeth Karabinakis, S Clark, *et al.* "Water Resources." *Agriculture, and the Environment. Ithaca (NY): New York State College of Agriculture and Life Sciences, Cornell University. Environmental Biology Report* (2004): 04-1.

Pimentel, David, Bonnie Berger, David Filiberto, Michelle Newton, Benjamin Wolfe, Elizabeth Karabinakis, Steven Clark, *et al.* "Water Resources: Agricultural and Environmental Issues." *BioScience* 54, no. 10 (2004): 909-18.

Polcari, David, Philippe Dauphin-Ducharme, and Janine Mauzeroll. "Scanning Electrochemical Microscopy: A Comprehensive Review of Experimental Parameters from 1989 to 2015." *Chemical Reviews* 116, no. 22 (2016): 13234-78.

Pourzamani, Hamidreza, Nezamaddin Mengelizadeh, Yaghoub Hajizadeh, and Hamed Mohammadi. "Electrochemical Degradation of Diclofenac Using Three-Dimensional Electrode Reactor with Multi-Walled Carbon Nanotubes." *Environmental Science and Pollution Research* 25, no. 25 (2018): 24746-63.

Preet, Anant, and Tzu-En Lin. "A Review: Scanning Electrochemical Microscopy (Secm) for Visualizing the Real-Time Local Catalytic Activity." *Catalysts* 11, no. 5 (2021): 594.

Qin, Changyong, and Jerry L Whitten. "Adsorption of O, H, Oh, and H2O on Ag (100)." *The Journal of Physical Chemistry B* 109, no. 18 (2005): 8852-56.

Qin, Frank GF, John Mawson, and Xin An Zeng. "Experimental Study of Fouling and Cleaning of Sintered Stainless Steel Membrane in Electro-Microfiltration of Calcium Salt Particles." *Membranes* 1, no. 2 (2011): 119-31.

Qiu, Chao, Ying Bao, Nathan L Netzer, and Chaoyang Jiang. "Structure Evolution and Sers Activation of Cuprous Oxide Microcrystals Via Chemical Etching." *Journal of Materials Chemistry A* 1, no. 31 (2013): 8790-97.

Radi, Abdullah, Debabrata Pradhan, Youngku Sohn, and KT Leung. "Nanoscale Shape and Size Control of Cubic, Cuboctahedral, and Octahedral Cu−Cu2O Core− Shell Nanoparticles on Si (100) by One-Step, Templateless, Capping-Agent-Free Electrodeposition." *ACS Nano* 4, no. 3 (2010): 1553-60.

Rajeshwar, KIJG, JG Ibanez, and GM Swain. "Electrochemistry and the Environment." *Journal of Applied Electrochemistry* 24, no. 11 (1994): 1077-91.

Rambabu, Gutru, and Santoshkumar D Bhat. "Amino Acid Functionalized Graphene Oxide Based Nanocomposite Membrane Electrolytes for Direct Methanol Fuel Cells." *Journal of Membrane Science* 551 (2018): 1-11.

Ran, Jin, Liang Ding, Dongbo Yu, Xu Zhang, Min Hu, Liang Wu, and Tongwen Xu. "A Novel Strategy to Construct Highly Conductive and Stabilized Anionic Channels by Fluorocarbon Grafted Polymers." *Journal of Membrane Science* 549 (2018): 631-37.

Rao, Xuehui, Xintai Su, Chao Yang, Jide Wang, Xinping Zhen, and Daishun Ling. "From Spindle-Like B-Feooh Nanoparticles to A-Fe2O3 Polyhedral Crystals: Shape Evolution, Growth Mechanism and Gas Sensing Property." *CrystEngComm* 15, no. 36 (2013): 7250-56.

Reipa, Vytas, Shannon K Hanna, Aaron Urbas, Lane Sander, John Elliott, Joseph Conny, and Elijah J Petersen. "Efficient Electrochemical Degradation of Multiwall Carbon Nanotubes." *Journal of Hazardous Materials* 354 (2018): 275-82.

Ren, Jia, Wenzhong Wang, Songmei Sun, Ling Zhang, Lu Wang, and Jiang Chang. "Crystallography Facet-Dependent Antibacterial Activity: The Case of Cu2O." *Industrial and Engineering Chemistry Research* 50, no. 17 (2011): 10366-69.

Rice, Katherine P, Aaron E Saunders, and Mark P Stoykovich. "Seed-Mediated Growth of Shape-Controlled Wurtzite Cdse Nanocrystals: Platelets, Cubes, and Rods." *Journal of the American Chemical Society* 135, no. 17 (2013): 6669-76.

Rodríguez-Lorenzo, Laura, José M Romo-Herrera, Jorge Pérez-Juste, Ramón A Alvarez-Puebla, and Luis M Liz-Marzán. "Reshaping and Lspr Tuning of Au Nanostars in the Presence of CTAB." *Journal of Materials Chemistry* 21, no. 31 (2011): 11544-49.

Rojas, Sergio, Francisco J García-García, Sven Järas, María V Martínez-Huerta, José Luis García Fierro, and Magali Boutonnet. "Preparation of Carbon Supported Pt and Ptru Nanoparticles from Microemulsion: Electrocatalysts for Fuel Cell Applications." *Applied Catalysis A: General* 285, no. 1-2 (2005): 24-35.

Rong-Ming, LI Wei CHENG, XU Xue-Cheng CHEN Yi-Wei, and SUN Ming-Li. "Effect of Hydroxyl Radical on the Surface and Structure of Multi-Walled Carbon Nanotubes." *Chinese Journal of Inorganic Chemistry* 2 (2005).

Rong, Shaopeng, Pengyi Zhang, Fang Liu, and Yajie Yang. "Engineering Crystal Facet of A-Mno2 Nanowire for Highly Efficient Catalytic Oxidation of Carcinogenic Airborne Formaldehyde." *ACS Catalysis* 8, no. 4 (2018): 3435-46.

Ross, Ian, Jeffrey McDonough, Jonathan Miles, Peter Storch, Parvathy Thelakkat Kochunarayanan, Erica Kalve, Jake Hurst, Soumitri S. Dasgupta, and Jeff Burdick. "A Review of Emerging Technologies for Remediation of Pfass." *Remediation Journal* 28, no. 2 (2018): 101-26.

Rossignol, N, L Vandanjon, P Jaouen, and F Quemeneur. "Membrane Technology for the Continuous Separation Microalgae/Culture Medium: Compared Performances of Cross-Flow Microfiltration and Ultrafiltration." *Aquacultural Engineering* 20, no. 3 (1999): 191-208.

Rudel, Holly E, Mary Kate M Lane, Christopher L Muhich, and Julie B Zimmerman. "Toward Informed Design of Nanomaterials: A Mechanistic Analysis of Structure–Property–Function Relationships for Faceted Nanoscale Metal Oxides." *ACS Nano* 14, no. 12 (2020): 16472-501.

Rui, Jicheng, Ning Deng, Yiying Zhao, Chen Tao, Jizhi Zhou, Zhenzhen Zhao, and Xin Huang. "Activation of Persulfate Via Mn Doped Mg/Al Layered Double Hydroxide for Effective Degradation of Organics: Insights from Chemical and Structural Variability of Catalyst." *Chemosphere* 302 (2022): 134849.

Sabate, J, MA Anderson, H Kikkawa, Qunyin Xu, Salvador Cervera-March, and CG Hill. "Nature and Properties of Pure and Nb-Doped TiO2 Ceramic Membranes Affecting the Photocatalytic Degradation of 3-Chlorosalicylic Acid as a Model of Halogenated Organic Compounds." *Journal of Catalysis* 134, no. 1 (1992): 36-46.

Sakata, Y, A Muto, Md A Uddin, and H Suga. "Preparation of Porous Carbon Membrane Plates for Pervaporation Separation Applications." *Separation and Purification Technology* 17, no. 2 (1999): 97-100.

Sánchez-Iglesias, Ana, Marek Grzelczak, Jorge Pérez-Juste, and Luis M Liz-Marzán. "Binary Self-Assembly of Gold Nanowires with Nanospheres and Nanorods." *Angewandte Chemie International Edition* 49, no. 51 (2010): 9985-89.

Santhosh, Chella, Venugopal Velmurugan, George Jacob, Soon Kwan Jeong, Andrews Nirmala Grace, and Amit Bhatnagar. "Role of Nanomaterials in Water Treatment Applications: A Review." *Chemical Engineering Journal* 306 (2016): 1116-37.

Sardar, Rajesh, Alison M Funston, Paul Mulvaney, and Royce W Murray. "Gold Nanoparticles: Past, Present, and Future." *Langmuir* 25, no. 24 (2009): 13840-51.

Sau, TK, and Catherine Jones Murphy. "Role of Ions in the Colloidal Synthesis of Gold Nanowires." *Philosophical Magazine* 87, no. 14-15 (2007): 2143-58.

Sayed, Sayed Youssef, Feng Wang, Marek Malac, Peng Li, Dong Wang, and Jillian Buriak. "Preferential Face Deposition of Gold Nanoparticles on Silicon Nanowires by Galvanic Displacement." *CrystEngComm* 14, no. 16 (2012): 5230-34.

Schaefer, Charles E., Christina Andaya, Ana Urtiaga, Erica R. McKenzie, and Christopher P. Higgins. "Electrochemical Treatment of Perfluorooctanoic Acid (PFOA) and Perfluorooctane Sulfonic Acid (PFOS) in Groundwater Impacted by Aqueous Film Forming Foams (AFFFs)." *Journal of Hazardous Materials* 295 (2015/09/15/ 2015): 170-75.

Schultz, Thorsten, Nathan C Frey, Kanit Hantanasirisakul, Soohyung Park, Steven J May, Vivek B Shenoy, Yury Gogotsi, and Norbert Koch. "Surface Termination Dependent Work Function and Electronic Properties of Ti3C2Tx Mxene." *Chemistry of Materials* 31, no. 17 (2019): 6590-97.

Schulz, KH, and DAVID F Cox. "Propene Oxidation over Cu2O Single-Crystal Surfaces: A Surface Science Study of Propene Activation at 1 Atm and 300 K." *Journal of Catalysis* 143, no. 2 (1993): 464-80.

Seifert, G, A Stalmashonak, H Hofmeister, J Haug, and M Dubiel. "Laser-Induced, Polarization Dependent Shape Transformation of Au/Ag Nanoparticles in Glass." *Nanoscale Research Letters* 4, no. 11 (2009): 1380.

Senokos, Evgeny, Moumita Rana, Cleis Santos, Rebeca Marcilla, and Juan J Vilatela. "Controlled Electrochemical Functionalization of Cnt Fibers: Structure-Chemistry Relations and Application in Current Collector-Free All-Solid Supercapacitors." *Carbon* 142 (2019): 599-609.

Seo, Daeha, Ji Chan Park, and Hyunjoon Song. "Polyhedral Gold Nanocrystals with OH Symmetry: From Octahedra to Cubes." *Journal of the American Chemical Society* 128, no. 46 (2006): 14863-70.

Shang, Yang, and Lin Guo. "Facet-Controlled Synthetic Strategy of Cu2O-Based Crystals for Catalysis and Sensing." *Advanced Science* 2, no. 10 (2015): 1500140.

Shannon, Mark A, Paul W Bohn, Menachem Elimelech, John G Georgiadis, Benito J Marinas, and Anne M Mayes. "Science and Technology for Water Purification in the Coming Decades." In *Nanoscience and Technology: A Collection of Reviews from Nature Journals*, 337-46: World Scientific, 2010.

Sharma, Virender K, Natalie Johnson, Leslie Cizmas, Thomas J McDonald, and Hyunook Kim. "A Review of the Influence of Treatment Strategies on Antibiotic Resistant Bacteria and Antibiotic Resistance Genes." *Chemosphere* 150 (2016): 702-14.

Shen, Zelin, Zhanhua Zhang, Tong Li, Qingqian Yao, Tong Zhang, and Wei Chen. "Facet-Dependent Adsorption and Fractionation of Natural Organic Matter on Crystalline Metal Oxide Nanoparticles." *Environmental Science and Technology* 54, no. 14 (2020): 8622-31.

Shi, Jing, Jin Li, Xiaojian Huang, and Yiwei Tan. "Synthesis and Enhanced Photocatalytic Activity of Regularly Shaped Cu2O Nanowire Polyhedra." *Nano Research* 4, no. 5 (2011): 448-59.

Shi, Minjie, Cheng Yang, Chao Yan, Jintian Jiang, Yongchao Liu, Zhenyu Sun, Weilong Shi, *et al.* "Boosting Ion Dynamics through Superwettable Leaf-Like Film Based on Porous G-C3N4 Nanosheets for Ionogel Supercapacitors." *NPG Asia Materials* 11, no. 1 (2019): 1-11.

Shi, Xiaonan, Qingquan Ma, Taha Marhaba, and Wen Zhang. "Probing Surface Electrochemical Activity of Nanomaterials Using a Hybrid Atomic Force Microscope-Scanning Electrochemical Microscope (AFM-SECM)." *Journal of Visualized Experiments*, no. 168 (2021): e61111.

Shi, Xiaonan, Weihua Qing, Taha Marhaba, and Wen Zhang. "Atomic Force Microscopy-Scanning Electrochemical Microscopy (Afm-SECM) for Nanoscale Topographical and Electrochemical Characterization: Principles, Applications and Perspectives." *Electrochimica Acta* 332 (2020): 135472.

Shi, Yifeng, Zhiheng Lyu, Ming Zhao, Ruhui Chen, Quynh N Nguyen, and Younan Xia. "Noble-Metal Nanocrystals with Controlled Shapes for Catalytic and Electrocatalytic Applications." *Chemical Reviews* 121, no. 2 (2020): 649-735.

Shinde, Vaishali R, Tanaji P Gujar, Takeshi Noda, Daisuke Fujita, Ajayan Vinu, Mathieu Grandcolas, and Jinhua Ye. "Growth of Shape-and Size-Selective Zinc Oxide Nanorods by a Microwave-Assisted Chemical Bath Deposition Method: Effect on Photocatalysis Properties." *Chemistry–A European Journal* 16, no. 34 (2010): 10569-75.

Shnoudeh, Abeer Jabra, Islam Hamad, Ruwaida W Abdo, Lana Qadumii, Abdulmutallab Yousef Jaber, Hiba Salim Surchi, and Shahd Z Alkelany. "Synthesis, Characterization, and Applications of Metal Nanoparticles." In *Biomaterials and Bionanotechnology*, 527-612: Elsevier, 2019.

Si, Satyabrata, Cecile Leduc, Marie-Hélène Delville, and Brahim Lounis. "Short Gold Nanorod Growth Revisited: The Critical Role of the Bromide Counterion." *ChemPhysChem* 13, no. 1 (2012): 193-202.

Sianipar, Merry, Seung Hyun Kim, Ferry Iskandar, and I Gede Wenten. "Functionalized Carbon Nanotube (CNT) Membrane: Progress and Challenges." *RSC advances* 7, no. 81 (2017): 51175-98.

Siddiqi, Khwaja Salahuddin, Azamal Husen, and Rifaqat AK Rao. "A Review on Biosynthesis of Silver Nanoparticles and Their Biocidal Properties." *Journal of Nanobiotechnology* 16, no. 1 (2018): 1-28.

Sikder, Mithun, Jamie R Lead, G Thomas Chandler, and Mohammed Baalousha. "A Rapid Approach for Measuring Silver Nanoparticle Concentration and Dissolution in Seawater by Uv–Vis." *Science of the Total Environment* 618 (2018): 597-607.

Singh, Abhishek, Wen-Che Hou, Tsair-Fuh Lin, and Richard G Zepp. "Roles of Silver–Chloride Complexations in Sunlight-Driven Formation of Silver Nanoparticles." *Environmental Science and Technology* 53, no. 19 (2019): 11162-69.

Singh, Ashwani Kumar, Mahe Talat, DP Singh, and ON Srivastava. "Biosynthesis of Gold and Silver Nanoparticles by Natural Precursor Clove and Their Functionalization with Amine Group." *Journal of Nanoparticle Research* 12, no. 5 (2010): 1667-75.

Son, Dong-Jin, Woo-Yeol Kim, Chan-Young Yun, Duk Chang, Dae-Gun Kim, Sung-Oun Chang, Jin-Ho Kim, *et al.* "Combination of Electrolysis Technology with Membrane for Wastewater Treatment in Rural Communities." *International Journal of Electrochemical Science* 9 (2014): 4548-57.

Song, Chengwen, Tonghua Wang, Huawei Jiang, Xiuyue Wang, Yiming Cao, and Jieshan Qiu. "Gas Separation Performance of C/CMs Membranes Derived from Poly (Furfuryl Alcohol)(PFA) with Different Chemical Structure." *Journal of Membrane Science* 361, no. 1-2 (2010): 22-27.

Song, Chengwen, Tonghua Wang, Yanqiu Pan, and Jieshan Qiu. "Preparation of Coal-Based Microfiltration Carbon Membrane and Application in Oily Wastewater Treatment." *Separation and Purification Technology* 51, no. 1 (2006): 80-84.

Song, Chengwen, Tonghua Wang, and Jieshan Qiu. "Preparation of C/CMs Composite Membranes Derived from Poly (Furfuryl Alcohol) Polymerized by Iodine Catalyst." *Desalination* 249, no. 2 (2009): 486-89.

Song, Chengwen, Tonghua Wang, Jieshan Qiu, Yiming Cao, and Tianxi Cai. "Effects of Carbonization Conditions on the Properties of Coal-Based Microfiltration Carbon Membranes." *Journal of Porous Materials* 15, no. 1 (2008): 1-6.

Song, Chengwen, Tonghua Wang, Xiuyue Wang, Jieshan Qiu, and Yiming Cao. "Preparation and Gas Separation Properties of Poly (Furfuryl Alcohol)-Based C/CMs Composite Membranes." *Separation and Purification Technology* 58, no. 3 (2008): 412-18.

Song, Ji Mei, Hong Wang, Gang Hu, Shao Juan Zhao, Hai Qin Hu, and Bao Kang Jin. "$ZnWO_4$–Cu System with Enhanced Photocatalytic Activity by Photo-Fenton-Like Synergistic Reaction." *Materials Research Bulletin* 47, no. 11 (2012): 3296-300.

Song, Lili, Bo Zhu, Stephen Gray, Mikel Duke, and Shobha Muthukumaran. "Performance of Hybrid Photocatalytic-Ceramic Membrane System for the Treatment of Secondary Effluent." *Membranes* 7, no. 2 (2017): 20.

Song, Qichao, Chunguang Yang, and Chun-Ming Yu. "The Green One-Step Electrodeposition of Oxygen-Functionalized Porous G-C3N4 Decorated with Fe3 O4 Nanoparticles onto Ni-Foam as a Binder-Free Outstanding Material for Supercapacitors." *New Journal of Chemistry* 45, no. 2 (2021): 657-70.

Song, Rui-Qi, Helmut Cölfen, An-Wu Xu, Jürgen Hartmann, and Markus Antonietti. "Polyelectrolyte-Directed Nanoparticle Aggregation: Systematic Morphogenesis of Calcium Carbonate by Nonclassical Crystallization." *ACS Nano* 3, no. 7 (2009): 1966-78.

Song, Xu Chun, Yang Zhao, Yi Fan Zheng, E Yang, Jian Fu, and Yong He. "Fabrication of Ag/C Coaxial Nanocables with Cross-Linked Structure by Sds-Assisted Hydrothermal Approach." *Crystal Growth and Design* 8, no. 6 (2008): 1823-26.

Soon, Aloysius, Mira Todorova, Bernard Delley, and Catherine Stampfl. "Thermodynamic Stability and Structure of Copper Oxide Surfaces: A First-Principles Investigation." *Physical Review B* 75, no. 12 (2007): 125420.

Staples, C. A., P. B. Dorn, G. M. Klecka, S. T. O'Block, and L. R. Harris. "A Review of the Environmental Fate, Effects, and Exposures of Bisphenol A." *Chemosphere* 36, no. 10 (Apr 1998): 2149-73.

Starov, Victor M, and Vjacheslav G Zhdanov. "Effective Viscosity and Permeability of Porous Media." *Colloids and Surfaces A: Physicochemical and Engineering Aspects* 192, no. 1-3 (2001): 363-75.

Stebounova, Larissa V, Ethan Guio, and Vicki H Grassian. "Silver Nanoparticles in Simulated Biological Media: A Study of Aggregation, Sedimentation, and Dissolution." *Journal of Nanoparticle Research* 13, no. 1 (2011): 233-44.

Sugimoto, Tadao, Xingping Zhou, and Atsushi Muramatsu. "Synthesis of Uniform Anatase Tio2 Nanoparticles by Gel–Sol Method: 3. Formation Process and Size Control." *Journal of Colloid and Interface Science* 259, no. 1 (2003): 43-52.

Sukeri, Anandhakumar, Lucas Patricio Hernández Saravia, and Mauro Bertotti. "A Facile Electrochemical Approach to Fabricate a Nanoporous Gold Film Electrode and Its Electrocatalytic Activity Towards Dissolved Oxygen Reduction." *Physical Chemistry Chemical Physics* 17, no. 43 (2015): 28510-14.

Sun, Mei, Gregory V Lowry, and Kelvin B Gregory. "Selective Oxidation of Bromide in Wastewater Brines from Hydraulic Fracturing." *Water Research* 47, no. 11 (2013): 3723-31.

Sun, Meng, Xiaoxiong Wang, Lea R Winter, Yumeng Zhao, Wen Ma, Tayler Hedtke, Jae-Hong Kim, and Menachem Elimelech. "Electrified Membranes for Water Treatment Applications." *ACS Environmental Sicence and Technology Engineering* 1, no. 4 (2021): 725-52.

Sun, Pengzhan, Kunlin Wang, and Hongwei Zhu. "Recent Developments in Graphene-Based Membranes: Structure, Mass-Transport Mechanism and Potential Applications." *Advanced Materials* 28, no. 12 (2016): 2287-310.

Sun, Ping, Hui Liu, Mingbao Feng, Zhicai Zhai, Yingsen Fang, Xuesheng Zhang, and Virender K Sharma. "Strategic Combination of N-Doped Graphene and G-C3N4: Efficient Catalytic Peroxymonosulfate-Based Oxidation of Organic Pollutants by Non-Radical-Dominated Processes." *Applied Catalysis B: Environmental* 272 (2020): 119005.

Sun, Shaodong, Xiaojing Zhang, Qing Yang, Shuhua Liang, Xiaozhe Zhang, and Zhimao Yang. "Cuprous Oxide (Cu2O) Crystals with Tailored Architectures: A Comprehensive Review on Synthesis, Fundamental Properties, Functional Modifications and Applications." *Progress in Materials Science* 96 (2018): 111-73.

Sun, Wen, Hang Liu, Juncheng Hu, and Jinlin Li. "Controllable Synthesis and Morphology-Dependent Photocatalytic Performance of Anatase Tio 2 Nanoplates." *RSC Advances* 5, no. 1 (2015): 513-20.

Sun, Xiao, Ya-Wen Zhang, Ya-Ping Du, Zheng-Guang Yan, Rui Si, Li-Ping You, and Chun-Hua Yan. "From Trifluoroacetate Complex Precursors to Monodisperse Rare-Earth Fluoride and Oxyfluoride Nanocrystals with Diverse Shapes through Controlled Fluorination in Solution Phase." *Chemistry–A European Journal* 13, no. 8 (2007): 2320-32.

Sun, Yugang. "Controlled Synthesis of Colloidal Silver Nanoparticles in Organic Solutions: Empirical Rules for Nucleation Engineering." *Chemical Society Reviews* 42, no. 7 (2013): 2497-511.

Sung, Jongbaek, Back Kyu Choi, Byunghoon Kim, Byung Hyo Kim, Joodeok Kim, Donghoon Lee, Sungin Kim, *et al.* "Redox-Sensitive Facet Dependency in Etching of Ceria Nanocrystals Directly Observed by Liquid Cell Tem." *Journal of the American Chemical Society* 141, no. 46 (2019): 18395-99.

Tahri, Nouha, Ilyes Jedidi, Sophie Cerneaux, Marc Cretin, and Raja Ben Amar. "Development of an Asymmetric Carbon Microfiltration Membrane: Application to the Treatment of Industrial Textile Wastewater." *Separation and Purification Technology* 118 (2013): 179-87.

Tanaka, Shunsuke, Tomohisa Yasuda, Yugo Katayama, and Yoshikazu Miyake. "Pervaporation Dehydration Performance of Microporous Carbon Membranes Prepared from Resorcinol/Formaldehyde Polymer." *Journal of Membrane Science* 379, no. 1-2 (2011): 52-59.

Tao, Andrea R, Susan Habas, and Peidong Yang. "Shape Control of Colloidal Metal Nanocrystals." *Small* 4, no. 3 (2008): 310-25.

Tao, Ping, Yuanlu Xu, Chengwen Song, Yanyan Yin, Zaili Yang, Shihong Wen, Shiyu Wang, *et al.* "A Novel Strategy for the Removal of Rhodamine B (Rhb) Dye from Wastewater by Coal-Based Carbon Membranes Coupled with the Electric Field." *Separation and Purification Technology* 179 (2017): 175-83.

Tao, Wenyan, Dawei Pan, Zanhua Gong, and Xia Peng. "Nanoporous Platinum Electrode Grown on Anodic Aluminum Oxide Membrane: Fabrication, Characterization, Electrocatalytic Activity toward Reactive Oxygen and Nitrogen Species." *Analytica Chimica Acta* 1035 (2018): 44-50.

Thakkar, Kaushik N, Snehit S Mhatre, and Rasesh Y Parikh. "Biological Synthesis of Metallic Nanoparticles." *Nanomedicine: Nanotechnology, Biology and Medicine* 6, no. 2 (2010): 257-62.

Thamaraiselvan, Chidambaram, Avner Ronen, Sofia Lerman, Moran Balaish, Yair Ein-Eli, and Carlos G Dosoretz. "Low Voltage Electric Potential as a Driving Force to Hinder Biofouling in Self-Supporting Carbon Nanotube Membranes." *Water Research* 129 (2018): 143-53.

Thanh, Nguyen TK, N Maclean, and S Mahiddine. "Mechanisms of Nucleation and Growth of Nanoparticles in Solution." *Chemical Reviews* 114, no. 15 (2014): 7610-30.

Tian, Na, Zhi-You Zhou, Shi-Gang Sun, Yong Ding, and Zhong Lin Wang. "Synthesis of Tetrahexahedral Platinum Nanocrystals with High-Index Facets and High Electro-Oxidation Activity." *Science* 316, no. 5825 (2007): 732-35.

Tian, Yang, Haiqing Liu, Guohua Zhao, and Tetsu Tatsuma. "Shape-Controlled Electrodeposition of Gold Nanostructures." *The Journal of Physical Chemistry B* 110, no. 46 (2006): 23478-81.

Ting, Chao-Cheng, Chih-Hsuan Chao, Cheng Yu Tsai, I-Kai Cheng, and Fu-Ming Pan. "Electrocatalytic Performance of Pt Nanoparticles Sputter-Deposited on Indium Tin Oxide toward Methanol Oxidation Reaction: The Particle Size Effect." *Applied Surface Science* 416 (2017): 365-70.

Tran, Quang Huy, and Anh-Tuan Le. "Silver Nanoparticles: Synthesis, Properties, Toxicology, Applications and Perspectives." *Advances in Natural Sciences: Nanoscience and Nanotechnology* 4, no. 3 (2013): 033001.

Tran, Toan Trong, and Xianmao Lu. "Synergistic Effect of Ag and Pd Ions on Shape-Selective Growth of Polyhedral Au Nanocrystals with High-Index Facets." *The Journal of Physical Chemistry C* 115, no. 9 (2011): 3638-45.

Trautmann, AM, H Schell, KR Schmidt, K-M Mangold, and A Tiehm. "Electrochemical Degradation of Perfluoroalkyl and Polyfluoroalkyl Substances (PFASs) in Groundwater." *Water Science and Technology* 71, no. 10 (2015): 1569-75.

Trellu, Clément, Clémence Coetsier, Jean-Christophe Rouch, Roseline Esmilaire, Matthieu Rivallin, Marc Cretin, and Christel Causserand. "Mineralization of Organic Pollutants by Anodic Oxidation Using Reactive Electrochemical Membrane Synthesized from Carbothermal Reduction of TiO2." *Water Research* 131 (2018): 310-19.

Trellu, Clément, Matthieu Rivallin, Sophie Cerneaux, Clémence Coetsier, Christel Causserand, Mehmet A Oturan, and Marc Cretin. "Integration of Sub-Stoichiometric Titanium Oxide Reactive Electrochemical Membrane as Anode in the Electro-Fenton Process." *Chemical Engineering Journal* 400 (2020): 125936.

Tsui, Eliza M, Maria M Cortalezzi, and Mark R Wiesner. "Proton Conductivity and Methanol Rejection by Ceramic Membranes Derived from Ferroxane and Alumoxane Precursors." *Journal of Membrane Science* 306, no. 1-2 (2007): 8-15.

Tsuji, Masaharu, Satoshi Gomi, Yoshinori Maeda, Mika Matsunaga, Sachie Hikino, Keiko Uto, Takeshi Tsuji, and Hirofumi Kawazumi. "Rapid Transformation from Spherical Nanoparticles, Nanorods, Cubes, or Bipyramids to Triangular Prisms of Silver with Pvp, Citrate, and H2o2." *Langmuir* 28, no. 24 (2012): 8845-61.

Tsuji, Masaharu, Ryoichi Matsuo, Peng Jiang, Nobuhiro Miyamae, Daisuke Ueyama, Michiko Nishio, Sachie Hikino, *et al.* "Shape-Dependent Evolution of Au@Ag Core− Shell Nanocrystals by Pvp-Assisted N, N-Dimethylformamide Reduction." *Crystal Growth and Design* 8, no. 7 (2008): 2528-36.

Tsuji, Masaharu, Nobuhiro Miyamae, Masayuki Hashimoto, Michiko Nishio, Sachie Hikino, Naoki Ishigami, and Izumi Tanaka. "Shape and Size Controlled Synthesis of Gold Nanocrystals Using Oxidative Etching by AuCl4− and Cl− Anions in Microwave-Polyol Process." *Colloids and Surfaces A: Physicochemical and Engineering Aspects* 302, no. 1-3 (2007): 587-98.

Tsuji, Masaharu, Michiko Nishio, Peng Jiang, Nobuhiro Miyamae, Seongyop Lim, Kisei Matsumoto, Daisuke Ueyama, and Xin-Ling Tang. "Role of Chloride Ions in the Formation of Au@ Ag Core–Shell Nanocrystal Structures by Using a Microwave–Polyol Method." *Colloids and Surfaces A: Physicochemical and Engineering Aspects* 317, no. 1-3 (2008): 247-55.

Ullah, Md Habib, Il Kim, and Chang-Sik Ha. "One-Step Synthetic Route for Producing Nanoslabs: Zn-Oriented Polycrystalline and Single-Crystalline Zinc Oxide." *Journal of Materials Science* 41, no. 11 (2006): 3263-69.

Vance, Marina E, Todd Kuiken, Eric P Vejerano, Sean P McGinnis, Michael F Hochella Jr, David Rejeski, and Matthew S Hull. "Nanotechnology in the Real World: Redeveloping the Nanomaterial Consumer Products Inventory." *Beilstein Journal of Nanotechnology* 6, no. 1 (2015): 1769-80.

Vatanpour, Vahid, Sayed Siavash Madaeni, Laleh Rajabi, Sirus Zinadini, and Ali Ashraf Derakhshan. "Boehmite Nanoparticles as a New Nanofiller for Preparation of Antifouling Mixed Matrix Membranes." *Journal of Membrane Science* 401–402 (2012): 132-43.

Vecitis, Chad D, Guandao Gao, and Han Liu. "Electrochemical Carbon Nanotube Filter for Adsorption, Desorption, and Oxidation of Aqueous Dyes and Anions." *The Journal of Physical Chemistry C* 115, no. 9 (2011): 3621-29.

Wagle, Durgesh V, Hua Zhao, and Gary A Baker. "Deep Eutectic Solvents: Sustainable Media for Nanoscale and Functional Materials." *Accounts of Chemical Research* 47, no. 8 (2014): 2299-308.

Wallace, Gordon, and Geoffrey Spinks. "Conducting Polymers–Bridging the Bionic Interface." *Soft Matter* 3, no. 6 (2007): 665-71.

Walsh, FC, and RGA Wills. "The Continuing Development of Magnéli Phase Titanium Sub-Oxides and Ebonex® Electrodes." *Electrochimica Acta* 55, no. 22 (2010): 6342-51.

Wan, Yu, Zhirui Guo, Xiaoli Jiang, Kun Fang, Xiang Lu, Yu Zhang, and Ning Gu. "Quasi-Spherical Silver Nanoparticles: Aqueous Synthesis and Size Control by the Seed-Mediated Lee–Meisel Method." *Journal of Colloid and Interface Science* 394 (2013): 263-68.

Wang, Changhua, Xintong Zhang, Yanli Zhang, Yan Jia, Bo Yuan, Jikai Yang, Panpan Sun, and Yichun Liu. "Morphologically-Tunable TiO2 Nanorod Film with High Energy Facets: Green Synthesis, Growth Mechanism and Photocatalytic Activity." *Nanoscale* 4, no. 16 (2012): 5023-30.

Wang, Dengjun, Navid B Saleh, Wenjie Sun, Chang Min Park, Chongyang Shen, Nirupam Aich, Willie JGM Peijnenburg, *et al.* "Next-Generation Multifunctional Carbon–Metal Nanohybrids for Energy and Environmental Applications." *Environmental Science and Technology* 53, no. 13 (2019): 7265-87.

Wang, Hailiang, and Hongjie Dai. "Strongly Coupled Inorganic–Nano-Carbon Hybrid Materials for Energy Storage." *Chemical Society Reviews* 42, no. 7 (2013): 3088-113.

Wang, Hui, Hong Wang, Jianxin Li, Deshan Bin, Zhen Yin, Jianli Kang, and Benqiao He. "An Electrocatalytic Reactor for the High Selectivity Production of Sodium 2, 2, 3, 3-Tetrafluoropropionate from 2, 2, 3, 3-Tetrafluoro-1-Propanol." *Electrochimica Acta* 123 (2014): 33-41.

Wang, Jie, Fangling Cui, Sibin Chu, Xiaoquan Jin, Jun Pu, and Zhenghua Wang. "In Situ Growth of Noble-Metal Nanoparticles on Cu2O Nanocubes for Surface-Enhanced Raman Scattering Detection." *ChemPlusChem* 79, no. 5 (2014): 684-89.

Wang, Jing, Sichao Hou, Lizhao Zhang, Jincai Chen, and Lan Xiang. "Ultra-Rapid Formation of Zno Hierarchical Structures from Dilution-Induced Supersaturated Solutions." *CrystEngComm* 16, no. 30 (2014): 7115-23.

Wang, Lin-Xia, Xin-Gui Li, and Yu-Liang Yang. "Preparation, Properties and Applications of Polypyrroles." *Reactive and Functional Polymers* 47, no. 2 (2001): 125-39.

Wang, Sheng-Chang, Ray-Kuang Chiang, and Pin-Jie Hu. "Morphological and Phase Control of Tin Oxide Single-Crystals Synthesized by Dissolution and Recrystallization of Bulk SnO Powders." *Journal of the European Ceramic Society* 31, no. 14 (2011): 2447-51.

Wang, Shengping, Changjiang Li, Tuo Wang, Peng Zhang, Ang Li, and Jinlong Gong. "Controllable Synthesis of Nanotube-Type Graphitic C3N4 and Their Visible-Light Photocatalytic and Fluorescent Properties." *Journal of Materials Chemistry A* 2, no. 9 (2014): 2885-90.

Wang, Tonghua, Bing Zhang, Jieshan Qiu, Yonghong Wu, Shouhai Zhang, and Yiming Cao. "Effects of Sulfone/Ketone in Poly (Phthalazinone Ether Sulfone Ketone) on the Gas Permeation of Their Derived Carbon Membranes." *Journal of Membrane Science* 330, no. 1-2 (2009): 319-25.

Wang, Wei, Jane Y Howe, Yuan Li, Xiaofeng Qiu, David C Joy, M Parans Paranthaman, Mitchel J Doktycz, and Baohua Gu. "A Surfactant and Template-Free Route for Synthesizing Ceria Nanocrystals with Tunable Morphologies." *Journal of Materials Chemistry* 20, no. 36 (2010): 7776-81.

Wang, Xiaoxiong, Meng Sun, Yumeng Zhao, Chi Wang, Wen Ma, Michael S Wong, and Menachem Elimelech. "In Situ Electrochemical Generation of Reactive Chlorine Species for Efficient Ultrafiltration Membrane Self-Cleaning." *Environmental Science and Technology* 54, no. 11 (2020): 6997-7007.

Wang, Xixi, Maochang Liu, Zhaohui Zhou, and Liejin Guo. "Toward Facet Engineering of Cds Nanocrystals and Their Shape-Dependent Photocatalytic Activities." *The Journal of Physical Chemistry C* 119, no. 35 (2015/09/03 2015): 20555-60.

Wang, ZY, QF Lu, XS Fang, XK Tian, and LD Zhang. "Manipulation of the Morphology of CdSe Nanostructures." *Advanced Functional Materials* 16, no. 5 (2006): 661-66.

Wei, Gaoliang, Xie Quan, Xinfei Fan, Shuo Chen, and Yaobin Zhang. "Carbon-Nanotube-Based Sandwich-Like Hollow Fiber Membranes for Expanded Microcystin-Lr Removal Applications." *Chemical Engineering Journal* 319 (2017): 212-18.

Wei, Kajia, Chenyang Shen, Weiqing Han, Jiansheng Li, Xiuyun Sun, Jinyou Shen, and Lianjun Wang. "Advance Treatment of Chemical Industrial Tailwater by Integrated Electrochemical Technologies: Electrocatalysis, Electrodialysis and Electro-Microfiltration." *Chemical Engineering Journal* 310 (2017): 13-21.

Wei, Wei, Shubin Yang, Haixin Zhou, Ingo Lieberwirth, Xinliang Feng, and Klaus Müllen. "3d Graphene Foams Cross-Linked with Pre-Encapsulated Fe3O4 Nanospheres for Enhanced Lithium Storage." *Advanced Materials* 25, no. 21 (2013): 2909-14.

Wei, Xin, Hong Wang, Zhen Yin, Saood Qaseem, and Jianxin Li. "Tubular Electrocatalytic Membrane Reactor for Alcohol Oxidation: Cfd Simulation and Experiment." *Chinese Journal of Chemical Engineering* 25, no. 1 (2017): 18-25.

Weir, Alex, Paul Westerhoff, Lars Fabricius, Kiril Hristovski, and Natalie Von Goetz. "Titanium Dioxide Nanoparticles in Food and Personal Care Products." *Environmental Science and Technology* 46, no. 4 (2012): 2242-50.

Wen, Jiuqing, Jun Xie, Xiaobo Chen, and Xin Li. "A Review on G-C3N4-Based Photocatalysts." *Applied Surface Science* 391 (2017): 72-123.

Weon, Seunghyun, Min-Jeong Suh, Chiheng Chu, Dahong Huang, Eli Stavitski, and Jae-Hong Kim. "Site-Selective Loading of Single-Atom Pt on TiO2 for Photocatalytic Oxidation and Reductive Hydrodefluorination." *ACS Environmental Science and Technology Engineering* 1, no. 3 (2021): 512-22.

Werner, Craig M, Krishna P Katuri, Ananda Rao Hari, Wei Chen, Zhiping Lai, Bruce E Logan, Gary L Amy, and Pascal E Saikaly. "Graphene-Coated Hollow Fiber Membrane as the Cathode in Anaerobic Electrochemical Membrane Bioreactors–Effect of Configuration and Applied Voltage on Performance and Membrane Fouling." *Environmental Science and Technology* 50, no. 8 (2016): 4439-47.

Wiesner, Mark R, Greg V Lowry, Pedro Alvarez, Dianysios Dionysiou, and Pratim Biswas. "Assessing the Risks of Manufactured Nanomaterials." ACS Publications, 2006.

Wiesner, Mark R, Gregory V Lowry, Kimberly L Jones, Jr Hochella, Michael F, Richard T Di Giulio, Elizabeth Casman, and Emily S Bernhardt. "Decreasing Uncertainties in Assessing Environmental Exposure, Risk, and Ecological Implications of Nanomaterials." ACS Publications, 2009.

Wiley, Benjamin, Yugang Sun, and Younan Xia. "Synthesis of Silver Nanostructures with Controlled Shapes and Properties." *Accounts of Chemical Research* 40, no. 10 (2007): 1067-76.

Windler, L, Christiane Lorenz, Natalie von Goetz, K Hungerbuhler, M Amberg, M Heuberger, and Bernd Nowack. "Release of Titanium Dioxide from Textiles During Washing." *Environmental Science and Technology* 46, no. 15 (2012): 8181-88.

Wu, Donghai, Guanghua Lu, Ran Zhang, Qiuhong Lin, Zhenhua Yan, Jianchao Liu, and Yi Li. "Enhanced Hydroxyl Radical Generation in the Combined Ozonation and Electrolysis Process Using Carbon Nanotubes Containing Gas Diffusion Cathode." *Environmental Science and Pollution Research* 22, no. 20 (2015): 15812-20.

Wu, Hongli, Xiaohui Ji, Lili Zhao, Shuang Yang, Renguo Xie, and Wensheng Yang. "Shape Evolution of Citrate Capped Gold Nanoparticles in Seeding Approach." *Colloids and Surfaces A: Physicochemical and Engineering Aspects* 415 (2012): 174-79.

Wu, Tiantian, Núria López, Tejs Vegge, and Heine Anton Hansen. "Facet-Dependent Electrocatalytic Water Splitting Reaction on CeO2: A DFT+U Study." *Journal of Catalysis* 388 (2020): 1-10.

Wu, Wei, Changzhong Jiang, and Vellaisamy AL Roy. "Recent Progress in Magnetic Iron Oxide–Semiconductor Composite Nanomaterials as Promising Photocatalysts." *Nanoscale* 7, no. 1 (2015): 38-58.

Wu, Wei, Zhaohui Wu, Taekyung Yu, Changzhong Jiang, and Woo-Sik Kim. "Recent Progress on Magnetic Iron Oxide Nanoparticles: Synthesis, Surface Functional Strategies and Biomedical Applications." *Science and Technology of Advanced Materials* 16, no. 2 (2015): 023501.

Wu, Wei, Xiangheng Xiao, Shaofeng Zhang, Juan Zhou, Lixia Fan, Feng Ren, and Changzhong Jiang. "Large-Scale and Controlled Synthesis of Iron Oxide Magnetic Short Nanotubes: Shape Evolution, Growth Mechanism, and Magnetic Properties." *The Journal of Physical Chemistry C* 114, no. 39 (2010): 16092-103.

Wu, YZ, M Chen, XH Yan, J Ren, Y Dai, JJ Wang, JM Pan, YP Wang, and XN Cheng. "Hydrothermal Synthesis of Fe3o4 Nanorods/Graphitic C3N4 Composite with Enhanced Supercapacitive Performance." *Materials Letters* 198 (2017): 114-17.

Wu, Zhaohui, Shuanglei Yang, and Wei Wu. "Shape Control of Inorganic Nanoparticles from Solution." *Nanoscale* 8, no. 3 (2016): 1237-59.

Xia, Kai, Liming Zhang, Yuanfu Huang, and Zhuoxuan Lu. "Preparation of Gold Nanorods and Their Applications in Photothermal Therapy." *Journal of Nanoscience and Nanotechnology* 15, no. 1 (2015): 63-73.

Xiang, Jiayuan, Zhewei Chen, and Jianming Wang. "Octahedral Core–Shell Cuprous Oxide/Carbon with Enhanced Electrochemical Activity and Stability as Anode for Lithium Ion Batteries." *Materials Research Bulletin* 70 (2015): 456-60.

Xie, Jiangzhou, Jinxing Ma, Shixin Zhao, and T David Waite. "Flow Anodic Oxidation: Towards High-Efficiency Removal of Aqueous Contaminants by Adsorbed Hydroxyl Radicals at 1.5 V Vs She." *Water Research* 200 (2021): 117259.

Xie, Shuifen, Xiang Yang Liu, and Younan Xia. "Shape-Controlled Syntheses of Rhodium Nanocrystals for the Enhancement of Their Catalytic Properties." *Nano Research* 8, no. 1 (2015): 82-96.

Xing, Ruimin, Fenglan Xu, Shanhu Liu, and Jingyang Niu. "Surfactant-Free Fabrication of Fe3o4 Nanospheres with Selective Shape." *Materials Letters* 134 (2014): 71-74.

Xu, Anlin, Xiang Dai, Kajia Wei, Weiqing Han, Jiansheng Li, Xiuyun Sun, Jinyou Shen, and Lianjun Wang. "Preparation and Characterization of a TiO2-Nt/SnO2–Sb Tubular Porous Electrode with Long Service Lifetime for Wastewater Treatment Process." *RSC Advances* 7, no. 60 (2017): 37806-14.

Xu, Haolan, Wenzhong Wang, and Wei Zhu. "Shape Evolution and Size-Controllable Synthesis of Cu2O Octahedra and Their Morphology-Dependent Photocatalytic Properties." *The Journal of Physical Chemistry B* 110, no. 28 (2006): 13829-34.

Xu, Li, Li-Shun Du, Cun Wang, and Wei Xu. "Nanofiltration Coupled with Electrolytic Oxidation in Treating Simulated Dye Wastewater." *Journal of Membrane Science* 409 (2012): 329-34.

Xu, Li, Zhi Guo, Lishun Du, and Jing He. "Decolourization and Degradation of Citic Acid by Anodic Oxidation and the Synergy Technology of Anodic Oxidation Coupling Nanofiltration." *Electrochimica Acta* 97 (2013): 150-59.

Xu, Li, Yukuan Sun, Lishun Du, and Jiejing Zhang. "Removal of Tetracycline Hydrochloride from Wastewater by Nanofiltration Enhanced by Electro-Catalytic Oxidation." *Desalination* 352 (2014): 58-65.

Xu, Li, Yi-Yi Wang, Jie Huang, Chun-Yuan Chen, Zhen-Xing Wang, and Hui Xie. "Silver Nanoparticles: Synthesis, Medical Applications and Biosafety." *Theranostics* 10, no. 20 (2020): 8996.

Xu, Li, Lichao Zhang, Lishun Du, and Shaoxing Zhang. "Electro-Catalytic Oxidation in Treating Wastewater Coupled with Nanofiltration and Energy Consumption Analysis." *Journal of Membrane Science* 452 (2014): 1-10.

Xu, Lin, Xiaoyan Yang, Zheng Zhai, Xing Chao, Zihui Zhang, and Wenhua Hou. "Edta-Mediated Hydrothermal Synthesis of Naeu (MoO4)2 Microrugbies with Tunable Size and Enhanced Luminescence Properties." *CrystEngComm* 13, no. 15 (2011): 4921-29.

Xu, Zhi-Chuan, Cheng-Min Shen, Cong-Wen Xiao, Tian-Zhong Yang, Huai-Ruo Zhang, Jian-Qi Li, Hu-Lin Li, and Hong-Jun Gao. "Wet Chemical Synthesis of Gold Nanoparticles Using Silver Seeds: A Shape Control from Nanorods to Hollow Spherical Nanoparticles." *Nanotechnology* 18, no. 11 (2007): 115608.

Yahya, N, Siti Kartom Kamarudin, NA Karim, MS Masdar, KS Loh, and KL Lim. "Durability and Performance of Direct Glycerol Fuel Cell with Palladium-Aurum/Vapor Grown Carbon Nanofiber Support." *Energy Conversion and Management* 188 (2019): 120-30.

Yang, Bin, Ping Geng, and Guohua Chen. "One-Dimensional Structured IrO2 Nanorods Modified Membrane for Electrochemical Anti-Fouling in Filtration of Oily Wastewater." *Separation and Purification Technology* 156 (2015): 931-41.

Yang, Kui, Jiale Xu, Hui Lin, Ruzhen Xie, Kai Wang, Sihao Lv, Jianbo Liao, *et al.* "Developing a Low-Pressure and Super Stable Electrochemical Tubular Reactive Filter: Outstanding Efficiency for Wastewater Purification." *Electrochimica Acta* 335 (2020): 135634.

Yang, Tung-Han, Jaewan Ahn, Shi Shi, Peng Wang, Ruoqi Gao, and Dong Qin. "Noble-Metal Nanoframes and Their Catalytic Applications." *Chemical Reviews* 121, no. 2 (2020): 796-833.

Yang, Yang, and Michael R Hoffmann. "Synthesis and Stabilization of Blue-Black Tio2 Nanotube Arrays for Electrochemical Oxidant Generation and Wastewater Treatment." *Environmental Science and Technology* 50, no. 21 (2016): 11888-94.

Yang, Yang, Han Wang, Zhen Ji, Yongsheng Han, and Jinghai Li. "A Switch from Classic Crystallization to Non-Classic Crystallization by Controlling the Diffusion of Chemicals." *CrystEngComm* 16, no. 33 (2014): 7633-37.

Yang, Yong, Yan Liang, Guozhong Wang, Liangliang Liu, Cailei Yuan, Ting Yu, Qinliang Li, Fanyan Zeng, and Gang Gu. "Enhanced Gas-Sensing Properties of the Hierarchical Tio2 Hollow Microspheres with Exposed High-Energy {001} Crystal Facets." *ACS Applied Materials and Interfaces* 7, no. 44 (2015): 24902-08.

Yang, Yue, Sen Qiao, Ruofei Jin, Jiti Zhou, and Xie Quan. "Fouling Control Mechanisms in Filtrating Natural Organic Matters by Electro-Enhanced Carbon Nanotubes Hollow Fiber Membranes." *Journal of Membrane Science* 553 (2018): 54-62.

Yaqoob, Asim Ali, Khalid Umar, and Mohamad Nasir Mohamad Ibrahim. "Silver Nanoparticles: Various Methods of Synthesis, Size Affecting Factors and Their Potential Applications–a Review." *Applied Nanoscience* 10, no. 5 (2020): 1369-78.

Yeap, Swee Pin, Pey Yi Toh, Abdul Latif Ahmad, Siew Chun Low, Sara A Majetich, and JitKang Lim. "Colloidal Stability and Magnetophoresis of Gold-Coated Iron Oxide Nanorods in Biological Media." *The Journal of Physical Chemistry C* 116, no. 42 (2012): 22561-69.

Yin, An-Xiang, Xiao-Quan Min, Ya-Wen Zhang, and Chun-Hua Yan. "Shape-Selective Synthesis and Facet-Dependent Enhanced Electrocatalytic Activity and Durability of Monodisperse Sub-10 Nm Pt− Pd Tetrahedrons and Cubes." *Journal of the American Chemical Society* 133, no. 11 (2011): 3816-19.

Yin, Xiafei, Xiufen Li, Zhaozhe Hua, and Yueping Ren. "The Growth Process of the Cake Layer and Membrane Fouling Alleviation Mechanism in a Mbr Assisted with the Self-Generated Electric Field." *Water Research* 171 (2020): 115452.

Yin, Xiaoju, GS Zhu, Weishen Yang, Yanshuo Li, GQ Zhu, Rui Xu, Jinyu Sun, Shilun Qiu, and RR Xu. "Stainless-Steel-Net-Supported Zeolite Naa Membrane with High Permeance and High Permselectivity of Oxygen over Nitrogen." *Advanced Materials* 17, no. 16 (2005): 2006-10.

Yin, Yanyan, Chen Li, Chengwen Song, Ping Tao, Menghan Sun, Zonglin Pan, Tonghua Wang, and Mihua Shao. "The Design of Coal-Based Carbon Membrane Coupled with the Electric Field and Its Application on the Treatment of Malachite Green (Mg) Aqueous Solution." *Colloids and Surfaces A: Physicochemical and Engineering Aspects* 506 (2016): 629-36.

Yin, Zhen, Yumei Zheng, Hong Wang, Jianxin Li, Qingjun Zhu, Ye Wang, Na Ma, *et al.* "Engineering Interface with One-Dimensional Co3O4 Nanostructure in Catalytic Membrane Electrode: Toward an Advanced Electrocatalyst for Alcohol Oxidation." *ACS Nano* 11, no. 12 (2017): 12365-77.

Ying, Yulong, Yefeng Yang, Wen Ying, and Xinsheng Peng. "Two-Dimensional Materials for Novel Liquid Separation Membranes." *Nanotechnology* 27, no. 33 (2016): 332001.

Ying, Yulong, Wen Ying, Qiaochu Li, Donghui Meng, Guohua Ren, Rongxin Yan, and Xinsheng Peng. "Recent Advances of Nanomaterial-Based Membrane for Water Purification." *Applied Materials Today* 7 (2017): 144-58.

Yong, Ken-Tye, Yudhisthira Sahoo, Mark T Swihart, and Paras N Prasad. "Shape Control of Cds Nanocrystals in One-Pot Synthesis." *The Journal of Physical Chemistry C* 111, no. 6 (2007): 2447-58.

You, Shijie, Bo Liu, Yifan Gao, Yu Wang, Chuyang Y Tang, Yibing Huang, and Nanqi Ren. "Monolithic Porous Magnéli-Phase Ti4O7 for Electro-Oxidation Treatment of Industrial Wastewater." *Electrochimica Acta* 214 (2016): 326-35.

You, Tingting, Li Jiang, Penggang Yin, Yang Shang, Dongfeng Zhang, Lin Guo, and Shihe Yang. "Direct Observation of P, P′-Dimercaptoazobenzene Produced from P-Aminothiophenol and P-Nitrothiophenol on Cu2O Nanoparticles by Surface-Enhanced Raman Spectroscopy." *Journal of Raman Spectroscopy* 45, no. 1 (2014): 7-14.

Yu, Mei, Xueke Wu, Jindan Zhang, Yanbing Meng, Yuxiao Ma, Jianhua Liu, and Songmei Li. "Platinum Nanoparticles-Loaded Holey Reduced Graphene Oxide Framework as Freestanding Counter Electrodes of Dye Sensitized Solar Cells and Methanol Oxidation Catalysts." *Electrochimica Acta* 258 (2017): 485-94.

Yu, Yue, Qingbo Zhang, Xianmao Lu, and Jim Yang Lee. "Seed-Mediated Synthesis of Monodisperse Concave Trisoctahedral Gold Nanocrystals with Controllable Sizes." *The Journal of Physical Chemistry C* 114, no. 25 (2010): 11119-26.

Zakersalehi, Abolfazl, Hyeok Choi, Joel Andersen, and Dionysios D Dionysiou. "Photocatalytic Ceramic Membranes." *Encyclopedia of Membrane Science and Technology* (2013).

Zaky, Amr M, and Brian P Chaplin. "Mechanism of P-Substituted Phenol Oxidation at a Ti4o7 Reactive Electrochemical Membrane." *Environmental science and technology* 48, no. 10 (2014): 5857-67.

Zen, Jyh-Myng, Yue-Shian Song, Hsieh-Hsun Chung, Cheng-Teng Hsu, and Annamalai Senthil Kumar. "Photoelectrochemical Oxygen Sensor Using Copper-Plated Screen-Printed Carbon Electrodes." *Analytical Chemistry* 74, no. 23 (2002): 6126-30.

Zeng, Shuwen, Dominique Baillargeat, Ho-Pui Ho, and Ken-Tye Yong. "Nanomaterials Enhanced Surface Plasmon Resonance for Biological and Chemical Sensing Applications." *Chemical Society Reviews* 43, no. 10 (2014): 3426-52.

Zhang, Bing, Tonghua Wang, Yonghong Wu, Qingling Liu, Shili Liu, Shouhai Zhang, and Jieshan Qiu. "Preparation and Gas Permeation of Composite Carbon Membranes from Poly (Phthalazinone Ether Sulfone Ketone)." *Separation and Purification Technology* 60, no. 3 (2008): 259-63.

Zhang, Changyong, Di He, Jinxing Ma, and T David Waite. "Active Chlorine Mediated Ammonia Oxidation Revisited: Reaction Mechanism, Kinetic Modelling and Implications." *Water Rresearch* 145 (2018): 220-30.

Zhang, Chao, Zhe Li, Shou Zhen Jiang, Chong Hui Li, Shi Cai Xu, Jing Yu, Zhen Li, *et al.* "U-Bent Fiber Optic Spr Sensor Based on Graphene/Agnps." *Sensors and Actuators B: Chemical* 251 (2017): 127-33.

Zhang, Chiqian, Zhiqiang Hu, and Baolin Deng. "Silver Nanoparticles in Aquatic Environments: Physiochemical Behavior and Antimicrobial Mechanisms." *Water Research* 88 (2016): 403-27.

Zhang, Dong-Feng, Hua Zhang, Lin Guo, Kun Zheng, Xiao-Dong Han, and Ze Zhang. "Delicate Control of Crystallographic Facet-Oriented Cu2O Nanocrystals and the Correlated Adsorption Ability." *Journal of Materials Chemistry* 19, no. 29 (2009): 5220-25.

Zhang, HUI, Mingshang Jin, Yujie Xiong, Byungkwon Lim, and Younan Xia. "Shape-Controlled Synthesis of Pd Nanocrystals and Their Catalytic Applications." *Accounts of Chemical Research* 46, no. 8 (2012): 1783-94.

Zhang, Huigang, Qingshan Zhu, Yang Zhang, Yong Wang, Li Zhao, and Bin Yu. "One-Pot Synthesis and Hierarchical Assembly of Hollow Cu2o Microspheres with Nanocrystals-Composed Porous Multishell and Their Gas-Sensing Properties." *Advanced Functional Materials* 17, no. 15 (2007): 2766-71.

Zhang, Jianhui, Huaiyong Liu, Zhenlin Wang, and Naiben Ming. "Synthesis of Gold Regular Octahedra with Controlled Size and Plasmon Resonance." *Applied Physics Letters* 90, no. 16 (2007): 163122.

Zhang, Jiatao, Junfeng Liu, Qing Peng, Xun Wang, and Yadong Li. "Nearly Monodisperse Cu2O and CuO Nanospheres: Preparation and Applications for Sensitive Gas Sensors." *Chemistry of Materials* 18, no. 4 (2006): 867-71.

Zhang, Kuibo, Shoutao Gong, Baolin Zhao, Yanxiang Liu, Naeem Akhtar Qaisrani, Lingdong Li, Fengxiang Zhang, and Gaohong He. "Bent-Twisted Block Copolymer Anion Exchange Membrane with Improved Conductivity." *Journal of Membrane Science* 550 (2018): 59-71.

Zhang, Lichao, Li Xu, Jing He, and Jiejing Zhang. "Preparation of Ti/SnO2-Sb Electrodes Modified by Carbon Nanotube for Anodic Oxidation of Dye Wastewater and Combination with Nanofiltration." *Electrochimica Acta* 117 (2014): 192-201.

Zhang, Liming, Kai Xia, Zhuoxuan Lu, Guopeng Li, Juan Chen, Yan Deng, Song Li, Feimeng Zhou, and Nongyue He. "Efficient and Facile Synthesis of Gold Nanorods with Finely Tunable Plasmonic Peaks from Visible to near-Ir Range." *Chemistry of Materials* 26, no. 5 (2014): 1794-98.

Zhang, Milin, Juan Li, Huaju Li, Yong Li, and Wenjie Shen. "Morphology-Dependent Redox and Catalytic Properties of CeO2 Nanostructures: Nanowires, Nanorods and Nanoparticles." *Catalysis Today* 148, no. 1 (2009): 179-83.

Zhang, Qiao, Na Li, James Goebl, Zhenda Lu, and Yadong Yin. "A Systematic Study of the Synthesis of Silver Nanoplates: Is Citrate a “Magic” Reagent?". *Journal of the American Chemical Society* 133, no. 46 (2011): 18931-39.

Zhang, Qiaoying, and Chad D Vecitis. "Conductive Cnt-Pvdf Membrane for Capacitive Organic Fouling Reduction." *Journal of Membrane Science* 459 (2014): 143-56.

Zhang, Qingbo, Jianping Xie, Jing Liang, and Jim Yang Lee. "Synthesis of Monodisperse Ag Au Alloy Nanoparticles with Independently Tunable Morphology, Composition, Size, and Surface Chemistry and Their 3-D Superlattices." *Advanced Functional Materials* 19, no. 9 (2009): 1387-98.

Zhang, Qingfeng, and Hui Wang. "Facet-Dependent Catalytic Activities of Au Nanoparticles Enclosed by High-Index Facets." *ACS Catalysis* 4, no. 11 (2014): 4027-33.

Zhang, Runnan, Yanan Liu, Mingrui He, Yanlei Su, Xueting Zhao, Menachem Elimelech, and Zhongyi Jiang. "Antifouling Membranes for Sustainable Water Purification: Strategies and Mechanisms." *Chemical Society Reviews* 45, no. 21 (2016): 5888-924.

Zhang, Teng Yun, You Yuan Shao, Jian Chen, and Hong Bo Fan. "Study and Preparation of Electrocatalytic Ceramic Membrane Electrode." Paper presented at the Advanced Materials Research, 2011.

Zhang, Wen, Andrew G Stack, and Yongsheng Chen. "Interaction Force Measurement between E. Coli Cells and Nanoparticles Immobilized Surfaces by Using Afm." *Colloids and Surfaces B: Biointerfaces* 82, no. 2 (2011): 316-24.

Zhang, Wen, Ying Yao, and Yongsheng Chen. "Imaging and Quantifying the Morphology and Nanoelectrical Properties of Quantum Dot Nanoparticles Interacting with DNA." *The Journal of Physical Chemistry C* 115, no. 3 (2011): 599-606.

Zhang, Wen, Ying Yao, Nicole Sullivan, and Yongsheng Chen. "Modeling the Primary Size Effects of Citrate-Coated Silver Nanoparticles on Their Ion Release Kinetics." *Environmental Science and Technology* 45, no. 10 (2011): 4422-28.

Zhang, Xia, Yang Wang, Yufeng Liu, Junli Xu, Yide Han, and Xinxin Xu. "Preparation, Performances of Pvdf/Zno Hybrid Membranes and Their Applications in the Removal of Copper Ions." *Applied Surface Science* 316 (2014): 333-40.

Zhang, Xiangyu, Mingqiang Wang, and Jijun Ding. "Shape-Selective Synthesis, Characterization and Upconversion Improvement of Yb3+/Er3+ Doped Liyf 4 Microphosphors through Ph Tuning." *RSC Advances* 4, no. 55 (2014): 29165-72.

Zhang, Xiaofeng, Yi Zhang, Huodi Huang, Jiannan Cai, Kaining Ding, and Shen Lin. "Electrochemical Fabrication of Shape-Controlled Cu2O with Spheres, Octahedrons and Truncated Octahedrons and Their Electrocatalysis for Orr." *New Journal of Chemistry* 42, no. 1 (2018): 458-64.

Zhang, Xuezhi, Qiang Hu, Milton Sommerfeld, Emil Puruhito, and Yongsheng Chen. "Harvesting Algal Biomass for Biofuels Using Ultrafiltration Membranes." *Bioresource Technology* 101, no. 14 (2010): 5297-304.

Zhang, Yejun, Yaping Du, Huarui Xu, and Qiangbin Wang. "Diverse-Shaped Iron Sulfide Nanostructures Synthesized from a Single Source Precursor Approach." *CrystEngComm* 12, no. 11 (2010): 3658-63.

Zhang, Yimei, Zhuang Chen, Lincheng Zhou, Panpan Wu, Yalong Zhao, Yuxian Lai, Fei Wang, and Shuai Li. "Efficient Electrochemical Degradation of Tetrabromobisphenol a Using Mno2/Mwcnt Composites Modified Ni Foam as Cathode: Kinetic Analysis, Mechanism and Degradation Pathway." *Journal of Hazardous Materials* 369 (2019): 770-79.

Zhang, Yiming, Linda Zou, Bradley P Ladewig, and Dennis Mulcahy. "Synthesis and Characterisation of Superhydrophilic Conductive Heterogeneous Pani/Pvdf Anion-Exchange Membranes." *Desalination* 362 (2015): 59-67.

Zhang, Yujun, Yubo Qi, Zhen Yin, Hong Wang, Benqiao He, Xiaoping Liang, Jianxin Li, and Zhenhuan Li. "Nano-V2O5/Ti Porous Membrane Electrode with Enhanced Electrochemical Activity for the High-Efficiency Oxidation of Cyclohexane." *Green chemistry* 20, no. 17 (2018): 3944-53.

Zhang, Zhong Jie, and Xiang Ying Chen. "Magnetic Greigite (Fe3s4) Nanomaterials: Shape-Controlled Solvothermal Synthesis and Their Calcination Conversion into Hematite (A-Fe2o3) Nanomaterials." *Journal of Alloys and Compounds* 488, no. 1 (2009): 339-45.

Zhang, Zixin, Guohe Huang, Yongping Li, Xiujuan Chen, Yao Yao, Shaojie Ren, Mengna Li, Yuwei Wu, and Chunjiang An. "Electrically Conductive Inorganic Membranes: A Review on Principles, Characteristics and Applications." *Chemical Engineering Journal* 427 (2022): 131987.

Zhao, Jian, Yang Li, Xinjie Wang, Xinghui Xia, Enxiang Shang, and Jawad Ali. "Ionic-Strength-Dependent Effect of Suspended Sediment on the Aggregation, Dissolution and Settling of Silver Nanoparticles." *Environmental Pollution* 279 (2021): 116926.

Zhao, Xueting, Lijuan Cheng, Ning Jia, Ruoxi Wang, Lifen Liu, and Congjie Gao. "Polyphenol-Metal Manipulated Nanohybridization of Cnt Membranes with Feooh Nanorods for High-Flux, Antifouling and Self-Cleaning Oil/Water Separation." *Journal of Membrane Science* 600 (2020): 117857.

Zhao, YC, DL Yu, HW Zhou, YJ Tian, and O Yanagisawa. "Turbostratic Carbon Nitride Prepared by Pyrolysis of Melamine." *Journal of Materials Science* 40, no. 9-10 (2005): 2645-47.

Zhao, Yiying, Ning Deng, Zhiheng Fan, Zhong-Ting Hu, Lili Fan, Jizhi Zhou, and Xin Huang. "On-Site H2o2 Electro-Generation Process Combined with Ultraviolet: A Promising Approach for Odorous Compounds Purification in Drinking Water System." *Chemical Engineering Journal* 430 (2022): 132829.

Zheng, Chao-Wen, Huai-Yuan Niu, Chao Liang, Cheng-Gang Niu, Xiu-Fei Zhao, Lei Zhang, Ji-Shan Li, *et al.* "A Study on Advanced Oxidation Mechanism of Mnco2o4/G-C3n4 Degradation of Nitrobenzene: Sacrificial Oxidation and Radical Oxidation." *Chemical Engineering Journal* 403 (2021): 126400.

Zheng, Fulin, Sin-Yee Luk, Tsz-Lung Kwong, and Ka-Fu Yung. "Synthesis of Hollow Ptag Alloy Nanospheres with Excellent Electrocatalytic Performances Towards Methanol and Formic Acid Oxidations." *RSC advances* 6, no. 50 (2016): 44902-07.

Zhou, Long, Fangyuan Xiu, Meng Qiu, Shuwei Xia, and Liangmin Yu. "The Adsorption and Dissociation of Water Molecule on Goethite (010) Surface: A DFT Approach." *Applied Surface Science* 392 (2017): 760-67.

Zhou, Xiezhen, Siqi Liu, Anlin Xu, Kajia Wei, Weiqing Han, Jiansheng Li, Xiuyun Sun, *et al.* "A Multi-Walled Carbon Nanotube Electrode Based on Porous Graphite-Ruo2 in Electrochemical Filter for Pyrrole Degradation." *Chemical Engineering Journal* 330 (2017): 956-64.

Zhou, Xingping, Siyu Ni, Xiao Zhang, Xiaqin Wang, Xuhua Hu, and Yong Zhou. "Controlling Shape and Size of Tio2 Nanoparticles with Sodium Acetate." *Current Nanoscience* 4, no. 4 (2008): 397-401.

Zhu, Jiejun, Caixia Kan, Hongchen Li, Yanli Cao, Xiaolong Ding, and Jianguo Wan. "Synthesis and Growth Mechanism of Gold Nanoplates with Novel Shapes." *Journal of Crystal Growth* 321, no. 1 (2011): 124-30.

Zhu, Wenlei, Ronald Michalsky, Önder Metin, Haifeng Lv, Shaojun Guo, Christopher J Wright, Xiaolian Sun, Andrew A Peterson, and Shouheng Sun. "Monodisperse Au Nanoparticles for Selective Electrocatalytic Reduction of CO2 to CO." *Journal of the American Chemical Society* 135, no. 45 (2013): 16833-36.

Zhuang, Houlong, Alexander J Tkalych, and Emily A Carter. "Surface Energy as a Descriptor of Catalytic Activity." *The Journal of Physical Chemistry C* 120, no. 41 (2016): 23698-706.

Zinadini, Sirus, Ali Akbar Zinatizadeh, Masoud Rahimi, Vahid Vatanpour, and Hadis Zangeneh. "Preparation of a Novel Antifouling Mixed Matrix Pes Membrane by Embedding Graphene Oxide Nanoplates." *Journal of Membrane Science* 453 (2014): 292-301.

Zong, Ruilong, Xiaolong Wang, Shikao Shi, and Yongfa Zhu. "Kinetically Controlled Seed-Mediated Growth of Narrow Dispersed Silver Nanoparticles up to 120 Nm: Secondary Nucleation, Size Focusing, and Ostwald Ripening." *Physical Chemistry Chemical Physics* 16, no. 9 (2014): 4236-41.

Zoolfakar, Ahmad Sabirin, Rozina Abdul Rani, Anthony J Morfa, Anthony P O'Mullane, and Kourosh Kalantar-Zadeh. "Nanostructured Copper Oxide Semiconductors: A Perspective on Materials, Synthesis Methods and Applications." *Journal of Materials Chemistry C* 2, no. 27 (2014): 5247-70.

Zou, Ningmu, Xiaochun Zhou, Guanqun Chen, Nesha May Andoy, Won Jung, Guokun Liu, and Peng Chen. "Cooperative Communication within and between Single Nanocatalysts." *Nature Chemistry* 10, no. 6 (2018): 607-14.